Third Generation Advanced High Strength Steels via Ultrafast Heating

Felipe Manuel Castro Cerda

Promotors: Prof R. Petrov, PhD, Prof A. Monsalve, PhD
Doctoral thesis submitted in order to obtain the academic degrees of
Doctor of Materials Engineering (Ghent University) and
Doctor en Ciencias de la Ingeniería Mención Ciencia e Ingeniería de los Materiales
(Universidad de Santiago de Chile)

GHENT UNIVERSITY

Department of Electrical Energy, Metals, Mechanical Constructions and Systems
Head of Department: Prof L. Dupré, PhD
Faculty of Engineering and Architecture

UNIVERSIDAD DE SANTIAGO DE CHILE

Departamento de Ingeniería Metalúrgica
Head of Department: Prof P. Navarro, PhD
Faculty of Engineering

Academic year 2016 - 2017

ISBN 978-90-8578-978-9
NUR 971
Wettelijk depot: D/2017/10.500/13

Members of the Examination Committee

Chair

Prof Patrick De Baets (Ghent University)

Faculty reading committee

Prof Stijn Hertelé (Ghent University)
Dr Ilchat Sabirov (Institute IMDEA Materials, Madrid, Spain)
Prof Bernd Schulz (Universidad de Santiago de Chile)
Prof Jilt Sietsma (Ghent University)
Prof Patricia Verleysen (Ghent University)

Promotors

Prof Roumen Petrov (Ghent University, *promotor*)
Prof Alberto Monsalve (Universidad de Santiago de Chile, *promotor*)

Other members

Prof Leo Kestens (Ghent University, *secretary*)

Acknowledgements

It is a pleasure to thank those who made this project possible. First of all, it is with immense gratitude that I acknowledge the support and encouragement of both of my promotors, Prof Roumen Petrov from Ghent University and Prof Alberto Monsalve from Universidad de Santiago de Chile, who offered their unconditional help, often far beyond their responsibilities, during all the stages of my Ph.D. Similarly, I owe my deepest gratitude to Prof Leo Kestens from Ghent University and Prof Bernd Schulz from Universidad de Santiago de Chile, whose contributions in the different topics of this project equals the efforts of my official promotors.

I am indebted to many of my colleagues at Ghent University for their assistance during the development of my Ph. D., particularly to Ilse Vercruysse, Roger Van Hecke, Marnix Van Dorpe, Christa Sonck, Ives De Baere and Vitaliy Bliznuk. I also wish to extend my appreciation to Prof Yvan Houbaert, Prof Patricia Verleysen and Prof Kim Verbeken for their good advice and support. Working at the Department of Materials Science and Engineering became an enjoyable activity largely due to the daily interaction in such a friendly working environment.

An important part of the experiments of this project were carried out in the laboratories of the Delft University of Technology (The Netherlands). I am deeply grateful to Richard Huizenga, Pina Mecozzi, Hans Hofman, for their technical assistance and particularly to Prof Jilt Sietsma for his support during the experiments and valuable discussions on the formation of austenite.

I consider it an honor to having worked with Ilchat Sabirov from IMDEA (Spain), for his valuable comments and experimental support on Gleeble trials. Likewise, the interest shown by Matthias Kretschmer from SMS Siemag AG. Prof Spyros Papaefthymiou from National Technical University of Athens (Greece) and Tanya Ross form Arcelor Mittal provided valuable insights on possible applications of ultrafast heating cycles to industrial lines. We hope this work might be of help in their own endeavors.

I share the credit of my work to the Department of Metallurgy of University of Santiago de Chile, particularly to Prof Stella Ordoñez, Prof Linton Carvajal, Prof Alfredo Artigas, and Prof Oscar Bustos for their support during the development of this project. The Ph.D. scholarship CONICYT-PCHA/Doctorado Nacional/2013 granted by the Comisión Nacional de Invesitgación Científica y Tecnológica (CONICYT), Chile, is also gratefully acknowledged.

During the development of my Ph.D. I had the opportunity to introduce myself in the field of computational thermodynamics and thereon finding possible applications. The always challenging first steps were assisted by Prof Malin Selleby from the Royal Institute of Technology (Sweden), whose patience to read long mails and to give detailed answers served as an encouragement for an in depth research on the subject. I would also like to thank Prof Mats Hillert form the Royal Institute of Technology (Sweden), for his valuable discussion and for sharing his opinion on the upcoming challenges in the field of physical metallurgy.

I have the feeling that for anyone who pursues a Ph.D. abroad, the people with whom one has everyday contact become the new family. I am thankful to all my colleagues at Ghent University and Delft University of Technology since I always felt part of the community.

Finally, my deepest acknowledgement goes to my beloved wife, Marion Durbahn, for her unconditional love and patience during the years I have enjoyed her company.

Table of Contents

Summary

The application of very rapid heating rates in the manufacturing of conventional steel grades has recently been proposed as a suitable means of improving both the strength and formability of these materials. This approach is desirable, because it yields a wide range of properties, without the use of heavily alloyed materials or excessively long heat treatments. Steel grades produced under very fast heating conditions have exhibited tensile properties that can fill the gap between first and second generation Advanced High Strength Steels (AHSS). Motivated by these promising results, the aim of this Doctoral project is to determine the effect of heating rate on the microstructure and mechanical properties of ultra-low, low, and medium carbon steels.

Ultrafast heating (UFH) has been widely used in the case-hardening of medium carbon steels. However, its application to low carbon sheet steel is relatively new. A yield stress of 1.2–1.5 GPa has been reported for a 0.2 %C steel subjected to the Flash® Bainite process. These values are roughly one order of magnitude higher than the yield stress obtained for the same material subjected to conventional heating (CH) rates. Furthermore, an ~200-MPa improvement in the yield stress has been reported for quenched and partitioned (Q&P) and dual-phase (DP) steel grades subjected to UFH. Very promising results have also been obtained in laboratory trials, but the implementation of the rapid heating process in large-scale industrial facilities remains an important engineering challenge.

The remarkable improvement in the mechanical properties is attributed to the general structure-refinement effect achieved after UFH. However, investigation of the microstructural interactions occurring during UFH of a cold-rolled steel is extremely challenging. This challenge arises from phase transformation of the steels during heating and cooling. Previous studies have considered the effect of the heating rate on the recrystallization and texture of, and phase transformations occurring, in carbon steels. Nevertheless, gaps in the knowledge of and a lack of consensus on some effects persist. Therefore, the experimental concept of the present work was aimed at improving the understanding of the microstructural interactions in cold-rolled steels subjected to UFH.

Experiments were performed by applying heating rates of 1–~10^3 °C/s, and then quenching the samples. To ensure repeatability, trials were performed under controlled heating and cooling conditions in a dilatometer and a Gleeble Thermomechanical Simulator. In all cases, the temperature was measured by either a type S or type K thermocouple spot welded to the sample. The resulting unique combination of microstructural features was evaluated via various characterization techniques, namely optical, scanning, and transmission electron microscopy (OM, SEM, and TEM, respectively). Texture analysis and phase quantification were performed via electron backscatter diffraction (EBSD). The x-ray diffraction (XRD) technique was employed to determine the fraction of retained austenite. Vickers hardness profiles combined with OM were used to determine the homogeneity of heat-treated specimens and to correctly select the size of the samples for tensile testing. Tensile tests on sub-sized samples from homogeneously heat-treated zones were used to measure the mechanical properties after different thermal cycles.

The initial materials and initial microstructures selected for this study were conveniently organized so that the findings in relatively simple systems can be compared with more complex ones. For example, the effect of the heating rate on the recrystallization was first investigated in a single phase ultra-low carbon steel, and then the recrystallization of cold rolled ferrite-pearlite and ferrite-martensite aggregates subjected to UFH was considered; the corresponding results are discussed in Chapter IV, VI, and VII. A similar approach was applied to the study of austenite formation under CH and UFH conditions. A thermodynamic and kinetic analysis of austenite formation is presented in Chapter V and then the concepts introduced are shown to valid for more complex systems (Chapter VI, VII, and VIII). The effect of heating rate on the mechanical properties is discussed in Chapters VII and VIII. Finally, the possibility for industrial implementation is addressed by varying all the processing parameters in a range considered realistic for industry.

The results revealed that increased heating rates yield increased kinetics of recrystallization of cold-rolled ultra-low carbon steel. This increase results in a decrease in the time required for 100% recrystallization. Consequently, the recrystallization start temperature is increased when the heating rate is raised. Consistent with the nucleation of recrystallization at high-stored-energy texture components (orientations), the texture of ferrite is characterized by near-rotated Goss {110}⟨110⟩ orientations during the initial stages of recrystallization. This represents the first-ever experimental observation of the effect of UFH on the texture of cold-rolled ultra-low carbon steel. Moreover, this finding is attributed to the reduced time for recovery and, hence, the larger stored energy (compared with that corresponding to longer recovery times) available for nucleation of new ferritic grains. The results of experiments on low carbon steel are consistent with those obtained for ULC steel. The higher carbon content of ferrite, compared with that of other phases, results in a significant difference in the kinetics of ferrite recrystallization, as well as the occurrence of the Goss {110}⟨001⟩ component at elevated temperatures.

The mechanism of austenite formation during continuous heating depends on the initial microstructure, degree of cold deformation, and the heating rate. In a ferrite-pearlite aggregate, the active mechanism can be carbon-diffusion controlled, massive, or a mixture of both. The temperature at which the mechanism transitions from diffusion controlled to massive is thermodynamically defined as A_S, and can be calculated for any steel. Furthermore, the results revealed that UFH can increase the driving force for nucleation within pearlite and in α/α interfaces. These (i.e., UFH) rates generate carbon gradients in austenite, thereby influencing the transformation products formed during cooling. In addition, carbon heterogeneities in austenite lead to a complex mixture of transformation products.

The results showed that steel grades with strength and elongation comparable to those of third generation advanced high strength steels can be produced starting from cold-rolled low carbon steels. The strength and elongation were significantly improved in low carbon steels with chemical composition suitable for DP and TRIP-assisted steels. In all cases, the best combination of mechanical properties was obtained at heating rates of ~400 °C/s, which corresponds to an intermediate value in our experiments. These results may enable the application of ultrafast heating rates in industrial-scale facilities.

Samenvatting

Het onderwerpen van conventionele staalsoorten aan zeer hoge opwarmsnelheden is onlangs voorgesteld als een geschikt middel ter verbetering van zowel de sterkte als de vervormbaarheid. Het duidelijke voordeel van een dergelijke behandeling is dat een breed gamma aan eigenschappen kan bereikt worden zonder de noodzaak van het gebruik van hoog-gelegeerde materialen of buitensporig lange warmtebehandelingen. Staalsoorten geproduceerd via deze zeer snelle gloeibehandelingen vertonen de mogelijkheid om de kloof tussen de eerste en tweede generatie van geavanceerde hoge-sterkte stalen te overbruggen. Gemotiveerd door deze veelbelovende resultaten is het doel van dit doctoraatsproject het begrijpen van het effect van de opwarmsnelheid op de microstructuur en de mechanische eigenschappen van staalsoorten met een zeer lage, lage en gemiddelde koolstofconcentratie.

Ultrasnel opwarmen (UFH) wordt reeds op grote schaal toegepast in de verharden van het oppervlak van medium koolstofstaal. Echter, de toepassing ervan op staal met een laag gehalte aan koolstof is relatief nieuw. De vloeispanning gerapporteerd in staalsoorten met 0,2% aan C geproduceerd via het 'Flash Bainite' proces was 1,2-1,5 GPa; deze waarde is ongeveer één grootte-orde hoger dan de vloeispanning die opgemeten wordt in hetzelfde materiaal dat geproduceerd werd aan conventionele opwarmsnelheden. Een verbetering van de vloeispanning met ~ 200 MPa is gerapporteerd in Q&P (afgeschrikt en gepartitioneerd) en DP (tweefazige) staalsoorten na het toepassen van ultrahoge opwarmsnelheden. Deze veelbelovende resultaten zijn echter verkregen in een laboratoriumopstelling. Voor de uitvoering ervan op een grootschalige, industriële schaal zijn er echter nog heel wat belangrijke technische uitdagingen die moeten aangepakt worden.

De significante verbetering van de mechanische eigenschappen wordt beschouwd als zijnde een gevolg van de algemene verfijning van de (micro)-structuur na toepassing van ultrasnelle opwarmingsexperimenten. Echter, de interacties die plaatsgrijpen op microstructureel niveau in koudgewalst staal dat blootgesteld wordt aan zeer hoge opwarmsnelheden zijn uitermate complex om te onderzoeken. Eén van dergelijke complicaties zijn de fasetransformaties die optreden in het staal gedurende het verhitten en afkoelen. In de literatuur is reeds sterk uiteenlopende informatie voorhanden die de invloed van opwarmsnelheden op de herkristallisatie, de textuurvorming en de fazetransformatie in koolstof staal behandelt. Niettemin hebben deze lacunes in de informatie enerzijds en het gebrek aan overeenstemming aangaande bepaalde invloeden anderzijds het huidige werk geïnspireerd; hieruit werden nieuwe inzichten bekomen voor het begrijpen van de interacties op een microstructureel niveau in koudgewalst staal dat blootgesteld werd aan zeer hoge opwarmsnelheden.

Experimenten werden uitgevoerd waarin opwarmsnelheden variërend van 1 - ~ 10^3 °C/s zijn toegepast, gevolgd door afschrikken. Om de reproduceerbaarheid te garanderen werden de experimenten uitgevoerd in de dilatometer en een Gleeble thermo-mechanische simulator onder gecontroleerde omstandigheden van opwarmen en afkoelen. Steeds werd de temperatuur gemeten door ofwel een S-type of K-type thermokoppel dat aan het te onderzoeken monster gepuntlast werd. De unieke combinatie van de microstructurele veranderingen gecreëerd door hoge opwarmsnelheden werd onderzocht via verschillende karakterisatietechnieken, namelijk

optische (OM), raster (SEM) en transmissie elektronen microscopie (TEM). Textuuranalyse en fasekwantificering werden uitgevoerd met behulp van diffractiemetingen van teruggestrooide elektronen diffractie (EBSD). X-stralendiffractie (XRD) werd toegepast om de fractie van austeniet te bepalen. Profielmetingen van de Vickers hardheid in combinatie met OM werden toegepast om de homogeniteit van de warmtebehandelingen te bepalen. Trekproeven op staalmonsters met kleine afmetingen werden uitgevoerd om de mechanische eigenschappen te kwantificeren na verschillende thermische cycli.

De basismaterialen en de initiële microstructuren werden voor dit onderzoek bewust zo geselecteerd dat de resultaten in relatief eenvoudige systemen kunnen vergeleken worden met de meer complexe. Zo werd het effect van de opwarmsnelheid op de herkristallisatie eerst onderzocht in enkelfazig ultralaag koolstofstaal (hoofdstuk IV) en later op aggregaten van ferriet-perliet en ferriet-martensiet (hoofdstukken VI en VII). Een soortgelijke werkwijze werd toegepast in de studie van de vorming van austeniet onder zowel conventionele als ultrahoge opwarmsnelheden. Een thermodynamische en kinetische analyse van de vorming van austeniet is beschreven in hoofdstuk V; de in hoofdstuk V geïntroduceerde concepten blijken ook consistent te zijn met/in de meer complexe systemen (hoofdstuk VI, VII en VIII). Het effect van de opwarmsnelheid op de mechanische eigenschappen is besproken in de hoofdstukken VII en VIII. Ten slotte werden de mogelijkheden van een industriële implementatie onderzocht door alle verwerkingsparameters te variëren in een gebied dat beschouwd wordt als realistisch/toepasbaar in de industrie.

Het is aangetoond voor koudgewalst staal met een ultralaag koolstofgehalte dat de verhoging van de opwarmsnelheid de kinetiek van de herkristallisatie versnelt. Dit volgt uit de vermindering van de tijd die nodig is om 100% herkristallisatie te bereiken als de opwarmsnelheid vergroot. Verder neemt de temperatuur waarbij de herkristallisatie begint toe wanneer hogere opwarmsnelheden worden toegepast. De textuurvorming van ferriet in een vroeg stadium van herkristallisatie vertoont oriëntaties kortbij de geroteerde Goss {110} <110>. Deze oriëntatie is in overeenstemming met een hoge opgeslagen energie. Deze bevinding, voor het eerst gerapporteerd als gevolg van UFH, kan worden verklaard door de verminderde hersteltijd en dus de grotere opgeslagen energie voor kiemvorming van nieuwe ferritische korrels. Experimenten in staal met een laag koolstofgehalte vertonen resultaten die in een sterke/goede overeenstemming zijn met het ULC staal. Het hogere koolstofgehalte in ferriet (in laag koolstofstaal vergeleken met de ultra-lage variant) resulteert in een duidelijk verschil in de kinetiek van de herkristallisatie, alsook in de verschijning van de Goss {110} <001> component bij hogere temperaturen.

Het mechanisme van de vorming van austeniet tijdens continue opwarming wordt beïnvloed door de initiële microstructuur, de graad van koudvervorming en de opwarmsnelheid. In een ferriet-perliet aggregaat kan het actieve mechanisme koolstofdiffusie gecontroleerd zijn, massief zijn of een combinatie van beiden zijn. De temperatuur waarbij het diffusie-gecontroleerde mechanisme overgaat in het massieve mechanisme is thermodynamisch gedefinieerd als A_S, en kan worden berekend voor elk staal. Ook wordt aangetoond dat UFH de drijvende kracht voor nucleatie binnenin perliet en α/α interfaces kunnen verhogen. Ultrasnelle opwarming produceert/geeft

aanleiding tot koolstofgradiënten in austeniet en beïnvloedt bijgevolg de transformatieproducten die gevormd worden tijdens het afkoelen. Het is aangetoond dat koolstof-heterogeniteiten in austeniet een complexe combinatie van transformatiesproducten creëert.

De resultaten hebben aangetoond dat staalsoorten met een sterkte en een vervormbaarheid in het gebied van de derde generatie van geavanceerde hoge-sterkte stalen geproduceerd kunnen worden uitgaande van een koudgewalst staal met een laag koolstofgehalte. De sterkte en vervormbaarheid zijn aanzienlijk verbeterd in koolstofarm staal waarvan de chemische samenstelling geschikt is voor de productie van DP en TRIP-geassisteerde stalen. In alle gevallen werd de beste combinatie van mechanische eigenschappen gemeten bij opwarmsnelheden van ~400 °C/s, wat overeenkomt met een tussenliggende waarde in onze experimenten. Deze resultaten tonen dat de toepassing van een ultrasnelle opwarming op industriële schaal mogelijk kan zijn.

List of abbreviations

AHSS	*Advanced High Strength Steels*
CH	*Conventional Heating*
EBSD	*Electron Backscattered Diffraction*
FM	*Ferrite And Martensite Initial Microstructure*
FP	*Ferrite And Pearlite Initial Microstructure*
HRTEM	*High Resolution Transmission Electron Microscopy*
HV	*Hardness Vickers*
LC	*Low Carbon*
OM	*Optical Microscopy*
PAG	*Parent Austenite Grain*
RA	*Retained Austenite*
RD	*Rolling Direction*
SEM	*Scanning Electron Microscopy*
TD	*Transversal Direction*
UFH	*Ultrafast Heating*
ULCS	*Ultra-Low Carbon Steels*
XRD	*X-Ray Diffraction*

List of publications

[1] F.M. Castro Cerda, C. Goulas, I. Sabirov, S. Papaefthymiou, A. Monsalve, R.H. Petrov, Microstructure, texture and mechanical properties in a low carbon steel after ultrafast heating, Mater. Sci. Eng. A. (2016) 17-20. doi:10.1016/j.msea.2016.06.056.

[2] F.M. Castro Cerda, F. vercruysse, T. Nguyen Minh, L. A. I. Kestens, A. Monsalve, R.H. Petrov, The effect of heating rate on the recrystallization behaviour in cold rolled ultra low carbon steel, Steel Res. Int. 88 (2017). doi: 10.1002/srin.201600351.

[3] F.M. Castro Cerda, L. A. I. Kestens, A. Monsalve, R.H. Petrov, The effect of ultrafast heating in cold-rolled low carbon steel: Recrystallization and texture formation, Metals (2016). doi: 10.3390/met6110288.

[4] F.M. Castro Cerda, B. Schulz, S. Papaefthymiou, A. Artigas, A. Monsalve, R.H. Petrov, The effect of ultrafast heating in cold-rolled low carbon steel: Formation and decomposition of austenite, Metals (2016). doi:10.3390/met6120321.

[5] F.M. Castro Cerda, I. Sabirov, C. Goulas, J. Sietsma, A. Monsalve, R.H. Petrov, Austenite formation in 0.2 %C and 0.45 %C steels under conventional and ultrafast heating, Mat. Des. 116 (2017) 448–460. doi: 10.1016/j.matdes.2016.12.009.

Presentations to congresses

[1] F.M. Castro Cerda, C. Goulas, B. Schulz, A. Artigas, R.H. Petrov, A. E. Monsalve, Development Of Third Generation Advanced High Strength Steels (AHSS) Via Ultrafast Heating, in: SAM/CONAMET, Córdova, 2016.

[2] F.M. Castro Cerda, K. Goulas, I. Sabirov, S. Papaefthymiou, A. Monsalve, R.H. Petrov, The effect of fast annealing on the strength and microstructure of CMnAlSi TRIP steel, in: THERMEC, 2016.

[3] F.M. Castro Cerda, F. Vercruysse, C. Goulas, L. Kestens, A. Monsalve, R. Petrov, The Effect of the Heating Rate in the Recrystallization of Pure Iron and Carbon Steel, in: 6th Int. Conf. Recryst. Grain Growth, Pittsburgh, 2016.

[4] A. Verdiere, A.B. Llanes, F.M. Castro Cerda, L. Crebolder, R. Petrov, Heat treatment, microstructure and properties of 75CR1 steel, for use in heavy loaded elements, in: XIII Int. Congr. Mach. Technologies, Mater., Borovets, 2016: pp. 38–41.

[5] F.M. Castro Cerda, A. Monsalve, R.H. Petrov, I. Sabirov, B. Schulz, Electron back-scattered diffraction study of the austenite formation in 0.2% C steel, in: CONAMET/SAM 2015, Concepción, 2015.

[6] F.M. Castro Cerda, B. Schulz, A. Monsalve, R.H. Petrov, Simulation of segregation in hardenable steels using Dictra software, in: CONAMET/SAM 2015, Concepción, 2015.

[7] S. Papaefthymiou, C. Goulas, F.M. Castro Cerda, J. Sietsma, R.H. Petrov, Microstructural Evolution During Ultrafast Heat Treament Of Medium Carbon Steels, in: Proc. Int. Conf. Solid-Solid Phase Transform. Inorg. Mater., Whistler, 2015: pp. 569–570.

Chapter I

Third Generation Advanced High Strength Steels

I-1 Introduction

Owing to the safety and fuel efficiency standards associated with the environmental and legal authority regulations (EU and USA) [1,2], it has become increasingly challenging for the steel industry to produce materials with enhanced properties. Under these regulations, the use of first and second generation AHSS [3,4] will decrease significantly. Automakers are therefore searching for materials with increased strength and formability capacities, in order to address the gap in properties associated with first and second generation AHSS [4]. These new engineering materials are referred to as third generation AHSS.

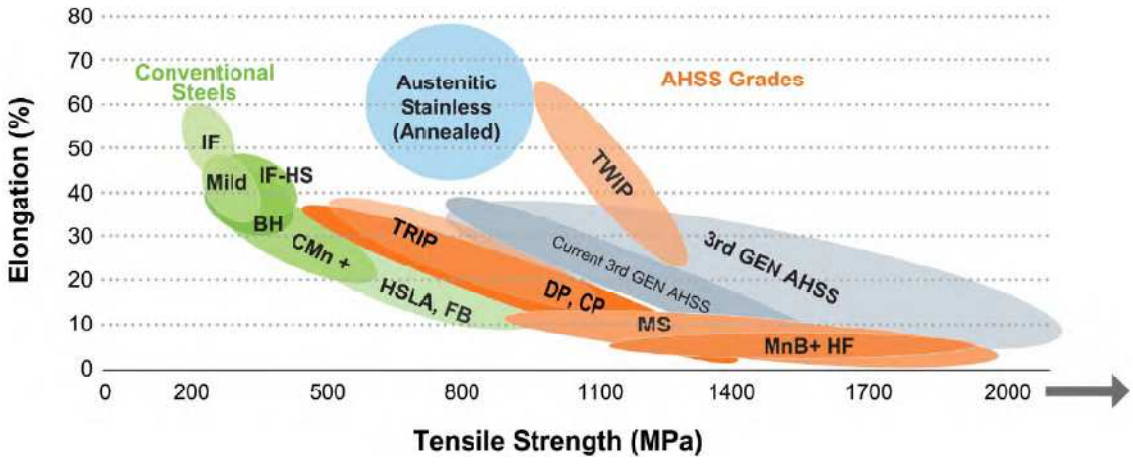

Fig. I-1. Tensile strength (MPa) versus elongation (%) of current steel grades [2].

Many iron alloys are potential candidates for becoming AHSS and, hence, a suitable classification system is required. However, various classifications are applied for steel used in automotive applications. The first and simplest classification is based on the chemical composition. The American Society for Automotive Engineers (SAE) standard for steel uses four numbers, XXYY, to describe each grade. The first two digits (XX) and the last two digits (YY) denote the main alloying elements and the carbon content in the alloy, respectively. In the second system, steels are classified based on microstructural features; for example, Interstitial Free (IF), Dual-Phase (DP), Transformation-Induced Plasticity (TRIP), Complex Phase (CP), Martensitic (M), Bake Hardened (BH), Twinning-Induced Plasticity (TWIP), and Quenched and Partitioned (Q&P) steels. Press hardened steels (PHS) [4] also fall under this classification. A third classification encompasses the various mechanical properties and forming parameters (including the yield strength, total

elongation, work hardening exponent) of different steels [2,3]. Fig. I-1 shows an example of two properties, tensile strength and elongation, of the current steel grades.

Tensile strengths and elongation of 0.6–1.6 GPa and 10–40%, respectively, are expected for third generation AHSS [2,3]. These mechanical properties result from a carefully selected chemical composition and processing path, which lead to a unique combination of microstructural features. In terms of processing path, the desired range of properties may be achieved via rapid heating followed by quenching.

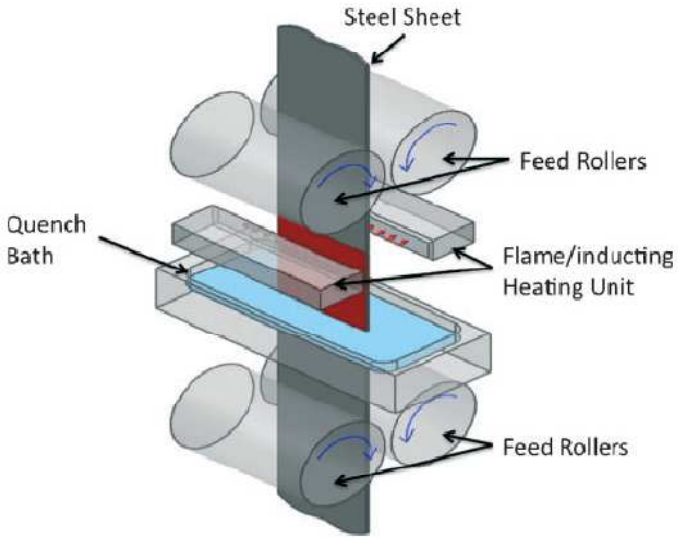

Fig. I-2. Experimental set-up for the Flash® Bainite process [5].

I-2 Ultrafast heating (UFH) as an approach to third generation AHSS

In the present study, a range of heating rates is defined to avoid terminology errors. Conventional Heating (CH) rates (maximum of ~10 °C/s) are achievable by current processing lines. Fast heating rates and ultrafast heating rates range from 10 °C/s to 100 °C/s and are >100 °C/s, respectively. Ultrafast heating experiments on pure iron and steel have been performed for several decades and have revealed [6] that various microstructures, and therefore mechanical properties, are obtained after rapid heating. Recently [3], this approach has been proposed as a possible means of obtaining steel grades with mechanical properties comparable to those of third generation AHSS. One potential industrial application of UFH is the Flash® Bainite process [7], where flame heating is followed by water quenching, as shown in Fig I-2. In tube production, yield and tensile strengths of 1.2 GPa and 1.5 GPa were obtained for AISI 1020 steel; values of 1.4 GPa and 1.8 GPa were obtained for AISI 4130 steel [7].

Other authors have reported that mechanical properties comparable to those of third generation AHSS were obtained after applying UFH rates to conventional grades of low carbon steel [8]. This improvement was attributed to the extremely fine average ferritic grain size and the mixture of

phases formed during the cooling stage; this mixture results from the compositional gradients produced during fast heating.

Despite the promising results that have been published to date, many unknowns persist regarding the UFH of steel. These include:

i. Other potential applications of UFH processes in flat products: Most of the previous and ongoing studies of flat steel products have focused mainly on recrystallization and austenite formation/decomposition. The application of UFH cycles to tempering of the martensitic microstructure may reduce the time required for this process.
ii. Large-scale mechanical characterization: Promising mechanical properties have been reported for steel subjected to UFH. However, these were obtained for material limited to the size of a heat-treatment sample. Cylindrical specimens with a maximum diameter of ~20 mm [9] are allowed for experiments in the Gleeble 3800. The type of mechanical tests possible on a specimen of such dimensions is rather limited and, hence, data are required to evaluate the following characteristics of the resulting UFH material:
    a. standard tensile properties
    b. hole expansion ratio
    c. crash performance
    d. formability/deep drawing performance
    e. fatigue properties
iii. Transferability of laboratory-scale treatments into industrial standards: Factors (for example, the temperature distribution within the sample) involved in the laboratory-scale development of UFH treatments must be carefully controlled. These factors must be considered during the scaling of laboratory set-ups to industrial scale. Among the most important factors that should be considered are:
    a. Heat transfer over the full width and thickness of the plate: The heating applied (magnetic induction, flame) may generate considerable fluctuations in the heat distribution over the width and thickness of the material.
    b. Influence of the heat distribution and time on the microstructure: Differences in heat distribution can produce significant changes in the microstructure and, hence, in the properties of the material.
    c. Material distortion after UFH and cooling cycles: Very fast heating rates might leave only a small amount of time for strain accommodation during austenite formation and subsequent decomposition.
iv. Effect of UFH on the microstructure: The number of studies aimed at determining the effect of fast and very fast heating on steel and other alloy systems has increased in recent years. However, an in-depth understanding of the following topics is still required:
    a. Formation of austenite: Austenite will transform during cooling. Therefore, direct observation of austenite formation is only achievable via in-situ techniques.
    b. Recrystallization of cold-rolled microstructure: The kinetics of recrystallization process is sensitive to the heating rate. However, the actual nature of the

interaction between (i) recovery and (ii) recrystallization with the heating rate must be determined.

c. Interaction between recrystallization and phase transformation: Recrystallization and phase transformations occur concurrently during the annealing of cold-rolled low carbon steel.
d. Texture formation: Compared with conventional heating rates, UFH rates result in more significant changes in the recrystallization textures of low carbon steel.
e. The effect of initial microstructure: Austenite formation is a structure-sensitive process and, hence, is affected by the starting microstructure as well as the heating rate.
f. The effect of the amount of cold deformation: The driving force for recrystallization stems from the stored energy introduced by cold working. The interaction of the amount of cold working with the heating rate can significantly affect the kinetics of the process and texture formation.
g. The effect of chemical composition: Carbide-stabilizing alloying elements can reduce the amount of carbon that dissolves in austenite during the limited times employed in UFH cycles.
h. Influence of electric/magnetic fields: UFH of steel is often achieved via the Joule effect or magnetic induction. The influence of magnetic or electric fields on the microstructure of steel subjected to very fast heating rates remains unexplored.

A thorough understanding of these variables will ensure that optimal processing variables are applied for obtaining suitable structure/property relationships from current and future applications of UFH.

I-3 Aim of this work

The aim of this work is to understand the formation of fine-grained steel microstructures in AHSS and determine their mechanical properties after UFH. For this purpose, steel grades obtained at CH rates are compared with their counterparts obtained via UFH cycles.

The chemical composition of each steel used in this work corresponds to the family of low to medium carbon steels. The effect of heating rate on austenite formation was first studied in as-rolled plain 0.2 %C and 0.45 %C steels (ferrite and pearlite, FP). Furthermore, microstructural evolution of the materials was evaluated via UFH experiments on cold-rolled FeCMnSi, FeCMnSiAl, and FeCMnCrMoNb steels and the mechanical properties of the heat-treated specimens were determined. In addition, experiments were performed on ULC steel to determine the effect of the heating rate on recrystallization and texture formation.

The UFH experiments were developed in the form of 'peak-annealing' cycles, which are most effectively performed in a Dilatometer and a Gleeble thermomechanical simulator. Microstructural variations, owing to thermal fluctuations along the specimens, were measured in

order to avoid sampling non-representative sections of the microstructure. Various heating and cooling rates have been selected to achieve similar scenarios to industrial conditions.

Microstructural characterization was performed via Optical (OM), Scanning (SEM), and High Resolution Transmission Electron Microscopy (HRTEM), and texture analysis was conducted via Electron Backscatter Diffraction (EBSD). The fraction of retained austenite (RA) was determined from X-ray diffraction (XRD) measurements. Owing to the nature of the experiments, microstructural variations were determined via Vickers hardness (HV) versus distance profiles and corroborated with OM analysis. Tensile tests were performed on sub-standard-sized specimens in the homogeneous regions of the heat-treated samples. The gage length of all the tensile specimens was kept parallel to the rolling direction (RD). After the tensile test, the fracture surface was examined via SEM, and the observations were correlated with the mechanical properties.

I.-4 References

[1] R. Kuziak, R. Kawalla, S. Waengler, Advanced high strength steels for automotive industry, Arch. Civ. Mech. Eng. 8 (2014) 511. doi:10.1016/S1644-9665(12)60197-6.

[2] S. Keeler, M. Kimchi, R. Kuziak, R. Kawalla, S. Waengler, Y. Weng, H. Dong, Y. Gan, Advanced high strength steels for automotive industry, Arch. Civ. Mech. Eng. 8 (2014) 511. doi:10.1016/S1644-9665(12)60197-6.

[3] E. De Moor, P.J. Gibbs, J.G. Speer, D.K. Matlock, A.S. Processing strategies for third-generation advanced high-strength steel development, AIST Trans. 7 (2015) 2010.

[4] K.D. Matlock, G.J. Speer, Third Generation of AHSS: Microstructure Design Concepts, in: A. Haldar, S. Suwas, D. Bhattacharjee (Eds.), Microstruct. Texture Steels Other Mater., Springer London, London, 2009: pp. 185–205. doi:10.1007/978-1-84882-454-6_11.

[5] T. Lolla, G. Cola, B. Narayanan, B. Alexandrov, S.S. Babu, Development of rapid heating and cooling (flash processing) process to produce advanced high strength steel microstructures, Mater. Sci. Technol. 27 (2011) 863–875. doi:10.1179/174328409x433813.

[6] Y.Y. Meshkov, E.V. Pereloma, Phase Transformations in Steels, Elsevier, 2012. doi:10.1533/9780857096104.4.581.

[7] G. Cola, Flash bainite, (n.d.). http://www.flashbainite.com/.

[8] R.H. Petrov, A. Puype, D. De Knijf, L. Kestens, Ultrafast heating of advanced high strength steels, in: M. Militzer, G. Botton, L.-Q. Chen, J. Howe, C. Sinclair, H. Zurob (Eds.), Proc. Int. Conf. Solid-Solid Phase Transform. Inorg. Mater. 2015, 2015: pp. 1157–1158.

[9] Gleeble® 3500 System, (n.d.). http://www.gleeble.com/products/gleeble-3500.html.

Chapter II

State of art

This chapter describes the microstructural evolution that occurs during rapid heating of pure iron and hypoeutectoid carbon steel with a ferrite-cementite initial microstructure. Particular attention has been given to the effect of heating rate on the recrystallization, phase transformations, and mechanical properties. Sections II-1 and II-2, where microstructural evolution is addressed in detail, present a summary of the findings from the most relevant studies on each of these topics. These sections serve as a building block for a discussion (Section II-3) of the corresponding structure-property relationships.

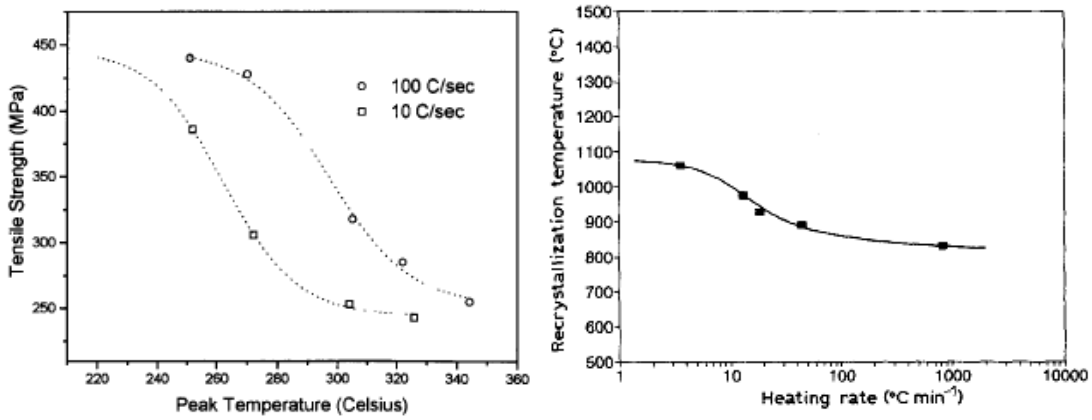

Fig. II-1. (a) Anisothermal recrystallization curves for ETP copper heated at 10 °C/s (squares) and 100 °C/s (circles) [6] and (b) Recrystallization temperature versus heating rate for cold worked tantalum [14].

II-1. The effect of HR on recrystallization

II-1.1 Metallic systems

A general description for the effect of heating rate on the recrystallization of cold-worked metals remains elusive. Clarebrough et al. [1–4] have shown that the recrystallization rate of a Cu-31Zn alloy increases when the heating rate is increased from ~0.03 °C/s to ~0.1 °C/s. Furthermore, as the heating rate is increased, the thermal peaks of recrystallization (and recovery) are shifted to higher temperatures than those associated with low heating rates. Similar trends were observed for copper [5,6] heated at rates ranging from 50 °C/s to 500 °C/s. An analogous effect on the displacement of recrystallization has been observed (albeit without a decrease in the reaction

time) for commercially pure titanium [7] heated at rates of 1 °C/s–500 °C/s. Fast recrystallization kinetics has also been reported for pure Mo heated at rates of up to 17 °C/s [8].

In contrast, the heating rate resulted in a marked decrease in the onset temperature of recrystallization in Al-based alloys, whereas the degree of softening and grain refinement both increased [9–13]. Similarly, the recrystallization temperature of high purity tantalum (Fig. II-1) [14] decreased substantially (i.e., from ~1100 °C to ~900 °C) when the heating rate was increased from ~1 °C/s to 1000 °C/s [14].

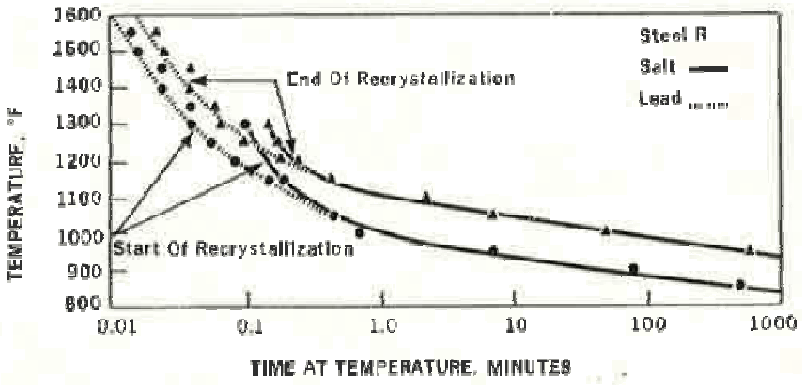

Fig. II-2. Mixed isochronal-isothermal experiments on rimmed steel (0.07C-0.3Mn-0.007Si) [16]. Samples inserted in molten lead and molten salt. Molten salt heats up faster than lead.

II-1.2 Recrystallization kinetics of steel

Early studies [5,15–17] reported that a marked softening effect occurred in cold-rolled ULC and low carbon steel subjected to fast and ultrafast heating rates. However, these experiments typically combined different heating rates and holding times at the peak temperature. In other words, a mixture of isochronal (also referred to as 'anisothermal') and isothermal processes was considered, as in the case of the rimmed and Al-killed steel shown in Fig. II-2. The figure shows that the time required for complete recrystallization decreases with increasing heating rate, and the onset of recrystallization is shifted to higher temperatures than those associated with low heating rates. In 1999, Atkinson [18] attributed the results obtained from early experiments on rapid recrystallization annealing of low carbon steel to specific mechanisms that operate during annealing. According to that work, in addition to dislocation-arrangement effects, ultrafast heating (UFH) leads to a decrease in the onset of recrystallization and rapid softening can be expected after. He argues that UFH provides ideal conditions at the recovery stage, thereby leading to accelerated softening. However, Muljono et al. [19,20] claimed that UFH would increase the temperature of recrystallization, and supported their conclusions with experiments on low and very low carbon steel heated at rates of up to 1000 °C/s. The effect of heating rate on the start and finishing of recrystallization is shown in Fig. II-3. As the figure shows, recrystallization is shifted to higher temperatures as the heating rate is increased. After applying a model for anisothermal

recrystallization, Muljono et al. concluded that Atkinson's conclusions were based on experimental artifacts.

In a subsequent paper, Atkinson [21] attributed the results presented by Muljono et al. to the interaction of interstitial solute atoms with the deformed ferrite matrix. These atoms might act as barriers to dislocation motion and thereby hinder the nucleation of new grains. This type of 'aging' step yields the high recrystallization temperatures reported in [19,20]. As proposed in [18], rapid heating may provide suitable conditions for significant changes in the recovery characteristics, thereby leading to an increased rate of recrystallization. This effect has already been described for Al-based alloys and tantalum (see Section II-1.1). However, detection of fast anisothermal recrystallization in steel might be rather difficult. This difficulty arises from either the (i) extremely low interstitial solute-atom content theoretically required to produce a barrier to dislocation movement or (ii) extremely high heating rates required to overcome the effect of interstitial solute atoms in dislocations.

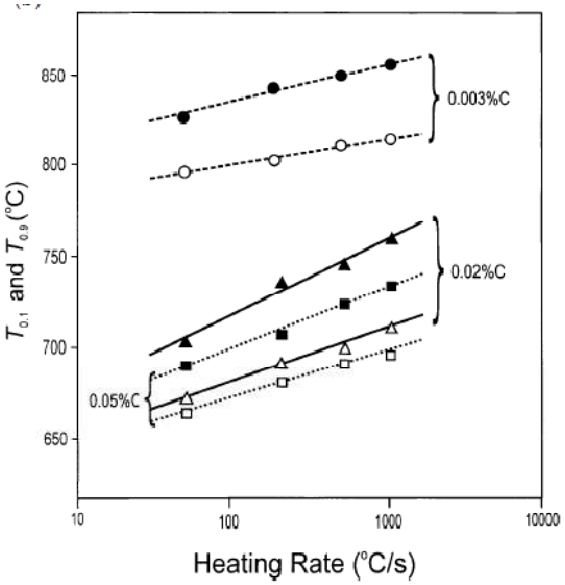

Fig. II-3. The temperatures required to start recrystallization ($T_{0.1}$) (open symbols) and complete recrystallization ($T_{0.9}$) (filled symbols) for 0.003 %C, 0.02 %C, and 0.05 %C steels [19].

In 2003, Kestens et al. [22], reported that the recrystallization temperature of ferrite increased with increasing heating rate of a 95% cold-deformed IF steel subjected to UFH (Fig. II-4). These results concur with those reported for low carbon steel, cf. Fig. II-3. According to [18,21], the absence of interstitial atoms in the deformed matrix should enhance the UFH softening effect. However, precipitates may also affect dislocation motion [23,24]. Moreover, IF steel exhibits sluggish recrystallization kinetics, even up to 99% cold deformation [25]. Relatively recent studies [26,27] on the effect of heating rate on a cold-deformed low carbon steel indicated that the onset temperature of recrystallization increases with increasing heating rate. Nevertheless, the heating rates employed in these references are significantly lower (~300 K/s) than those employed in the present work. The effect of the C and N in solution was evaluated during annealing of a very low

carbon steel at heating rates of up to 1000 °C/s [28]. The results revealed that, at low heating rates, interstitial atoms have a considerably greater influence on recrystallization kinetics than at higher heating rates. The general conclusions concur with previous experiments on low and ULC steels. Furthermore, the features associated with recrystallization of ferrite in low carbon steel of chemical composition suitable for DP and TRIP-aided grades are consistent with those reported in previous studies [29–34].

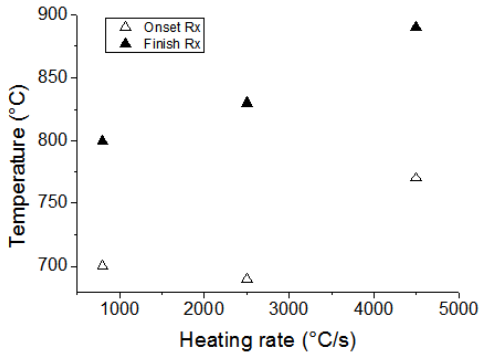

Fig. II-4. The onset (outlined) and finish (filled) temperature of recrystallization versus the heating rate applied to IF steel [22].

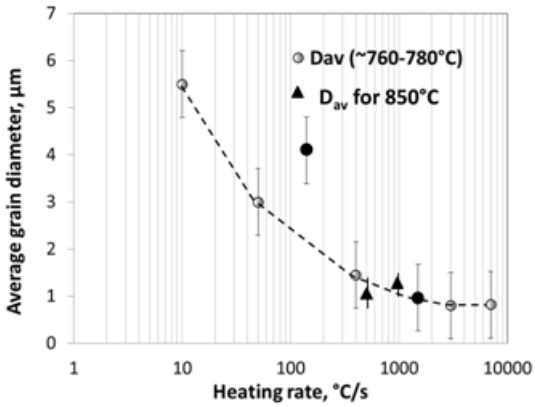

Fig. II-5. Average grain diameter versus heating rate applied to low carbon steel [33].

II-1.3 Effect on ferrite grain size

The refinement effect of UFH on recrystallized ferritic grains in low carbon steel has been widely reported [15,17,19,20,22,29–36]. Measurements in low and ULC steels show that the grain size of recrystallized ferrite decreases after annealing cycles at temperatures of up to 1000 °C/s [19,20]. This refinement effect was also reported for IF steels [22], where the average ferrite grain size was reduced to a saturation value of 6 µm (at ~1000 °C/s), after which no further grain refinement was observed. Similar results were obtained from measurements of the ferrite grain size of TRIP steels

subjected to various heating rates [29–34]. The refinement effect results from the large driving force available for nucleation. However, a small saturated ferrite grain size (~1.5 μm, cf. Fig. II-5) is measured for material with significant fractions of other constituents (for example, pearlite) in the initial microstructure. This suggests that the deformed ferrite interacts with second-phase grains during recrystallization and various stages of phase transformation. The banding of the microstructure may also play a role in the extent of ferrite growth.

II-1.4 Effect on texture evolution

When complete recrystallization occurs before the onset of austenite formation, the orientation components in IF steel are (in general) retained [22]. Similar trends are observed for low and ULC steels [17,26,27]. However, the texture of cold-rolled low carbon steels with initial microstructure of ferrite and pearlite changes substantially after CH at fast heating rates (10 °C/s and 50 °C/s). Specifically, the initial cold-rolling texture changes to a recrystallization-type texture, which is characterized by a strong {111}⟨uvw⟩ (ND fibre) with significant curvature, and a rather weak {hkl}⟨110⟩ RD-fibre component [29]. In contrast, the texture of the cold-rolled samples heated at 1000 °C/s and 3000 °C/s remains almost unchanged even after reheating to 880 °C; in other words, the characteristic features of the BCC cold rolling texture are retained. Petrov et al. [30,33,34] attributed the textural influence of UFH to carbide-precipitate stabilization of the recovered structure of deformed ferrite and the subsequent contribution of this stabilization to the overall texture. Fig. II-6 shows the typical textures formed at low and very rapid heating rates. Previous studies [29–34] have also shown that UFH and quenching resulted in negligible changes in the rolling texture of steels with initial microstructure of cold-rolled ferrite and martensite.

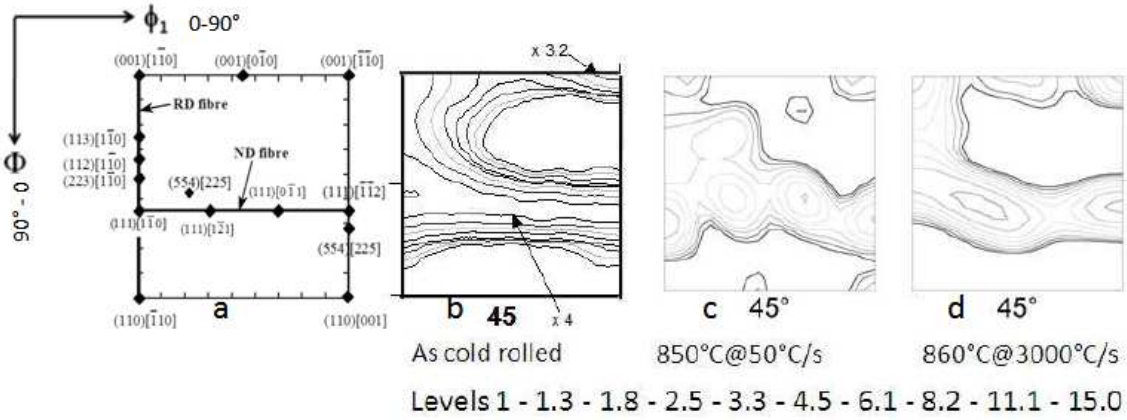

Fig. II-6. The effect of heating rate on cold-rolled ferrite plus pearlite low carbon steel. (a) Ideal positions of the most important BCC texture components in the φ_2 = 45° section of Euler space, (b) 95% cold-rolled material, (c) heated at 50 °C/s–860 °C and quenched, and (d) heated at 3000 °C/s–860 °C and quenched [30].

II-2 The effect of HR on the formation of austenite

Seminal studies of austenite formation have focused mainly on pure iron [37–40] and steel with initial microstructure consisting of ferrite and spheroidized cementite [39,41–46], as well as ferrite and pearlite [39,46–48]. Other pioneering works have focused on martensite [48,49], bainite, and mixtures of these constituents as starting microstructures for the isothermal formation of austenite [50–52]. However, most of these experiments were conducted under isothermal conditions [50–62]. Therefore, in this chapter, the analysis will focus on the isochronal (anisothermal) formation of austenite starting from pure iron and steel with ferrite and pearlite initial microstructure.

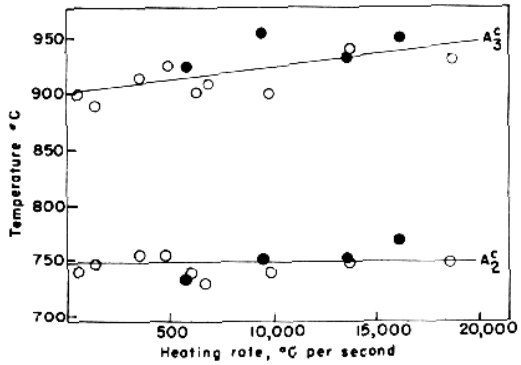

Fig. II-7. The effect of heating rate on the formation of austenite in ARMCO pure iron [37]. Outlined circles show data of samples in which the alumel is the central thermocouple element, whereas filled circles correspond to chromel as the central element.

II-2.1 Pure iron

In pure-iron polycrystalline aggregates, austenite is formed by means of a massive transformation [37,39]. However, evidence has also been presented of a martensitic transformation mechanism that operates during heating of pure iron whiskers and UFH of pure polycrystalline iron [38,40]. The onset temperature of austenite formation A_{c1} changes only slightly with the heating rate, cf. Fig. II-7. In general, nucleation begins at grain corners and edges. In the case of accelerated heating, austenite formation is displaced to higher temperatures, compared with the equilibrium transformation temperature. The mobility of the γ–α interface and the driving force for the reaction both increase with increasing temperature, thereby resulting in fast kinetics of austenite formation during UFH experiments.

II-2.2 Carbon steel with pearlite initial microstructure

Most of the main characteristics of austenite formation starting from ferrite and pearlite aggregates have been summarized by Mehl [48]. These characteristics are given as follows: (i) Austenite formation is a thermally activated process, (ii) austenite is nucleated at pearlite

boundaries, (iii) carbon gradients form during the growth of austenite [47], (iv) the time for 100% austenite formation decreases with decreasing pearlite interlamellar spacing and is relatively independent of the colony size, and (v) the kinetics of cementite dissolution is significantly slower than that of ferrite transformation. Subsequent studies [46,51–63,71–82] have validated these conclusions which have served as a reference for diffusion models of austenite formation. Fig-II-8 shows austenite formation in a ferrite plus pearlite microstructure. Consistent with (ii), austenite (transformed into martensite on quenching) forms at the ferrite/pearlite boundaries, as indicated by the arrows.

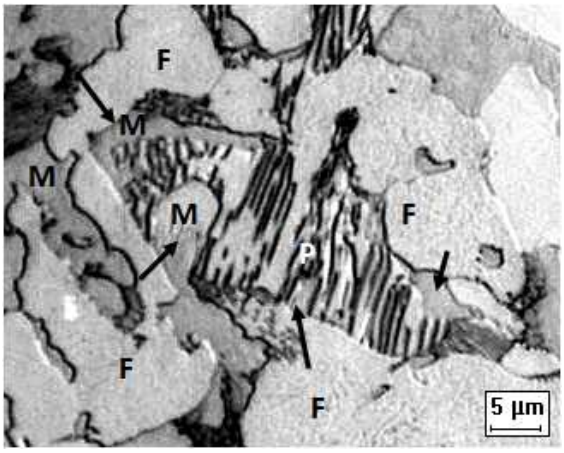

Fig. II-8. Austenite formation in a ferrite plus pearlite microstructure. F, P, and M denote ferrite, pearlite, and martensite, respectively. Scale bar is 5 µm.

II-2.3 Mixed ferrite and pearlite

Recently, Meshkov and Pereloma [64] summarized some of the key theoretical aspects associated with UFH of carbon steel. The most important features are, namely: the (i) initial microstructure has an effect on the mechanism of austenite formation (as previously reported by Gridnev and Trefilov [49]), (ii) nucleation stage is governed by either diffusional or diffusionless mechanisms, and (iii) growth stage is governed by either diffusion-controlled or interface-controlled (massive) mechanisms. Regarding (ii), Kaluba et al. [65] have initiated debates [65–69] by attributing austenite formation during the application of extremely high heating rates to a so-called bainitic transformation mechanism. Based on the results of experiments performed on low carbon steels, the present authors concur with Hillert [68] about the observations reported by Kaluba et al. [63]. Experimental evidence of massive transformation in medium carbon steel has been published elsewhere [70,78,81], even for heating rates as low as 1 °C/s.

Several attempts have been made to model the anisothermal formation of austenite from ferrite-pearlite initial microstructures [71–84]. Most of the data used in the model were obtained via dilatometry experiments, where heating rates of 0.01–20 °C/s were applied. Heating rates of up to 300 °C/s were considered in some cases [76], and a rate of 1000 °C/s represents the highest-ever

rate applied during modeling [80]. The main results of that model concur with those reported in [64] and are consistent with the trends observed for heating in the UFH range. During heating, austenite forms via two simultaneous reactions:

$$\alpha + \theta \rightarrow \gamma \qquad \text{(II-1)}$$

and

$$\alpha \rightarrow \gamma \qquad \text{(II-2)}$$

where θ, γ, and α denote cementite, austenite, and ferrite, respectively. Some authors consider austenite formation a two-stage process, where reaction (II-1) occurs only after (II-2) has occurred [73,75,78–80,82]. This is an oversimplification of the actual situation occurring during austenite formation, where the kinetics of (II-1) differs significantly from that of (II-2). In fact, for a heating rate of 20 K/s, the interface velocity of austenite growing from pearlite is approximately two times higher than the velocity of austenite growing from ferrite [78]. This trend is confirmed via metallographic observation (Fig. II-8) and from volume fractions of austenite determined via dilatometry, cf. Fig. II-9. Experimental data [81] have also shown that the kinetics of reaction (II-2) changes during heating above a certain thermodynamic threshold. This change results from a transition of the austenite-formation mechanism from carbon diffusion control to interface mobility control. However, this change is only noticeable above certain heating rates. When heating rates are significantly lower than 1 °C/s and the carbon content approaches that of the eutectoid composition, 100% austenite may form (via reaction (II-2)) before the thermodynamic threshold is reached. The assumption of local equilibrium conditions at the α/γ interface can noticeably underestimate the calculation of the thermodynamic threshold for massive austenite formation.

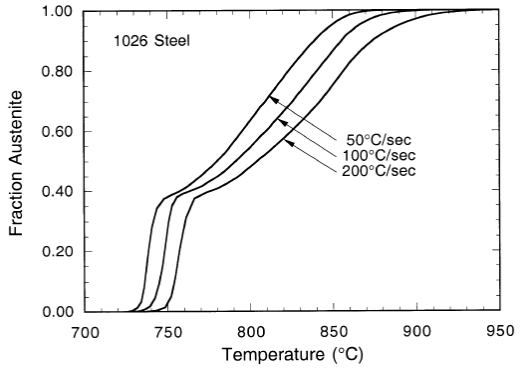

Fig. II-9. Temperature dependence of the austenite formed in an initially ferrite-pearlite microstructure subjected to different heating rate. Data obtained from dilatometric experiments [76].

Petrov et al. [30,33,34,91] reported that the dwell time (holding time) at the peak temperature has a significant effect on the microstructures formed during UFH experiments. Due to the high diffusivities and mobilities at temperatures in the intercritical range of steel, significant austenitic grain growth can be expected in relatively short times. Fig. II-10 shows the effect of the dwell time at 900 °C. After 0.2 s, the microstructure consists of ferrite and martensite (plus retained austenite), whereas a fully martensitic structure is formed after 2.5 s. These microstructural differences result from the distribution of carbon in austenite (see Chapter V for further details). This distribution has a significant effect on the mechanical properties, as discussed in the following section.

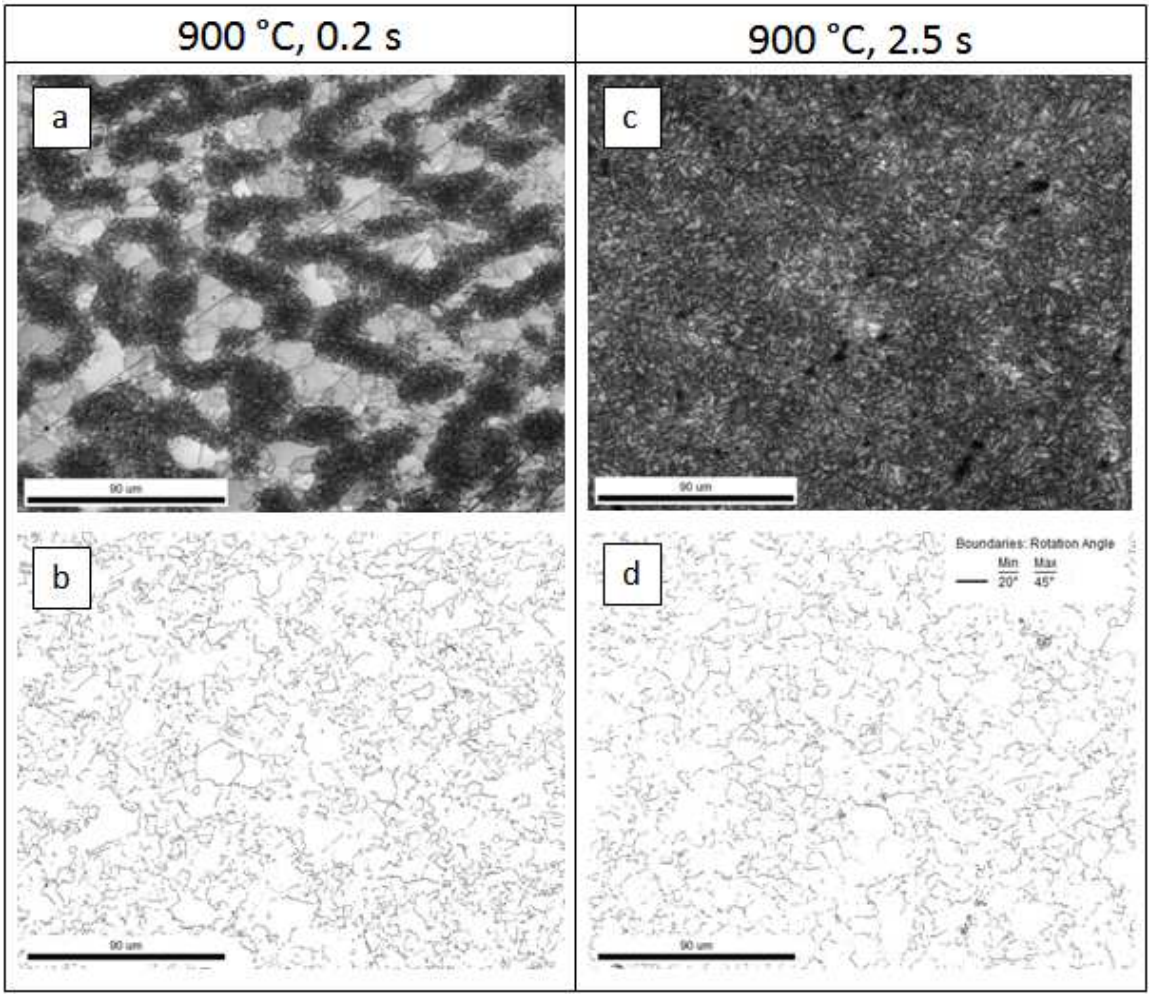

Fig. II-10. EBSD maps showing the effect of dwell time at the peak temperature in UFH experiments. Material with an initial ferrite-pearlite microstructure is heated at a rate of 450 °C/s to 900 °C for 0.2 s (a, b) and 2.5 s (c, d). (a, c) Image Quality (IQ) maps and (b, d) parent austenite grain boundaries. Scale bar is 90 µm.

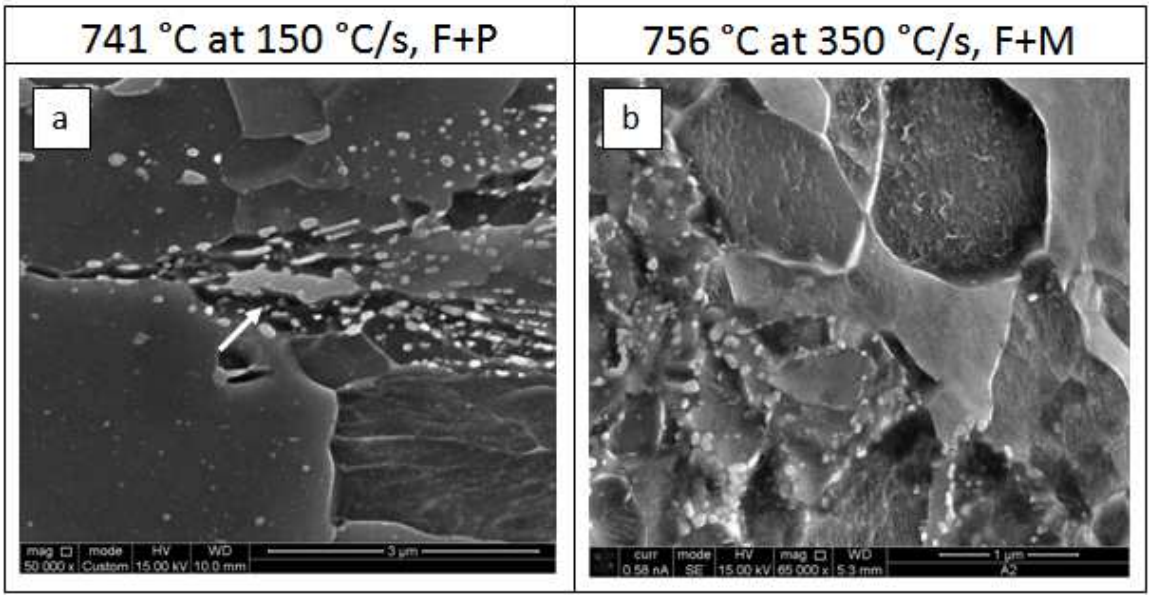

Fig. II-11. SEM images of 70% cold-deformed ferrite plus pearlite (F+P, a) and ferrite plus martensite (F+M, b) initial microstructures UFH to a similar peak temperature (~750 °C) and quenched [29]. The recrystallization of ferrite and the formation of austenite occur simultaneously. Scale bar is 3 μm in a 1 μm in b.

The interaction between recrystallization and phase transformation has been studied extensively in steel with starting microstructure consisting of cold-deformed ferrite plus pearlite [29,30,32,33,34,85–88]. The results revealed that these processes occur rather independently of each other. Recrystallization and phase transformation processes are expected to overlap at heating rates ranging from fast to ultrafast, owing to the displacement of the onset of ferrite recrystallization. Under such circumstances, austenite grows into deformed or partially recovered ferrite as well as fully recrystallized ferrite; this growth is described by (II-2). Cold-rolling-induced fragmentation of pearlite plays a role in ferrite recrystallization and austenite formation; in the former, this role is manifested as grain boundary pinning of the new ferrite grains by small fragmented cementite and in the latter, as an increase in the potential nucleation sites for austenite [87,88]. Fig. II-11a shows the microstructure of a 70% cold-rolled partially recrystallized F+P initial microstructure, where the pinning effect of pearlite colonies is illustrated. Austenite formation (indicated by white arrow) occurs concurrently with ferrite recrystallization. In a mixture of cold-deformed ferrite plus martensite, cf. Fig. II-11b, the recrystallization of ferrite is hindered by cementite particles, which formed during the tempering of the martensite. A detailed description of the interactions occurring during UFH of both initial microstructures is provided in Chapters VI and VII.

II-2.4 Austenite-formation diagrams

The kinetics of phase transformations can be expressed in terms of time-temperature-transformation diagrams [41], which are widely applied in steel heat-treatment design. Mehl [48] described the isothermal formation of austenite in a fully pearlitic steel exposed to several temperatures in the intercritical range. Fig. II-12a shows the start and finishing of austenite formation, as indicated by the lower half of the 'C-shaped' transformation curve. The shape of the curve indicates that the rate of transformation increases with increasing temperature. Speich et al. [53] investigated the isothermal formation of austenite in ferrite-pearlite aggregates and proposed a similar diagram (Fig. II-12b) to that reported by Mehl [48]. Although cementite dissolution and carbon homogenization were not explicitly included in the proposed diagram, the concepts of local equilibrium, carbon-diffusion control, and (substitutional) alloying-element control of the kinetics associated with austenite formation were applied.

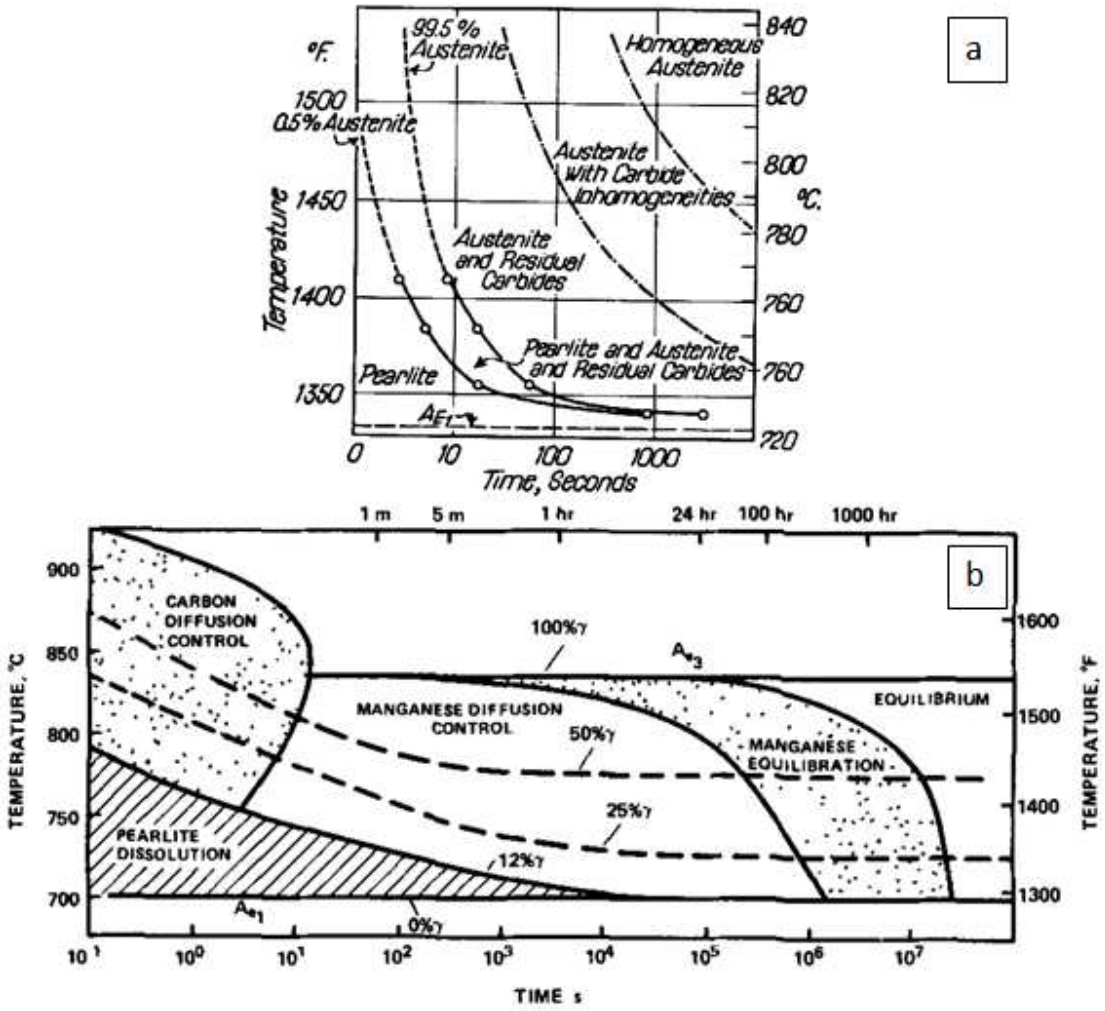

Fig. II-12. Time-temperature-transformation diagrams describing austenite formation in: (a) fully pearlitic microstructure [48] and (b) ferrite-pearlite aggregate [53].

II-3. Mechanical properties after UFH experiments

As stated in the previous chapter, the application of UFH cycles yields significant improvement in the mechanical properties of low carbon steel [31–34,85,89–91]. In fact, the strength of a UFH-produced microstructure is (on average) ~200-MPa higher than that of a CH-produced microstructure; the ductility is also higher, albeit by a lower margin [85,89–91]. This improvement in strength and ductility has been attributed principally to the (i) general grain size refinement effect in ferrite and martensite and (ii) mixture of phases/constituents formed during cooling. However, the carbon gradients in austenite and the holding time at the peak temperature may also play a role in this improvement. These gradients seem to play a major role in the higher strength and ductility realized for a UFH-produced Q&P steel, compared with those obtained for a CH-produced steel [91]. The effect of the holding time is manifested as a decrease in the strength after 5 min of holding. Fig. II-13 shows the tensile properties realized after UFH. The change in fracture mode is indicative of a change in the overall microstructure. Similar findings are described in Chapters VII and VIII, and a microstructural and mechanical-property characterization is presented for samples subjected to various heating rates.

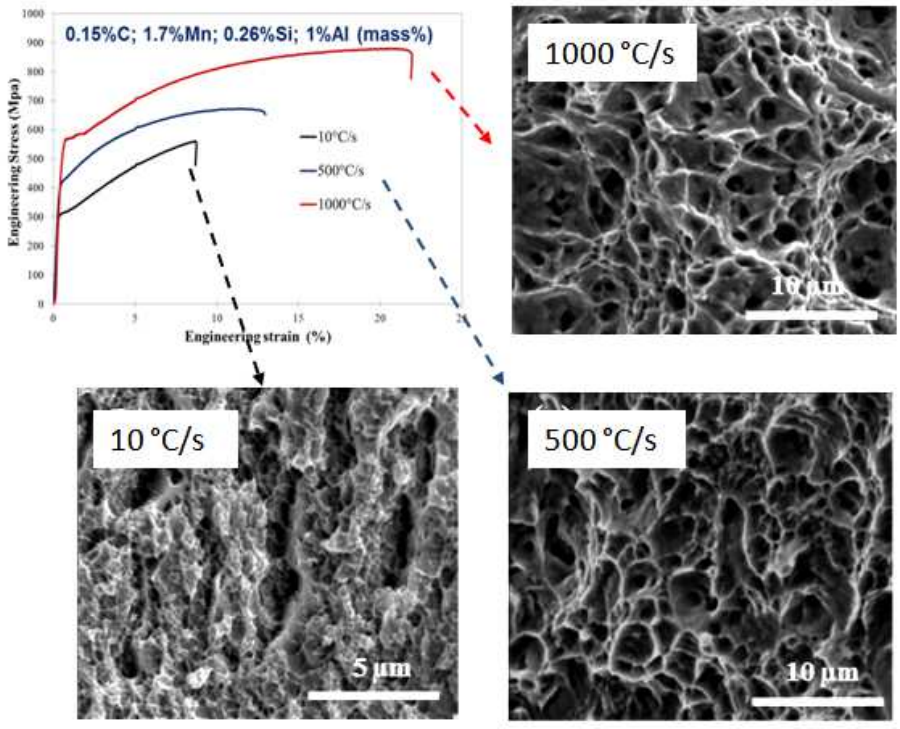

Fig. II-13. Engineering stress-strain curves of Q&P steel produced at different heating rates [91]. SEM images of the fracture surface reveal a change in fracture mode from quasi-cleavage (10 °C/s) to ductile (<500 °C/s).

II-4. Summary

The literature describing general aspects of recrystallization and the phase transformations occurring in pure iron and steel with ferrite and pearlite initial microstructure have been reviewed; the mechanical properties resulting from these microstructural processes have also been examined. The effect of the heating rate on the recrystallization of ferrite was discussed from the viewpoint of kinetics, grain size, and texture evolution. As established in section II-1, contradictory results have been reported for cold-rolled metals and alloys subjected to UFH rates. In particular, some studies have claimed that cold-rolled ULC steel undergoes very specific kinetic and crystallographic changes when recrystallization annealing is performed at UFH rates. Such changes are thoroughly evaluated in Chapter IV. Previous studies on the effect of heating rate on the recrystallization texture have considered only the growth stage and, hence, knowledge of the nucleation and initial growth stages is lacking. Chapter IV describes (in detail) the location and orientation of recrystallized ferrite nuclei, as well as their contribution to the overall texture.

The effect of UFH rates on the recrystallization of cold-rolled low carbon steels is described in Chapters VI and VII. The interaction of ferrite recrystallization with the deformed pearlitic matrix was investigated using a novel EBSD-based approach that allowed a clear distinction between the recrystallization of ferrite from pearlite and austenite formation. Similarly, recrystallized and non-recrystallized ferrite were distinguished via an EBSD-based analysis. Previous studies have considered the effect of heating rate on ferrite or the entire microstructure of cold-rolled low carbon steel (see Section II-1.2). However, until now, the effect on only recrystallized ferrite has not been considered. Therefore, Chapters VI and VII provide new experimental data from UFH experiments, and specific features describing the interaction of recrystallization with second-phase particles and austenite formation are discussed in detail.

The effect of heating rate on austenite formation was investigated in detail. Most of the experimental data from previous studies on austenite formation was obtained via isothermal experiments. Owing to the overlapping effect, the effect of heating rate on austenite formation cannot be determined by analyzing this data. Therefore, anisothermal experiments were performed in this work. These experiments represent the most convenient thermal path for determining the effect of the heating rate on the microstructure. A clear distinction of the transformation mechanisms that operate during different stages of austenite formation under UFH remains elusive. Clear experimental evidence of the transition from one mechanism to the other is also lacking. As such, thermodynamic and kinetic descriptions of the transformation mechanisms are provided in Chapter V, which describes the effect of the heating rate on austenite formation in ferrite-pearlite aggregates; conclusive experimental evidence of these transformations is also provided. The kinetic data are summarized in the form of time-temperature-transformation diagrams, which reveal the effect of UFH rates on the formation of austenite.

Ultrafast heating results in improved strength and ductility of cold-rolled low carbon steel. However, the basis of this improvement remains unclear. Several studies (see Section II-3) have attributed the remarkable improvement in mechanical properties to the general refining effect.

This explanation is unsatisfactory, however, for complex materials (such as DP, TRIP, and Q&P composition steels) subjected to UFH. A detailed characterization of the microstructure and the mechanical properties of cold-rolled steel with TRIP and DP compositions is presented in Chapters VII and VIII. The following factors are taken into consideration to explain the results of tensile tests performed on selected samples: parent austenite grain diameter, martensite grain diameter, carbon gradients in austenite, ferrite grain size, ferrite recrystallized fraction, and retained austenite fraction. More importantly, this work presents the first-ever metallographic evidence of the complex microstructure generated by UFH. The results indicate that the unique combination of strength and ductility results directly from the complex interaction of phases and microconstituents.

II-5- References

[1] L. M. Clarebrough, M. E. Hargreaves, M. H. Loretto, Order-Disorder Phenomena in alpha-Brass. I. Development of Order, Proc. Roy. Soc. A257 (1960) 363.

[2] L. M. Clarebrough, M. H. Loretto, Order-Disorder Phenomena in alpha-Brass. II. Influence of Quenching, Proc. Roy. Soc. A257 (1960) 326.

[3] L. M. Clarebrough, M. E. Hargreaves, M. H. Loretto, Order-Disorder Phenomena in alpha-Brass. III. Influence of Plastic Deformation, Proc. Roy. Soc. A257 (1960) 338.

[4] L. M. Clarebrough, M. E. Hargreaves, M. H. Loretto, Order-Disorder Phenomena in alpha-Brass. IV. Nature of Order and Role of Atomic Mobility, Proc. Roy. Soc. A261 (1961) 500.

[5] M. N. Bodyako, YU. M. Loiko, B. L. Pavlyukevich, V. I. Parkhimovich, Recrystallization diagrams for induction heating, Metalloved. Term. Obrab. Met. 1 (1960) 49–53G.

[6] F. F. Kraft, R. N. Wright, M. K. Jensen, Kinetics of nonisothermal recrystallization, J. Mater. Eng. Perform. 5 (1996) 213–219.

[7] S. L. Semiatin, I. M. Sukonnik, V. Seetharaman, Metall. Mater. Trans. A 27 (1996) 2051.

[8] S. Primig, H. Leitner, W. Knabl, A. Lorich, H. Clemens, R. Stickler, Influence of the heating rate on the recrystallization behavior of molybdenum, Mater. Sci. Eng. A 535 (2012) 316–324.

[9] A. W. Bowen, Texture development in high strength aluminium alloys, Mater. Sci. Tech. Ser. 6, (1990) 1058–1071.

[10] J. A. Wert, N. E. Paton, C. H. Hamilton, M. W. Mahoney, Grain refinement in 7075 aluminum by thermo-mechanical processing, Metall. Trans A 12A (1981) 1267–1276.

[11] M. Ferry, D. Jones, High-rate annealing of single-phase and particle-containing aluminium alloys, Scripta Mater. 38 (1998) 177–183.

[12] W. J. Poole, M. Militzer, M. A. Wells, Modelling recovery and recrystallisation during annealing of AA 5754 aluminium alloy, Mater. Sci. Tech. 19 (2003) 1361–1368.

[13] M. M. Attallah, M. Strangwood, C. L. Davis, Influence of the heating rate on the initiation of primary recrystallization in a deformed Al–Mg alloy, Scripta Mater. 63 (2010) 371–374.

[14] D. Beckenhauer, P. Niessen, R. Pick, Effect of heating rate on the recrystallization temperature of tantalum, J. Mater. Sci. Letters 12 (1993) 449–450.

[15] G. K. L'vov, Accelerated recrystallization of low carbon steel, Metalloved. Term. Obrab. Met. 1 (1959) 8–16.

[16] R. H. Goodenow, Recrystallization and grain structure in rimmed and aluminum killed low carbon steel, Trans. ASM 59 (1966) 804–823.

[17] A. I. Vitkin, S. S. Guseva, Z. I. Sokolova, G. M. Vorob'ev, Effect of heating rate on the recrystallization texture of low-carbon steel 08 kp, Metalloved. Term. Obrab. Met. 4 (1972) 63–67.

[18] M. Atkinson, Bifurcation of thermal restoration processes in deformed iron and steel, Mater. Sci. Eng. A 262 (1999) 33–38.

[19] D. Muljono, M. Ferry, D. P. Dunne, Influence of heating rate on anisothermal recrystallization in low and ultra-low carbon steels, Mater. Sci. Eng. A 303 (2001) 90–99.

[20] M. Ferry, D. Muljono, D. P. Dunne, Recrystallization kinetics of low and ultra low carbon steels during high-rate annealing, ISIJ Int. 41 (2001) 1053–1060.

[21] M. Atkinson, On the credibility of ultrarapid annealing, Mater. Sci. Eng. A 354 (2003) 40–47.

[22] A. C. Reis, L. Bracke, R. Petrov, L. Kestens, Grain refinement and texture change in interstitial free steels after severe rolling and ultra-short annealing, ISIJ Int. 43 (2003) 1260–1267.

[23] C. S. Smith, Grains, phases, and interfaces—an interpretation of microstructure, Trans. AIME 175 (1948) 15–51.

[24] M. Hillert, On the theory of normal and abnormal grain growth, Acta Metall. 13 (1965) 227–238.

[25] I. Samajdar, B. Verlinden, P. Van Houtte, D. Vanderschueren, γ-Fibre recrystallization texture in IF-steel: An investigation on the recrystallization mechanisms, Mater. Sci. Eng. A 238 (1997) 343–350.

[26] J. Stockemer, P. Vanden Brande, Recrystallization of a cold-rolled low-carbon steel by cold-plasma-discharge rapid annealing, Metall. Mater. Trans. A 34 (2003) 1341.

[27] S. G. Chowdhury, E. V. Pereloma, D. B. Santos, Evolution of texture at the initial stages of continuous annealing of cold rolled dual-phase steel: Effect of heating rate, Mater. Sci. Eng. A 480 (2008) 540–548.

[28] T. Senuma, K. Kawasaki, Y. Takemoto, Recrystallization behavior and texture formation of rapidly annealed cold-rolled extra low carbon steel sheets, Mater. Trans. 47 (2006) 1769–1775.

[29] R. H. Petrov, L. Kestens, W. Kaluba Y. Houbaert, Recrystallization and austenite formation in a cold rolled TRIP steel during ultrafast heating, Steel Grips 1 (2003) 289–293.

[30] R. H. Petrov, J. J. Sidor, W. Kaluba, L. Kestens, Grain refinement of a cold rolled TRIP assisted steel after ultra short annealing, Mater. Sci. Forum 715–716 (2012) 661–666.

[31] F. Ramos, MSc Thesis, Ghent University, July 2012.

[32] A. Puype, MSc Thesis, Ghent University, July 2014.

[33] R. H. Petrov, A. Puype, D. De Knijf, L. Kestens, Ultrafast heating of advanced high strength steels, Proc. of the International Conference on Solid-Solid Phase Transformations in Inorganic Materials, Whistler, (2015).

[34] R. Petrov, F. Hajy Akbary, J. Sidor, M. J. Santofimia, J. Sietsma, L. Kestens, Ultra-fast annealing of high strength steel, Int. J Mach. Technol. Mater., Publisher: Scientific–technical Union of Mechanical Engineering, Bulgaria, Sofia, Year VI, issue 8 (2012) 68–71.

[35] G. Liu, J. Li, S. Zhang, J. Wang, Q. Meng, Dilatometric study on the recrystallization and austenization behavior of cold-rolled steel with different heating rates, J. Alloy Compd. 666 (2016) 309–316.

[36] De. Xu, J. Li, Q. Meng, Y. Liu, P. Li, Effect of heating rate on microstructure and mechanical properties of TRIP-aided multiphase steel, J. Alloy Compd. 614 (2014) 94–101.

[37] W. I. Haworth, J. G. Parr, The effect of rapid heating on the alpha-gamma transformation of iron, Trans. ASM 58 (1965) 476–488.

[38] R. P. Zerwekh, C. M. Wayman, On the nature of the $\alpha \rightarrow \gamma$ transformation in iron: A study of whiskers, Acta Metall. Mater. 13 (1965) 99–107.

[39] G. R. Speich, A. Szirmae, Formation of austenite from ferrite and ferrite-carbide aggregate, Trans. AIME 245 (1969) 1063–1073.

[40] M. J. Bibby, J. G. Parr, The martensitic transformation in pure iron, J. Iron Steel Inst. 202 (1964) 100.

[41] E. S. Davenport, E. C. Bain, Transformation of austenite at constant subcritical temperatures, Trans. AIME, 90 (1930) 117–154.

[42] E. C. Bain, The Alloying Elements in Steel, ASM, Cleveland, Ohio, 1939.

[43] G. Mölinder, A quantitative study of the formation of austenite and the solution of cementite at different austenitizing temperatures for a 1.27% carbon steel, Acta Metall. Mater. 4 (1956) 565–571.

[44] K. J. Albutt, S. Garber, Effect of heating rate on the elevation of the critical temperatures of low carbon mild steel, J. Iron Steel Inst. 204 (1966) 1217–1222.

[45] R. R. Judd, H. W. Paxton, Kinetics of austenite formation from a spheroidized ferrite-carbide aggregate, Trans. AIME 242 (1968) 206–215.

[46] M. Hillert, K. Nilsson, L. E. Törndahl, Effect of alloying elements on the formation of austenite and dissolution of cementite, J. Iron Steel Inst., 209 (1971) 49–66.

[47] E. Walldow, The mechanism of the solution of cementite in carbon steel and the influence of heterogeneity, J. Iron Steel Inst. 2 (1930) 301–339.

[48] R. F. Mehl, The mechanism and rate formation of austenite from ferrite-cementite aggregates, Trans. ASM 31 (1943) 613–650.

[49] V. N. Gridnev, V. I. Trefilov, Dokl. Akad. Nauk SSS R 95 (1954) 741–743.

[50] N. N. Lipchin, T. G. Kryukova, N. L. Oslon, Effect of heating rate on phase recrystallization of quenched 60S2 steel, Metalloved. Term. Obrab. Met. 8 (1964) 5–8.

[51] N. C. Law, D. V. Edmonds, The formation of austenite in a low-alloy steel, Metall. Trans. 11A (1980) 33–46.

[52] C. I. García, A. J. Deardo, Formation of austenite in 1.5 pct Mn steels, Metall. Trans. 12A (1981) 521–530.

[53] G. R. Speich, V. A. Demarest, R. L. Miller, Formation of austenite during intercritical annealing of dual-phase steels, Metall. Trans. 12A (1981) 1419–1428.

[54] G. E. Abrosimova, G. I Kohanchik, A. M. Markov, A. V. Serebryakov, On the α–γ transfomation in plain carbon steel by rapid thermal treatment, Scripta Metall. Mater. 13 (1979) 531–534.

[55] D. P. Datta, A. M. Gokhale, Austenitization kinetics of pearlite and ferrite aggregates in a low carbon steel containing 0.15 wt pct C, Metall. Trans. 12A (1981) 443–450.

[56] A. Roosz, Z. Gacsi, E. G. Fuchs, Isothermal formation of austenite in eutectoid plain carbon steel, Acta Metall. Mater. 31 (1983) 509–517.

[57] C. Atkinson, T. Akbay, R. C. Reed, Theory for reaustenitisation from ferrite/cementite mixtures in Fe-C-X steels, Acta Metall. Mater. 43 (1995) 2013–2031.

[58] R. C. Reed, T. Akbay, Z. Shen, J. M. Robinson, J. H. Root, Determination of reaustenitisation kinetics in a Fe–0.4C steel using dilatometry and neutron diffraction, Mater. Sci. Eng. A 256 (1998) 152–165.

[59] A. Jacot, M. Rappaz, R. C. Reed, Modelling of reaustenitization from the pearlite structure in steel, Acta Mater. 46 (1998) 3949–3962.

[60] R. Mancini, C. Budde, Reaustenitisation in Fe-C steels revisited, Acta Mater. 47 (1999) 2907–2911.

[61] G. D. Verros, N. A. Malamataris, Finite element analysis of ferrite–austenite diffusion controlled phase transformation, Comput. Mater. Sci. 24 (2002) 380–392.

[62] B. J. Yang, L. Chuzhoy, M. L. Johnson, Modeling of reaustenitization of hypoeutectoid steels with cellular automaton method, Comput. Mater. Sci. 41 (2007) 186–194.

[63] G. R. Speich, M. J. Richards, Diffusion equations for pearlite dissolution, Trans. AIME 245 (1969) 1073–1074.

[64] Y. Y. Meshkov, E. V. Pereloma, The effect of heating rate on reverse transformations in steels and Fe-Ni-based alloys, in book: Phase transformations in steel, Vol. 1. Ed. E. V. Pereloma, D. V. Edmonds. 2012.

[65] W. J. Kaluba, R. Taillard, J. Foct, The bainitic mechanism of austenite formation during rapid heating, Acta Mater. 46 (1998) 5917–5927.

[66] H. I. Aaronson, J. F. Nie, Discussion to “The bainitic mechanism ofaustenite formation during rapid heating”, Scripta Mater. 42 (2000) 505–509.

[67] W. J. Kaluba, R. Taillard, J. Foct, A reply to “Discussion to “the bainitic mechanism of austenite formation during rapid heating”, Scripta Mater. 42 (2000) 511–516.

[68] M. Hillert, comments on “The bainite mechanism of austenite formation during rapid heating”, Scripta Mater. 43 (2000) 1045–1046.

[69] W. J. Kaluba, R. Taillard, J. Foct, A reply to “Comments on ‘the bainitic mechanism of austenite formation during rapid heating’”, Scripta Mater. 43 (2000) 1047–1049.

[70] V. I. Savran, S. E. Offerman, J. Sietsma, Austenite nucleation and growth observed on the level of individual grains by three-dimensional x-ray diffraction microscopy, Metall. Mater. Trans. A 41A (2010) 583–591.

[71] A. S. Oddy, J. M. J. McDill, L. Karlsson, Microstructural predictions including arbitrary thermal histories, reaustenization and carbon segregation effects, Can. Metall. Quart. 35 (1996) 275–283.

[72] A. Jacot, M. Rappaz, A two-dimensional diffusion model for the prediction of phase transformations: application to austenitization and homogenization of hypoeutectoid Fe-C steels, Acta Mater. 45 (1997) 575–585.

[73] C. García de Andrés, F. G. Caballero, C. Capdevila, Dilatometric characterization of pearlite dissolution in 0.1C-0.5Mn low carbon low manganese steel, Scripta Mater. 38 (1998) 835–1842.

[74] C. García de Andrés, F. G. Caballero, C. Capdevila, H. K. D. H. Bhadeshia, Modelling of kinetics and dilatometric behavior of non-isothermal pearlite-to-austenite transformation in an eutectoid steel, Scripta Mater. 39 (1998) 791–796.

[75] A. Jacot, M. Rappaz, A combined model for the description of austenitization, homogenization and grain growth in hypoeutectoid Fe-C steels during heating, Acta Mater. 47 (1999) 1645–1651.

[76] R. C. Dykhuizen, C. V. Robino, G. A. Knorovsky, A method for extracting phase change kinetics from dilatation for multistep transformations: Austenitization of a low carbon steel, Metall. Mater. Trans. 30B (1999) 107–117.

[77] F. G. Caballero, C. Capdevila, C. García de Andrés, Influence of scale parameters of pearlite on the kinetics of anisothermal pearlite-to-austenite transformation in a eutectoid steel, Scripta Mater. 42 (2000) 1159–1165.

[78] E. Schmidt, Y. Wang, S. Sridhar, A study of nonisothermal austenite formation and decomposition in Fe-C-Mn alloys, Metall. Mater. Trans. 37A (2006) 1799–1810.

[79] F. L. G. Oliveira, M. S. Andrade, A. B. Cota, Kinetics of austenite formation during continuous heating in a low carbon steel, Mater. Charact. 58 (2007) 256–261.

[80] A. I. Katsamas, A computational study of austenite formation kinetics in rapidly heated steels, Surf. Coat. Tech. 201 (2007) 6414–6422.

[81] E. D. Schmidt, E. B. Damm, S. Sridhar, A study of diffusion- and interface-controlled migration of the austenite/ferrite front during austenitization of a case-hardenable alloy steel, Metall. Mater. Trans. 38A (2007) 244–260.

[82] D. San Martín, P. E. J. Rivera-Díaz-del-Castillo, C. García-de-Andrés, In situ study of austenite formation by dilatometry in a low carbon microalloyed steel, Scripta Mater. 58 (2008) 926–929.

[83] B. J. Yang, A. Hattiangadi, W. Z. Li, G. F. Zhou, T. E. McGreevy, Simulation of steel microstructure evolution during induction heating, Mater. Sci. Eng. A 527 (2010) 2978–2984.

[84] D. San Martín, Y. Palizdar, C. García -Mateo, R. C. Cochrane, R. Brydson, A. J. Scott, Influence of aluminum alloying and heating rate on austenite formation in low carbon-manganese steels, Metall. Mater. Trans. 42A (2011) 2591–2608.

[85] D. Xu, J. Li, Q. Meng, Y. Liu, P. Li, Effect of heating rate on microstructure and mechanical properties of TRIP-aided multiphase steel, J. Alloy Compd. 614 (2014) 94–101.

[86] A. Chbihi, D. Barbier, L. Germain, A. Hazotte, M. Goune, Interactions between ferrite recrystallization and austenite formation in high-strength steels, J. Mater Sci. 49 (2014) 3608–3621.

[88] G. Liu, J. Li, S. Zhang, J. Wang, Q. Meng, Dilatometric study on the recrystallization and austenization behavior of cold-rolled steel with different heating rates, J. Alloy Compd. 666 (2016) 309–316.

[89] T. Lolla, G. Cola, B. Narayanan, B. Alexandrov, S. S. Babu, Development of rapid heating and cooling (flash processing) process to produce advanced high strength steel microstructures, Mater. Sci. Tech. 27 (2011) 863–875.

[90] Q. Meng, J. Li, H. Zheng, High-efficiency fast-heating annealing of a cold-rolled dual-phase steel, Mater. Des. 58 (2014) 194–197.

[91] D. De Knijf, A. Puype, C. Föjer, R. Petrov, The influence of ultra-fast annealing prior to quenching and partitioning on the microstructure and mechanical properties, Mater. Sci. Eng. A 627 (2015) 182–190.

Chapter III

Materials and experimental techniques

The different steel grades as well as the data collection and measurement techniques employed in the present experiments are introduced in this chapter. The chemical composition, initial microstructure, and phase fractions of the materials are presented in Section III-1. Thermodynamic and kinetics calculations are also explained. Section III-2 explains the experimental set-up for conventional heating (CH) and ultrafast heating (UFH) experiments. In addition, dilatometry and the Gleeble thermomechanical simulators are introduced. The practical aspect of Gleeble experiments is emphasized, especially with regards to determining the homogeneous zone. Section III-3 describes the characterization techniques employed in this work, and the post-processing of EBSD data is explained in detail.

III-1 Materials

The chemical composition of each material (ULC steel, C20, C45, FeCMnSi, FeCMnAlSi, and FeCMnCrMoNb steels) considered in this work is shown in Table III-1.

Table III-1. Chemical composition (in wt. %) of each material considered in this work.

Material	C	Mn	Si	Cr	Mo	Al	Cu	Nb	S	P	Fe
ULC Steel	0.005	0.125	0.016	-	-	-	-	-	0.016	0.004	Rest
C20	0.17	1.08	0.22	-	-	-	0.27	-	0.013	0.012	Rest
C45	0.44	0.63	0.26	-	-	-	0.23	-	0.017	0.018	Rest
FeCMnSi	0.14	2.05	1.20	-	-	-	-	-	0.001	0.012	Rest
FeCMnAlSi	0.19	1.61	0.50	-	-	1.06	-	-	0.003	0.016	Rest
FeCMnCrMoNb	0.11	1.87	0.03	0.45	0.18	-	-	0.03	0.002	0.011	Rest

The thickness of the cold-rolled initial material are in the range of 0.5 - 1.5 mm. Hot-rolled material samples have a diameter of 6 mm. The initial microstructures are shown in Fig. III-1. The microstructures shown in Fig. III-1b–f are all characterized by a mixture of ferrite and pearlite (F+P). However, those shown in Fig. III-1a and Fig. III-1g consist of pure ferrite (F) and ferrite and martensite (F+M), respectively. C20 (Fig. III-1b) and C45 (Fig. III-1c) steels were treated from the as-rolled condition. The ULC (Fig. III-1a), FeCMnAlSi (Fig. III-1e, 1f), and FeCMnCrMoNb (Fig. III-1g) steels were 50% cold rolled, whereas the FeCMnSi (Fig. III-1d) steel was 70% cold rolled. The relative phase fractions of the initial microstructures are shown in **Table III-2**.

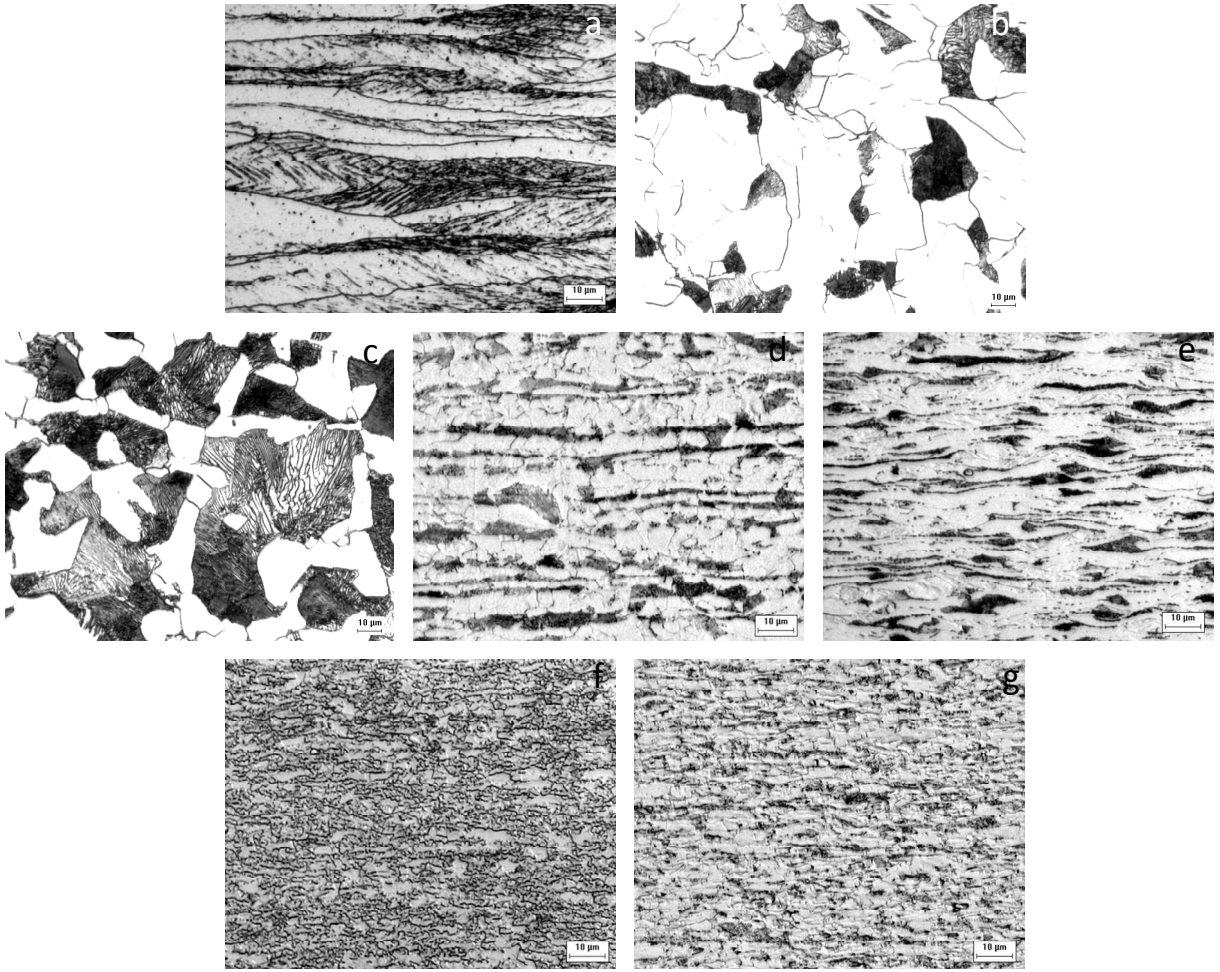

Fig. III-1. Initial microstructures. (a) ULC steel 50% cold-rolled F, (b) C20 steel as-rolled F+P, (c) C45 steel as-rolled F+P, (d) FeCMnSi steel as-rolled F+P, (e) FeCMnAlSi steel 50% cold-rolled F+P, (f) FeCMnAlSi steel 50% cold-rolled F+M, (g) FeCMnCrMoNb steel 50% cold rolled. (a) Etched with Marshall´s reagent and (b–g) etched with nital 4%. Scale bar is 10 µm.

Table III-2. The initial phase fractions.

Material	% Ferrite	% Pearlite	% Martensite
ULC Steel	100	-	-
C20	66.1	33.9	-
C45	33.7	66.3	-
FeCMnSi	63.9	36.1	-
FeCMnAlSi	76.4	23.6	-
FeCMnAlSi*	52	-	48
FeCMnCrMoNb**	70.5	-	29.5

**Ferrite and martensite initial microstructure*

***The initial microstructure is a mixture of ferrite, pearlite, bainite, and martensite.*

III-1.1 Thermodynamic and kinetic calculations

Thermodynamic calculations (of phase diagrams, phase fractions, and equilibrium critical temperatures) were performed using the commercial software ThermoCalc [1], database TCFE7. In addition, the movement of the austenite-cementite interface and the compositional gradients in the microstructure were evaluated via simulations of the microstructure after different times at various soaking temperatures. These simulations were performed using the Dictra software, which allows the derivation of diffusion-controlled reactions in multicomponent metallic systems. A general description of the software and the models can be found elsewhere [1–3]. The initial chemical composition and relative initial fractions of ferrite and cementite were estimated with ThermoCalc (databases TCFE6 and TCFE7) at a temperature associated with metastable equilibrium of ferrite and cementite. The volumetric phase fractions were estimated without considering the effect of carbon. Moreover, cementite dissolution was computed based on the assumption that, above A_1, ferrite is completely transformed into austenite. This assumption is based on the rapid advance of the austenite-ferrite interface, compared with that of the austenite-cementite interface [4]. Nucleation was not considered in the simulations.

III-2 Experimental techniques

III-2.1 Dilatometry

During dilatometry, the heat-induced dilatation or contraction in the volume of a specimen is measured. The underlying principle of this technique and details of the equipment are provided elsewhere [5–8]. The specimens are heated by a magnetic field induced in the sample, and cooled by the spraying of argon gas. During the experiments, 10×5×1 mm³ specimens were heated at rates of up to 200 °C/s in a DIL805AD Bähr Dilatometer. The temperature was controlled by an S-type thermocouple spot welded to the midsection of each test sample.

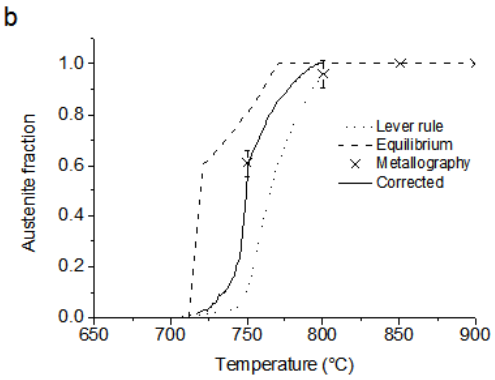

Fig. III-2. Austenite fraction versus temperature of a C45 steel heated at 10 °C/s. Dashed, dotted, and solid lines represent equilibrium, lever rule-determined, and corrected phase fractions, respectively.

The phase fractions generated during an anisothermal heat treatment are typically approximated via the lever rule. However, this approach leads to significant deviations from actual values [6,7,9–12] and therefore, the correction proposed in [6] is employed in the present study. Fig. III-2 shows the: equilibrium phase fraction (dashed line), fraction calculated via the lever rule (dotted line), corrected fraction (solid line), and metallography-determined austenite fraction of C45 steel heated at 10 °C/s.

III-2.2 Gleeble thermomechanical simulator

Steel samples can be heated at rates of up to 10,000 °C/s using the Gleeble 3800 Thermomechanical Simulator. The heat is introduced by passing an electric current through the sample. The other capabilities of the equipment are described in detail elsewhere [13]. The Gleeble experiments have been carried out in the Delft University of Technology, Holland, and in the IMDEA Institute, Spain.

III-2.2.1 Samples

Two types of heat-treatment specimens were produced, namely: 5 mm (diameter)×116 mm (length) bars threaded at both ends, and 60–120 mm (length)×10–50 mm (width) plates; the plates had thicknesses of 1 mm and 1.5 mm. The specifications of the bar specimens are shown in **Fig. III-3**.

A thin wire K-type thermocouple is welded to the midsection of each specimen to control the temperature during ultrafast heating/quenching experiments. Two other K-type thermocouples are welded at distances of 3 mm and 6 mm from the midsection to determine the temperature gradients during the experiments.

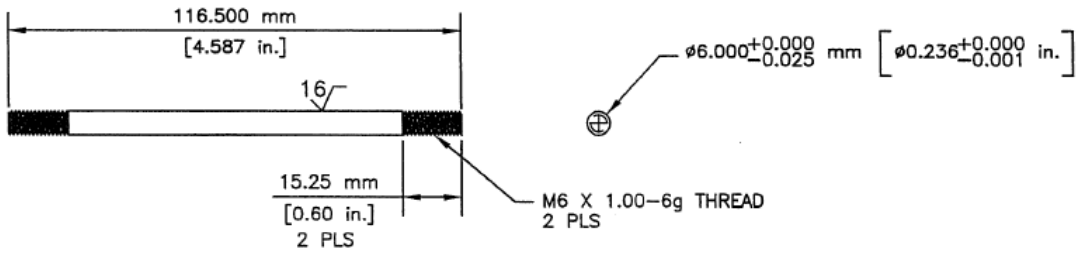

Fig. III-3. Bar specimen used for Gleeble tests.

III-2.2.2 Set-up

Nuts made from high strength steel are placed on both threaded ends of the specimen. The specimen is placed between full-contact copper grips, resulting in a 30.5-mm (length) contact area. The grips cover both ends of the specimen and are in perfect contact with the specimen surface (see Fig. III-4).

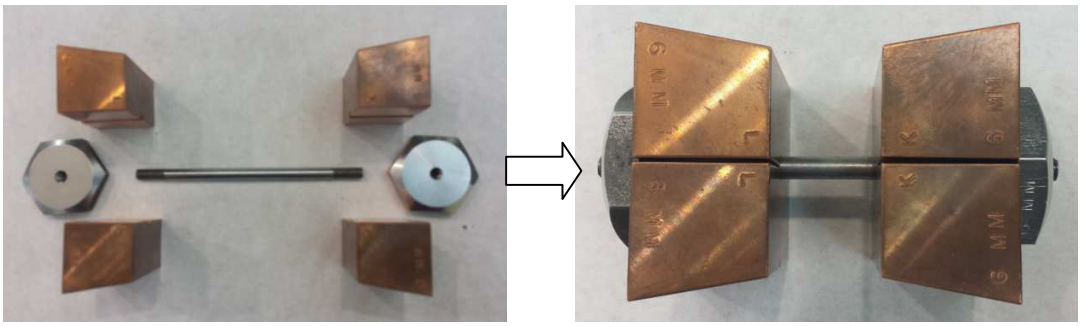

Fig. III-4. Experimental set-up.

In the case of flat samples, flat copper grips are used. The experimental set-up is inserted between the jaws in the Gleeble chamber, and perfect contact between the grips and the jaws is ensured. Furthermore, the gas gun is placed in the Gleeble chamber to enable rapid gas cooling. When required, the cooling gas is replaced by pressurized water for water quenching. The testing chamber is filled with argon gas. The specimens are then heated, via resistance heating, at rates of 10 °C/s–1500 °C/s to temperatures ranging from 750 °C to 1100 °C (±5 °C), and held at temperature for a maximum of ~0.5 s. Afterwards, the specimens are rapidly cooled via gas cooling or water quenching. The temperature of the specimen during heating/cooling experiments is recorded, at high frequency (50 Hz), from all three thermo-couples. An example of a ´peak-annealing´ experiment is illustrated in **Fig. III-5**.

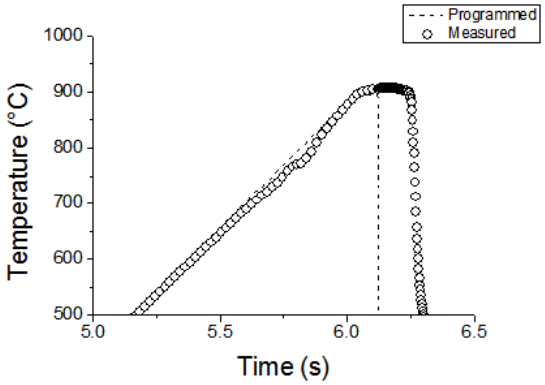

Fig. III-5. Peak-annealing experiment performed in the Gleeble. Cylindrical specimen heated at 450 °C/s to 900 °C and water quenched to room temperature. Actual heating rate: 446 °C/s, actual peak temperature: 904 °C/s, and actual cooling rate: -3200 °C/s.

III-2.2.3 Measurements

The heat distribution across the sample is inhomogeneous. The heat extraction at both extremes of the specimen is extremely rapid, owing to the contact with the cooper grips, and leads to a thermal gradient along the length of each specimen. In flat specimens, edge effects play a role in the heat extraction during cooling, and therefore temperature gradients also occur along the width. To circumvent possible artifacts in the characterization and property measurement, the homogeneous zone was determined from a profile of Vickers hardness measurements. The material outside the homogeneous zone was discarded, and sampling for microstructural and mechanical characterization was performed in the homogeneous material. Fig. III-6 shows an example of a flat specimen after the thermal cycle and the corresponding hardness profile (across the length) associated with two different heating rates.

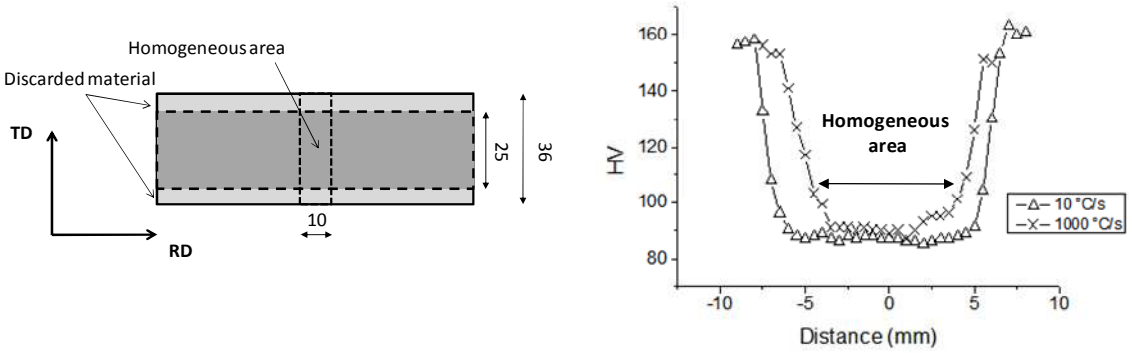

Fig. III-6. Schematic of a heat-treated specimen and the hardness profile, across the length, associated with two different heating rates. The dimension in the specimen are in mm.

III-3 Characterization

III-3.1 Optical and scanning electron microscopy

Optical Microscopy (OM) was performed under direct and oblique light, using a Zeiss microscope. Samples were prepared, via the standard procedure [14], i.e., by grinding and polishing to a mirror-like finish with 1 μm diamond paste. The microstructure was revealed by etching, for ~4 s–10 s at room temperature, with a solution of 4% HNO_3 in ethanol (nital 4%) (Fig. III-1b–1h). ULC steel was additionally swabbed in a solution of 4% v/v picric acid in ethanol (picral 4%) at room temperature, for surface activation. Subsequently, the polished and activated sample was etched, at 80 °C, in Marshall's reagent (solution of 8 g oxalic acid and 5 mL sulfuric acid in 100 mL water and 100 mL oxygenated water (concentration: 30% v/v)) [14,15]. The microstructure shown in Fig. III-1a was etched with this reagent. Scanning Electron Microscopy (SEM) was performed on a FEI Quanta™ 450-FEG-SEM operated at 15 kV. The samples prepared for OM were subsequently used for SEM.

III-3.2 Electron backscatter diffraction

The crystallographic orientations of individual grains may be determined via electron backscatter diffraction (EBSD). This technique is based on the capture of electron diffraction patterns produced by an electron beam incident on the sample surface. The basic principles of this technique have been covered in detail elsewhere [16–19]. The sample preparation was analogous to the procedure used for OM and SEM imaging prior to etching. After polishing with 1-μm diamond paste, the samples were polished, for 40 min under a polishing force of ~5 N, in a solution of 0.035-μm colloidal silica.

EBSD analysis was performed with a FEI Quanta™ 450-FEG-SEM operated under the following conditions: accelerating voltage: 20 kV, beam current: corresponding to an FEI spot size of 5, aperture size: 30 μm, and working distance: 16 mm. The sample was tilted by 70° toward the EBSD detector, and the corresponding EBSD patterns were acquired on a hexagonal scan grid by a Hikari detector operated with EDAX-TSL-OIM-Data Collection version 7 software. Scans were performed at a step size of 0.3 μm, and the orientation data were post-processed using the following grain definition: misorientation: >5°, minimum number of points per grain: four, and confident index (CI): >0.1.

The raw EBSD data were post-processed (cleaned) and the misindexed points were re-assigned using the grain CI standardization procedure embedded in the TSL-OIM Analysis V6.3 software. The phases in the material were quantified from the cleaned dataset. To distinguish between martensite and ferrite (both indexed as BCC phases), a plot of the Grain Average Image Quality (GAIQ) versus the area fraction of grains was constructed following the procedure described in [20,21]. Each grain was defined as the arrangement of at least four points with a misorientation angle and confidence index of >5° and >0.1, respectively. The plot shown in Fig. III-7 reveals that

the martensite fraction and the ferrite fraction are associated with the low-IQ region and the high-IQ region, respectively, of the histogram.

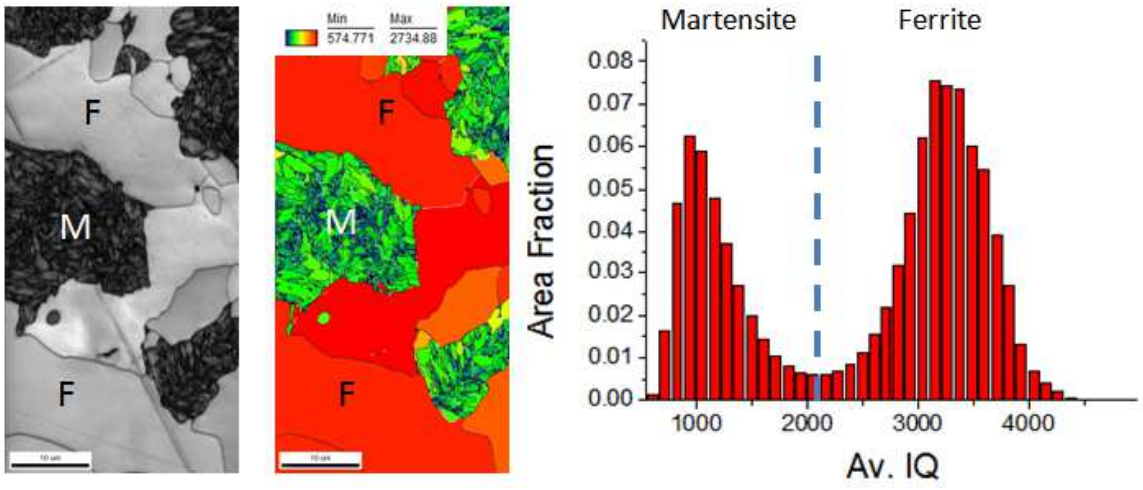

Fig. III-7. EBSD-based phase quantification. Image quality map (IQ, left), average image quality map (AV. IQ, center), and plot of Av. IQ versus area fraction of grains (right). Scale bar is 10 μm.

The ferrite fraction accounts for both recrystallized and unrecrystallized grains. However, IQ-based determination of the recrystallized-ferrite fraction was difficult, because some unrecrystallized but recovered ferritic grains have high IQ and, hence, distinguishing between these and the truly recrystallized grains was difficult. Several methodologies have been proposed [22–24] for separating recrystallized microstructure from the matrix. In the present study, recrystallized grains were identified using a plot of the Grain Average Misorientation (GAM) versus the area fraction of the grains; this approach has been applied elsewhere [25] to identify recrystallized grains. Grains with a GAM of <0.6 - 0.7° were considered recrystallized, whereas those with a GAM of >0.6 - 0.7° were considered non-recrystallized. The GAM range selected in each case will depend on the specific microstructure.

III.3.3 Transmission electron microscopy

Transmission electron microscopy was performed in a Jeol (S)TEM JEM-2200FS operated at 200 kV and equipped with an aberration corrector of the objective lens (CETCOR, CEOS GmbH), a column electron energy filter (omega type), and a Jeol EDX spectrometer.

Samples were prepared by mechanically grinding to a thickness of 50–100 μm, and 3-mm-diameter disks were subsequently cut from the thin slice samples. Using Struers Tenupol-5 equipment, these disks were prepared via twin-jet electropolishing in an electrolyte composed of 4 vol.% $HClO_4$ in 63% water-diluted CH_3COOH.

III-3.4 X-ray diffraction

X-ray diffraction analysis was performed using a Siemens D5000 diffractometer, equipped with a Mo source (λ = 0.7107 Å). Scans were performed over 2θ ranging from 26°to 40° at a step size and time per step of 0.03 °/step and 20 s, respectively. Austenite fractions were calculated using the formula introduced by Cullity [26].

III-3.5 Mechanical tests

III-3.5.1 Standard mechanical tests

Tensile tests were performed in a 5 kN Deben stage and an Instron 5569 tensile testing machine. For the Deben stage, sub-size tensile samples were cut parallel to the rolling direction (RD) of each heat-treated specimen. The gage length and width of the tensile samples described in Chapters VII and VIII are 3×1 mm^2, respectively. Tensile samples for the Instron device were machined to a gage length and width of 7×4 mm^2, respectively. The instantaneous elongation was assumed to be the displacement of the cross-head of the tensile machine and, hence, a reliable value of the yield stress was not obtained. In addition, the ductility was taken as the elongation to fracture, as measured with respect to initial marks on the test sample. Ductility measurements (see Chapter VIII) were performed via the Digital Image Correlation (DIC) technique, which yields complete stress-strain curves. Further details of the experimental set-up, sample dimensions, and data analysis are provided in Section VIII-2.

III-4 References

[1] J.-O. Andersson, T. Helander, L. Höglund, P. Shi, B. Sundman, Thermo-Calc & DICTRA, computational tools for materials science, Calphad. 26 (2002) 273–312. doi:10.1016/S0364-5916(02)00037-8.

[2] A. Borgenstam, L. Höglund, J. Ågren, A. Engström, DICTRA, a tool for simulation of diffusional transformations in alloys, J. Phase Equilibria. 21 (2000) 269–280. doi:10.1361/105497100770340057.

[3] J.-O. Andersson, L. Höglund, B. Jönsson, J. Ågren, Fundamentals and Applications of Ternary Diffusion, Elsevier, 1990. doi:10.1016/B978-0-08-040412-7.50023-2.

[4] E. Schmidt, Y. Wang, S. Sridhar, A study of nonisothermal austenite formation and decomposition in Fe-C-Mn alloys, Metall. Mater. Trans. A. 37A (2006) 1799–1810. doi:10.1007/s11661-006-0122-y.

[5] D. V Doane, J.S. Kirkaldy, M.S. of AIME. Heat Treatment Committee, A.S. for Metals. Activity on Phase Transformations, Hardenability Concepts with Applications to Steel: proceedings of a symposium held at the Sheraton-Chicago Hotel, October 24–26, 1977, Metallurgical Society of AIME, 1978.

[6] T.A. Kop, Dilatometric study of the austenite/ferrite interface mobility, TU Delft, 2000.

[7] V.I. Savran, Austenite formation in C-Mn steel, TU Delft, 2009.

[8] TA Instruments, Dilatometry, 2013. http://www.tainstruments.com/wp-content/uploads/DIL_805.pdf.

[9] A. Oddy, J. Mcdill, L. Karlsson, Microstructural predictions including arbitrary thermal histories, reaustenization and carbon segregation effects, Can. Metall. Quart. 35 (1996) 275–283. doi:10.1016/0008-4433(96)00001-8.

[10] M. Onink, F.D. Tichelaar, C.M. Brakman, E.J. Mittemeijer, S. van der Zwaag, An in situ hot stage transmission electron microscopy study of the decomposition of Fe-C austenites, J. Mater. Sci. 30 (1995) 6223–6234.

[11] S.L. Semiatin, I.M. Sukonnik, V. Seetharaman, An analysis of static recrystallization during continuous, rapid heat treatment, Metall. Mater. Trans. A. 27 (1996) 2051–2053. doi:10.1007/BF02651955.

[12] R.C. Dykhuizen, C. V Robino, G.A. Knorovsky, A method for extracting phase change kinetics from dilatation for multistep transformations: Austenitization of a low carbon steel, Metall. Mater. Trans. B. 30 (1999) 107–117. doi:10.1007/s11663-999-0011-z.

[13] Gleeble® 3500 System, (n.d.). http://www.gleeble.com/products/gleeble-3500.html.

[14] G.F. Vander Voort, Metallography, Principles and Practice, ASM International, 1984. https://books.google.be/books?id=GRQC8zYqtBIC.

[15] A. Benscoter, M. Perricone, Marshall's reagent: Origins, modifications, and new applications, Microsc. Microanal. 11 (2005) 76–77. doi:10.1017/S1431927605505415.

[16] V. Randle, Theoretical Framework for Electron Backscatter Diffraction, in: A.J. Schwartz, M. Kumar, B.L. Adams (Eds.), Electron Backscatter Diffr. Mater. Sci., Springer US, Boston, MA, 2000: pp. 19–30. doi:10.1007/978-1-4757-3205-4_2.

[17] T. Maitland, S. Sitzman, Backscattering Detector and EBSD in Nanomaterials Characterization, in: W. Zhou, Z.L. Wang (Eds.), Scanning Microsc. Nanotechnol. Tech. Appl., Springer New York, New York, NY, 2007: pp. 41–75. doi:10.1007/978-0-387-39620-0_2.

[18] R.A. Schwarzer, D.P. Field, B.L. Adams, M. Kumar, A.J. Schwartz, Present State of Electron Backscatter Diffraction and Prospective Developments, in: J.A. Schwartz, M. Kumar, L.B. Adams, P.D. Field (Eds.), Electron Backscatter Diffr. Mater. Sci., Springer US, Boston, MA, 2009: pp. 1–20. doi:10.1007/978-0-387-88136-2_1.

[19] S. Melzer, J. Moerman, Diffraction Techniques in Steel Research: An Overview, in: A. Haldar, S. Suwas, D. Bhattacharjee (Eds.), Microstruct. Texture Steels Other Mater., Springer London, London, 2009: pp. 267–284. doi:10.1007/978-1-84882-454-6_16.

[20] R.H. Petrov, L.A.I. Kestens, Advanced High-Strength Steels: Electron Backscatter Diffraction (EBSD), in: Encycl. Iron, Steel, and Their Alloys., n.d.: pp. 46–69. doi:10.1081/E-EISA-120050786.

[21] P.T. Pinard, A. Schwedt, A. Ramazani, U. Prahl, S. Richter, Characterization of dual-phase

steel microstructure by combined submicrometer EBSD and EPMA carbon measurements, Microsc. Microanal. 19 (2013) 996–1006. doi:10.1017/S1431927613001554.

[22] D.P. Field, Quantification of partially recrystallized polycrystals using electron backscatter diffraction, Mater. Sci. Eng. A. 190 (1995) 241–246. doi:10.1016/0921-5093(94)09601-R.

[23] S.I. Wright, M.M. Nowell, D.P. Field, A review of strain analysis using electron backscatter diffraction., Microsc. Microanal. 17 (2011) 316–329. doi:10.1017/S1431927611000055.

[24] H. Jazaeri, F.J. Humphreys, Quantifying recrystallization by electron backscatter diffraction, J. Microsc. 213 (2004) 241–246. doi:10.1111/j.0022-2720.2004.01296.x.

[25] R. Petrov, L. Kestens, Y. Houbaert, Recrystallization of a cold rolled Trip-assisted steel during reheating for intercritical annealling., ISIJ Int. 41 (2001) 883–890. doi:10.2355/isijinternational.41.883.

[26] B.D. Cullity, Elements of X Ray Diffraction, Second ed., Addison-Wesley Publishing Company Inc., Reading, Massachusetts, 1978.

Chapter IV

The effect of heating rate on the recrystallization behaviour in cold rolled ultra low carbon steel[1]

Ultrafast heating (UFH) experiments have been carried out in cold rolled ultra low carbon (ULC) steel, followed by quenching. The selected heating rates are in the range between 10°C/s - 800 °C/s. The recrystallization curves are slightly shifted to higher temperatures as the heating rate is increased. The average recrystallized grain size and texture are virtually unaffected by increasing the heating rate. Nucleation took place at grain boundaries as well as inside deformed grains. Electron backscattered diffraction (EBSD) analysis revealed that the texture of grains nucleated inside deformed ferrite grains prevails at later stages of recrystallization. The results obtained in this work demonstrate that similar microstructure and textures are obtained after very short annealing cycles.

IV-1 Introduction

As yet there is no unanimously accepted explanation for the observed effects of heating rate on the recrystallization behaviour of cold worked metals. In anisothermal experiments, some metallic systems evince a shift of the onset of recrystallization to higher temperatures when the heating rate is increased. Examples of this are found in the literature for Brass [1–4], Copper [5,6], Titanium [7] and Molybdenum [8]. These results contrast with the marked drop in the onset of recrystallization temperature measured in Al-based alloys [9–13] and high purity tantalum [14]. Early works in very low carbon steel [5,15–17] reported a marked softening effect in cold rolled ultra low carbon (ULC) and low carbon steel after heating rates in the fast to ultrafast range. However, these experiments combined different heating rates and holding times at the peak temperatures, i.e., a mixture of anisothermal and isothermal processes. In 1999, a inventory of early experiments on rapid recrystallization annealing of low carbon steel was published by Atkinson [18]. His work pointed out that, among other factors, dislocation arrangement effect, a decrease in the onset of recrystallization and a fast softening can be expected after ultrafast heating (UFH). He argues that UFH promotes the ideal conditions at the recovery stage, thus favoring the acceleration of softening. In 2001, Muljono and coworkers [19,20] claimed that ultrafast heating would increase the temperature of recrystallization, contrary to Atkinson´s claim. They supported their conclusions with experiments in low and very low carbon steel at heating rates up to 1,000 °C/s. In a subsequent paper, Atkinson [21] interpreted the data of the

[1] This chapter has been partially published as F.M. Castro Cerda, F. Vercruysse, T.N. Minh, L. Kestens, A. Monsalve, R. Petrov, The Effect of Heating Rate on the Recrystallization Behavior in Cold Rolled Ultra Low Carbon Steel, Steel Res. Int. 88 (2017). doi:10.1002/srin.201600351

experiments of Muljono et al. regarding the interaction of interstitial solute atoms with the deformed ferrite matrix. Such atoms might act as barriers to the dislocation mobility, hence becoming a hindrance for nucleation of new grains. This would require an aging step, which is responsible for the higher recrystallization temperatures reported in [19,20]. As proposed in [18], rapid heating might produce the particular conditions for a notorious change of the nature of recovery, enhancing faster recrystallization. This effect has already been described for Al-based alloys and tantalum.

However, fast anisothermal recrystallization might be rather difficult to be detected in steel, either due to the extremely low interstitial solute atom content theoretically required to produce a barrier for dislocation movement or the extremely high heating rates that are necessary to overcome the effect of interstitial solute atoms on dislocation mobility in a thermally activated process. In 2003, new experimental evidence on the effect of UFH on the recrystallization of ferrite in 95% cold deformed IF steel was reported by Kestens et al. [22], observing an increase in the recrystallization temperature, in agreement with the results on low carbon steel. The absence of interstitial atoms in the deformed matrix should enhance the UFH softening effect, according to [18,21] but this was not observed. On the other hand, it is also possible that small (nano-sized) precipitates are playing a role in the movement of dislocations [23,24]. Moreover, it is well known that IF steel shows a markedly sluggish recrystallization kinetics, even up to 99% cold deformation [25].

More recent studies [26,27] on the effect of the heating rate in a cold deformed low carbon steel also indicate a tendency to raise the onset of recrystallization as the heating rate is increased. Nevertheless, the heating rates employed in the references above are maximum ~300 K/s. The effect of C and N in solution was evaluated during the annealing of very low carbon steel at heating rates up to 1,000 °C/s [28]. It was shown that, although interstitial atoms influence the recrystallization kinetics at low heating rates, the effect is much less pronounced at higher heating rates. The general conclusions are in agreement with previous experiments on low and ULC steels. Recrystallization of ferrite in low carbon steel of chemical composition suitable for DP and TRIP-aided grades also show a close match with the previous descriptions [29–31]. With regard to texture formation it can be said that when recrystallization is finished before the onset of austenite formation, no general changes in the orientation components are observed in IF steel [22]. The trends are similar for low and ULC steel [17,26,27].

The ranges of heating rates are defined as follows: *conventional* heating with a maximum of 10 °C/s, *fast* from 10 to 100 °C/s and *ultrafast* when higher than 100 °C/s. The heating rate plays an important role in the final microstructure and hence in the mechanical properties of ULC steel. In the present study, the effect of conventional and ultrafast heating rates on the texture formation during recrystallization is investigated. The experimental heating rates were chosen according to potential industrial conditions [32].

IV-2 Experimental

The chemical composition of the initial material is shown in Table IV-1. The steel sheet of 1.5 mm thickness was received in the 50 % cold rolled condition. Specimens for heat treatment were cut from the cold rolled sheet. The controlled heating experiments were carried out in a Gleeble thermo-mechanical simulator. The size of the specimens the annealing experiments was 120x10x1.5 mm^3. For all samples, the longest axis was kept parallel to the rolling direction (RD) of the cold rolled sheet. The temperature was controlled by an S-type thermocouple, spot welded to the midsection of each test sample. Specimens were subjected to peak annealing experiments, i.e. heated up to a certain temperature and then gas quenched, with a holding time of less than 0.3 s. This sequence was repeated for several temperatures. The selected heating rates were 10 °C/s, 400 °C/s and 800 °C/s. The quenching rates were ~-50 °C/s. A summary of the average heating rates and peak temperatures in shown in Table IV-2.

Table IV-1. Chemical composition

C	Mn	Si	S	P	Fe
0.005	0.124	0.016	0.016	0.004	Rest

Table IV-2. Summary of average heating rates and peak temperatures.

Heating rate, °C/s	Peak Temperature, °C						
10	650	750	799	850	870	910	980
400	650	756	808	850	884	920	1015
800	665	747	812	850	885	924	1018

IV-3 Characterization

The microstructure evolution was observed by Optical (OM) and Scanning Electron Microscopy (SEM). Samples were cut from each heat treated specimen. The zone of homogeneous microstructure along the specimen was determined by a plot of the Vickers hardness (HV3) versus distance on the TD plane (i.e. the plane perpendicular to TD), as shown in Fig. IV-1. The characterization and data collection was performed within the limits of the homogeneous zone. Samples were taken from each tested specimen and prepared according to the standard procedure, by grinding and polishing to 1 µm diamond paste, and selective etching revealed the microstructure. The polished surface was swabbed in a solution of 4% v/v HNO_3 in ethanol (Nital 4%) for ~4 s and then in 4% v/v Picric acid in Ethanol (Picral 4%) at room temperature, for surface activation. Subsequently, the polished and activated sample was etched in a solution of 8 g oxalic acid and 5 ml sulphuric acid in 100 ml water and 100 ml oxygenated water of 30% v/v concentration, at 80 °C (Marshall's reagent) [33,34]. Electron backscatter diffraction (EBSD) was performed with a FEI Quanta™ 450-FEG-SEM operated at 20kV, beam current corresponding to FEI spot size 5 for aperture 30 µm and working distance of 16 mm. The sample was 70° tilted towards

the EBSD detector, and the EBSD patterns were acquired on hexagonal scan grid with a Hikari detector operated with EDAX-TSL-OIM-Data Collection version 7 software. The step size of the scans was 0.3 µm. The orientation data were post-processed using the following grain definition: misorientation with neighbouring grains higher than 5°, minimum 4 points per grain and a confident index (CI) larger than 0.1.

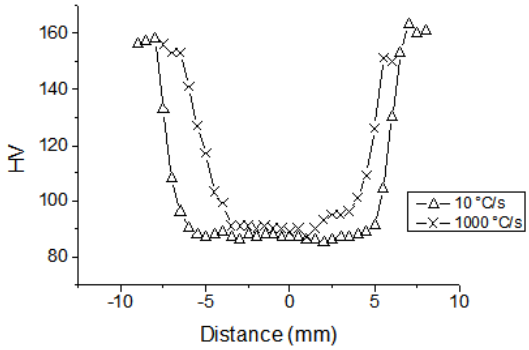

Fig. IV-1. Hardness (HV3) profile on samples treated at 10 °C/s and 1000 °C/s.

IV-4 Analysis

The quantification of the recrystallized ferrite fraction was performed on EBSD data with TSL-OIM Analysis V6.3. The raw EBSD data were post-processed (cleaned) to correct incorrectly indexed points using the grain confidence index standardization procedure. The microstructure is composed of recrystallized and unrecrystallized grains. Several methodologies to separate the recrystallized grains from the deformed matrix have been proposed in the literature [35–37]. In the present study, the plot of Grain Average Misorientation (GAM) versus the area fraction was employed. Such approach has been applied elsewhere [38] for determining the recrystallized grains. Grains with GAM less than 0.7° were considered as recrystallized. The grains with GAM larger than 0.7° were considered as non-recrystallized.

IV-5 Results

IV-5.1 Microstructure evolution

Fig. IV-2 shows the fraction of recrystallized ferrite and the ferritic grain size versus temperature, respectively. The curves were constructed from EBSD data. The curves of the recrystallized ferrite fraction are slightly displaced to higher temperatures as the heating rate is increased. The average ferritic grain size is larger for samples heated at 10 °C/s, compared to values of samples heated to the same peak temperatures at higher heating rates.

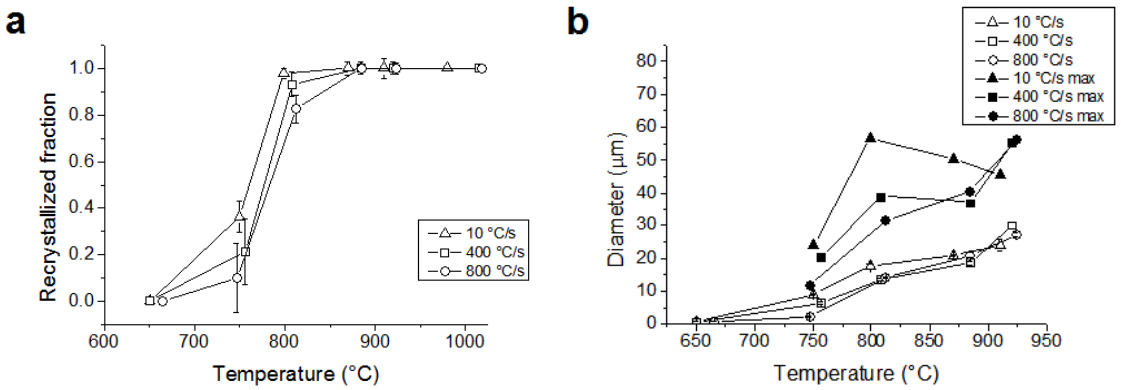

Fig. IV-2. Recrystallized ferrite fraction (a) and average ferritic grain size (b) versus temperature for samples heated at 10 °C/s (triangles), 400 °C/s (squares) and 800 °C/s (circles). Plots constructed from EBSD data.

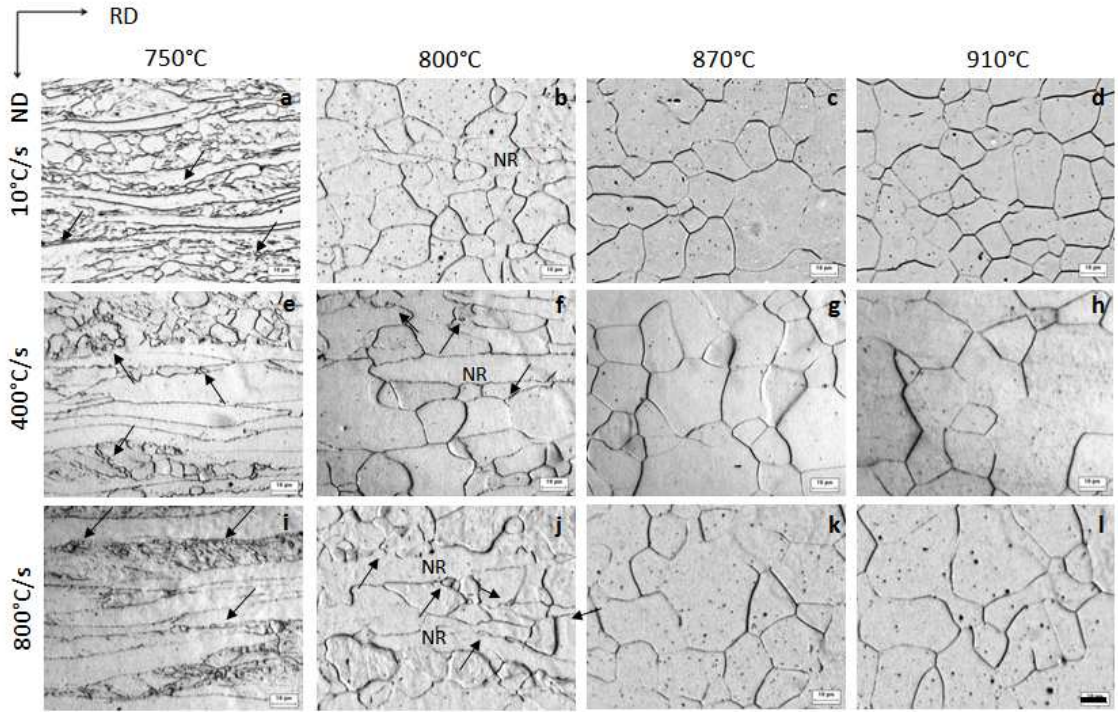

Fig. IV-3. Microstructure of samples heated at 10 °C/s (a, b, c and d), 400 °C/s (e, f, g and h) and 800 °C/s (i, j, k and l). The peak temperatures are 750 °C (a, e, and i), 800 °C (b, f and j), 870 °C (c, g and k) and 910 °C (d, h and l). NR indicates non-recrystallized ferrite. Etched with Marshall´s reagent. Scale bar (black line in the bottom right) is 10 µm.

The microstructure evolution after heating to different peak temperatures is shown in Fig. IV-3. The etching reveals deformation bands all across the microstructure. At ~750 °C, the recrystallization of ferrite has already started for the three heating rates. Nucleation has taken place at deformation bands and with somewhat less frequency at grain boundaries (GB), as

indicated by arrows in Figs. IV-3a, IV-3e, and IV-3i. At 800 °C (Figs. IV-3b, IV-3f and IV-3j) the recrystallization is almost complete for samples heated at 10 °C/s, whereas a significant fraction of non-recrystallized (NR) ferrite is still present after heating at the two increased heating rates. Arrows in Figs. IV-3f and 3j indicate the presence of very small equiaxed grains combined with large deformed ones, suggesting that nucleation is still an ongoing process in samples heated to 800 °C at 400 °C/s and 800 °C/s. Fully recrystallized equiaxed grains are observed above 870 °C, irrespective of the heating rate. The precipitation and Ostwald ripening of cementite is clearly shown as black spots in the microstructure in all heating rates as the peak temperature is raised above 750 °C (from left to right in Fig. IV-3). At 750 °C (in Figs. IV-3a, 3e, and 3i) only a few cementite black spots can be discerned, which indicates that carbon is either in solution or precipitates are too fine to be resolved by optical microscopy.

IV-5.2 Textures

Fig 4a shows the key for the main BCC texture components in the ϕ_2 = 45°section of Euler space and Fig. IV-4b displays the orientation distribution function (ODF) of the 50% cold rolled steel sample. The highest intensities in the cold rolled material are for the {113}⟨110⟩, {554}⟨225⟩, {111}⟨121⟩, and {111}⟨112⟩ components with values above 9 mrd (multiples of random density). The overall texture distribution is similar to cold rolled textures of ferrite published elsewhere [39].

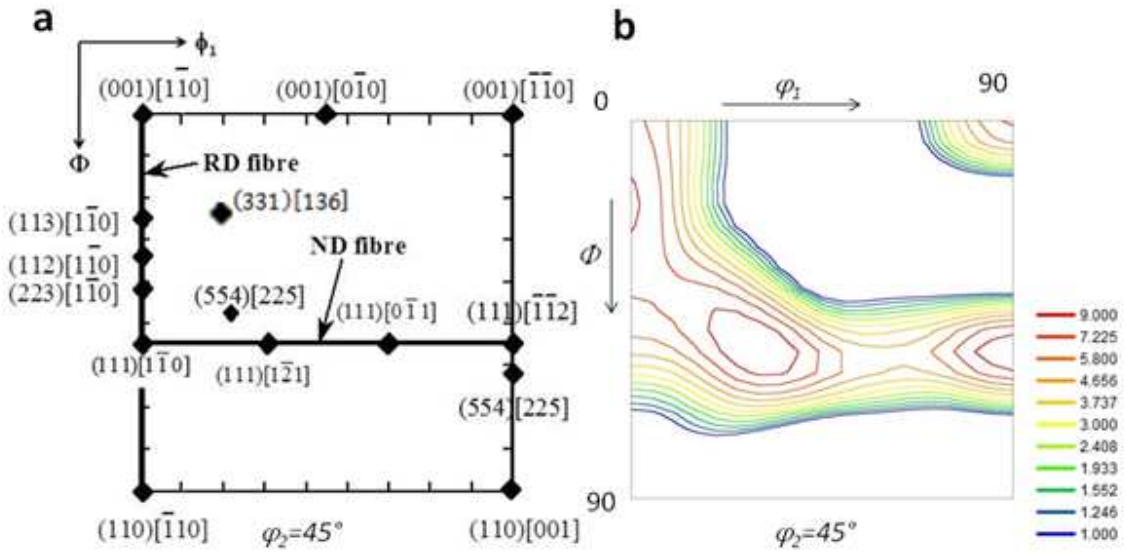

Fig. IV-4. (a) Ideal positions of the most important BCC texture components in the φ_2 =45° section of Euler space and (b) plot of ODF of 50 %cold rolled initial microstructure.

The texture evolution of samples heated at different heating rates to three different peak temperatures (750 °C, 870 °C and 910 °C) is shown in Fig. IV-5. The ODFs at 750 °C were split in the ODF corresponding to the overall material heated at 10 °C/s, 400 °C/s and 800 °C/s (Figs. IV-5a, 5b

and 5c, respectively) and the ODFs corresponding to the recrystallized ferrite grains only (Figs. IV-5d, 5e and 5f, respectively). The ODFs corresponding to the overall microstructure heated at 10 °C/s, 400 °C/s and 800 °C/s to 870 °C are illustrated in Figs. IV-5g, 5h, and 5i, respectively. Similarly, ODFs of the overall microstructure heated at 910 °C for the three heating rates are shown in Figs. IV-5j, 5k, and 5l, respectively.

Recrystallized grains at 750 °C (Figs. IV-5b, 5d and 5f) are oriented around the {111}⟨uvw⟩ ND fiber components, particularly the {111}⟨112⟩ and {554}⟨225⟩ components. The relative intensity of recrystallized grains tends to increase more sharply around such components as the heating rate is accelerated from 10 °C/s to 400 °C/s, although the maximum intensity has decreased from ~5.8 mrd to ~4.6 mrd as the heating rate has increased from 400 °C/s to 800 °C/s. The intensity decrease may be a consequence of the lower recrystallized ferrite fraction (~0.1) in the sample heated at 800 °C/s compared to the sample heated at 400 °C/s (~0.2). No changes in recrystallization gamma fiber components were detected in the material in all thermal cycles at peak temperatures above 750 °C. However, as the peak temperature is elevated, the general intensity of {111}⟨uvw⟩ ND fiber decreases as the heating rate has increased.

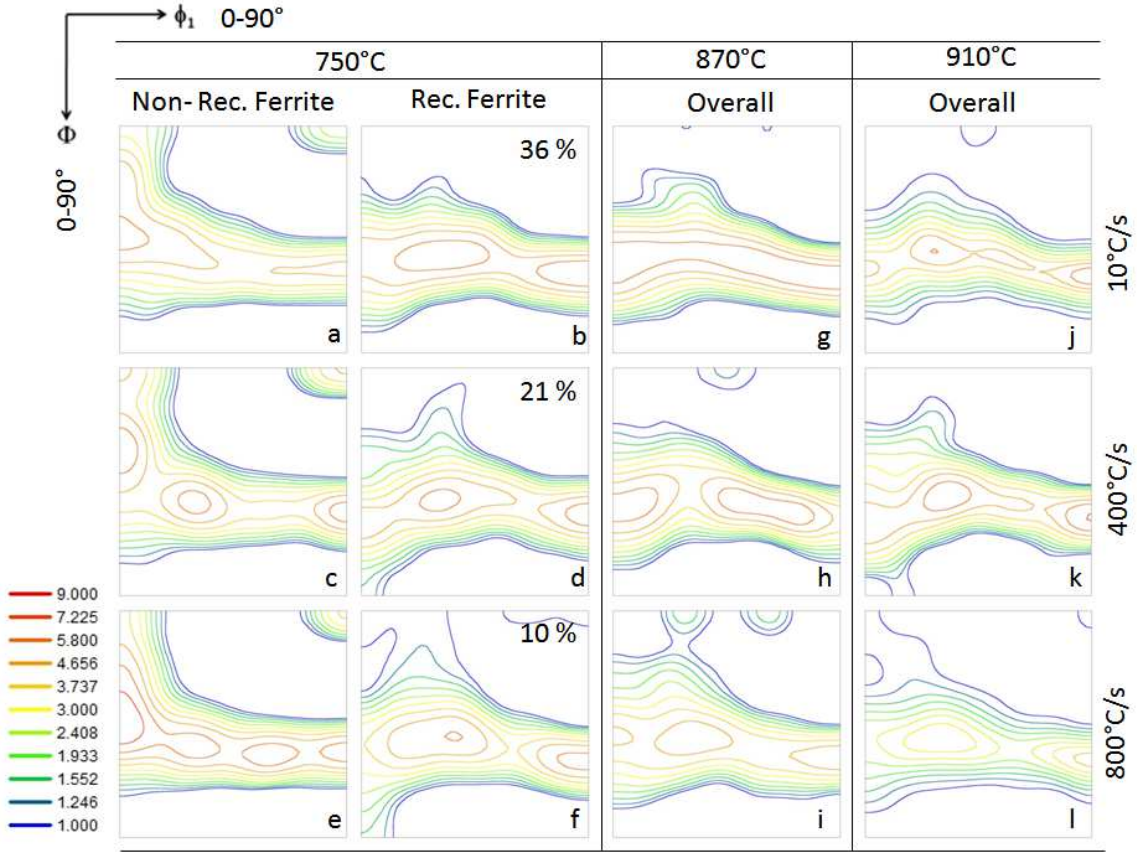

Fig. IV-5. ODF of ferrite at ϕ_2 = 45° from samples heated at 10 °C/s (a - f),400 °C/s (g - i) and 800 °C/s (j - l). (a - f) correspond to a peak temperature of 750 °C, (g - i) to 870 °C and (j - l) to 910 °C. (a), (c), (e) and (g - l) correspond to the non-recrystallized fraction of ferrite, whereas (b, d, and f)

correspond to recrystallized ferrite. Numbers in (b), (d), and (f) indicate the recrystallized ferrite fraction.

IV-6 Discussion

IV-6.1 Nucleation

EBSD analysis has detected a negligible fraction of recrystallized grains at temperatures below 750°C. However, SEM SE images have revealed zones where recrystallization has already begun at temperatures of ~650 °C for heating rates of 10 °C/s, 400 °C/s and 800 °C/s, cf. Fig. IV-6. This temperature is lower than the nucleation temperatures reported by Muljono et al. [19], but in fairly good agreement with data reported by Senuma et al. [28] for steel of similar chemical composition, although the authors do not make any specific comment in this regard. In the current experiments, the size of recrystallized ferrite grains at this temperatures is similar for the three heating rates and is in the range of 0.2 to 1 µm diameter. The step size of EBSD scans (0.3 µm) and the grain definition (5 points per grain, in at least 2 rows) would allow identifying grains of diameter < ~0.75 µm. Thus, the early recrystallized grains of diameter lower than ~0.75 µm will not be detected by the EBSD scan and cannot be accounted in the recrystallized fraction in Fig. IV-2a.

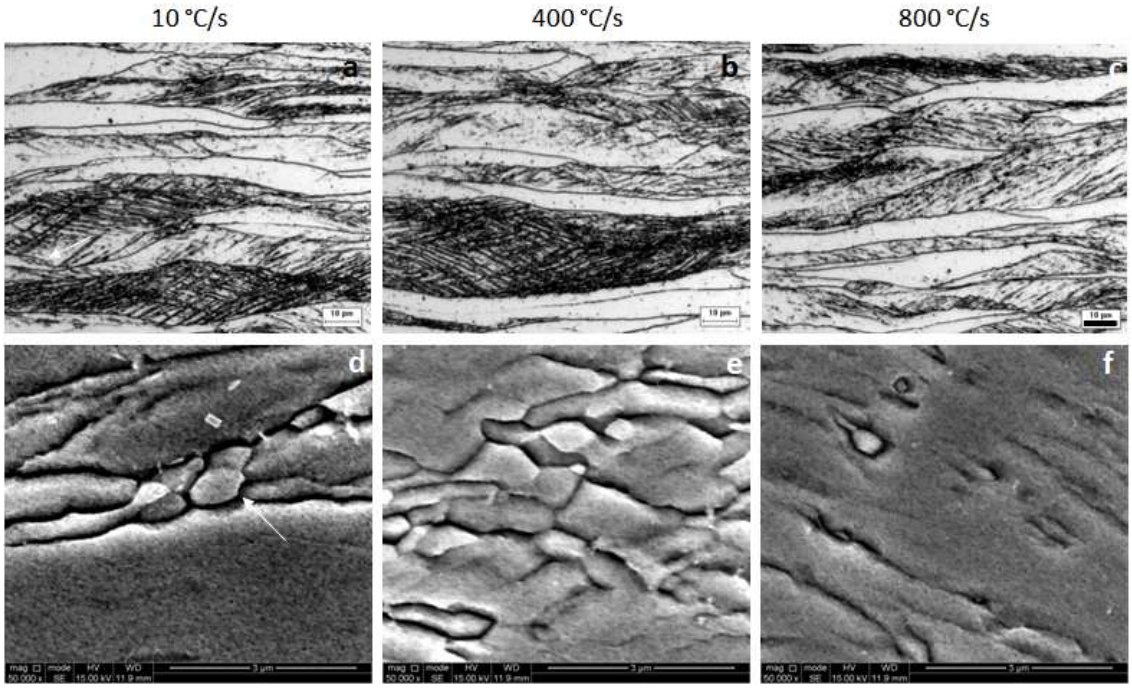

Fig. IV-6. OM (a-c) and SEM (d-f) images of samples heated at 10 °C/s (a, d), 400 °C/s (b, e) and 800 °C/s (c, f) to 650 °C and quenched. Etched with Marshall´s reagent. Scale bar (black line in c) is 10 µm.

Detailed EBSD characterization has confirmed the presence of recrystallized ferrite nuclei in the microstructure at 650 °C. Fig. IV-7 shows different EBSD maps of the microstructure of a sample heated at 10 °C/s and 400 °C/s to 650 °C, immediately followed by quench. Shear bands and grain boundaries, as shown in Fig 3 and Fig. IV-6, are readily observed in Fig. IV-7a and Fig. IV-7d (Inverse Pole Figure map, IPF). The black lines mark the high angle grain boundaries (15° - 63°) whereas the white lines mark the grain boundaries between 5° and 15°. Arrows indicate the presence of ferrite nuclei in Fig 7. White arrows indicate recrystallized ferrite grains formed inside deformed grains (in shear bands or deformation bands), whereas black arrows show ferrite nuclei at grain boundaries. Unique Grain (UG) maps (Figs. IV-7c and 7f) clearly confirm the position of ferrite nuclei either within deformed grains or at the boundaries. Notice that black lines outline ferrite nuclei (i. e. high angle grain boundaries). Figs. IV-7b and 7e show the Grain Average Misorientation (GAM) maps in which recrystallized ferrite grains are clearly revealed. Low GAM grains are green, whereas high GAM are yellow-red.

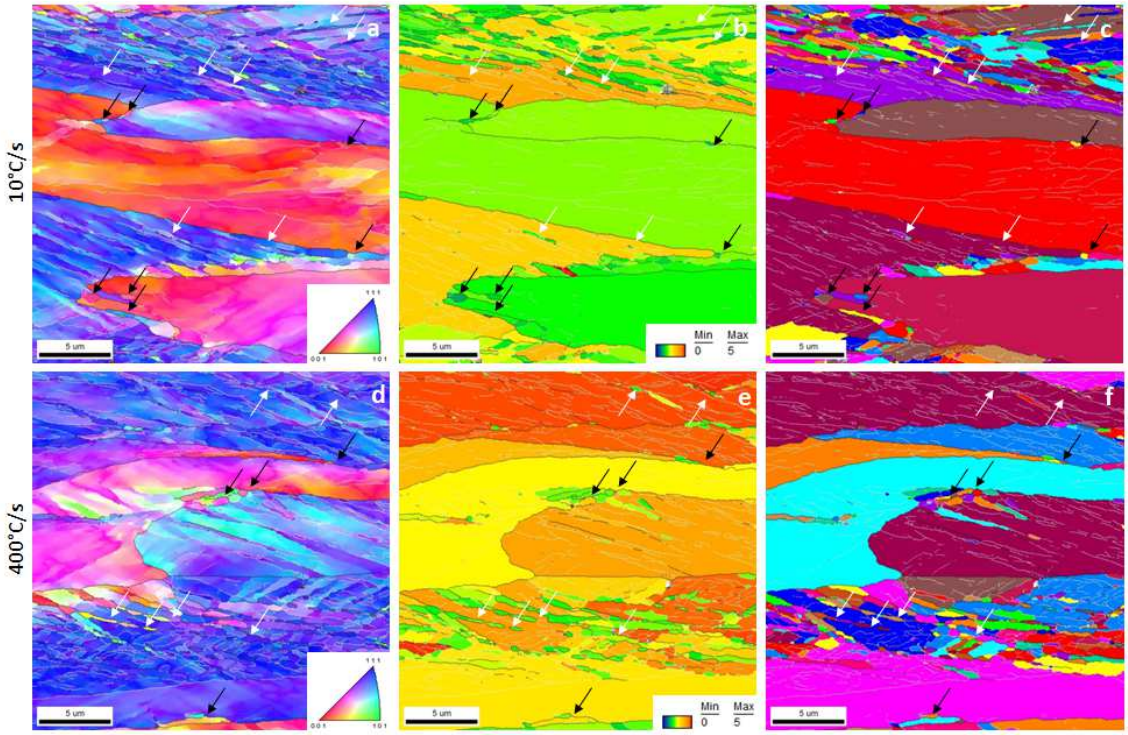

Fig. IV-7. EBSD scan of samples heated at 10 °C/s (a-c) and 400 °C/s (d-f) to 650 °C and quenched showing recrystallization within deformed grains (white arrows) and grain boundaries (black arrows). (a,d) Inverse Pole Figure (IPF) map, (b,e) Average Misorientation (GAM) map, (c,f) Unique Grain (UG) map. Black lines show grain boundaries with misorientation between 15° and 63°, whereas white line show grain boundaries between 5° and 15°. Step size 45 nm. Scale bar is 5 µm.

Nucleation takes place during heating and is not restricted by site saturation, as pointed out in the previous section, probably because the available sites for stabilization of ferritic embryos have not

been fully consumed by existing recrystallized grains. Shear bands (SB) were observed to be the preferred nucleation sites for recrystallization at 650 °C (Figs. IV-7e and 7f). Grain boundary nucleation (as indicated by the arrow in Fig. IV-7c and 7d) was observed with less frequency. Nucleation is still taking place at 750 °C and 800 °C for heating rates of 10 °C/s, 400 °C/s and 800 °C/s (arrows in Fig 3At 750 °C, shear bands are the preferred nucleation sites, whereas at 800 °C grain boundary nucleation becomes dominant. Notice that shear bands are not visible at 800 °C, which is a consequence of the recrystallization of deformed grains full of SB. One could thus conclude that shear bands, which are generally associated to {111}⟨211⟩, are the preferred nucleation sites because of the large stored energy [40,41] and thus high driving force.

The crystallographic orientations of ferrite nuclei in samples heated at 10 °C/s and 400 °C/s is shown in Fig. IV-8. As previously indicated in Fig. IV-7, recrystallized ferritic grains were observed at grain boundaries and inside deformed grains. The ODF for nuclei formed at GB is shown in Figs. IV-8a and 8c. The orientations do not show a marked texturization, only some weak traces of {111}⟨uvw⟩ ND fiber in Fig. IV-8c. GB nucleated ferrite show strong {110}⟨001⟩, {116}⟨391⟩ and {111}⟨341⟩ components, whereas ferrite nucleated inside deformed grain (Figs. IV-8b and 8d) clearly show strong {111}⟨uvw⟩ ND fiber texture. Notice that the maximum intensity of {111}⟨uvw⟩ ND fiber components decreases when the heating rate is accelerated from 10 °C/s to 400 °C/s, consistent with results shown in Fig. IV-5. Moreover, the overall texture of grains recrystallized within the deformed grains, i. e., {111}⟨uvw⟩ ND fiber, seems to prevail at later stages (higher temperatures) over the orientations of GB nuclei for all heating rates.

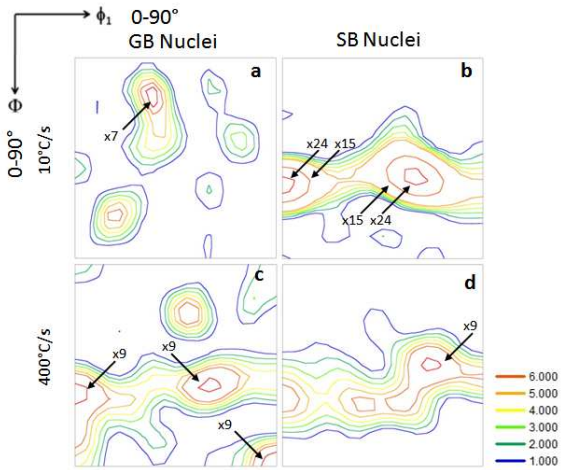

Fig. IV-8. ODF of ferrite at ϕ_2 = 45° of recrystallized ferrite grains located at grain boundaries (GB Nuclei, left) and within the grains (SB Nuclei, right), as indicated by arrows in Fig. IV-7. (a,b) samples heated at 10 °C/s to 650 °C and quenched, (c,d) samples heated at 400 °C/s to 650 °C and quenched. An average of 20 grains located at GB and 20 grains located at SB were considered for the plots.

IV-6.2 Recrystallization

The general features of recrystallization are in agreement with previous works [19,20,22,26,28]. The fraction of recrystallized grains decreases as heating rate is accelerated when the samples are heated to the same peak temperature. The curves of average and maximum grain sizes are displaced to the left as the heating rate is increased. This displacement is caused by the shift in recrystallization temperature. Fig. IV-2b show a clear indication of austenite formation at temperatures above 870 °C. The average diameter (outlined points) as well as the largest ferritic grain (solid points) describe an increase of the slope of the curve, which is associated with the formation of austenite.

The variation in recrystallized orientation components at 750 °C (shown in Figs. IV-5b, 5d and 5f) reveals that when the heating rate is increased, there is a significant spread of the iso-intensity lines parallel to the higher Φ values on the α fibre, particularly towards the $\{110\}\langle 110\rangle$ component with $\Phi=90°$. One can, thus, conclude that a more significant fraction of grains with crystallographic orientations parallel to ~$\{110\}\langle 110\rangle$ have recrystallized in the microstructure when high heating rates are applied. The fact that such components are present at high heating rates can be understood in terms of the driving force for recrystallization, i. e., the stored energy. Measurements of stored energy in 70% cold rolled iron were published in 1972 by Dillamore et al. [40], associating the crystallographic planes aligned with the rolling plane with the cell size of the deformed structure. In 1992, Tóth and Jonas [42] modeled the dynamic recrystallization in grains of different orientations introducing the Taylor factor (M). In 1999, Hutchinson [41] successfully correlated the grain orientation and the stored energy of cold rolled iron with the M. One could, therefore, obtain a reasonable approximation of the stored energy in the cold rolled microstructure by calculating the Taylor factor map of all possible orientations, cf. Fig. IV-10. It can be observed that for α-fibre orientations the Taylor factor M (and thus, the stored energy) is increasing for ascending values of Φ, in agreement with the findings of Dillamore et al. [40].

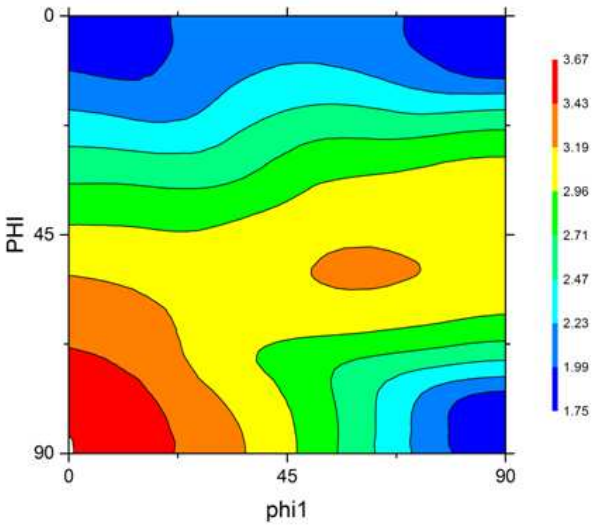

Fig. IV-9. Taylor factor map for cold rolled low carbon steel.

IV-6.2.1 Effect of UFH in the recovery stage

Although very scattered data are available [43], a kinetic effect is to be expected when recrystallization at conventional heating rates (<10 °C/s) is compared with its counterpart at high heating velocities (<400 °C/s). Processes under conventional (slow) heating rates show in fact fast kinetics of recrystallization, cf. Fig. IV-2a; whereas the acceleration of heating velocities is shifting the anisothermal recrystallization curve to the right, i. e., to higher temperatures. It is thus suggested that recrystallization is more difficult as the heating rate is increased, hence only grains with high stored energy can nucleate at ultrafast heating rates. As shown in Figs. IV-5d and 5f, new ferritic grains display orientations between Φ = ~30° and Φ = 90° at ϕ_1 = 0°. The orientations close to Φ = 90° or {110}⟨110⟩ correspond to the highest stored energy, thus the largest driving force for recovery. Such components have an intensity below 1 mrd in the material recrystallized at 10 °C/s (Fig. IV- 5b).

IV-6.2.2 Effect of UFH during recrystallization

It should be noted that the fraction of recrystallized grains at 750 °C decreases as the heating rate increases (Fig. IV-2). Materials heated at 10 °C/s show some small spread around {hkl}⟨110⟩ (Fig. IV-5b) which seems to concentrate towards {111}⟨uvw⟩ at higher temperatures (Figs. IV-5g and 5j). One can conclude that some of the {hkl}⟨110⟩ components were consumed by {111}⟨uvw⟩ oriented grains during the recrystallization process and have thus decreased its relative intensity in the ODF plots. At heating rates above 400 °C/s (Fig. IV-5d and 5f), the recrystallized grains have very sharp {111}⟨121⟩ and {554}⟨225⟩ components that prevail at higher temperatures (Fig. IV-5k and 5l). At 870 °C, most of the {110}⟨110⟩ components are not present in the ODF plots. However, some of the {hkl}⟨110⟩ components have also grown in the recrystallized microstructure, although with less intensity. The texture evolution in samples heated at 800 °C/s suggest that some small fraction of {hkl}⟨110⟩ components have recrystallized, as shown by Fig. IV-5i and 5l. It is believed that the fraction of {hkl}⟨110⟩ components at UFH rates is also partially explaining the somewhat lower intensities of {111}⟨uvw⟩ ND fiber components, compared to conventional heating rates.

IV-7 Conclusions

Ultrafast heating experiments followed by quenching have been carried out in ultra low carbon steel. Detailed microstructural characterization showed that the recrystallized fraction curves are slightly shifted to high temperatures when the heating rate is increased. Virtually no changes in average recrystallized grain size and recrystallization texture were detected between conventional and ultrafast heating cycles. The {111}⟨uvw⟩ ND fiber of ferrite nucleated inside deformed grain is also found as the predominant fiber at later stages of recrystallization. Differences in stored energy, a consequence of the heating rates, could account for the slight differences in texture components at early stages of recrystallization.

IV-8 References

[1] L.M. Clarebrough, M.H. Loretto, Order-Disorder Phenomena in alpha-Brass. I. Development of Order, Proc. R. Soc. London A Math. Phys. Eng. Sci. 257 (1960) 326–337. http://rspa.royalsocietypublishing.org/content/257/1290/326.abstract.

[2] L.M. Clarebrough, M.E. Hargreaves, M.H. Loretto, Order-Disorder Phenomena in alpha-Brass. II. Influence of Quenching, Proc. R. Soc. London A Math. Phys. Eng. Sci. 257 (1960) 338–362. http://rspa.royalsocietypublishing.org/content/257/1290/338.abstract.

[3] L.M. Clarebrough, M.E. Hargreaves, M.H. Loretto, Order-Disorder Phenomena in alpha-Brass. III. Influence of Plastic Deformation, Proc. R. Soc. London A Math. Phys. Eng. Sci. 257 (1960) 363–385. http://rspa.royalsocietypublishing.org/content/257/1290/363.abstract.

[4] L.M. Clarebrough, M.E. Hargreaves, M.H. Loretto, Order-Disorder Phenomena in alpha-Brass. IV. Nature of Order and Role of Atomic Mobility, Proc. R. Soc. London A Math. Phys. Eng. Sci. 261 (1961) 500–515. http://rspa.royalsocietypublishing.org/content/261/1307/500.abstract.

[5] M.N. Bodyako, Y.M. Loiko, B.L. Pavlyukevich, V.I. Parkhimovich, Recrystallization diagrams for induction heating, Met. Sci. Heat Treat. Met. 2 (1962) 57–59. doi:10.1007/BF00655595.

[6] F.F. Kraft, R.N. Wright, M.K. Jensen, Kinetics of nonisothermal recrystallization, J. Mater. Eng. Perform. 5 (1996) 213–219. doi:10.1007/BF02650889.

[7] S.L. Semiatin, I.M. Sukonnik, V. Seetharaman, An analysis of static recrystallization during continuous, rapid heat treatment, Metall. Mater. Trans. A. 27 (1996) 2051–2053. doi:10.1007/BF02651955.

[8] S. Primig, H. Leitner, W. Knabl, A. Lorich, H. Clemens, R. Stickler, Influence of the heating rate on the recrystallization behavior of molybdenum, Mater. Sci. Eng. A. 535 (2012) 316–324. doi:10.1016/j.msea.2011.12.099.

[9] J.A. Wert, N.E. Paton, C.H. Hamilton, M.W. Mahoney, Grain refinement in 7075 aluminum by thermomechanical processing, Metall. Trans. A. 12 (1981) 1267–1276. doi:10.1007/BF02642340.

[10] A.W. Bowen, Texture development in high strength aluminium alloys, Mater. Sci. Technol. 6 (1990) 1058–1071. doi:10.1179/026708390790190045.

[11] M. Ferry, D. Jones, High-rate annealing of single-phase and particle-containing aluminium alloys, Scr. Mater. 38 (1998) 177–183.

[12] W.J. Poole, M. Militzer, M. a. Wells, Modelling recovery and recrystallisation during annealing of AA 5754 aluminium alloy, Mater. Sci. Technol. 19 (2003) 1361–1368. doi:10.1179/026708303225005980.

[13] M.M. Attallah, M. Strangwood, C.L. Davis, Influence of the heating rate on the initiation of primary recrystallization in a deformed Al-Mg alloy, Scr. Mater. 63 (2010) 371–374. doi:10.1016/j.scriptamat.2010.04.016.

[14] D. Beckenhauer, P. Niessen, R. Pick, Effect of heating rate on the recrystallization

temperature of tantalum, J. Mater. Sci. Lett. 12 (1993) 449–450. doi:10.1007/BF00452788.

[15] G.K. L'vov, Accelerated recrystallization of low carbon steel, Met. Sci. Heat Treat. Met. 1 (1959) 11–16. doi:10.1007/BF00820268.

[16] R.H. Goodenow, Recrystallization and grain structure in rimmed and aluminum killed low carbon steel, Trans. ASM. 59 (1966) 804–823.

[17] A.I. Vitkin, S.S. Guseva, Z.I. Sokolova, G.M. Vorob'ev, Effect of heating rate on the recrystallization texture of low-carbon steel 08 kp, Met. Sci. Heat Treat. 14 (1972) 350–353. doi:10.1007/BF00657029.

[18] M. Atkinson, Bifurcation of thermal restoration processes in deformed iron and steel, Mater. Sci. Eng. A. 262 (1999) 33–38. doi:10.1016/S0921-5093(98)01031-4.

[19] D. Muljono, M. Ferry, D.P. Dunne, Influence of heating rate on anisothermal recrystallization in low and ultra-low carbon steels, Mater. Sci. Eng. A. 303 (2001) 90–99. doi:10.1016/S0921-5093(00)01882-7.

[20] M. Ferry, D. Muljono, D.P. Dunne, Recrystallization Kinetics of Low and Ultra Low Carbon Steels during High-rate Annealing, ISIJ Int. 41 (2001) 1053–1060. doi:10.2355/isijinternational.41.1053.

[21] M. Atkinson, On the credibility of ultra rapid annealing, Mater. Sci. Eng. A. 354 (2003) 40–47. doi:10.1016/S0921-5093(02)00830-4.

[22] L. Kestens, A.C.C. Reis, W.J. Kaluba, Y. Houbaert, Grain Refinement and Texture Change in Interstitial Free Steels after Severe Rolling and Ultra-Short Annealing, Mater. Sci. Forum. 467–470 (2004) 287–292. doi:10.4028/www.scientific.net/MSF.467-470.287.

[23] C.S. Smith, Grains, Phases, and Interfaces—an Interpretation of Microstructure, Trans. AIME. 175 (1948) 15–51.

[24] M. Hillert, On the theory of normal and abnormal grain growth, Acta Metall. 13 (1965) 227–238. doi:10.1017/CBO9781107415324.004.

[25] I. Samajdar, B. Verlinden, P. Van Houtte, D. Vanderschueren, γ-Fibre recrystallization texture in IF-steel: an investigation on the recrystallization mechanisms, Mater. Sci. Eng. A. 238 (1997) 343–350. doi:10.1016/S0921-5093(97)00455-3.

[26] J. Stockemer, P. Vanden Brande, Recrystallization of a cold-rolled low-carbon steel by cold-plasma-discharge rapid annealing, Metall. Mater. Trans. A. 34 (2003) 1341–1348. doi:10.1007/s11661-003-0245-3.

[27] S.G. Chowdhury, E. V. Pereloma, D.B. Santos, Evolution of texture at the initial stages of continuous annealing of cold rolled dual-phase steel: Effect of heating rate, Mater. Sci. Eng. A. 480 (2008) 540–548. doi:10.1016/j.msea.2007.07.060.

[28] T. Senuma, K. Kawasaki, Y. Takemoto, Recrystallization Behavior and Texture Formation of Rapidly Annealed Cold-Rolled Extralow Carbon Steel Sheets, Mater. Trans. 47 (2006) 1769–1775. doi:10.2320/matertrans.47.1769.

[29] R. Petrov, L. Kestens, W.J. Kaluba, Y. Houbaert, Recrystallization and austenite formation in a cold rolled TRIP steel during ultra fast heating, Steel Grips. 1 (2003) 289–293.

[30] R. Petrov, J. Sidor, W.J. Kaluba, L. Kestens, Grain Refinement of a Cold Rolled TRIP Assisted Steel after Ultra Short Annealing, Mater. Sci. Forum. 715–716 (2012) 661–666. doi:10.4028/www.scientific.net/MSF.715-716.661.

[31] R.H. Petrov, A. Puype, D. De Knijf, L. Kestens, Ultrafast heating of advanced high strength steels, in: M. Militzer, G. Botton, L.-Q. Chen, J. Howe, C. Sinclair, H. Zurob (Eds.), Proc. Int. Conf. Solid-Solid Phase Transform. Inorg. Mater. 2015, 2015: pp. 1157–1158.

[32] V.T. G. Griffay, M. Anderhuber, P. Klinkenberg, New continuous annealing technology with high-speed induction heating followed by ultra-fast cooling, Brussels, 2002.

[33] A. Benscoter, M. Perricone, Marshall's Reagent: Origins, Modifications, and New Applications, Microsc. Microanal. 11 (2005) 76–77. doi:10.1017/S1431927605505415.

[34] G.F. Vander Voort, Metallography, Principles and Practice, ASM International, Metals Park, OH, 1999. https://books.google.be/books?id=GRQC8zYqtBIC.

[35] D.P. Field, Quantification of partially recrystallized polycrystals using electron backscatter diffraction, Mater. Sci. Eng. A. 190 (1995) 241–246. doi:10.1016/0921-5093(94)09601-R.

[36] S.I. Wright, M.M. Nowell, D.P. Field, A review of strain analysis using electron backscatter diffraction., Microsc. Microanal. 17 (2011) 316–329. doi:10.1017/S1431927611000055.

[37] H. Jazaeri, F.J. Humphreys, Quantifying recrystallization by electron backscatter diffraction, J. Microsc. 213 (2004) 241–246. doi:10.1111/j.0022-2720.2004.01296.x.

[38] R. Petrov, L. Kestens, Y. Houbaert, Recrystallization of a Cold Rolled Trip-assisted Steel during Reheating for Intercritical Annealling., ISIJ Int. 41 (2001) 883–890. doi:10.2355/isijinternational.41.883.

[39] R.K. Ray, J.J. Jonas, R.E. Hook, Cold rolling and annealing textures in low carbon and extra low carbon steels, Int. Mater. Rev. 39 (1994) 129–172. doi:10.1179/095066094790326112.

[40] I.L. Dillamore, P.L. Morris, C.J.E. Smith, W.B. Hutchinson, Transition Bands and Recrystallization in Metals, Proc. R. Soc. London. Ser. A, Math. Phys. Sci. 329 (1972) 405–420. doi:10.1098/rspa.1972.0120.

[41] B. Hutchinson, Deformation microstructures and textures in steels, Philos. Trans. R. Soc. A Math. Phys. Eng. Sci. 357 (1999) 1471–1485. doi:10.1098/rsta.1999.0385.

[42] L.S. Tóth, J.J. Jonas, Modelling the texture changes produced by dynamic recrystallization, Scr. Metall. Mater. 27 (1992) 359–363. doi:10.1016/0956-716X(92)90526-K.

[43] M.B. Bever, D.L. Holt, A.L. Titchner, The Stored Energy of Cold Work, Prog. Mater. Sci. 17 (1973) 1–177. doi:10.1016/0079-6425(73)90001-7.

Chapter V

Austenite formation in 0.2 %C and 0.45 %C steels subjected to conventional and ultrafast heating[2]

Austenite formation was investigated in 0.2 %C and 0.45 %C steels with initial microstructures consisting of ferrite and pearlite. The effect of conventional (10 °C/s), and ultrafast heating rates (>100 °C/s) on the nucleation and growth mechanisms was determined. Scanning Electron Microscopy (SEM), and Electron BackScatter Diffraction (EBSD) revealed that these mechanisms are active at ultrafast heating rates. Two mechanisms of austenite formation were identified: diffusional and massive. In addition, at conventional heating rates, the austenite formation kinetics was determined by carbon diffusion. However, at ultrafast heating rates, austenite formation was initially controlled by carbon diffusion, and subsequently by a massive mechanism. Thermodynamic and kinetic descriptions of austenite nucleation and growth were developed based on the experimental results.

V-1 Introduction

The ferrite-pearlite microstructure is the most produced microstructure in low and medium carbon steels and, hence, this microstructure is the most appropriate for investigating austenite formation. Pioneering studies [1–4] have clarified many important aspects associated with the isothermal formation of austenite from pearlite, and the knowledge garnered has been applied to the study of austenite formation in ferrite-pearlite aggregates [5,6]. These seminal studies established that austenite is a structure-sensitive process, and thus the initial microstructure plays an important role in the formation process and the morphology of the resulting austenite. This realization spurred extensive studies on the formation of austenite in pure iron [3,7–9] and steels with initial microstructure consisting of ferrite and spheroidized cementite [3,4,10–14]. Other early studies have considered martensite [15,16], bainite and, mixtures of these constituents as starting microstructures for the isothermal formation of austenite [17,18]. The main characteristics of austenite formation from ferrite-pearlite aggregates were first summarized by Mehl [1]. The key findings reported therein may be summarized as follows: (i) austenite formation is a thermally activated process, (ii) austenite is nucleated at pearlite boundaries, (iii) carbon gradients form during austenite growth [2], (iv) the time for complete formation of austenite decreases with decreasing pearlite interlamellar spacing and is only weakly dependent on the size

[2] This chapter has been partially published as F.M. Castro Cerda, I. Sabirov, C. Goulas, J. Sietsma, A. Monsalve, R.H. Petrov, Austenite formation in 0.2% C and 0.45% C steels under conventional and ultrafast heating, Mater. Des. 116 (2017) 448–460. doi:10.1016/j.matdes.2016.12.009

of the colony, and (v) the dissolution kinetics of cementite is significantly slower than that of ferrite. Subsequent studies [3,4] have confirmed these findings, and have served as a basis for the development of diffusion-controlled models describing austenite formation. However, most of the kinetic descriptions of austenite formation are based on isothermal conditions [16,19–23], rather than on heating experiments.

Some of the key theoretical aspects associated with the ultrafast heating of carbon steels were recently summarized by Meshkov and Pereloma [24]. The most important features are given as follows: (i) the initial microstructure influences the mechanism of austenite formation (as reported by Gridnev and Trefilov in 1954 [15]), (ii) the nucleation stage is governed by either diffusional or diffusionless mechanisms, and (iii) the growth stage is governed by either diffusion-controlled or interface-controlled (massive) mechanisms. Regarding (ii), Kaluba et al. [25] have initiated a debate [26–28] by attributing austenite formation during ultrafast heating to a novel 'bainitic transformation' mechanism. This mechanism was proposed based on the assumption that austenite sheaves form at grain boundaries and then grow into the grain interior, as in the case of a bainitic transformation. Aaronson and Nie [26] questioned these interpretations and proposed alternative explanations based on existing mechanisms of bainitic transformation. In subsequent work, Hillert [27] attributed Kaluba's observations to the formation of Widmanstätten ferrite. Regarding (iii), experimental evidence of the massive transformation in medium carbon steels has been provided [29,30], even for heating rates as low as 1°C/s.

Several attempts have been made to model anisothermal austenite formation starting from ferrite-pearlite microstructures [29,31–44]. The data used in most of these studies were collected via dilatometry, where heating rates are limited to values of 0.01–20 °C/s. Heating rates of up to 300 °C/s have been considered in a few cases [37]. A heating rate of 1000 °C/s (the highest-ever) was employed in a one-dimensional (1D) simulation of austenite growth [41]. However, these simulations considered only the carbon-diffusion-controlled growth of austenite, and the results were not compared with experimental data. A complete treatment of austenite formation, including the transition from a diffusion-controlled to an interface-controlled mechanism during heating, is presented in [31]. However, a clear thermodynamic definition of the transition temperature (referred to as $T_{massive}$) and experimental evidence of the change in mechanism are lacking. Based on in-situ observations of austenite formation during heating, Schmidt et al. [29] suggested that the change in mechanism of austenite formation occurs at T_0. The definition of the temperature associated with transition of the austenite formation mechanism remains debatable. However, the main features of austenite formation reported in [29,31–44] correspond closely to those reported in [1]. During heating, austenite forms via simultaneous transformations of (a) pearlite $\rightarrow$ austenite and (b) ferrite $\rightarrow$ austenite. Some authors consider austenite formation a two-stage process, where transformation (b) occurs only after (a) has occurred [34,36,39–42]. This represents, however, a simplification of the actual situation, where the kinetics associated with the transformation of pearlite differs significantly from that associated with the transformation of ferrite [39]. Experimental data have shown that the kinetics of transformation (b) changes gradually during heating above a certain thermodynamic threshold [29]. This change is attributed

to a transition of the austenite-formation mechanism from carbon diffusion control to interface mobility control. However, this shift is only noticeable above certain heating rates. Ultrafast heating (UFH) experiments provide the ideal conditions for investigating the kinetics of the transition, as well as the microstructural features occurring in the initial stages of formation. The main objective of the present work is to determine, through a combination of experimental and theoretical techniques, the effect of heating rate and carbon content on the mechanisms of austenite nucleation and growth. In-depth microstructural characterization is performed and the temperature associated with transition of the austenite-formation mechanism is determined. The results are expected to be of significance for understanding the effect of ultrafast heating on the formation of austenite in low-carbon ferrite-pearlite aggregates.

V-2 Material and experiments

Heating experiments were performed on two different steel grades, namely 0.2 %C and 0.45 %C, in the hot-rolled condition. The chemical composition of each steel is shown in Table V-1. Two types of heating tests were performed at different heating rates: 1) heating to 100% austenite formation and 2) peak-annealing tests followed by quenching, resulting in partial austenite formation. In the first type of testing, the specimen was heated at a constant rate to a certain temperature in the fully austenitic range. However, in the second type of test, the specimen was quenched after reaching a certain temperature between the onset and finishing of austenite formation. The first type of experiments (i.e., heating to complete austenitization) were conducted at heating rates of up to 200 °C/s in a DIL805bD Bähr Dilatometer. The-peak annealing tests were conducted at heating rates of 10 °C/s, 450 °C/s, and 1500 °C/s and temperatures of 750 °C, 800 °C, 850 °C, 900 °C, and 1100 ^{o}C (with holding times of <0.1 s) in a Gleeble 3800 thermomechanical simulator. Cooling (quenching) rates of ~-160 °C/s and ~-2000 °C/s were applied during the dilatometry and Gleeble experiments, respectively. The dilatometry measurements were performed on 10×5×1 mm³ rectangular specimens, whereas Gleeble tests were conducted on 6 mm (diameter)×116 mm (length) cylindrical specimens, which were threaded at both ends. The axis of each type of sample was parallel to the rolling direction (RD). In both cases, a thin wire thermocouple (S-type) was spot welded to the midsection of each specimen to control the temperature during annealing. Another S-type thermocouple was welded 3 mm away from the midsection to measure the temperature gradient during the experiments.

Table V-1. Chemical composition (in wt.%) of the studied steels.

Steel	C	Mn	Si	Cu	Fe
0.2 %C	0.17	1.08	0.22	0.27	Bal.
0.45 %C	0.44	0.63	0.26	0.23	Bal.

V-3 Characterization and data analysis

V-3.1 OM, SEM, and EBSD

The microstructural evolution of each sample was evaluated via Optical Microscopy (OM), Scanning Electron Microscopy (SEM), and Electron Backscatter Diffraction (EBSD). Metallographic specimens were cut from the middle section of each test sample to avoid the effect of temperature gradients along the sample length (i.e., along RD). The characterization was thus performed on the rolling plane at the center of the heat-treated sample, where the thermocouple was placed. The metallographic samples were prepared, in accordance with standard procedure, by grinding and polishing to a mirror-like finish with 1-μm diamond paste. The microstructure was revealed by etching, for ~10 s, with a solution of 4% HNO_3 in ethanol (nital 4%) at room temperature. Electron backscatter diffraction (EBSD) analysis was performed using a FEI Quanta™ 450-FEG-SEM (described in Chapter IV) The orientation data were post-processed using the following grain definition: grain boundary misorientation, minimum number of pixels per grain, and a confidence index (CI) of >5°, four, and >0.1, respectively.

Table V-2. Critical temperatures (°C) of each steel. The superscript indicates the heating rate in °C/s.

Steel	A_1	A_1^{10}, °C	A_3	A_3^{10}, °C	A_S
0.2 %C	690	713	817	860	870
0.45 %C	711	722	770	804	893

The phase fractions generated during the anisothermal dilatometric heat treatment are typically estimated via the lever rule. However, this approach yields significant deviations from actual values, owing to the difference in density of pearlite and ferrite [32,37,45–48]. Therefore, in the present study, a correction [47] was applied to the austenite phase fractions calculated from the dilatometric data. The phase fractions measured from OM (cf. Table 4) were estimated from the area fraction of each microstructural constituent. The measurements of area fraction were performed using the software ImageJ. The volume fraction of austenite (martensite) estimated from EBSD measurements (cf. Fig. 3) was carried out using the Grain Average Image Quality (GAIQ) criteria described elsewhere [49].

Table V-3. Parameters used in the Dictra calculations. f_P is the volume fraction of pearlite.

Steel	R_1, μm	R_2, μm	f_P
0.2 %C	10	6.07	0.24
0.45 %C	10	1.85	0.60

Thermodynamic calculations were performed using the software ThermoCalc, database TCFE7. The critical temperature of each material is shown in Table V-2. A_m has been defined as the temperature above which the free energy of austenite is lower than the free energy of ferrite when the carbon content approaches zero. In addition, the migration of the γ/α interface in

proeutectoid ferrite was evaluated via simulations of the microstructure during heating at different rates. These simulations were performed using the Dictra software, which allows the computation of diffusion-controlled transformation kinetics in multicomponent metallic systems. A general description of the software and the model is provided elsewhere [50–52]. The microstructure was simulated assuming an initially spherical representative volume, where the phases are distributed as shown in Fig. V-1. The dimensions (R_1 radius of the pearlite colony; R_2: difference between the total radius and the radius of the pearlitic colony) as well as the chemical composition and relative fractions (f_P: volume fraction of pearlite) of each phase (Table 3) were determined while maintaining the mass balance of the initial material. Three heating rates were simulated: 10 °C/s, 450 °C/s and 1500 °C/s. Simulations were performed assuming that all the pearlite was rapidly transformed into austenite when the system reached the $\alpha + \gamma$ equilibrium range. As shown in Section 4, this assumption is consistent with the results of dilatometry and metallographic analysis. The initial chemical composition of each phase was estimated, with ThermoCalc, at one of the temperatures associated with the metastable equilibrium of ferrite and cementite. The effect of carbon on the phase density was neglected during the calculation of the volumetric phase fractions.

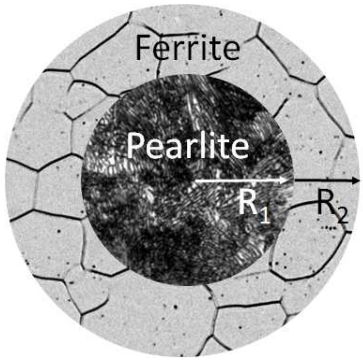

Fig. V-1. Schematic of the ferrite-pearlite initial microstructure used to simulate the diffusion-controlled formation of austenite.

V-4 Results

V-4.1 Austenite formation at a conventional heating rate

The initial microstructure of each steel (Fig. V-2a and 2e) consists of a mixture of ferrite and pearlite (see Table 4 for volume fraction of these phases). The micrographs shown in Fig. V-2b–2d and Fig. V-2f–2h reveal the microstructural evolution of samples heated at 10 °C/s to different peak annealing temperatures.

Table V-4. Phase quantification of the initial microstructure (revealed via orientation microscopy).

Steel	Ferrite fraction [%]	Pearlite fraction [%]	Standard deviation [%]
0.2 %C	66.1	33.9	1.3
0.45 %C	33.7	66.3	0.7

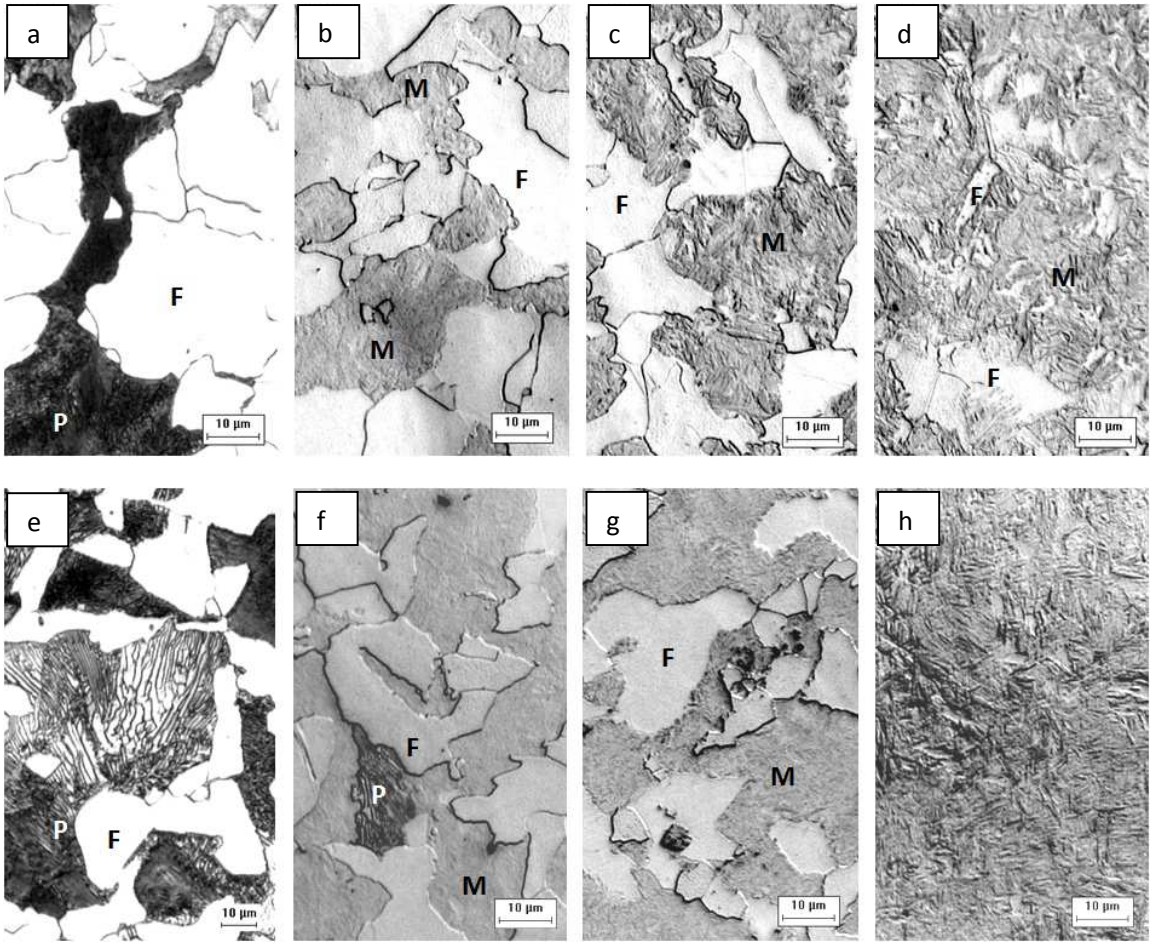

Fig. V-2. Microstructure of 0.2 %C (a, b, c, and d), and 0.45 %C (e, f, g, and h) steels heated at 10 °C/s to 750 °C (b, f), 800 °C (c, g), and 850 °C (d, h). (a, b) images of the initial microstructure. M, P, and F denote martensite, pearlite, and ferrite, respectively. Etched with nital (4%). Scale bar is 10 µm.

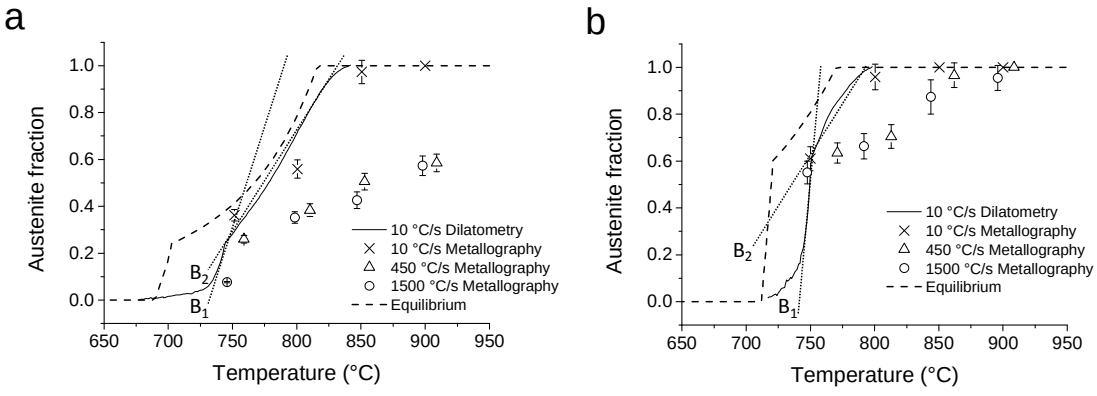

Fig. V-3. Temperature dependence of the austenite fraction (measured as martensite volume fraction) of 0.2 %C (a) and 0.45 %C (b) steels.

Although austenite nucleation sites cannot be identified from the OM images, these micrographs reveal that, at 750 °C, austenite rapidly consumes the pearlite colonies (Fig. V-2b and 2f)[3]. Austenite grows more rapidly into pearlite than into proeutectoid ferrite, owing to the absence of pearlite from the heat-treated specimens (Fig. V-2c, 2d, 2g, and 2h). The rate of advance of the γ/pearlite and γ/α interfaces is also revealed in the austenite fraction versus temperature curves obtained from dilatometry experiments (Fig. V-3). As the figure shows, each curve has a steep slope at temperatures lower than ~750 °C (B_1 lines), where austenite grows mainly into pearlitic grains.This slope decreases with increasing temperature (B_2 lines), when austenite grows into ferrite after pearlite has been fully consumed.

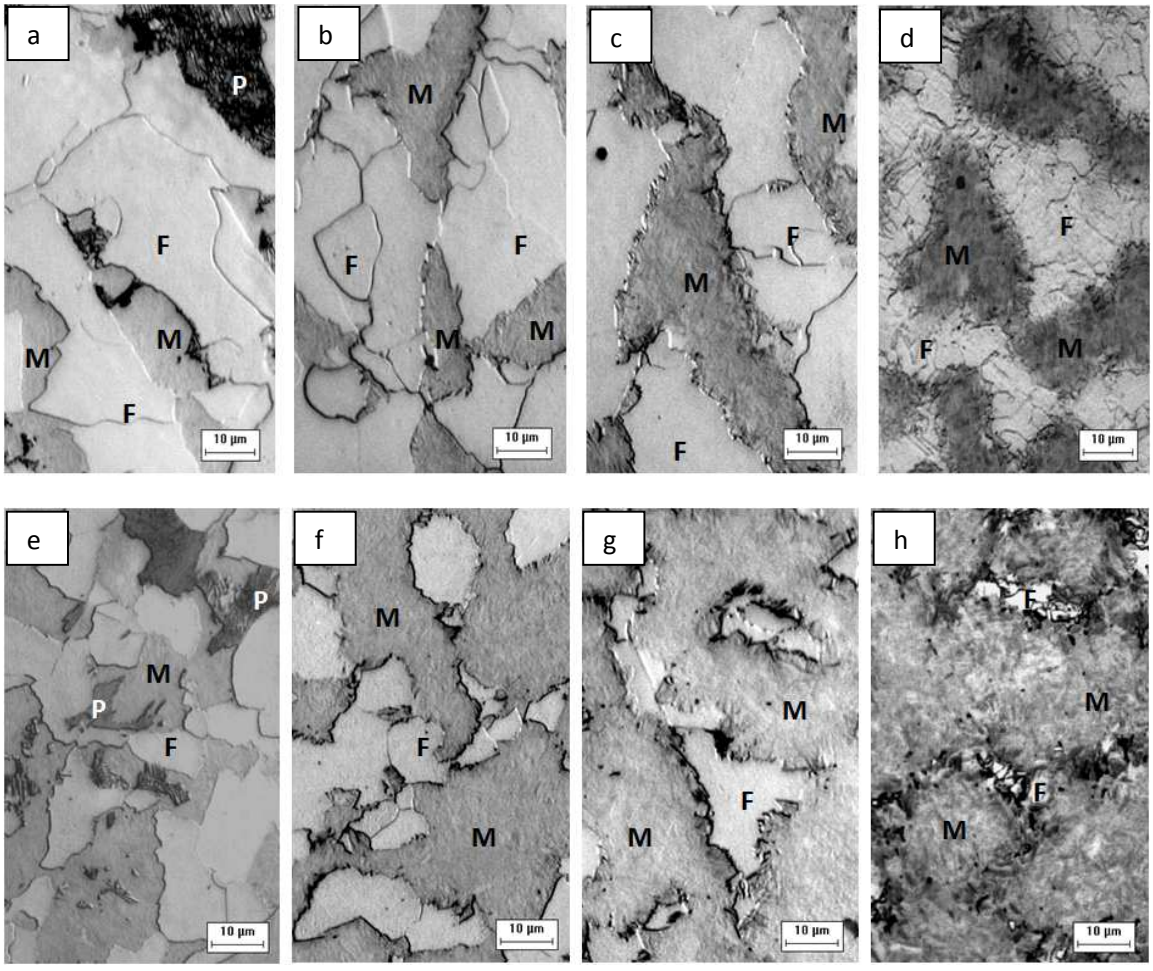

Fig. V-4. Microstructure of 0.2 %C steel (a, b, c and d), and 0.45 %C steel (e, f, g, and h) heated at 1500 °C/s to 750 °C (a, e), 800 °C (b, f), 850 °C (c, g), and 900 °C (d, h). M, P, and F denote martensite, pearlite, and ferrite, respectively. Etched with nital (4%). Scale bar is 10 µm.

[3] Owing to its transformation into martensite after quenching, austenite is absent from the OM, SEM, and EBSD images.

V-4.2 Austenite formation during ultrafast heating at 1500 °C/s

The evolution of the microstructure after heating at 1500 °C/s is shown in Fig. V-4. Regarding the formation of austenite, a consistent trend was observed: pearlite was rapidly transformed and the transformation rate at temperatures above 750 °C was somewhat lower than the rate associated with temperatures below 750 °C. This trend is also observed for samples heated at rates of 450 °C/s and 1500 °C/s (see Fig. V-4). At temperatures above 750 °C, lower volume fractions of austenite are formed during heating at 450 °C/s and 1500 °C/s than at 10 °C/s. The effect of the heating rate on the volume fraction is discussed further in Section 5.2.4.

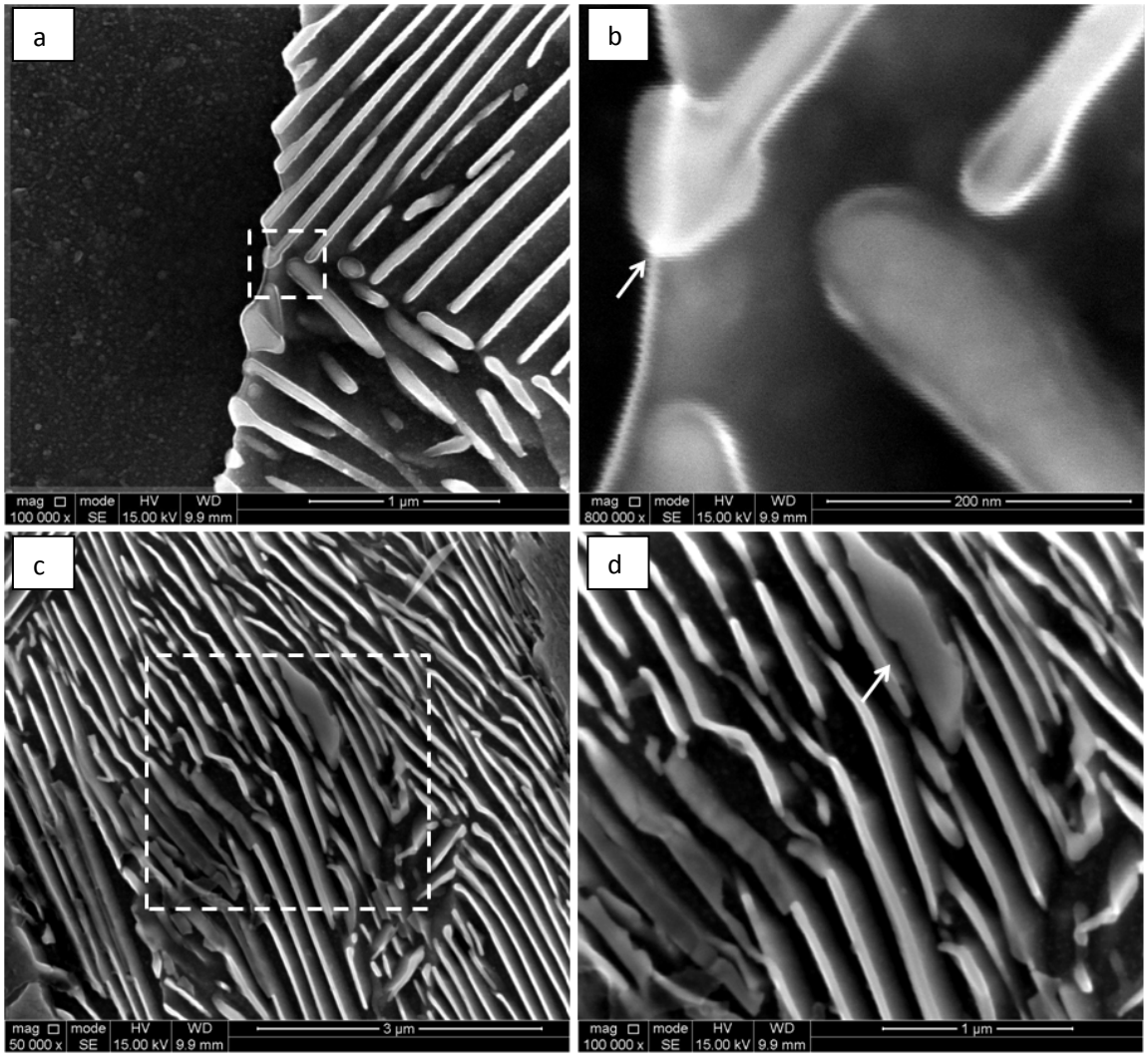

Fig. V-5. SEM images showing the microstructure of 0.2 %C steel heated at 1500 °C/s to 750 °C and quenched. (b) and (d) magnified view of the region enclosed in the white square shown in (a) and (c), respectively. The white arrow in 5b shows the nucleation of austenite at a junction between a ferrite/pearlite and a pearlite/pearlite boundary, whereas the white arrow in 5d shows the nucleation of austenite inside the pearlitic colony. Etched with nital (4%). Scale bar in a and d is 1 µm, b 200 nm and c 3 µm.

V-4.2.1 Nucleation of austenite

The UFH experiments, which allow observation of the initial stages of austenite formation, revealed that austenite nucleation occurs at α/pearlite and pearlite/pearlite boundaries. Fig. V-5a and 5b show a nucleus of austenite that formed in front of a cementite plate (arrow). The formation of the nucleus on a junction between an α/pearlite boundary and a pearlite/pearlite boundary is indicative of enhanced local energy. Nucleation also occurred within pearlitic colonies, as shown in Fig. V-5c and 5d.

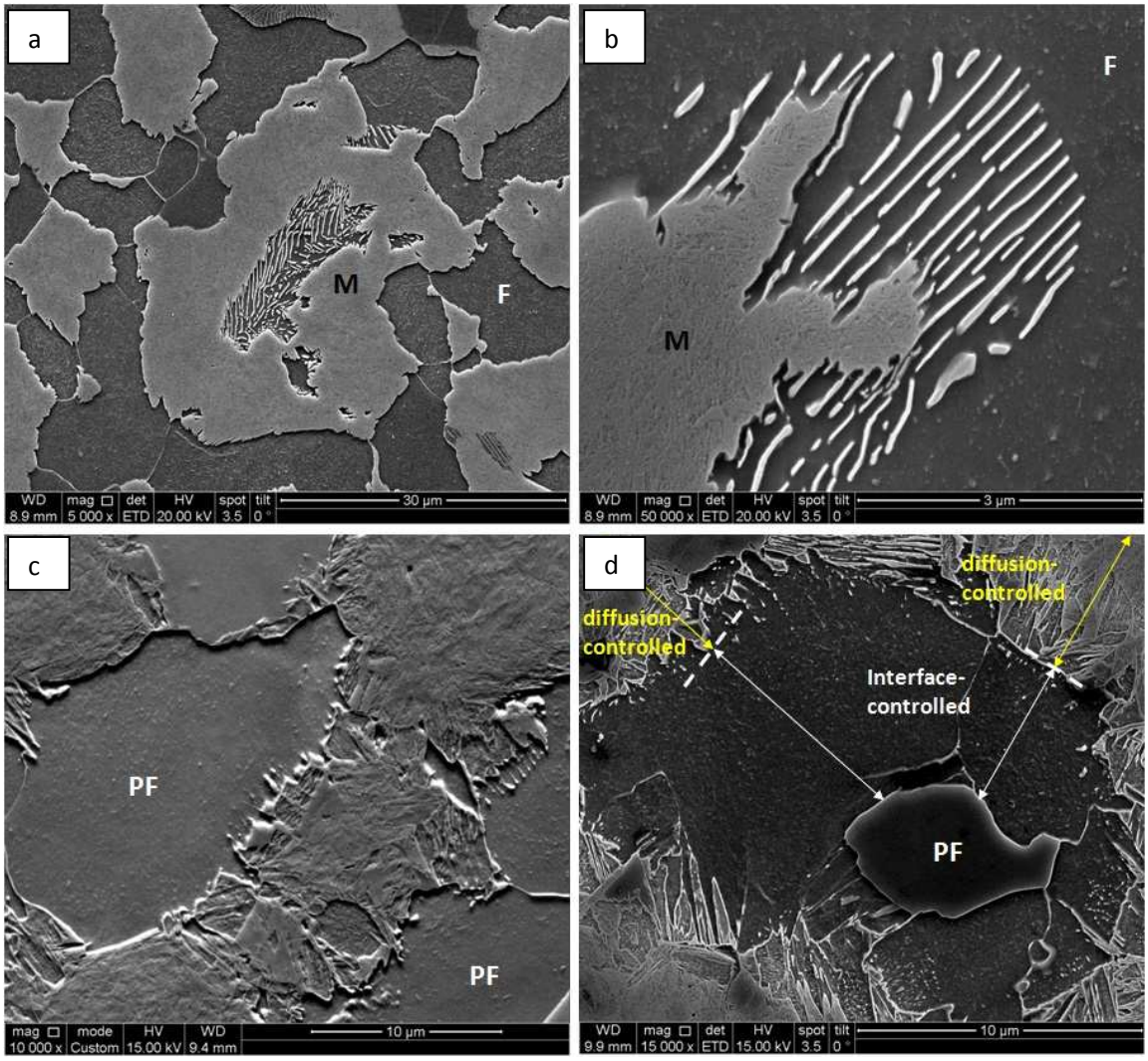

Fig. V-6. Microstructure of the (a)–(b) 0.45 %C steel heated at 1500 °C/s to 750 °C and quenched, showing the rapid advance of austenite into pearlite and (c)–(d) 0.2 %C steel heated at 1500 °C/s to (c) 850 °C and quenched and (d) 900 °C and quenched. The morphology of ferrite changed during heating. Arrows in (d) indicate the possible mechanisms governing the phase transformation. M, F, and PF denote martensite, ferrite, and proeutectoid ferrite, respectively. Etched with nital (4%). Scale bar in a is 30 µm, b 3 µm, c and d 10 µm.

V-4.2.2 Growth of austenite

Austenite, once nucleated, grows in all directions, and more rapidly into pearlite than into proeutectoid ferrite. The preferential growth of austenite into pearlite (as shown in Fig. V-6a and 6b) is indicative of the rapid kinetics of austenite formation. Consistent with Fig. V-3, the transformation of pearlite has the most influence on the overall kinetics of austenite formation at temperatures of up to ~750 °C; at higher temperatures, the process is controlled by the kinetics of austenite growth into proeutectoid ferrite.

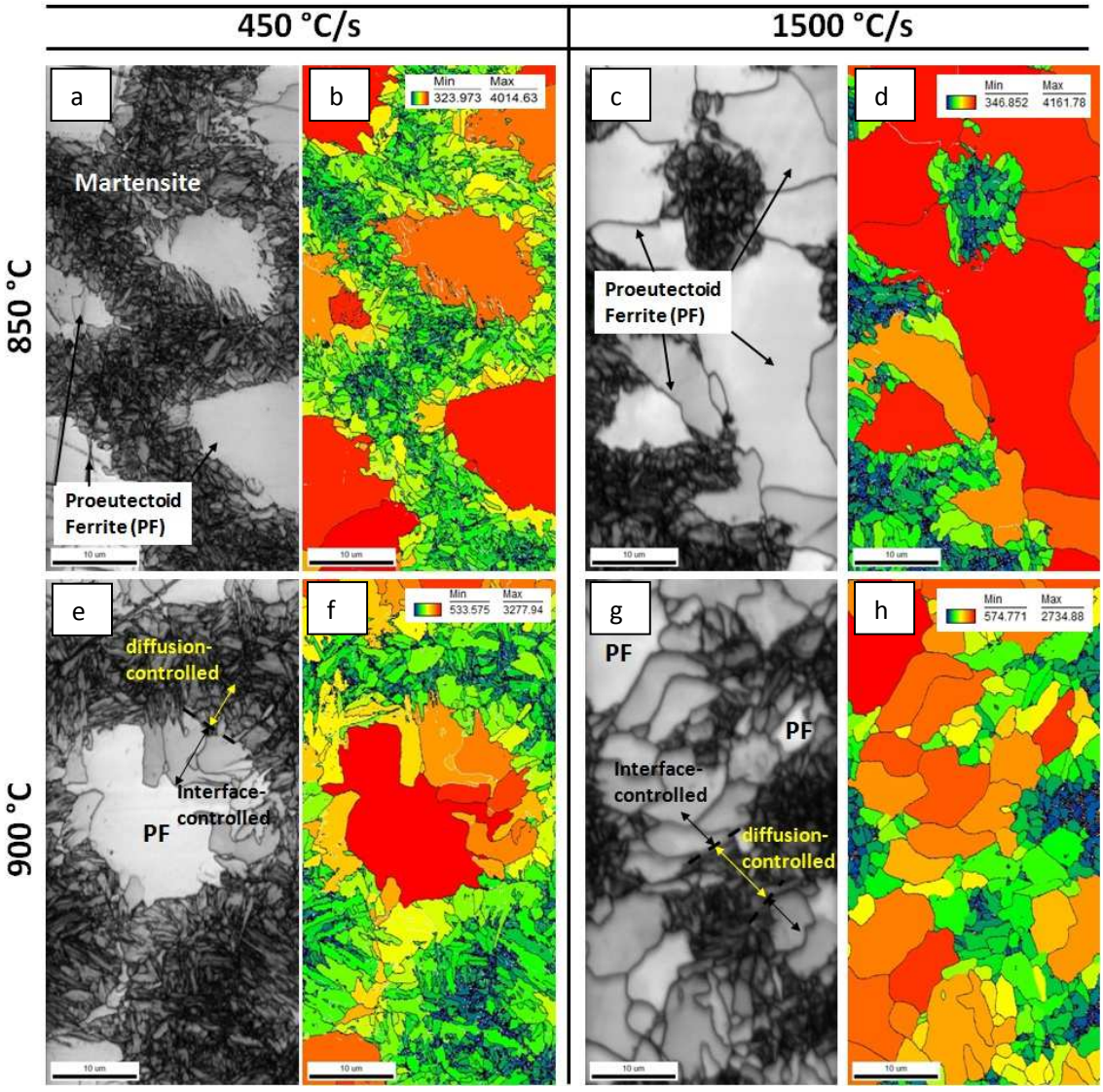

Fig. V-7. Image Quality (IQ) maps (a, c, e, and g) and Grain Average IQ maps (b, d, f, and h) obtained via EBSD of 0.2 %C steel heated at a rate of 450 °C/s (a, b, e, and f) and 1500 °C/s (c, d, g, and h) to peak temperatures of 850 °C (a, b, c, and d) and 900 °C (e, f, g, and h). The color bars in b, d, f and h illustrates the intensity of the GAIQ values from the minimum (blue) to the maximum

(red), of which the values are indicated in the legends. The arrows shown in (e) and (g) indicate the possible mechanisms governing the phase transformation. Step size: 50 nm. Scale bar is 10 μm.

The microstructure of samples UFH at 1500 °C/s to ~850 °C differs considerably from the microstructure formed after heating to ~900 °C. Although the ferrite formed at 850 °C has similar morphology to that of the proeutectoid ferrite (see Fig. V-2a and 2e), the microstructure changes significantly at 900 °C. This change is readily observed for the 0.2 %C steel shown in Fig. V-4c and 4d, and is especially evident in the ferrite grain size and morphology (see SEM images in Fig. V-6c and 6d). The change in the morphology of ferrite is attributed to changes in the mechanism of austenite formation.

EBSD maps (cf. Fig. V-7) show that a heating rate of 450 °C/s also leads to changes in the morphology of ferrite. As reported elsewhere [53], low-image quality (IQ) regions and high-IQ regions correspond to martensite and ferrite, respectively. The IQ maps reveal similar features to those shown in Fig. V-2. In the grain average IQ maps, grains of proeutectoid ferrite and martensite are colored as red-orange and blue-green, respectively. The ferrite grains are smaller at 900 °C than at 850 °C. The phase fraction of ferrite was calculated using the average IQ criteria described elsewhere [53], and the equivalent grain diameter (Table 5) was determined for samples subjected to UFH to different peak temperatures. As qualitatively shown in Fig. V-6c, 6d, and Fig. V-7, the ferritic grain size decreases significantly (by ~50%) when the temperature is increased from 850 °C to 900 °C. This change is substantially larger than the decrease in ferritic grain diameter measured from 750 °C to 850 °C (Table 5), and may have resulted from a transition in the transformation mechanism of austenite; the transition is further discussed in Section 5.

Table V-5. Average equivalent grain diameter calculated from EBSD-measured diameters of ferrite in 0.2 %C steel samples heated at rates of 450 °C/s and 1500 °C/s to different peak temperatures.

Heating rate, °C/s	**Average ferrite grain diameter, μm**			
	750 °C	**800 °C**	**850 °C**	**900 °C**
10	18.3	14.9	7.7	-
450	16.2	16.7	13.9	7.56
1500	19.9	20.2	18.7	8.2

V-5 Discussion

V-5.1 Thermodynamics of austenite formation during anisothermal heating

Microstructural observations indicate that austenite is nucleated at the α/θ interface. Consider a transformation that starts at a certain temperature *T* in the intercritical range of the Fe-C system. The driving force for the nucleation of austenite is given by the maximum difference associated with the common tangent between the Gibbs free energy of ferrite in equilibrium with cementite (L_2 in Fig. V-8a) and the Gibbs free energy of austenite. The tangent (L_2') to the carbon concentration associated with the maximum driving force $X_C^{\gamma,\,N}$ on the austenite curve has the same slope as L_2, as demonstrated by Hillert [54,55].

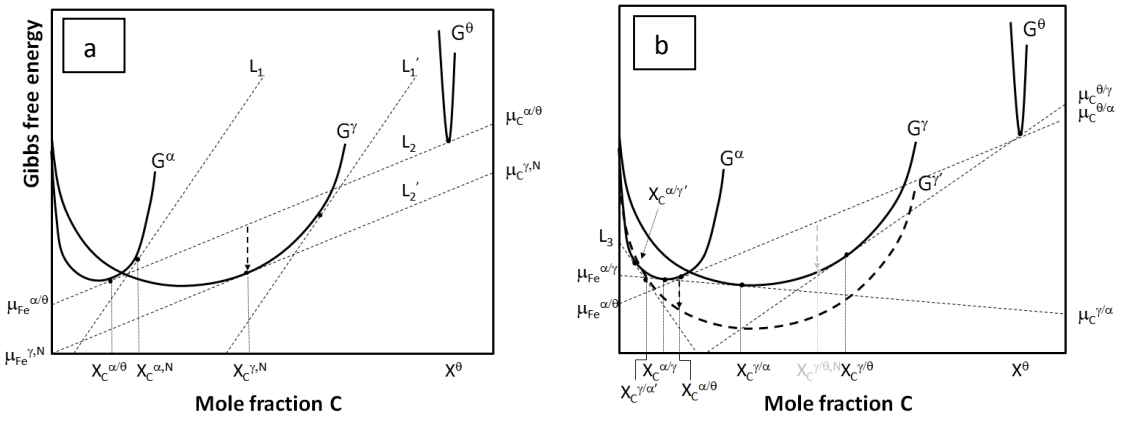

Fig. V-8. Schematic showing Gibbs free energy versus composition curves (a) of the most favorable composition for austenite nucleation from supersaturated ferrite (represented by L_1 and L_1' lines), and from the α/θ interface (represented by L_2 and L_2' lines) for a temperature *T* above the eutectoid and (b) for γ/α and γ/θ equilibrium after nucleation (solid curves), represented by G^{α}, G^{γ}, and G^{θ}, at a temperature *T* slightly above the eutectoid, and γ/α equilibrium at a significantly higher temperature *T'* than the eutectoid, represented by $G^{\gamma'}$ (dashed curve).

The driving force ξ^N for the nucleation of austenite at the α/θ interface is defined as $\xi = -\Delta G$ and can be expressed as:

$$\xi^N = \left(\mu_{Fe}^{\alpha/\theta} - \mu_{Fe}^{\gamma,N}\right) = \left(\mu_C^{\alpha/\theta} - \mu_C^{\gamma,N}\right) \qquad 1$$

where $X_i^{k/m}$ and $\mu_i^{k/m}$ are, respectively, the mole fraction and the chemical potential of element *i* in phase *k* at the *k/m* interface; the superscript *N* refers to the nucleation process. This driving force is applicable only for nucleation adjacent to a cementite plate (see Fig. V-5). Under the maximum driving force, austenite is nucleated at the α/α interface when the compositional fluctuation of ferrite reaches a value of $X^{\alpha,N}$ (see Fig. V-8a). This would require diffusion of carbon into ferrite of composition $X^{\alpha/\theta}$, which is improbable because any compositional change will spontaneously raise the Gibbs free energy of ferrite. Therefore, from a thermodynamic point of view, nucleation of austenite should rarely occur at the α/α interface.

At the heating rates used in the present experiments, austenite is always nucleated at a temperature in the intercritical range. The stability of austenite increases, i.e., its free energy decreases (cf. $G^{\gamma'}$, the dashed line in Fig. V-8b), when the temperature is raised to a certain value *T'*. This leads to an increase in the driving force for nucleation ξ^N. In fact, at sufficiently high heating rates, ferrite can transform into austenite of the same chemical composition, i.e., the reaction $\alpha \rightarrow \gamma$ will occur at compositions of ferrite where $G^{\gamma,N} < G^{\alpha/\theta}$ ($G^{\gamma,N}$: Gibbs free energy of austenite nuclei and $G^{\alpha/\theta}$: Gibbs free energy of the ferrite in equilibrium with cementite). Under these conditions, nucleation occurs by means of a massive transformation, i.e., without long-range diffusion. The dashed arrow in Fig. 8b represents the driving force for the formation of austenite, through a massive transformation of ferrite with composition $X^{\alpha/\theta}$. However, in multicomponent

alloys, the composition of proeutectoid ferrite may differ significantly from that of pearlitic ferrite owing to the partitioning of substitutional alloying elements and macrosegregation effects. The nucleation of austenite, by means of a massive transformation, will therefore depend on local chemical conditions and may occur at other sites in addition to the α/θ interface.

Austenite grows into both pearlite and proeutectoid ferrite. When austenite nucleated at the α/θ interface begins to grow, the newly formed γ/α interface moves towards both pearlite and proeutectoid ferrite. The derivation for the general case of precipitation from a supersaturated phase under local equilibrium conditions has been presented elsewhere [55]. In the initial stages of growth, austenite encounters cementite at one interface and ferrite at the other (see Fig. V-5 and Fig. V-6). The driving force for the growth of austenite at the interface with the cementite phase is given as:

$$\xi^{\theta\rightarrow\gamma} = X_{Fe}^{\gamma/\theta}\left(\mu_{Fe}^{\alpha/\theta} - \mu_{Fe}^{\gamma/\theta}\right) + X_{C}^{\gamma/\theta}\left(\mu_{C}^{\alpha/\theta} - \mu_{C}^{\gamma/\theta}\right) \qquad 2$$

whereas the driving force for growth at the γ/α interface is given as follows:

$$\xi^{\alpha\rightarrow\gamma} = X_{Fe}^{\gamma/\alpha}\left(\mu_{Fe}^{\alpha/\theta} - \mu_{Fe}^{\gamma/\alpha}\right) + X_{C}^{\gamma/\alpha}\left(\mu_{C}^{\alpha/\theta} - \mu_{C}^{\gamma/\alpha}\right) \qquad 3$$

Owing to the local equilibrium conditions, the composition of austenite at the γ/θ interface differs from the composition at the γ/α interface, resulting in a driving force ($\xi^{D} = \mu_C{}^{\gamma/\theta} - \mu_C{}^{\gamma/\alpha}$) for carbon diffusion through austenite. Once the cementite is completely dissolved, this diffusion yields a reduction in the local fluctuations of carbon in austenite. ξ^{D}, like ξ^{N}, will increase with increasing temperature (owing to a reduction in the Gibbs free energy of austenite G^{γ} (Fig. V-8b)), thereby leading to a decrease in $\mu_C{}^{\gamma/\alpha}$ and an increase in $\mu_C{}^{\gamma/\theta}$.

The growth of austenite during heating in the intercritical range will be controlled by carbon diffusion to the γ/α interface. At sufficiently low heating rates (for example, 10 °C/s, see Fig. V-3), austenite forms solely via carbon diffusion and negligible deviation from equilibrium can be expected. When the heating rate is increased, the resulting austenite fractions deviate significantly from equilibrium values. The kinetic nature of the deviation is discussed in a subsequent section. At ultrafast heating rates (for example, above 450 °C/s for 0.2 %C steel, see Fig. V-3), the formation rate of austenite is only partly controlled by carbon diffusion. In such cases, the system will reach some temperature where austenite is more stable than ferrite in equilibrium with cementite (cf. arrow Fig. V-8b). Schmidt et al. [29] suggested that the temperature T_0, where $G^{\gamma} = G^{\alpha/\theta}$, is the upper limit for carbon-diffusion-controlled austenite formation (i.e., the onset of austenite formation by means of a massive transformation). However, this upper limit does not satisfy local equilibrium conditions. For example, consider the chemical composition of ferrite in equilibrium with austenite. The chemical composition at each side of the interface is given by the solvus lines. At temperatures above T_0, corresponding to the α/γ tangent L_3 in Fig. V-8b, the solvus lines can still be defined by the common tangent and, hence, carbon-diffusion-controlled growth of austenite remains the active mechanism. The actual transition to the formation of austenite, by

means of a massive transformation, will occur at $G^{\gamma} < G^{\alpha}$ when $X_C \rightarrow 0$. The transition temperature (referred to as, see Table V-2) of both steels was calculated using ThermoCalc. The change in the free energy of the system, owing to the diffusionless transformation of austenite ξ^{M} is expressed as:

$$\xi^{M} = G^{\alpha} - G^{\gamma} \quad (4)$$

Under continuous heating, A_m (above which austenite is stable) depends on the local equilibrium conditions at the interface. In the case of pure iron, A_m corresponds to the temperature at which the allotropic change from α to γ occurs, i.e., 912 °C. The arrows in Fig. V-6d and Fig. V-7 point to features associated with the formation of austenite, by means of a massive transformation, and subsequent massive transformation of ferrite on cooling. Furthermore, the occurrence of proeutectoid ferrite (PF; see Fig. V-6c, Fig. V-7a, 7b, 7c, and 7d) indicates that the advance of the γ/α interface is controlled by the diffusion of carbon. The PF grains have a similar morphology to the grains in the initial microstructure (Fig. V-2a). However, Fig. V-6d and Fig. V-7e, 7f, 7g, and 7h reveal that the morphology and grain size of PF have changed significantly. These changes indicate that the mechanism of austenite formation has transitioned from diffusion controlled to interface controlled. Therefore, the subsequent cooling-induced transformation of ferrite, which started as an interface-controlled process, proceeded as a diffusion-controlled process. The occurrence of a ferrite grain at the center of the micrograph shown in Fig. V-6d suggests that the massive formation of austenite is incomplete. In addition, the various grains of ferrite surrounding PF may have resulted from the several austenite grains formed during heating.

V-5.2 Kinetics of austenite growth

V-5.2.1 The mixed-mode model

The mixed-mode model [56] is a sharp interface model, where the growth of a new phase from a supersaturated matrix is described by two processes, namely the: diffusion of alloying elements across the interface and the reconfiguration of the atomic structure, owing to the migration of the interface. Austenite formation under UFH conditions can be described in the framework of this model. The velocity of the interface (v) during the growth of austenite can be defined as follows:

$$v = M \cdot \xi = M\chi \cdot \left(X_C^{\gamma} - X_C^{\gamma\prime}\right)$$

where M, χ, X_C^{γ}, and X_C^{γ} are the mobility of the γ/α interface, a proportionality constant, the composition of the carbon-rich austenite, and the composition of austenite at the γ/α interface, respectively. The mixed nature of the transformation kinetics is accounted for by introducing a parameter S, which acts a multiplier of the maximum driving force $\chi \cdot (X_C^{\gamma} - X_C^{\gamma/\alpha})$:

$$v = M\chi \cdot S\left(X_C^{\gamma} - X_C^{\gamma/\alpha}\right)$$

In the kinetic model for austenite formation, *S* constitutes the fraction of the available driving force that is consumed solely by the movement of the interface. The extreme values (i.e., 0 and 1) of this parameter are associated with two different scenarios. When $S \rightarrow 0$, the mobility *M* is relatively high. The advance of the interface is therefore controlled by the diffusion of carbon, which results in extremely slow austenite formation at low temperatures in the intercritical range (low *S* values) [6,39]. When $S \rightarrow 1$, the phase transformation is controlled by the relatively low interface mobility. The intermediate case ($0 < S < 1$) represents a compromise between the extremes and, hence, the available driving force for austenite formation is dissipated by both diffusion and interface movement. When the temperature is increased, diffusion occurs more rapidly than interface movement suggesting that austenite formation will gradually approach an interface-control mode, as predicted by the values of *S* at high temperatures. The mixed-mode model provides an overall picture of the kinetics of austenite formation during heating. In subsequent sections, the conditions governing the formation of austenite will be adapted to the initial microstructure of interest and the effect of the heating rate will be determined.

V-5.2.2 Diffusional growth of austenite

As stated in the previous section, austenite nucleates preferentially at α/θ interfaces and subsequently grows into pearlite and proeutectoid ferrite, with significantly differing kinetics. Based on the mass balance proposed by Brandt [57], Speich and Richards [58] derived a kinetic expression for the velocity of isothermal austenite growth into pearlite. Hillert [4] has obtained a similar relation, which also accounts for the diffusion of carbon into ferrite. In this work, we employ Hillert's equation [4], which is rewritten as:

$$v^{\gamma \rightarrow P} = \frac{D_C^{\gamma}\left(X_C^{\gamma/\theta} - X_C^{\gamma/\alpha}\right) - D_C^{\alpha}\left(X_C^{\alpha/\gamma} - X_C^{\alpha/\theta}\right)}{S_P\left(X_C^{\gamma/\alpha} - X_C^{\alpha}\right)} \qquad 5$$

where $v^{\gamma \rightarrow P}$: velocity of the γ/α interface moving towards pearlite, D_i^k: diffusion coefficient of element *i* in phase *k*, and S_P: pearlite interlamellar spacing; volume changes are neglected. The advance of austenite into proeutectoid ferrite can be approximated by a mass-balance relation similar to that proposed by Zener [14]; this relation is given as:

$$v^{\gamma \rightarrow \alpha} = \frac{D_C^{\gamma}\left(X_C^{\gamma} - X_C^{\gamma/\alpha}\right)}{L\left(X_C^{\gamma/\alpha} - X_C^{\alpha/\gamma}\right)} \qquad 6$$

where $v^{\gamma \rightarrow \alpha}$: velocity of the γ/α interface moving towards proeutectoid ferrite, X_C^{γ}: composition of the carbon-rich austenite, and *L*: considered the effective diffusion distance in austenite. According to Eq. V-6, growth will stop when the carbon is homogeneously distributed in the austenite, i.e., when $X_C^{\gamma} = X_C^{\gamma/\alpha}$. The diffusion distance S_P (interlamellar spacing, see Eq. V-5) is expected to be one or two orders of magnitude smaller than *L* (which is ~50% smaller than the pearlite colony). This suggests that austenite grows more rapidly into pearlite than into proeutectoid ferrite. In fact, for a heating rate of 20 °C/s, the experimentally determined interface

velocity for austenite growth into pearlite was almost two times higher than the velocity for growth into ferrite [39]. Similar results were obtained in this work (see Section 4.1, Fig. V-3).

V-5.2.3 Massive growth of austenite

As described in the previous section, when $\Delta G^M < 0$, austenite may form in a diffusionless manner during UFH experiments. The velocity (v^M) of an γ/α interface formed by means of a massive mechanism is given as:

$$v^M = M \cdot \xi^M = -M \cdot \Delta G$$

where M is the mobility of the interface. The mobility of the interface at temperatures below A_m is almost the same as the mobility occurring above A_m. However, diffusion-related driving force dissipation is absent above A_m [61,62].

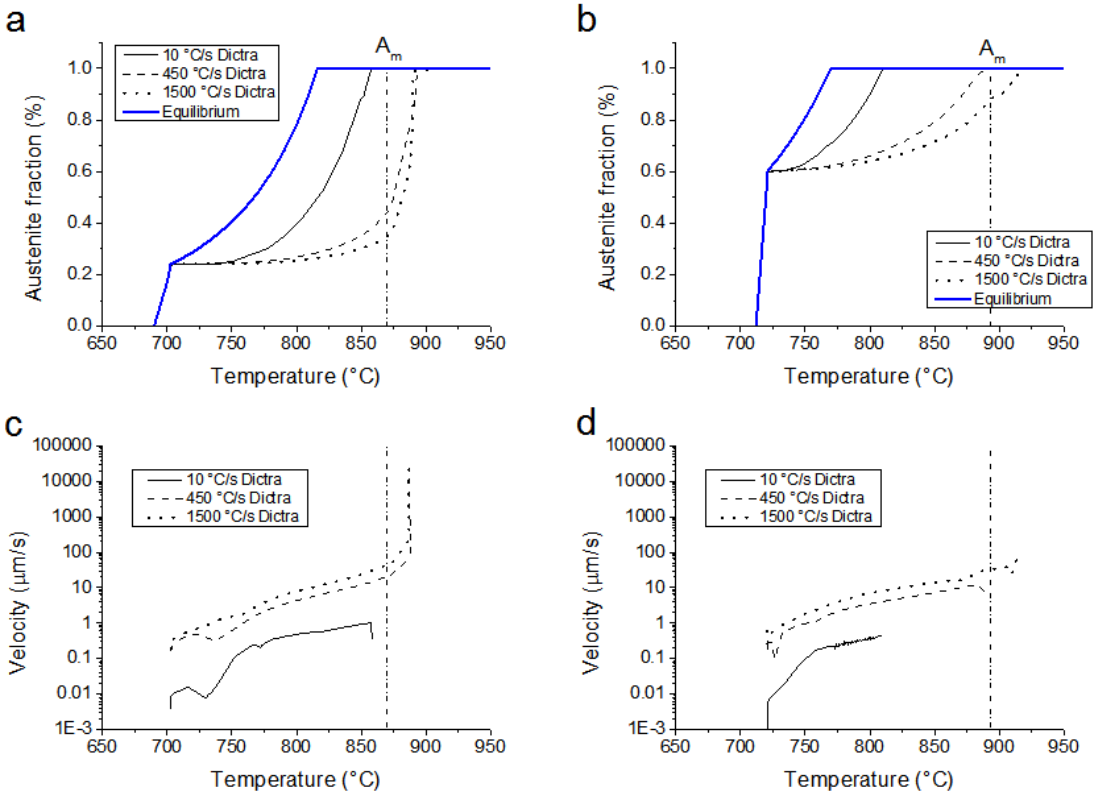

Fig. V-9. Heating-rate and temperature dependence of the (a, b) austenite fraction and (c, d) velocity of the γ/α interface, as calculated (using Dictra) for (a, c) 0.20 %C steel and (b, d) 0.45 %C steel. A_m (dashed-dotted line) represents the lowest temperature of the fully austenitic range (see Table V-2).

The images shown in Fig. V-4d, Fig. V-6d, and Fig. V-7e reveal features stemming from the massive formation of austenite. Several transformation products were also formed during cooling (Fig. V-6d). The mixture of microconstituents results from gradients in the carbon content of austenite. These transformation products have also been obtained via UFH experiments performed in previous studies [53,63]. The points corresponding to heating rates of 450 °C/s and 1500 °C/s at temperatures above A_m (see Fig. V-3a) represent the fraction of martensite formed during cooling. The fraction of austenite is not included in this data, because the significant fraction formed (through a massive transformation) during heating was subsequently transformed back into ferrite under the same mechanism. Therefore, the points corresponding to heating above A_m are associated with the position of the carbon diffusion front in austenite (cf. dashed line in Fig. V-6d), rather than the fraction of austenite formed during heating.

V-5.2.4 Dictra Calculations

Dictra was used to perform simulations of austenite growth into proeutectoid ferrite during heating at different rates. Plots showing the temperature dependence of the simulated austenite fraction and simulated interface velocity (see Fig. V-9) can be interpreted by considering Eq. V-6. Fig. V-9a and 9b show the phase fractions of austenite formed during heating at 10 °C/s, 450 °C/s, and 1500 °C/s. The slope of each curve decreases gradually with increasing heating rate. These results concur with experimental observations of austenite formation from ferrite-pearlite aggregates in samples subjected to different heating rates [37,64] and also with our experimental observations (Section 4.1, Fig. V-3).

The change in the slope of the phase-volume-fraction curve can be determined from:

$$\beta = \frac{dT}{dt} \tag{7}$$

where β: heating rate, T: temperature, and t: time.

Integration of Eq. V-6 yields an expression where the distance and temperature are related by a factor $1/\beta$. In the case of spherical geometry, as in the Dictra calculations, the volume fraction can be determined from:

$$v^{\gamma\to\alpha} = \frac{dr}{dt} = \beta\frac{dr}{dT} = \beta \cdot v(T)^{\gamma\to\alpha}$$

$$v^{\gamma\to\alpha} = \frac{1}{\beta}\cdot\frac{dr}{dt} = \frac{1}{\beta}\cdot\frac{D_C^{\gamma}\left(X_C^{\gamma} - X_C^{\gamma/\alpha}\right)}{L\left(X_C^{\gamma/\alpha} - X_C^{\alpha/\gamma}\right)} \tag{8}$$

$$f = \frac{r_T^3}{r_0^3} \tag{9}$$

where $v^{\gamma\to\alpha}$: temperature-dependent velocity of the interface, f: temperature-dependent phase fraction of austenite, r_0: radius of the volume, and r_T: position of the γ/α interface at temperature

T and heating rate β. As the heating rate is increased, a decrease in the fraction of austenite at a given temperature, or a displacement in the curve towards higher temperatures (as shown in Fig. V-9a and 9b) is expected.

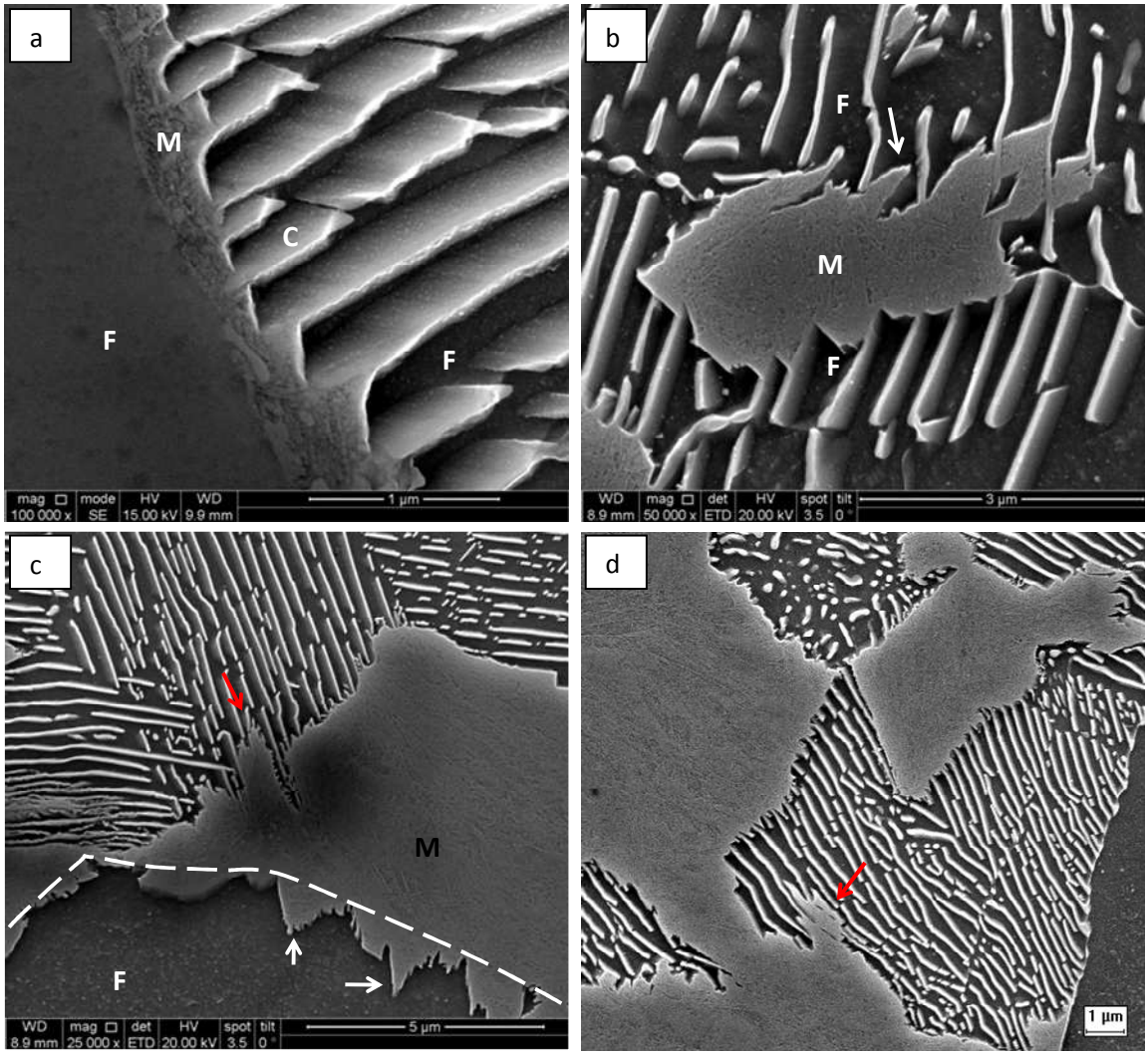

Fig. V-10. Growth of austenite with different interface morphologies in the microstructure of 0.2 %C (a) and 0.45 %C (b, c, and d) steels heated at 1500 °C/s to 750 °C and quenched. M, F, and C denote martensite, cementite, and ferrite, respectively. Etched with nital (4%). Scale bar in a is 1 µm, b 3 µm, c 5 µm, and d 1 µm.

Fig. V-9c and 9d show that, consistent with Eq. V-6, the velocity of the γ/α interface increases with increasing heating rate. In other words, at low heating rates, the value of $X_C^{\gamma} - X_C^{\gamma/\alpha}$ is smaller than those obtained at high heating rates, because the differences in the carbon composition of austenite are lower at low heating rates; high heating rates yield larger values of $X_C^{\gamma} - X_C^{\gamma/\alpha}$, and a steeper carbon gradient in austenite, thereby leading to an increase in the velocity of the γ/α interface. The effect of heating rate on the formation of carbon gradients in austenite has been

considered in a previous study [53]. In the present work, the interface velocities of the 0.2 %C and 0.45 %C steels are virtually identical for temperatures ranging from the onset of austenite formation to A_m (see Fig. V-9c and 90d). This shows that the relative volume fraction of the ferrite-pearlite aggregate has only a slight influence on the driving force and mobility of the advancing interface. Hence, the simplified model described by Eq. V-6 (which mainly defines the interface conditions of the moving boundary) represents a suitable description of the diffusion-controlled growth of austenite.

In addition to the high value of D^{γ}, the factor $X_C^{\gamma/\alpha} - X_C^{\alpha/\gamma}$ decreases at temperatures close to A_m for heating rates higher than 450 °C/s. This results in extremely high predicted interface-velocity values, which are unrealistic for austenite formation processes. Dictra only performs calculations under conditions of infinite interface mobility ($S \rightarrow 0$ for the mixed-mode model). Fig. V-9c shows that very steep interface velocities are calculated at temperatures above A_S; these values do not correspond to the actual kinetics of γ/α interface formation. As stated in Sections 5.1 and 5.2.1, austenite formation above A_m is interface controlled, and the corresponding kinetics is governed by the interface mobility and the available driving force. Dictra, therefore, significantly overestimates the transformation rate, owing to the assumption of infinite interface mobility. The actual onset temperature of the massive formation of austenite (i.e., A_S) is therefore considered the temperature where G^{γ} becomes lower than G^{α} when $X_C \rightarrow 0$. However, significant partitioning is expected of alloying elements in pearlite and proeutectoid ferrite in the initial microstructures. As such, to formulate a realistic thermodynamic and kinetic description of austenite formation, variations in the Gibbs free energy curves and, hence, in the interface equilibrium conditions within the microstructure must be considered.

V-5.2.5 Morphology of the γ/α interface

The γ/α interface is, in most cases, planar during the initial stages of austenite formation. However, the interface may exhibit acicular morphology, during its advance towards either pearlite or proeutectoid ferrite. Both cases are shown in Fig. V-10. Fig. V-10a and 10b show a planar γ/α interface growing towards proeutectoid ferrite and the lower side of an austenite grain growing into pearlite, respectively. Although Meshkov and Pereloma [24] reported that planar γ/α interfaces advance into pearlite during fast heating experiments, the growth of acicular austenite into pearlite has yet to be reported. The white arrows (Fig. V-10b) show Widmanstätten austenite in an initial stage of advance towards pearlite (upper side) and during movement into proeutectoid ferrite (Fig. V-10c). In some cases, a non-planar advance of the γ/α interface into pearlite is observed (see the red arrow in Fig. V-10c and 10d). This interface morphology corresponds possibly to a Widmanstätten plate or nucleation of austenite (as shown in Fig. V-5d) immediately in front of the moving boundary.

The red arrow in Fig. 10d shows a a zone with similar features to that of the zone marked by the red arrow in Fig. V-10c. In this case, a flat interface formed between austenite and pearlite, except in the region marked by the arrow. Martensite occurs in several unconnected regions, which may

act as different nucleation sites for austenite. As previously stated, the driving force for the nucleation of austenite increases with increasing heating rate. Therefore, spontaneous nucleation within pearlite is expected during continuous heating at UFH rates. This nucleation yields certain morphologies at the γ/α interface, as shown in Fig. V-10c and Fig. V-10d. These morphologies have not been observed after isothermal experiments [1–4], owing possibly to the rapid growth of austenite into, and complete consumption of, pearlite at relatively low heating rates. The results also suggest that the formation of austenite, which subsequently consumes pearlite, occurs in a continuous nucleation regime during UFH heating experiments.

V-5.3 Time-transformation diagrams

Fig. V-11 shows the continuous transformation (CT) diagram describing austenite formation during heating of both steels. As discussed in the previous section, 100% austenite formation was assumed for samples heated to temperatures above A_m at rates exceeding 450 °C/s; the metallographic data was included in Fig. V-11. The data points corresponding to austenite fractions of 1% and 99% were fitted with the following relation:

$$A_c^i - A_e = k \cdot \beta^{1/3} \qquad 11$$

where A_c^i: measured temperature at the onset of austenite formation at the heating rate i, A_e: equilibrium temperature for the onset of austenite formation (Table V-2), and k: a constant. Eq. V-11 can also be used to fit the temperature of any other transformed fraction of austenite.

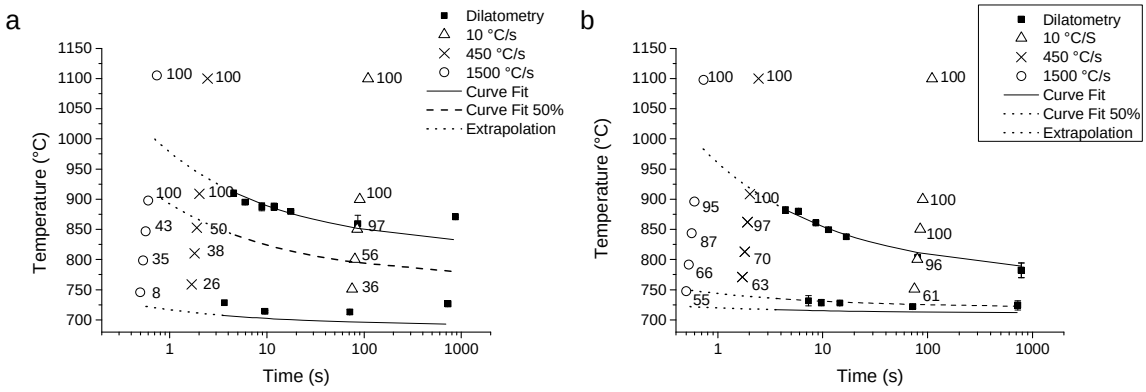

Fig. V-11. Continuous transformation (CT) diagram describing the formation of austenite during heating. Solid and dashed lines were obtained from Eq. V-11, whereas the dotted lines correspond to extrapolations of the diffusion-controlled transformed fraction. Filled squares and outlined symbols represent the experimental data and metallographic data, respectively.

A close correspondence is obtained between the predicted (Eq. V-11) and experimentally determined onset and finishing of austenite formation. In the case of the 0.45 %C steel, this

correspondence occurs only for experiments performed at 450 °C/s. This may be explained by considering Fig. V-10b, which shows that (owing to carbon diffusion) austenite was completely transformed during heating at 450 °C/s to temperatures below A_S. However, at 1500 °C/s, the transformation finished above A_m and, hence, the massive mechanism may have been triggered. Consequently, Eq. V-11, which applies to the diffusion-controlled formation of austenite, may be unsuitable for predicting the actual finishing temperature of the massive mechanism. Similarly, the extrapolation of Eq. V-11 yields inaccurate phase fractions of austenite for heating rates exceeding 200 °C/s (Fig. V-11a). This indicates that the mechanism governing austenite formation transitions from diffusion controlled to interface controlled at some critical heating rate. Under local equilibrium conditions, the transition temperature is *As*, although the transition is smoother than that shown in Fig. V-11a.

V-6 Conclusions

The effect of conventional (10 °C/s), and ultrafast heating rates (higher than 100 °C/s) on the nucleation and growth of austenite is investigated via experiments and simulations. This investigation is performed on 0.2 %C and 0.45 %C steels with initial ferrite-pearlite microstructures. The main findings of this work are summarized as follows:

1. Austenite nucleation occurs preferentially at the α/pearlite boundaries. Ultrafast heating may yield a substantial increase in the driving force for nucleation, thereby increasing the likelihood of austenite formation at the α/θ interfaces (which are less favorable than the α/pearlite interfaces). The newly formed austenite grows in all directions, but its growth rate into pearlite is higher than the growth rate into proeutectoid ferrite. The experimental results demonstrate for the first-time ever that nucleation of austenite ahead of the γ/α interface results in significant modification in the shape of the boundary moving through pearlite.
2. Carbon diffusion governs austenite formation and growth during heating at conventional heating rates. In ultrafast heating regimes, this mechanism controls growth during the initial stages of austenite formation, but is subsequently replaced by a massive mechanism. This transition occurs at the so-called A_m temperature, which is defined thermodynamically.
3. A simplified kinetic description of austenite formation is provided. Below A_S, the local chemical composition at the γ/α interface determines the velocity of the moving boundaries. The kinetic description shows that the heating rate has a considerable impact on the carbon relaxation in austenite and thus on the interface velocity. In addition, below A_S, the γ/α interface moves with almost the same velocity towards proeutectoid ferrite in the 0.2 %C and 0.45 %C steels.

V-References

[1] R.F. Mehl, The mechanism and rate formation of austenite from ferrite-cementite aggregates, Trans. ASM. 31 (1943) 613–650.

[2] E. Walldow, The mechanism of the solution of cementite in carbon steel and the influence of heterogeneity, J. Iron Steel Inst. 2 (1930) 301–339.

[3] G.R. Speich, A. Szirmae, Formation of austenite from ferrite and ferrite-carbide aggregates, Trans. AIME. 245 (1969) 1063–1073.

[4] M. Hillert, K. Nilsson, L.-E.Torndahl, Effect of alloying elements on the formation of austenite and dissolution of cementite, J. Iron Steel Inst. (1971) 50–66.

[5] C.I. Garcia, A.J. DeArdo, Formation of austenite in 1.5 pct Mn steels, Metall. Trans. A. 12 (1981) 521–530. doi:10.1007/BF02648551.

[6] G.R. Speich, V.A. Demarest, R.L. Miller, Formation of austenite during intercritical annealing of dual-phase steels, Metall. Trans. A. 12 (1981) 1419–1428. doi:10.1007/BF02643686.

[7] M.J. Bibby, J.G. Parr, The martensitic transformation in pure iron, J. Iron Steel Inst. Iron Steel Inst. 202 (1964) 100-.

[8] W.I. Haworth, J.G. Parr, he effect of rapid heating on the alpha-gamma transformation of iron, Trans. ASM. 58 (1965) 476–488.

[9] R. Zerwekh, C. Wayman, On the nature of the α → γ transformation in iron: A study of whiskers, Acta Metall. 13 (1965) 99–107. doi:10.1016/0001-6160(65)90159-8.

[10] E.S. Davenport, E.C. Bain, Transformation of austenite at constant subcritical temperatures, Trans. AIME. 90 (1930) 117–154.

[11] E.C. Bain, The alloying elements in steel, ASM Int., Cleveland, OH, 1939.

[12] G. Molinder, A quantitative study of the formation of austenite and the solution of cementite at different austenitizing temperatures for a 1.27% carbon steel, Acta Metall. 4 (1956) 565–571. doi:10.1016/0001-6160(56)90157-2.

[13] K.J. Albutt, S. Garber, Effect of heating rate on the elevation of the critical temperatures of low carbon mild steel, J. Iron Steel Inst. 204 (1966) 1217–1222.

[14] R.R. Judd, H.W. Paxton, Kinetics of austenite formation from a spheroidized ferrite-carbide aggregate, Trans. AIME. 242 (1968) 206–215.

[15] V.N. Gridnev, V.I. Trefilov, Over the reversability of the martensitic transformation in Fe- C alloys during heating, Dokl. Akad. Nauk SSS. 95 (1954) 741–743.

[16] N.N. Lipchin, T.G. Kryukova, N.L. Oslon, Effect of heating rate on phase recrystallization of quenched 60S2 steel, Metalloved. I Termicheskaya Obrab. Met. 8 (1964) 5–8.

[17] N.C. Law, D. V Edmonds, The formation of austenite in a low-alloy steel, Metall. Mater. Trans. A. 11 (1980) 33–46. doi:10.1007/BF02700436.

[18] J.R. Yang, H.K.D.H. Bhadeshia, Continuous heating transformation of bainite to austenite, Mater. Sci. Eng. A. 131 (1991) 99–113. doi:10.1016/0921-5093(91)90350-R.

[19] G.E. Abrosimova, G.I. Kohanchik, A.M. Markov, A.V. Serebryakov, On the $\gamma \rightarrow \alpha$ transformation in plain carbon steel by rapid thermal treatment, Scripta Metall. 13 (1979) 531–534. doi:10.1016/0036-9748(79)90101-7.

[20] D.P. Datta, A.M. Gokhale, Austenitization kinetics of pearlite and ferrite aggregates in a low carbon steel containing 0.15 wt pct C, Metall. Trans. A. 12 (1981) 443–450. doi:10.1007/BF02648541.

[21] A. Roósz, Z. Gácsi, E.G. Fuchs, Isothermal formation of austenite in eutectoid plain carbon steel, Acta Metall. 31 (1983) 509–517. doi:10.1016/0001-6160(83)90039-1.

[22] C. Atkinson, T. Akbay, R.C. Reed, Theory for reaustenitisation from ferrite/cementite mixtures in Fe-C-X steels, Acta Metall. Mater. 43 (1995) 2013–2031. doi:10.1016/0956-7151(94)00366-P.

[23] R.C. Reed, T. Akbay, Z. Shen, J.M. Robinson, J.H. Root, Determination of reaustenitisation kinetics in a Fe–0.4C steel using using dilatometry and neutron diffraction, Mater. Sci. Eng. A. 256 (1998) 152–165. doi:10.1016/S0921-5093(98)00800-4.

[24] Y.Y. Meshkov, E.V. Pereloma, Phase transformations in steels, Elsevier, 2012. doi:10.1533/9780857096104.4.581.

[25] W.J. Kaluba, R. Taillard, J. Foct, The bainitic mechanism of austenite formation during rapid heating, Acta Mater. 46 (1998) 5917–5927.

[26] H.I. Aaronson, J.F. Nie, Discussion To “The Bainitic Mechanism Of Austenite Formation During Rapid Heating,” Scripta Mater. 42 (1998) 505–509.

[27] M. Hillert, Comments On “ The Bainite Mechanism Of Austenite Formation During Rapid Heating ,” Scripta Mater. 43 (2000) 1045–1046.

[28] W.J. Kaluba, R. Taillard, J. Foct, Reply to ’Comments on “The bainitic mechanism of austenite formation during rapid heating,” Scripta Mater. 43 (2000) 1047–1050. doi:10.1016/S1359-6462(00)00533-9.

[29] E.D. Schmidt, E.B. Damm, S. Sridhar, A study of diffusion- and interface-controlled migration of the austenite/ferrite front during austenitization of a case-hardenable alloy steel, Metall. Mater. Trans. A Phys. Metall. Mater. Sci. 38 (2007) 698–715. doi:10.1007/s11661-007-9208-4.

[30] V.I. Savran, S.E. Offerman, J. Sietsma, Austenite nucleation and growth observed on the level of individual grains by three-dimensional x-ray diffraction microscopy, Metall. Mater. Trans. A. 41 (2010) 583–591. doi:10.1007/s11661-009-0142-5.

[31] J. Rödel, H.J. Spies, Modelling of austenite formation during rapid heating, Surf. Eng. 12 (1996) 8–13.

[32] A. Oddy, J. Mcdill, L. Karlsson, Microstructural predictions including arbitrary thermal

histories, reaustenization and carbon segregation effects, Can. Metall. Quart. 35 (1996) 275–283. doi:10.1016/0008-4433(96)00001-8.

[33] A. Jacot, M. Rappaz, A two-dimensional diffusion model for the prediction of phase transformations: Application to austenitization and homogenization of hypoeutectoid Fe-C steels, Acta Mater. 45 (1997) 575–585. doi:10.1016/S1359-6454(96)00199-1.

[34] C. García de Andrés, F.G. Caballero, C. Capdevila, Dilatometric characterization of pearlite dissolution in 0.1C-0.5Mn low carbon low manganese steel, Scripta Mater. 38 (1998) 1835–1842. doi:10.1016/S1359-6462(98)00131-6.

[35] C. García de Andrés, F.G. Caballero, C. Capdevila, H.K.D.H. Bhadeshia, Modelling of kinetics and dilatometric behavior of non-isothermal pearlite-to-austenite transformation in an eutectoid steel, Scripta Mater. 39 (1998) 791–796. doi:10.1016/S1359-6462(98)00146-8.

[36] A. Jacot, M. Rappaz, A combined model for the description of austenitization, homogenization and grain growth in hypoeutectoid Fe–C steels during heating, Acta Mater. 47 (1999) 1645–1651. doi:10.1016/S1359-6454(99)00005-1.

[37] R.C. Dykhuizen, C. V Robino, G.A. Knorovsky, A method for extracting phase change kinetics from dilatation for multistep transformations: Austenitization of a low carbon steel, Metall. Mater. Trans. B. 30 (1999) 107–117. doi:10.1007/s11663-999-0011-z.

[38] F.G. Caballero, C. Capdevila, C. García de Andrés, Influence of scale parameters of pearlite on the kinetics of anisothermal pearlite-to-austenite transformation in a eutectoid steel, Scripta Mater. 42 (2000) 1159–1165. doi:10.1016/S1359-6462(00)00352-3.

[39] E. Schmidt, Y. Wang, S. Sridhar, A study of nonisothermal austenite formation and decomposition in Fe-C-Mn alloys, Metall. Mater. Trans. A. 37 (2006) 1799–1810. doi:10.1007/s11661-006-0122-y.

[40] F.L.G. Oliveira, M.S. Andrade, A.B. Cota, Kinetics of austenite formation during continuous heating in a low carbon steel, Mater. Charact. 58 (2007) 256–261. doi:10.1016/j.matchar.2006.04.027.

[41] A.I. Katsamas, A computational study of austenite formation kinetics in rapidly heated steels, Surf. Coat. Tech. 201 (2007) 6414–6422. doi:10.1016/j.surfcoat.2006.12.014.

[42] D. San Martín, P.E.J. Rivera-Díaz-del-Castillo, C. García-de-Andrés, In situ study of austenite formation by dilatometry in a low carbon microalloyed steel, Scripta Mater. 58 (2008) 926–929. doi:10.1016/j.scriptamat.2008.01.019.

[43] B.J. Yang, A. Hattiangadi, W.Z. Li, G.F. Zhou, T.E. McGreevy, Simulation of steel microstructure evolution during induction heating, Mater. Sci. Eng. A. 527 (2010) 2978–2984. doi:10.1016/j.msea.2010.01.038.

[44] D. San Martín, Y. Palizdar, C. García-Mateo, R.C. Cochrane, R. Brydson, A.J. Scott, Influence of aluminum alloying and heating rate on austenite formation in low arbon-manganese steels, Metall. Mater. Trans. A. 42 (2011) 2591–2608. doi:10.1007/s11661-011-0692-1.

[45] M. Onink, F.D. Tichelaar, C.M. Brakman, E.J. Mittemeijer, S. van der Zwaag, An in situ hot

stage transmission electron microscopy study of the decomposition of Fe-C austenites, J. Mater. Sci. 30 (1995) 6223–6234.

[46] S.L. Semiatin, I.M. Sukonnik, V. Seetharaman, An analysis of static recrystallization during continuous, rapid heat treatment, Metall. Mater. Trans. A. 27 (1996) 2051–2053. doi:10.1007/BF02651955.

[47] T.A. Kop, Dilatometric study of the austenite/ferrite interface mobility, Ph. D. Thesis, TU Delft, 2000.

[48] V.I. Savran, Austenite formation in C-Mn steel, Ph. D. Thesis, TU Delft, 2009.

[49] Petrov, R. H.; Kestens, L. A. I. Advanced High-Strength Steels: Electron Backscatter Diffraction (EBSD). In *Encyclopedia of Iron, Steel, and Their Alloys*; Colás, R.; Totten, G. E., Eds.; CRC Press, 2016; pp. 46–69.

[50] J.-O. Andersson, L. Höglund, B. Jönsson, J. Ågren, Fundamentals and applications of ternary diffusion 65, Elsevier, 1990. doi:10.1016/B978-0-08-040412-7.50023-2.

[51] A. Borgenstam, L. Höglund, J. Ågren, A. Engström, DICTRA, a tool for simulation of diffusional transformations in alloys, J. Phase Equilibria. 21 (2000) 269–280. doi:10.1361/105507100770340057.

[52] J.-O. Andersson, T. Helander, L. Höglund, P. Shi, B. Sundman, Thermo-Calc & DICTRA, computational tools for materials science, Calphad. 26 (2002) 273–312. doi:10.1016/S0364-5916(02)00037-8.

[53] F.M. Castro Cerda, C. Goulas, I. Sabirov, S. Papaefthymiou, A. Monsalve, R.H. Petrov, Microstructure, texture and mechanical properties in a low carbon steel after ultrafast heating, Mater. Sci. Eng. A. (2016). doi:10.1016/j.msea.2016.06.056.

[54] M. Hillert, Nuclear composition—A factor of interest in nucleation, Acta Metall. 1 (1953) 764–766. doi:10.1016/0001-6160(53)90043-1.

[55] M. Hillert, The uses of free energy-composition diagrams, in: H.I. Aaronson (Ed.), Lect. Theory Phase Transform., Metallurgical Society of AIME, 1975: pp. 1–50.

[56] J. Sietsma, S. van der Zwaag, A concise model for mixed-mode phase transformations in the solid state, Acta Mater. 52 (2004) 4143–4152. doi:10.1016/j.actamat.2004.05.027.

[57] W.H. Brandt, Solution of the diffusion equation applicable to the edgewise growth of pearlite, J. Appl. Phys. 16 (1945) 139–146. doi:10.1063/1.1707565.

[58] G.R. Speich, M.J. Richards, Appendix - Diffusion equations for pearlite dissolution, Trans. AIME. 245 (1969) 1073–1074.

[59] C. Zener, Kinetics of the decomposition of austenite, Trans. AIME. 167 (1946) 550–583.

[60] C. Zener, Theory of growth of spherical precipitates from solid solution, J. Appl. Phys. 20 (1950) 950–953. doi:10.1063/1.1698258.

[61] M. Hillert, Thermodynamics of the massive transformation, Metall. Mater. Trans. A. 15

(1984) 411–419. doi:10.1007/BF02645064.

[62] M. Hillert, Solute drag, solute trapping and diffusional dissipation of Gibbs energy, Acta Mater. 47 (1999) 4481–4505. doi:10.1016/S1359-6454(99)00336-5.

[63] T. Lolla, G. Cola, B. Narayanan, B. Alexandrov, S.S. Babu, Development of rapid heating and cooling (flash processing) process to produce advanced high strength steel microstructures, Mater. Sci. Tech. 27 (2011) 863–875. doi:10.1179/174328409x433813.

[64] V.I. Savran, Y. Van Leeuwen, D.N. Hanlon, C. Kwakernaak, W.G. Sloof, J. Sietsma, Microstructural features of austenite formation in C35 and C45 alloys, Metall. Mater. Trans. A. 38 (2007) 946–955. doi:10.1007/s11661-007-9128-3.

Chapter VI

Recrystallization and phase transformations in a cold rolled low carbon steel under ultrafast heating[4]

The microstructure and texture evolution of cold-rolled low carbon steel after ultrafast heating and quenching is investigated. Experiments were carried out at heating rates of 150 °C/s and 1500 °C/s. The recrystallization of ferrite, the formation of austenite during heating and the subsequent transformations during quenching are studied by scanning electron microscopy and electron backscattered diffraction techniques. The texture evolution of cold rolled steel during ultrafast heating was studied, allowing to estimate the precise effect of heating rate on the orientations of newly formed grains. The effect of heating rate on the formation mechanism of austenite is analysed combinig thermodynamic calculations and experimental data. The results provide indirect evidence for transition of the transformation from carbon diffusion control mode to interface control mode. The resulting microstructure after the application of ultrafast heating rates is a complex mixture of ferrite with different morphologies, undissolved cementite, martensite and retained austenite.

VI-1 Introduction

New processing routes for the production of the third generation Advanced High Strength Steels (AHSS) are currently under development [1–5]. The application of ultrafast heating (UFH) to cold-rolled low carbon steel is a growing research field which has recently gained considerable attention from both the science and the industry. Recent studies [3–8] revealed the potential of UFH for enhancing the mechanical properties of the standard low alloy steel grades. The advantage of applying UFH rates to cold-rolled low carbon steel stems in the great variety of microstructures and, thus, of the properties that can be derived thereof. However, the adaptability of UFH rates to conventional steel processing lines remains still an issue [9].

In the present study, the heating rates have been classified in the following ranges: conventional, (maximum 10 °C/s), fast (from 10 to 100 °C/s) and ultrafast (higher than 100 °C/s). The effect of UFH rates on the recrystallization of cold-rolled ultra low carbon (ULC) steel during continuoes heating (anisothermal conditions) was subject of a number of studies in the past years [10–15].

[4] This chapter has been partially published as F.M. Castro Cerda, L.A.I. Kestens, A. Monsalve, R.H. Petrov, The Effect of Ultrafast Heating on Cold-Rolled Low Carbon Steel: Recrystallization and Texture Evolution, Metals (Basel). 6 (2016) 288. doi:10.3390/met6110288, and F.M. Castro Cerda, B. Schulz, S. Papaefthymiou, A. Artigas, A. Monsalve, R.H. Petrov, The Effect of Ultrafast Heating on Cold-Rolled Low Carbon Steel: Formation and Decomposition of Austenite, Metals (Basel). 6 (2016) 321. doi:10.3390/met6120321

Ferry et al. [11] and Muljono et al. [12] reported faster recrystallization kinetics when UFH rates are applied in comparison to conventional heating rates. However, the increase of the heating rate decreases the recrystallized fraction of ferrite for a given temperature. The pinning effect of carbon atoms on the dislocation structure is claimed to play a significant role in slowing the recrystallization and decreasing the ferrite recrystallized fraction at the same heating temperatures. Similar findings are reported by Stockemer and Vanden Brande [14] and Senuma et al. [15]. It is also reported that the recrystallization is completed before the onset of austenite formation in low and very low carbon steels, as well as in interstitial free (IF) [16]. Results on the texture evolution during fast and ultrafast heating of ULC steel and low carbon steel heating have been published elsewhere [4–7,14,15,17,18]. The orientation measurements do not show significant deviations from {111}⟨uvw⟩ ND fiber [19,20], suggesting that the recrystallization textures in ferrite are practically independent of the heating rate. In cold-rolled low carbon steel of ferrite-pearlite initial microstructure, the recrystallization is completely suppressed at heating rates above ~3000 °C/s [6]. Petrov et al. [6,7] explained the influence of UFH in the final textures as an effect of the stabilization of the recovered structure of the deformed ferrite due to very high heating rate and absence of isothermal soaking.

The austenite formation during UFH experiments is summarized elsewhere [21]. It is claimed that the nucleation and growth of austenite can be accomplished either by diffusion-controlled or interface-controlled [22] mechanisms. Kaluba et al [23] proposed a so-called 'bainitic' mechanism active in the formation of austenite at UFH rates. However, Aaronson and Nie [24] and Hillert [25] have suggested alternative interpretations for the results of Kaluba et al. [23] based on well-established transformation mechanisms. The initial microstructure has an impact on the kinetics of austenite formation, as pointed out in early works [26–28]. Experimental studies [29,30] of the anisothermal formation of austenite in ferrite-pearlite aggregates revealed different kinetics of γ/α interface migration towards pearlite, in comparison to its advance into proeutectoid ferrite. Dilatometric data [31] are in agreement with the different kinetics of austenite growth in pearlite and proeutectoid ferrite. The massive formation of austenite during heating was experimentally measured by in-situ techniques [30,32].

The microstructure of the carbon steels after ultrafast heating is strongly influenced by the chemical composition, the initial microstructure, and the heating rate. In the present study, the goal is to investigate the microstructural evolution of a 70% cold rolled steel with a ferrite-pearlite microstructure under two heat treatment conditions: (i) a heating rate of 150°C/s and (ii) a heating rate of 1500 °C/s. In both cases, the steels were subsequently quenched practically without any isothermal soaking. The selected heating rates represent achievable intermediate and upper limit values under industrial conditions [9].The obtained results are expected to be of significance for the potential application of fast heating cycles in newly designed production lines.

VI-2 Experimental

VI-2.1 Steel and heat treatment

The chemical composition of the steel used in this work is shown in Table VI-1. The initial material was received in hot-rolled condition, and it was subsequently cold rolled to 70% deformation. Rectangular specimens for heat treatment were cut from cold rolled sheet with a long axis parallel to the rolling direction (RD) of the steel plate. The heating experiments were carried out in a DIL805AD Bähr Dilatometer at a heating rate of 150 °C/s, and the UFH experiments in a Gleeble 3800 thermomechanical simulator at 1500 °C/s. The sizes of the dilatometry specimens were 10x5x1mm³ and 60x10x1 mm^3 for the Gleeble specimens. The temperature was controlled by an S-type thermocouple spot welded to the midsection of each test specimens. Peak annealing (also called "flash annealing") experiments, i.e. heated up to a certain temperature and then quenched, after very small isothermal soaking (less than 0.5s) were carried out in the test specimens at several temperatures in the intercritical and fully austenitic range. A summary of the peak temperatures is shown in Table VI-2. Cooling (quenching) rates were ~-160 °C/s for dilatometric and ~-2000 °C/s for Gleeble experiments.

Table VI-1. Chemical composition of the steel (in mass-%).

C	Mn	Si	S	P	Fe
0.14	2.05	1.20	0.001	0.012	Rest

Table VI-2. Summary of peak temperatures.

Heating rate °C/S	Peak Temperature °C				
150	704	741	782	838	1000
1500	749	842	862	1000	1050

VI-2.2 Characterization

Thermodynamic calculations were performed using ThermoCalc, database TCFE7. The calculated equilibrium temperatures for the studied steel were Ae_1 = 674 °C and Ae_3 = 834 °C. Although the α/γ phase transformation does not start and end at these equilibrium temperatures in real heating conditions, the calculated temperatures were used to estimate the limits of the intercritical transformation range. The microstructure evolution was analyzed by dilatometry experiments, Optical (OM), Scanning Electron Microscopy (SEM) and Electron Backscatter Diffraction (EBSD). Specimens were cut from the middle of each test sample to avoid any effect of temperature gradients along the length (RD). The characterization was thus performed on the RD plane (the plane which is perpendicular to the sample rolling direction) at the center of the heat treated zone, where the thermocouple was placed. Metallographic samples were prepared according to the standard procedures by grinding and polishing to 1 μm diamond paste. The microstructure was revealed by etching with a solution of 4% HNO_3 in ethanol (Nital 4%) for ~10 s at room temperature. EBSD measurements were performed after additional 40 min mechanical polishing of the samples with colloidal silica with particle size of 35 nm and 10 N force.

The EBSD data acquisition was carried out with a Hikari detector operated with the EDAX-TSL-OIM-Data Collection version 6 software. The measuring set-up was installed on a FEI Quanta™ 450-FEG-SEM (described in Chapter IV) with a step size of 60 nm. The textures are represented via orientation distribution functions (ODFs) using Bunge notation. They were calculated with series rank (L) = 16, Gaussian half-width of 5° and orthotropic sample symmetry. Each texture calculation is based on a minimum area of 10.000 μm^2 and contains more the 5000 orientations (grains).

VI-2.3 Data post-processing and analysis

Phase quantification was performed on EBSD data with TSL-OIM Analysis V6.3. The raw EBSD data were post-processed (cleaned) to re-assign the dubiously indexed points using the grain confidence index standardization procedure. To distinguish between martensite and ferrite (both indexed as BCC phases), a plot of the Grain Average Image Quality (GAIQ) versus the area fraction of grains was constructed following the procedure described in [33,34]. The grains were defined as the arrangement of at least 4 points with a misorientation angle higher than 5° and confidence index higher than 0.1. Martensite fraction was associated with the low IQ part of the histogram, whereas ferrite fraction corresponds to the part with high IQ values. The ferrite fraction is composed of recrystallized and non-recrystallized grains. However, the fraction of the recrystallized ferrite was difficult to be obtained accurately from the IQ values. One reason for this is the high IQ of some unrecrystallized but recovered ferritic grains, which makes it difficult to separate them from truly recrystallized ones. To better distinguish between the recrystallized and recovered grains, the Grain Average Misorientation (GAM) versus the area fraction of the grains plot was employed. In the present study, the approach of [17] was applied where the recrystallized grains were regarded to have a grain average misorientation less than 0.4°. With the aim of such plot, the grains with a grain average misorientation larger than 0.4° were considered as non-recrystallized.

The phase fractions during the anisothermal heat treatment in dilatometer are commonly quantified using the lever rule. Such approach, however, produces significant deviations from actual values because of the density difference between pearlite and ferrite [31,35–39]. In the present study, the correction proposed in [38] was accepted and was used to calculate the austenite phase fractions from dilatometric data.

VI-3 Results

VI-3.1 Microstructure after UFH

The microstructures after different heating cycles are shown in Fig. VI-1 a-f. All microstructures consist of a mixture of ferrite and martensite and, in some (Fig. VI-1a and Fig. VI-1d), small fractions of spheroidized cementite are also resolved. The later are products of partial decomposition of pearlite. The morphology of martensite and its specific location in the microstructure is a direct consequence of the formation of austenite and its further

transformation after quenching. In the present work, the features of austenite formation will be described concerning the martensite size and morphology in the microstructure.

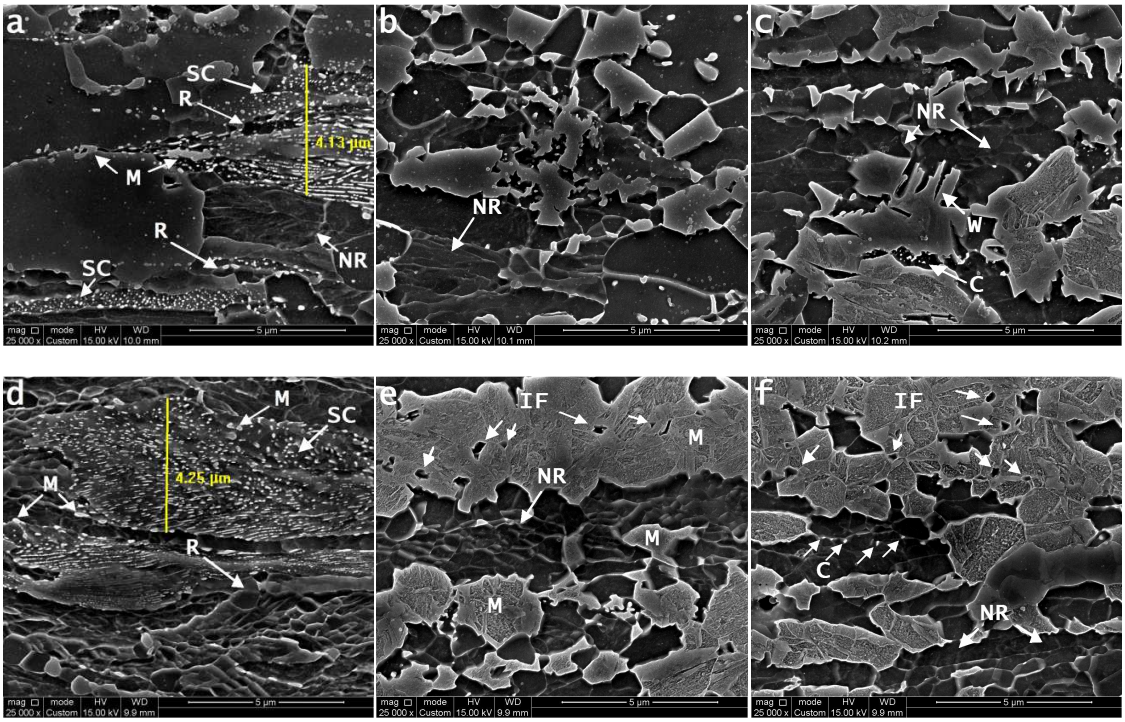

Fig. VI-1. SEM images of samples heated at 150 °C/s to: 738 °C (a), 782 °C (b) and 838 °C (c) and at 1500 °C/s to: 749 °C (d), 842 °C (e) and 862 °C (f). Arrows point to cementite (C), martensite (M), non-recrystallized ferrite (NR), recrystallized ferrite (R), spheroidized cementite (SC), intragranular ferrite (IF) and Widmanstätten ferrite (W). Scale bar is 5µm.

The recrystallization starts below 738 °C in samples annealed at 150 °C/s (cf. R in Fig. VI-1a, and 1d). The new (recrystallized) grains of ferrite were observed to grow from two different sites: in deformed ferrite grains and inside of some former pearlitic colonies. The pearlitic cementite was spheroidized in the samples heated at 150°C/s to 738 °C (cf. arrows in Fig. VI-1a) and 1500°C/s to 749°C (arrows in Fig. VI-1b). No recrystallized ferrite was observed to nucleate inside the lamellar or slightly spheroidized aggregates. The recrystallization is not complete below the A_3 temperature for both heating rates. The arrows (NR) in Fig. VI-1 indicate several non-recrystallized ferritic grains. It is suggested that these grains are recovered due to their specific cellular structure [17]. However, such grains will be called both recovered or deformed in the following sections , because they have the shape of the deformed grains and higher dislocation density than the recrystallized grains as it will be shown later. Widmanstätten (W) and intragranular ferrite (IF) were also observed in samples heated at 150 °C/s and 1500 °C/s above ~800 °C (arrows in Fig. VI-1c, 1e, and 1f). It is believed that ferrite with such morphologies was formed during the cooling of the specimens. The morphology of the ferrite formed during cooling will be further discussed in Section 4.2.4.

The metallographic data show that the formation of austenite already started at 738 °C in samples heated at 150 °C/s. The austenite was found to nucleate at the boundaries of the former pearlitic colonies (cf. M in Fig. VI-1a, and 1d). At higher temperatures, a morphological difference in austenite (martensite) morphology between samples heated at 150 °C/s and samples heated at 1500 °C/s can be noted. In samples heated at 1500 °C/s, the austenite mainly forms in bands aligned with the prior pearlitic colonies (cf. Fig. VI-1e and 1f). In samples heated at 150 °C/s the grains of austenite, although also banded, were somewhat more equiaxed than the former (Fig. VI-1b and 1c). Under both heating rates, the cementite was not fully dissolved even after heating at the highest temperatures (cf. C in Fig. VI-1c and 1f).

VI-3.2 Anisothermal recrystallization

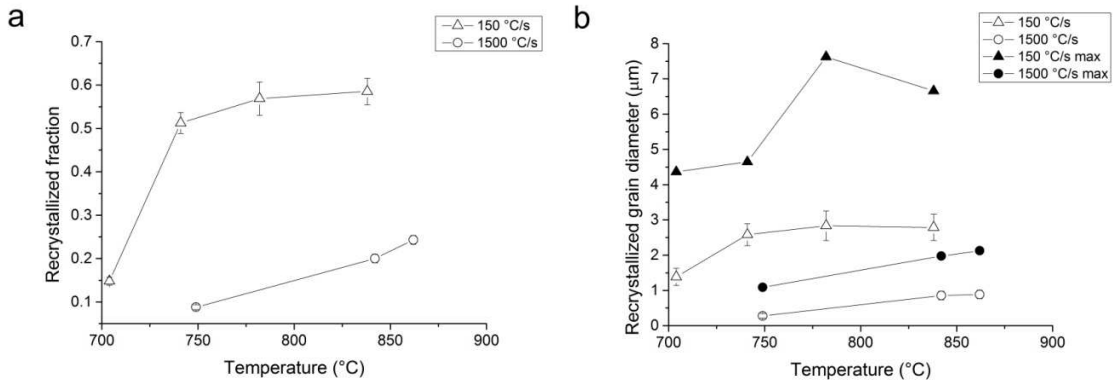

Fig. VI-2. (a) Fraction of recrystallized ferrite and (b) average ferritic grain size (outlined) and maximum ferritic grain size (filled) versus annealing temperature. In both plots, triangles and circles represent samples annealed with 150 °C/s and 1500 °C/s respectively.

Fig. VI-2a displays the fraction of recrystallized ferrite versus temperature, whereas Fig. VI-2b shows the average (outlined) and the maximum (filled) calculated grain diameter of recrystallized ferrite versus temperature. Both plots were calculated from EBSD measurements as described in Section 2.3. The recrystallization of ferrite was not 100% complete in both sets of experiments, in concordance with SEM images in Section 3.1. The recrystallization process estimated via the fraction of recrystallized ferrite is markedly displaced to higher temperatures when the heating rate is increased. The fraction of recrystallized ferrite in samples heated at 150 °C/s (cf. triangles in Fig. VI-2a) is gradually approaching a maximum of around 60% at ~850°C, which is related to the simultaneous formation of austenite, whereas at the same temperature the fraction of recrystallized ferrite in the samples heated at 1500°C/s is ~20%.

The average grain diameter of recrystallized ferrite in samples heated at 150 °C/s (cf. outlined triangles in Fig. VI-2b) displays a growing tendency up to ~741 °C and then it stabilizes around the value of ~3 µm. In samples heated at 1500 °C/s (cf. outlined circles in Fig. VI-2b) the average grain diameter of recrystallized ferrite is gradually approximating to a value ~1 µm. The marked

difference between recrystallized grain sizes as a result of both heating rates is consequence of the reduced time for grain growth as the heating rate is increased.

VI-3.3 Texture

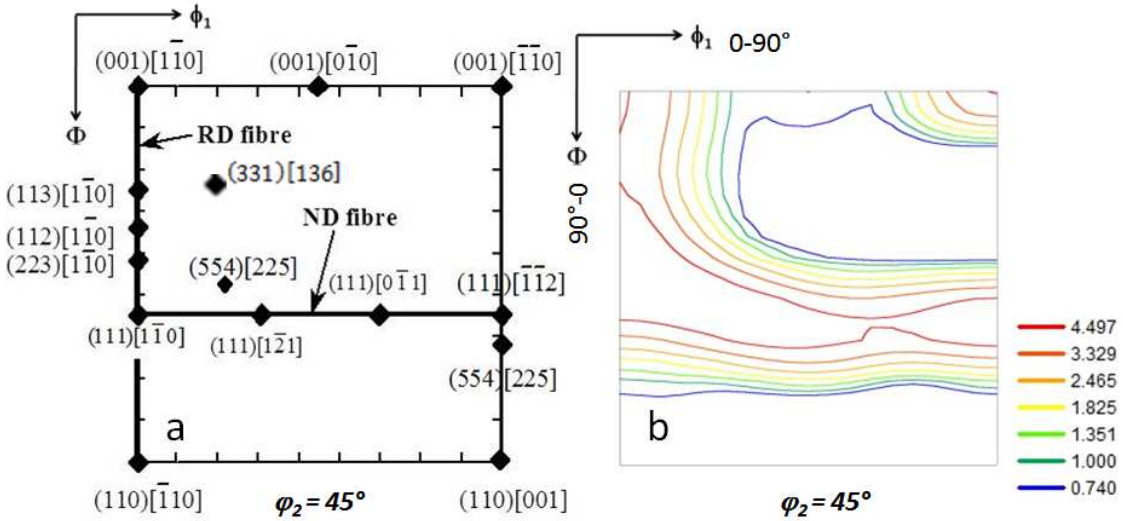

Fig. VI-3. (a) Ideal positions of the most important BCC texture components in the φ_2 =45° section of Euler space and (b) plot of ODF of the cold rolled steel used in this work.

Fig. VI-3a shows the key for the main BCC texture components in φ_2 = *45°*section of the Euler space and Fig. VI-3b displays the orientation distribution function (ODF) of the 70% cold rolled initial material. Fig. VI-3b shows typical rolling texture with ND {111}⟨uvw⟩ and RD {hkl}⟨110⟩ fibers with the intensity of ~4.5 multiples of random density (mrd) [40].

Fig. VI-4 illustrates *only the ferrite textures* derived from the EBSD scans using GAIQ partitioning criteria, as described in Section 2.3. Fig. VI-4a, 4c, 4e, and 4g show the ODFs of recrystallized and non-recrystallized ferrite, whereas Fig. VI-4b, 4d, 4f, and 4h show the ODFs of recrystallized ferrite grains only. The recrystallized ferritic grains were selected using GAM criteria. The recrystallized ferrite grains in samples heated at 150 °C/s (cf. Fig. VI-4b, 4d) show orientations close to {111}⟨uvw⟩ ND fiber components. In samples heated at 150 °C/s, the recrystallized grains have an orientation in the vicinity of the {111}⟨112⟩ and {113}⟨110⟩ texture components (Fig. VI-4b), whereas the strongest intensity after heating to 838 °C at 150°C/s is 7.1 mrd and belongs mainly to the {001}⟨110⟩ components.

The ODF of ferrite in samples heated at 1500 °C/s to 749 °C (Fig. VI-4e) is very similar to the ODF of the cold-rolled initial material (Fig. VI-3b). Fig. VI-4f shows the ODF of ferrite at a very early stage of recrystallization in a sample heated at 1500 °C/s. The maximum intensities of 3.1 mrd are close to {112}⟨110⟩. The ODF of samples heated at 1500 °C/s to 862 °C (cf. Fig. VI-4g) shows that the ferrite texture intensities are similar to the cold-rolled texture in the main components of ND

{111}⟨uvw⟩ and RD {hkl}⟨110⟩ fibers. Recrystallized grains in the same sample show strong intensities on {112}⟨110⟩ and {111}⟨112⟩ components (cf. Fig. VI-4h).

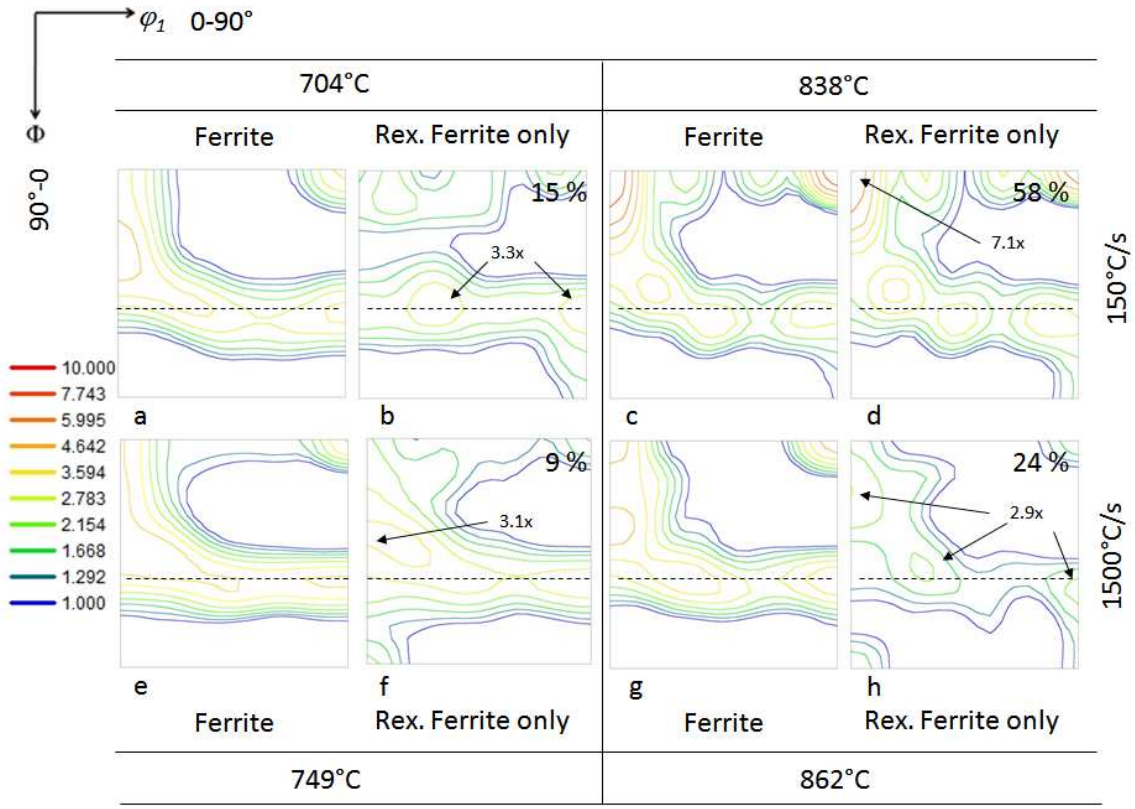

Fig. VI-4 ODF of ferrite at φ_2 = 45° from samples heated at 150 °C/s (a - d) and 1500 °C/s (e - h). (a) and (b) correspond to peak temperature of 704 °C, (c) and (d) to 838 °C, (e) and (f) to 749 °C and (g) and (h) to 862 °C. (a, c, e, f) correspond to recrystallized and non- recrystallized ferrite, whereas (b, d, f, h) correspond to recrystallized ferrite. Numbers in (b), (d), (f), and (h) indicate the recrystallized ferrite fraction.

The appearance of the Goss {110}⟨001⟩ texture component with intensity of ~1.7 mrd is observed after heat treatments at both heating rates (cf. Fig. VI-4b, 4d, and 4h). The Goss component is associated with oriented nucleation at shear bands in deformed ferrite [19]. The rotated Goss {110}⟨110⟩ component appears in the recrystallized ferrite after UFH at 1500 °C/s (cf. Fig. VI-4f, and 4h). These components are claimed to originate along shear bands in deformed ferrite [19,41,42]. The {331}⟨136⟩ components shown in recrystallized ferrite (cf. Fig. VI-4b, 4d, 4f, and 4h) have been proposed [43] to originate from specific deformation features, like intra-grain deformation bands in deformed ferrite of RD {hkl}⟨110⟩ fiber.

VI-3.4 Phase quantification

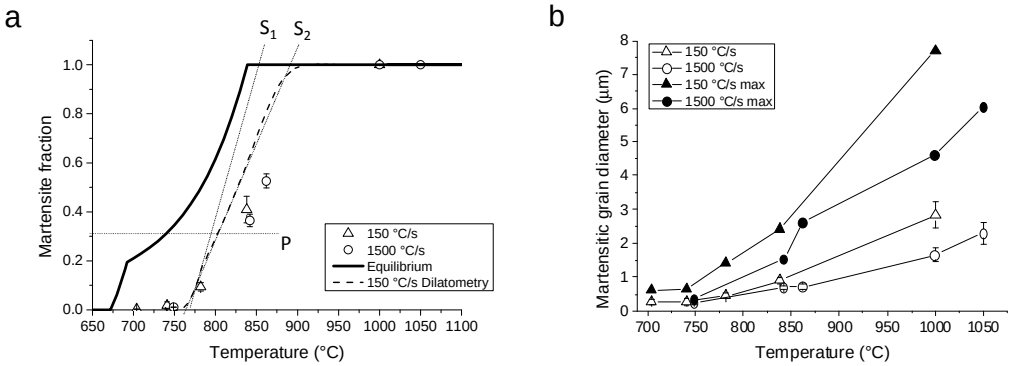

Fig. VI-5.(a) Martensite fraction versus annealing temperature for samples heated at 150 °C/s and 1500 °C/s and (b) average martensitic grain size (outlined) and maximum martensitic grain size (filled) versus annealing temperature. The solid black line in (a) represents the equilibrium fraction of austenite calculated with ThermoCalc, whereas the black dashed line represents the austenite fraction measured by dilatometry. S_1 and S_2 respectively represent the slopes at the beginning and later stages of austenite formation. The line labeled P represent the initial volume fraction of pearlite. In both plots, triangles and circles represent samples annealed with 150 °C/s and 1500 °C/s, respectively.

Although there might be some amount of bainite and retained austenite associated to the transformation of austenite after quenching, in the following sections it will be regarded as martensite as the retained austenite fractions do not exceed 0.5% and bainite is practically impossible to be distinguished based on the EBSD data. The martensite fraction in the microstructure after each thermal cycle is shown in Fig. VI-5a. The solid line shows the equilibrium fraction of austenite in the intercritical range calculated with ThermoCalc. The dashed line represents the calculated austenite fraction from dilatometric experiments, whereas the triangles and circles are data obtained from EBSD measurements. The dilatometric curve show two distinctive zones, one with a steep slope between ~750 °C - ~770 °C (S_1), and another between ~770 °C - ~900 °C with a smoother slope (S_2). The first zone is mainly influenced by the formation of austenite in pearlitic colonies, whereas the second zone corresponds to the formation of austenite in proeutectoid ferrite. The EBSD data from samples heated at 1500 °C/s suggest that the austenite is formed in a similar way to samples heated at 150 °C/s.

Fig. VI-5b displays the variation of martensitic average grain diameter (outlined) and maximum measured diameter (filled) versus temperature, measured by EBSD as described in Section 2.3. The average martensitic grain diameters in samples heated at both heating rates show similar values in the range between ~700 °C - ~860 °C. Above ~860 °C, the curve is steeper for samples heated at 150 °C/s. The maximum martensitic diameters (filled) displays similar tendencies as the average values.

VI-4 Discussion

VI-4.1 Recrystallization of ferrite

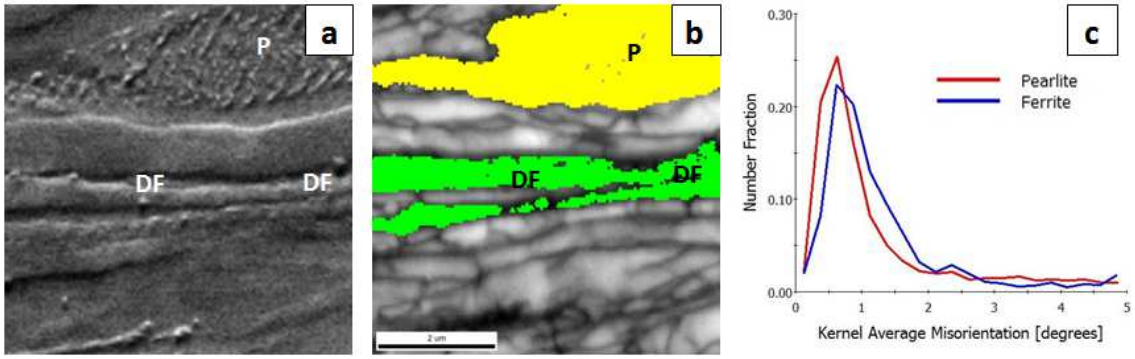

Fig. VI-6. (a) is SEM image, (b) IQ map and (c) KAM versus number fraction for 70% cold-rolled material. Letters in arrows are **P** for pearlite; and **DF** for deformed ferrite. Step size 50 nm. Scale bar is 2 µm.

Recrystallization begins in cold-rolled ferrite. No recrystallized grains were observed within lamellar pearlitic aggregates. One explanation for this is related to the energy stored in the different phases and constituents of the initial microstructure after cold-rolling. Homogeneous macroscopic deformation (as introduced in cold-rolling) distributes heterogeneously among the phases with very different properties on a microscopic level. The lower strength and higher ductility of proeutectoid ferrite, compared to pearlite, suggests that proeutectoid ferrite will accumulate more strain than the pearlitic structure during cold rolling. Pearlitic ferrite will bear the strain accommodation in pearlite, whereas cementite remains practically non-deformed (rotated and/or fractured) [44]. Experimental evidence of the strain accommodation in the different microconstituents was obtained from a representative deformed area shown in Fig. VI-6a, 6b, and 6c. Fig. VI-6a shows a SEM image corresponding to the same area of the EBSD scan (IQ map) in Fig. VI-6b. In the upper right corner of Fig. VI-6a, a pearlite colony (P) can be readily identified. Elongated ferrite grains (DF) are situated just below or above the pearlitic colony. The distribution of elongated ferrite below and above deformed pearlitic colonies shown in Fig. VI-6a is commonly observed through the cold-rolled microstructure. Both constituents are highlighted in Fig. VI-6b, pearlite in yellow and ferrite in green. Fig. VI-6c illustrates the KAM versus the number fractions of points, for the partitioned zones (pearlite and neighboring ferrite) indicating a slight displacement of the KAM curve corresponding to ferrite (blue) towards higher misorientation angles, compared to pearlite (red). The displacement of the curve is a clear indication that the BCC lattice of the proeutectoid ferrite is more distorted than the BCC lattice of the pearlitic ferrite.

Another possible explanation for the absence of recrystallization inside pearlite is due to the interlamellar spacing. A critical nucleus larger than the width of the pearlitic ferrite will not be able to form, in spite of the fact that highly strained regions of pearlitic ferrite may form between cementite plates. Local increases in carbon content of pearlitic ferrite [45] might also hinder recrystallization due to the dislocation-pinning effect of carbon.

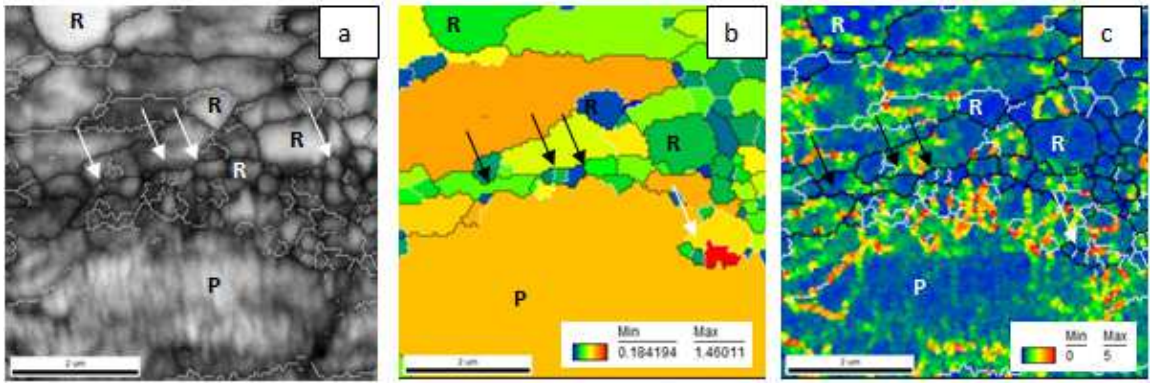

Fig. VI-7. (a) corresponds to a gray scale IQ map, (b) to a GAM map, and (c) to a KAM map (1st neighbor 5°max) for the sample heated at 150 °C/s to 704 °C and quenched. Letters in arrows are **P** for pearlite; and **R** for recrystallized ferrite. Step size 80 nm. Scale bar is 2 µm.

The growth of the recrystallized ferrite nuclei is thermodynamically more favorable in the heavily deformed zones, due to the larger amount of defects and hence higher driving force. The metallographic observations of the recrystallized ferrite in cold-rolled ferrite described in Section 3.1 are consistent with the previous statement. Fig. VI-7a, 7b, and 7c illustrate the recovery and recrystallization of deformed ferrite (arrows) in a region adjacent to a pearlitic colony in material heated at 150 °C/s to 704 °C. The GAM map (Fig. VI-7b) shows higher average misorientation values for pearlite (cf. P in Fig. VI-7b), compared to the ferrite just above (cf. arrows in Fig. VI-7b) in the recovered and partially recrystallized structures. The EBSD data indicate that at this stage of recrystallization the proeutectoid ferrite is already recrystallized and hence its lattice is less distorted than the one of the pearlitic ferrite. The KAM map in Fig. VI-7c shows large misorientation angles between points in ferrite above the pearlitic colony, which is also consistent with a highly deformed structure.

Fig. VI-7a, 7b, and 7c also show the presence of small equiaxed grains separated by high angle grain boundaries (black lines, >15°) in the ferritic matrix above the pearlitic colony. These grains are recrystallized ones. The ferrite recrystallization at 704 °C is an ongoing process, as illustrated by the white arrows in Fig. VI-7b and 7c which point to the recrystallization nuclei. Recrystallized grains (cf. blue and dark green grains in Fig. VI-7b) are outlined by high angle grain boundaries and are advancing into adjacent deformed grains (red grain in Fig. VI-7b). The recrystallized grains have very low KAM (blue), as shown in Fig. VI-7c. In contrast, the red grain shows areas of high KAM. The recrystallization of ferrite is not advancing into the pearlitic colony below, which also has a certain amount of distortion. Recrystallized ferritic grains (R) located next to pearlitic colonies are also shown in Fig. VI-1a, 1d, and 7a.

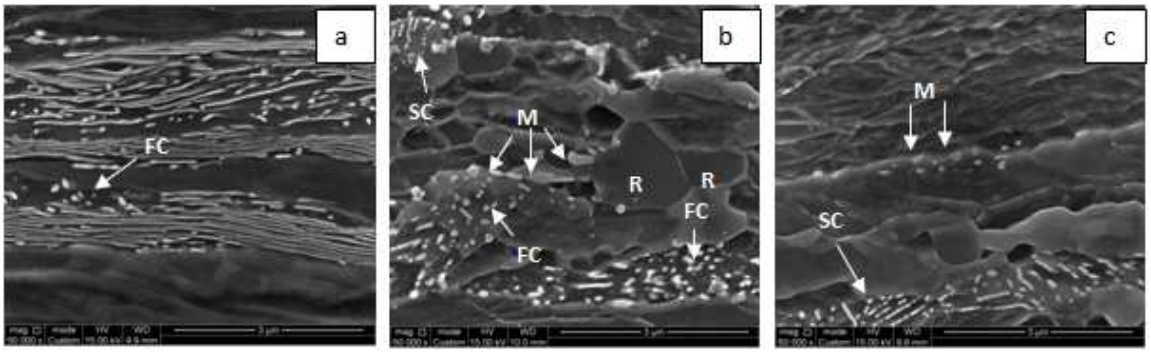

Fig. VI-8. (a) is a SEM image of 70% cold-rolled material, (b) SEM of the sample heated at 150 °C/s to 704 °C and quenched and (c) SEM sample heated at 1500 °C/s to 749 °C and quenched (etched with 4% Nital). Letters in arrows are **FC** for fragmented cementite, **SC** for spheroidized cementite, and **R** for recrystallized ferrite. Scale bar is 3 μm.

Recrystallization in pearlitic ferrite was only observed in former colonies where cementite is spheroidized (cf. Fig. VI-8b and 8c). The recovery and the recrystallization are thus developing together with spheroidization of the pearlitic cementite. Observations in the cold-deformed structure (Fig. VI-8a) have shown that the fragmentation of cementite already occurs during cold rolling of the steel sheet. During heating, some cementite plates tend to decompose into aligned spheres (cf. SC in Fig. VI-8b and 8c). Due to the short times involved in UFH experiments, it was possible to observe readily the difference between fragmented and spheroidized cementite. Fragmented cementite tends to cluster into bands and does not have a well-defined alignment, whereas spheroidized cementite grains have smaller sizes and are aligned resembling the previous cementite plate. It is clear that fragmented cementite will also undergo spheroidization during heating. Arrows show examples of both morphologies in Fig. VI-1a, 1d, 8b, and 8c. A comparison of the mentioned Fig. ures suggests a somewhat lesser degree of spheroidization of cementite in samples heated at 1500 °C/s, compared to samples heated at 150 °C/s. This observation and its implication in the formation of austenite will be discussed in Section 4.2.2. However, the recrystallization has not begun in the pearlitic colonies that have kept the lamellar arrangement. The cementite plates might act as a barrier to the movement of the ferritic grain boundary. Therefore, new or existing grains cannot grow into the colony.

The advancing of the α/α interface is also hindered by spheroidized cementite particles, as long as their size is small enough to interact effectively with dislocation movement [46,47]. Evidence of the previous statement is clearly shown in Fig. s. VI-1a, 1d, 8b, and 8c. Small particles of cementite are blocking the advance of the recrystallized ferrite into pearlite, thus hindering the process at one side of the recrystallized grains. Otherwise, the recrystallization would progress into both deformed ferrite and pearlite as expected under no barriers for growth (for instance, low-angle grain boundaries [48]). Instead, it has grown along ferrite bands and has stopped at cementite and pearlite areas. Notice from Fig. VI-7b and 7c that the boundary between recrystallized ferrite and pearlite has a misorientation angle between 15° and 63°, which predicts a higher mobility than in the case of low-angle grain boundaries [48]. The high-angle grain boundary between recrystallized

ferrite and pearlite supports the effect of cementite particles as a barrier for the interface movement.

A mixture of recrystallized and non-recrystallized ferritic grains are observed at all temperatures above ~700 °C in samples treated at both heating rates until the formation of 100% austenite. Fig. VI-9 shows the distributions of grain diameters in the recrystallized ferrite for different temperatures at both heating rates. At the beginning of recrystallization, the fraction of grains of diameter less than 1 µm is 53% in samples heated at 150 °C/s, and 99% in samples heated at 1500 °C/s. At later stages, the fraction of grains of diameter less than 1 µm is 14 % in samples heated at 150 °C/s, and 66% in samples heated at 1500 °C/s. It can thus be concluded that the nucleation is an ongoing process during heating at both heating rates.

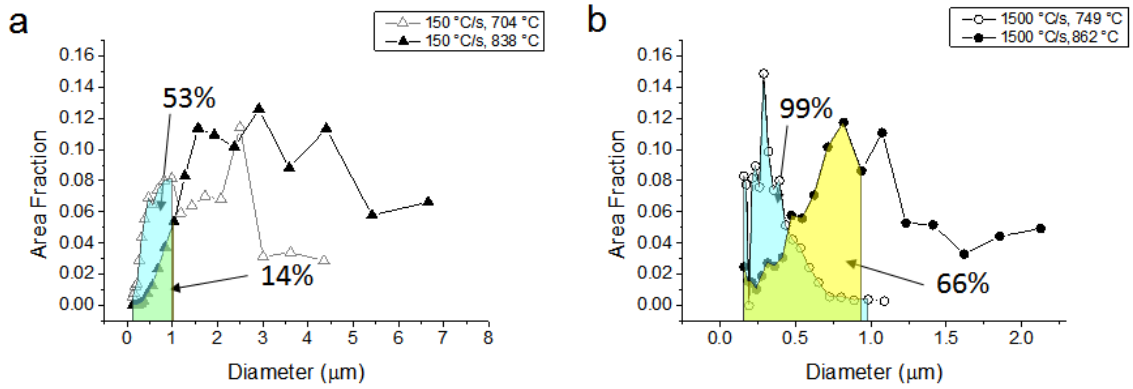

Fig. VI-9. Grain diameter versus area fraction of recrystallized ferritic grains from samples heated at 150 °C/s (a) and 1500 °C/s (b). Outlined and filled triangles show data of samples heated at 704 °C and 838 °C, whereas outlined and filled circles show data from samples heated at 749 °C and 862 °C, respectively. The data were obtained from EBSD measurements as described in Section 2.3.

The ferritic grain size grows until it reaches a maximum value, around the same order of magnitude of the deformed maximum pearlite band spacing (~3.4 µm). Evidence of this was obtained from measurements of average recrystallized ferrite grain sizes (Fig. VI-2b), which supports the previous statement. However, the validity of the later descriptions is restricted to the early stages of austenite transformation. At some point during heating, the fraction of austenite becomes larger than the initial fraction of pearlite, and the austenite further grows into ferrite, which is a reasonable explanation for the decreasing of the maximum ferritic grain size measured at 838 °C in samples heated at 150 °C/s (Fig. VI-2b). In samples heated at 1500 °C/s, the average ferritic grain size is lower than 1 µm in the temperature range below 862 °C. At the same temperature, the fraction of recrystallized grains is not larger than 24%. Such low fraction indicates that the recrystallization at 1500 °C/s is still in an early stage.

Although the complete recrystallization of ferrite under UFH experiments in the current material was not possible due to the unavoidable formation of austenite, it is clear that very fast heating

rates affect both the starting and the finishing of recrystallization processes. The pearlite is interacting with the deformed ferritic structure during recrystallization and thereby hindering the movement of the α/α interface. The nucleation and growth of austenite can take place either towards deformed or recrystallized ferrite. Thus, the austenite growth will have an impact on the experimentally observed fractions and size of recrystallized ferrite as shown indirectly in Fig. VI-2. An effect in the textures of martensite can also be expected and will be discussed in Section 4.2.6.

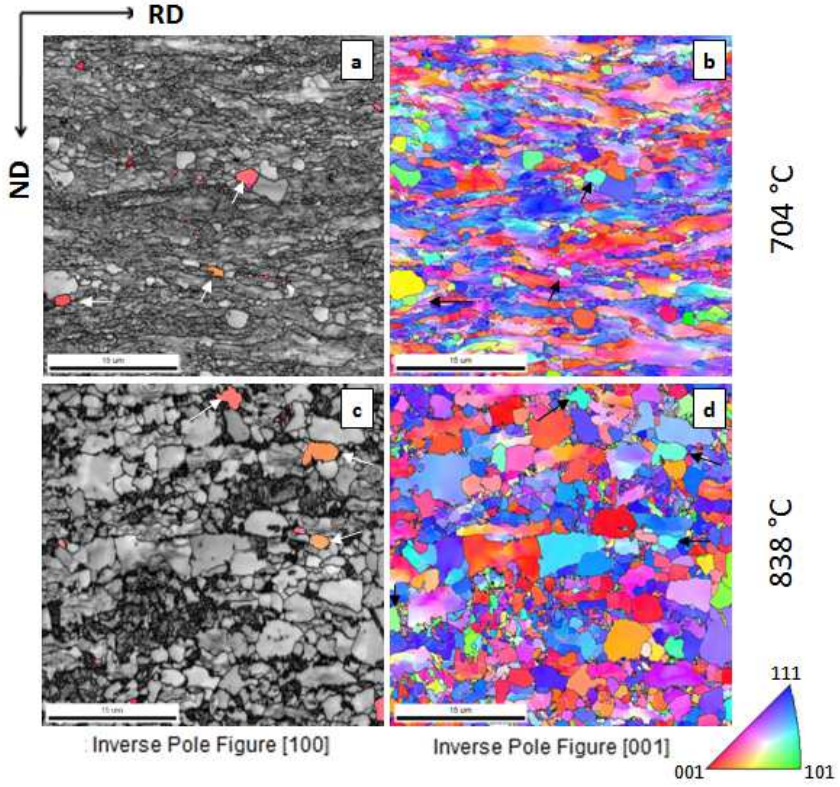

Fig. VI-10. Microstructure of samples heated at 150 °C/s to 704 °C (a, and b), and to 838 °C (c, and d). The microstructure consists of a mixture of ferrite and martensite. Arrows indicate grains oriented close to the Goss {110}⟨001⟩ (c, and d). (a, and c) correspond to IQ maps in which the recrystallized grains of ferrite are highlighted by a [100] RD Inverse Pole Fig. ure (IPF) map. (b, and d) are [001] ND IPF maps. Scale bar is 15 µm.

VI-4.2 Textures in recrystallized ferrite

Texture measurements have shown that the first recrystallized grains of ferrite in samples treated at 150 °C/s to 704 °C are mainly oriented around the {111}⟨112⟩ components (cf. Fig. VI-4b). It is well known that such orientations are the most frequently occurring recrystallization components in cold-rolled low carbon steel [41,49]. Grains oriented close to {001}⟨110⟩ are also present, which might be due to nucleation at low stored energy grains [50] at the beginning of recrystallization.

Grains with Goss {110}⟨001⟩ texture component have nucleated and grown in samples heated at 150 °C/s (cf. Fig. VI-4b).

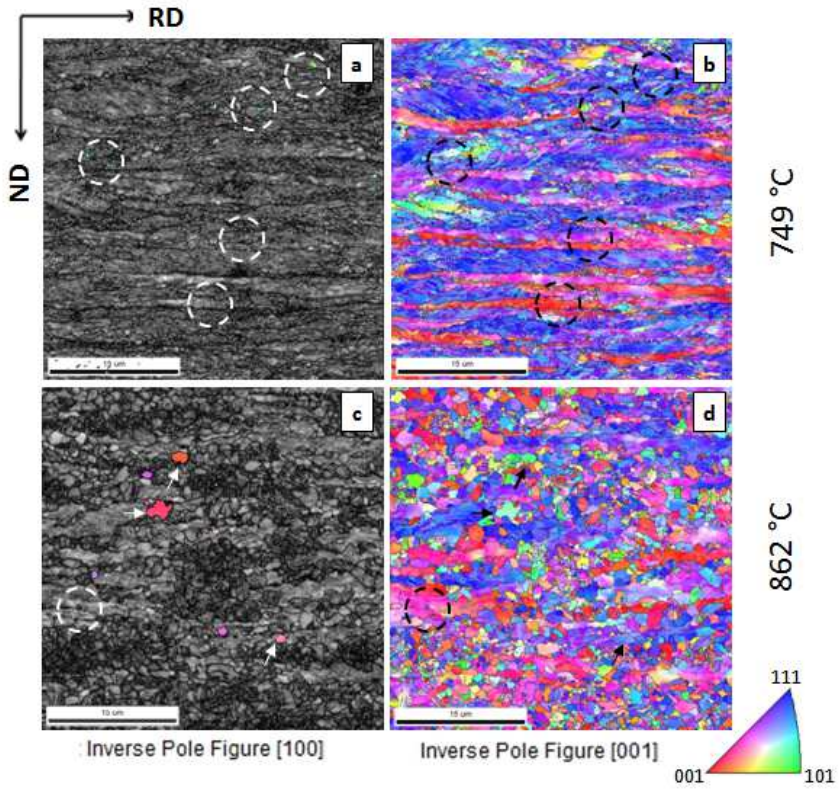

Fig. VI-11. Microstructure of samples heated at 1500 °C/s to 749 °C (a, and b), and to 862 °C (c, and d). The microstructure consists of a mixture of ferrite and martensite. Arrows indicate grains oriented close to the Goss {110}⟨001⟩ (c, and d), and circles the rotated Goss {110}⟨011⟩ (a, and b) components. (a, and c) correspond to IQ maps in which the recrystallized grains of ferrite are highlighted by a [100] RD Inverse Pole Fig. ure (IPF) map. (b, and d) are [001] ND IPF maps. Scale bar is 15 µm.

Fig. VI-10 and Fig. VI-11 display different EBSD maps of the microstructure heated at 150 °C/s and 1500 °C/s for different temperatures. Inverse Pole Fig. ure (IPF) maps parallel to ⟨100⟩ (RD direction) of recrystallized ferrite are plotted on top of IQ maps in Fig. VI-10a, 8c, 9a, and 9c. Grains oriented close to the Goss {110}⟨001⟩ (Fig. VI-10a, 8c, and 9c) and rotated Goss {110}⟨110⟩ (Fig. VI-11a) components are highlighted on the IQ maps. Fig. VI-10b, 8d, 9b, and 9d show the corresponding IPF maps parallel to ⟨001⟩ (ND direction) for each IQ map on the left-hand side. With the aim of the IPF maps, grains oriented close to the Goss component can be identified in the microstructure as the reddish grains in Fig. VI-10a, 8c, and 9c; which are at the same time greenish in Fig. VI-10b, 8d, and 9d. Grains oriented close to the rotated Goss component can be identified in the microstructure as the greenish grains in Fig. VI-11a; which are at the same time greenish in Fig.

VI-11b. Arrows are indicating grains with Goss and dashed circles the grains with Rotated Goss components in Fig. VI-10 and Fig. VI-11.

Fig. VI-10a and 10b show the recrystallized ferritic grains oriented close to the Goss {110}⟨001⟩ component in a sample heated at 150 °C/s to 704 °C. The grains are aligned with other recrystallized grains forming an angle of ~45° with RD. One could thus infer that grains oriented close to the Goss {110}⟨001⟩ in samples heated at 150 °C/s are likely to originate in shear bands. Recrystallized ferritic grains oriented close to the Goss {110}⟨001⟩ component are not observed in samples heated at 1500 °C/s to 749 °C. However, Fig. VI-11c and 11d display grains oriented close to the Goss {110}⟨001⟩ with similar alignments as in Fig. VI-10a and 8b. It can, therefore, be suggested that nucleation of ferrite at shear bands is delayed to higher temperatures in samples heated to 1500 °C/s, compared to samples heated at 150 °C/s.

The diffusion of carbon might also be playing a role in the nucleation of grains oriented in the vicinity of the Goss {110}⟨001⟩ component in samples heated at 150 °C/s (cf. Fig. VI-4b) and at higher temperatures in samples heated at 1500 °C/s (cf. Fig. VI-4h). It has been claimed [51] that carbon dissolved in the cold-rolled ferrite strengthens the Goss {110}⟨001⟩ component in recrystallized ferrite. The longer heat-treatment times involved in samples heated at 150 °C/s, compared to samples heated at 1500 °C/s, can produce significant diffusion of carbon in ferrite and thus enhance the early appearance of Goss orientation in samples heated at 150 °C/s. Consequently, grains with Goss orientation nucleate at higher temperatures and longer times in samples heated at 1500 °C/s, possibly influenced by the carbon diffusion into ferrite.

In sample heated at 1500 °C/s to 749 °C (cf. Fig. VI-4f), the highest intensity in the ODF is located in the vicinity of {112}⟨110⟩ components. However, considerable intensities are present at Φ in the range from 0 to 90° for $\varphi_1 = 0$, and for the {111}⟨uvw⟩ ND fiber components. It is suggested that the nucleation of the previously mentioned components is related to the stored energy in cold-rolled ferrite. Under ultrafast heating, the time for the recovery in the cold-rolled material is drastically reduced. The release of energy during the recovery is also reduced, and thus high stored energy components can nucleate. In cold-rolled ferrite, the amount of energy that a component can store increases as Φ increase from 0 to 90° for $\varphi_1 = 0$ [50]. The maximum strain energy is accommodated by the rotated Goss {110}⟨110⟩ component, which is present in the recrystallization textures of samples heated at 1500 °C/s (cf. Fig. VI-4f). The recrystallized ferrite from sample heated at 150 °C/s to 704 °C (cf. Fig. VI-4b) does not show high stored energy components ($\Phi \rightarrow 90°$ for $\varphi_1 = 0$). It is believed to be a consequence of the larger time for recovery, compared to samples heated at 1500 °C/s.

Fig. VI-4h shows that grains oriented close to the rotated Goss component are still present in samples heated at 1500 °C/s to 704 °C and 862°C. The circles in Fig. VI-11a and 11c indicate that such grains nucleated at grain boundaries. In contrast, moderated intensities are also observed at 862 °C (cf. Fig. VI-4f) in components close to {001}⟨110⟩ and {113}⟨110⟩. These components were very weak at 749 °C, which indicates that nucleation in some low stored energy {hkl}⟨001⟩ RD fiber components is taking place at high temperatures. The appearance of similar low stored energy

{hkl}⟨001⟩ RD fiber components of recrystallized ferrite are observed in samples heated at 150 °C/s to 838 °C (cf. Fig. VI-4d). These observations are consistent with the data of Fig. VI-9, which shows that nucleation accounts for a considerable fraction of the recrystallized ferrite in samples heated at 150°C/s and 1500 °C/s.

VI-4.3 Formation of austenite

VI-4.3.1 Nucleation

The first austenite grains are observed at the boundaries of the former pearlitic colonies, as shown in Fig. VI-1a and 1b. Austenite nuclei were also found inside some spheroidized pearlite colonies, as shown in Fig. VI-1b (dashed circle). Evidence of nucleation of austenite in the α/α interface is shown in Fig. VI-1e and 1f. Austenite (martensite) is formed at the triple junctions in deformed ferrite grains in samples heated at 1500 °C/s to 842 °C and 862 °C. The nucleation of austenite at the α/α grain boundaries can be thermodynamically explained with the aim of Fig. VI-12a. G^{α}, G^{γ}, and G^{θ} respectively represent the Gibbs free energy of ferrite, austenite, and cementite at a temperature slightly above the eutectoid. $G^{\gamma'}$ is the Gibbs free energy of austenite at a temperature T' much above the eutectoid. When ferrite is the leading supersaturated phase, the composition of the austenite nucleus with the maximum driving force $\xi^{\alpha\to\gamma,N} = -\Delta G$ is given by the common tangent to G^{α} (L_1) and $G^{\gamma'}$ (L_1'), expressed as [52]

$$\xi^{\alpha\to\gamma,N} = \mu_{Fe}^{\gamma} - \mu_{Fe}^{\alpha} = \mu_{C}^{\gamma} - \mu_{C}^{\alpha} \qquad 1$$

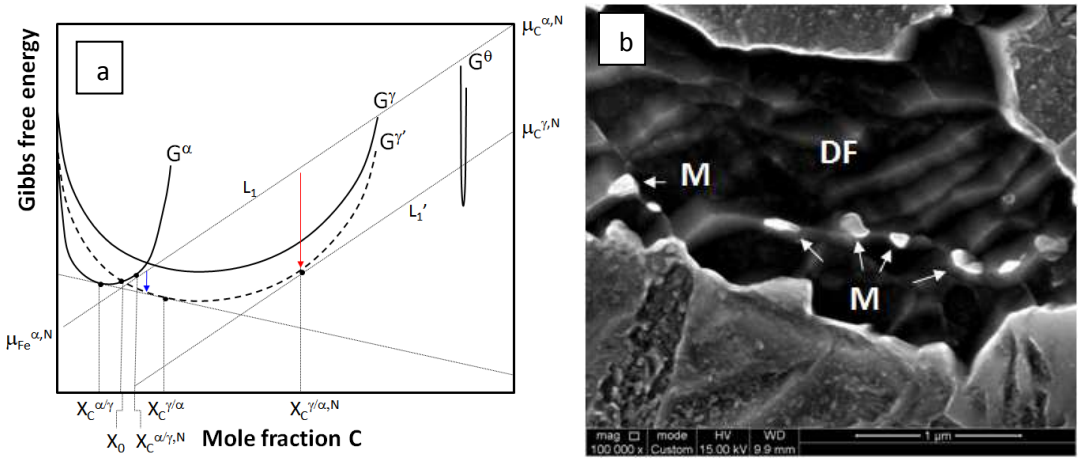

Fig. VI-12. (a) Scheme of a Gibbs free energy G versus composition (in mole fraction) plot for a temperature slightly above the eutectoid (solid lines) and much above the eutectoid (dashed line). G^{α}, G^{γ}, and G^{θ} respectively represent the Gibbs free energy of ferrite, austenite, and cementite. L_1 and L_1' are common tangents determining the driving force for austenite nucleation from ferrite. (b) is a SEM image of a sample heated at 1500 °C/s to 862 °C and quenched. White arrows show the nucleation of austenite (martensite, M) at the α/α grain boundaries in deformed ferrite (DF). Etched with Nital 4%. Scale bar is 1 µm.

where $X_i^{k/m}$ and $\mu_i^{k/m}$ are respectively the mole fraction and the chemical potential of element *i* in phase *k* at the *k/m* interface, as shown in Fig. VI-12a. The maximum driving force for the nucleation of austenite of composition $X_C^{\gamma/\alpha,N}$ in ferrite is given by the red arrow in Fig. VI-12a. However, it is also possible to have available driving force for fluctuations of compositions less than $X_C^{\gamma/\alpha,N}$, as shown by the blue arrow in Fig. VI-12a. When the temperature is increased, the G^{γ} is displaced downwards, as indicated by the dashed G^{γ} curve, and thus decreasing $\mu_{Fe}^{\gamma,N}$ and $\mu_C^{\gamma,N}$ and increasing ξ. One can thus conclude that the driving force for the nucleation of austenite from ferrite increases when the temperature is increased.

Fig. VI-12a also illustrates that the composition of ferrite in equilibrium with austenite $X_C^{\alpha/\gamma}$ is lower than the composition of ferrite $X_C^{\alpha/\gamma,N}$ giving the maximum driving force for the nucleation of austenite. Thus, ferrite must increase its carbon content to allow the nucleation of austenite. One could reasonably expect that α/α grain boundaries can dissolve more carbon than bulk α, thus favoring the nucleation of austenite. Similarly, the presence of imperfections in deformed ferrite might also increase the carbon solubility and thus increase the chances for the nucleation of austenite. A combination of the cases previously described could explain the nucleation of austenite (martensite) in Fig. VI-12b, which corresponds to the microstructure of a sample heated at 1500 °C/s to 862 °C. It is suggested that the nucleation of austenite in α/α interfaces in cold-rolled and UFH is thus thermodynamically possible.

The heating rate influences the onset of austenite nucleation. The estimated overheating (Fig. VI-2b) for samples heated at 150 °C/s is ~75 °C, and at least ~75 °C in samples heated at 1500 °C/s. The displacement in the onset of austenite formation when the heating rate is increased is related to the diffusion time. UFH rates will decrease the time for diffusion. Thus, under the assumption that the diffusion of carbon controls the nucleation of austenite, the nucleation will be displaced to higher temperatures [21]. The onset of austenite transformation will be displaced to higher temperatures in samples heated at 1500 °C/s, compared to samples heated at 150 °C/s.

VI-4.3.2 Austenite growth into pearlite

The formation of austenite in the intercritical range is a carbon diffusion controlled process [53]. Thus the kinetics of the movement of the γ/α interface is determined by the distance for carbon diffusion. The carbon diffusion distance is on the order of one-half of the pearlitic interlamellar spacing. This assumption, first proposed by Zener for the growth of pearlite [54], has been accepted and applied to the modeling of austenite formation in pearlitic steels [27,28]. Experimental measurements [30] confirmed that the kinetics of the γ/α interface into pearlite is ~2 times faster than its movement into proeutectoid ferrite.

Fig. VI-1a show that in samples heated at 150 °C/s to 704 °C the austenite is forming at the α/θ interfaces, preferentially at triple junctions of ferritic grains. The pearlite is considerably spheroidized in some areas at 704 °C (cf. dashed circles in Fig. VI-1a). Fig. VI-1b show no traces of lamellar pearlite in samples heated at 150 °C/s to 782 °C. The observation of areas with a mixture

of ferrite, martensite and spheroidized cementite is indicating that the formation of austenite took place in lamellar pearlitic structure, and the remaining pearlite is spheroidized (cf. Fig. VI-13a). The steep slope (S_1) in the dilatometric curve shown in Fig. VI-2a is a consequence of the fast advance of the γ/α interface into the lamellar pearlite. However, as the spheroidization process of cementite is taking place simultaneously, the actual fraction of austenite that quickly forms in pearlite is much lower than the initial volume fraction of pearlite (cf. P in Fig. VI-2a). Therefore, the transition from the zone of fast austenite formation (S_1) to the zone of slow austenite formation (S_2) is rather smooth. A somewhat sharp transition has been reported in dilatometric experiments of austenite formation during the continuous heating of annealed ferrite-pearlite microstructure [31,32] under heating rates from 1 °C/s to 200 °C/s. One could thus conclude that the cold-rolling of the ferrite-pearlite initial microstructure is enhancing the spheroidization of cementite, which has an impact on the formation of austenite in samples heated at 150 °C/s.

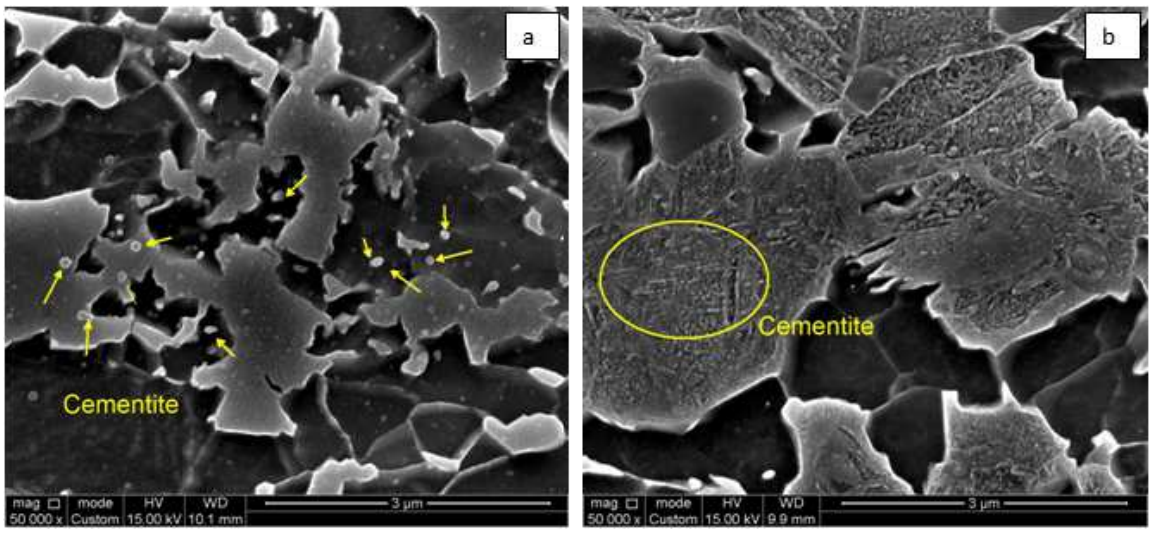

Fig. VI-13. SEM images of a sample heated at 150 °C/s to 738 °C and quenched (a), and a sample heated at 1500 °C/s to 838 °C and quenched (b). The cementite is spheroidized in (a), whereas it still has a lamellar structure in (b). Etched with Nital 4%. Scale bar is 3 µm.

In contrast, the lamellar structure of pearlite is kept in samples heated at 1500 °C/s to 749 °C (cf. Fig. VI-1d) and can still be observed at 842 °C (cf. Fig. VI-13b). It is reasonable to expect that samples heated at 150 °C/s have a higher degree of cementite spheroidization than samples heated at 1500 °C/s. The change in cementite morphology is thought to be related to the change in austenite distribution in the matrix, as described in Section 3.1. When cementite structure in pearlite is still mainly lamellar, as in samples heated at 1500 °C/s, the formation of austenite takes place quickly into the pearlitic areas [31,32]. A banded mixture of ferrite and austenite (martensite) is thus observed in the microstructure (cf. Fig. VI-1e and 1f). When cementite is partially spheroidized, as the case of samples heated at 150 °C/s, the formation of austenite does not fully resembles the spatial distribution of previous pearlitic colonies. The spheroidization of cementite implies that the growth of austenite will be mainly radial wise and slower than in the lamellar arrangement, as the distances between cementite spheres are larger than the

interlamellar spacing. The cementite located at the α/α boundaries will be most suitable places for nucleation of austenite, as early stated elsewhere [26]. Thus, not all the cementite spheres are associated to austenite, as shown in Fig. VI-13a.

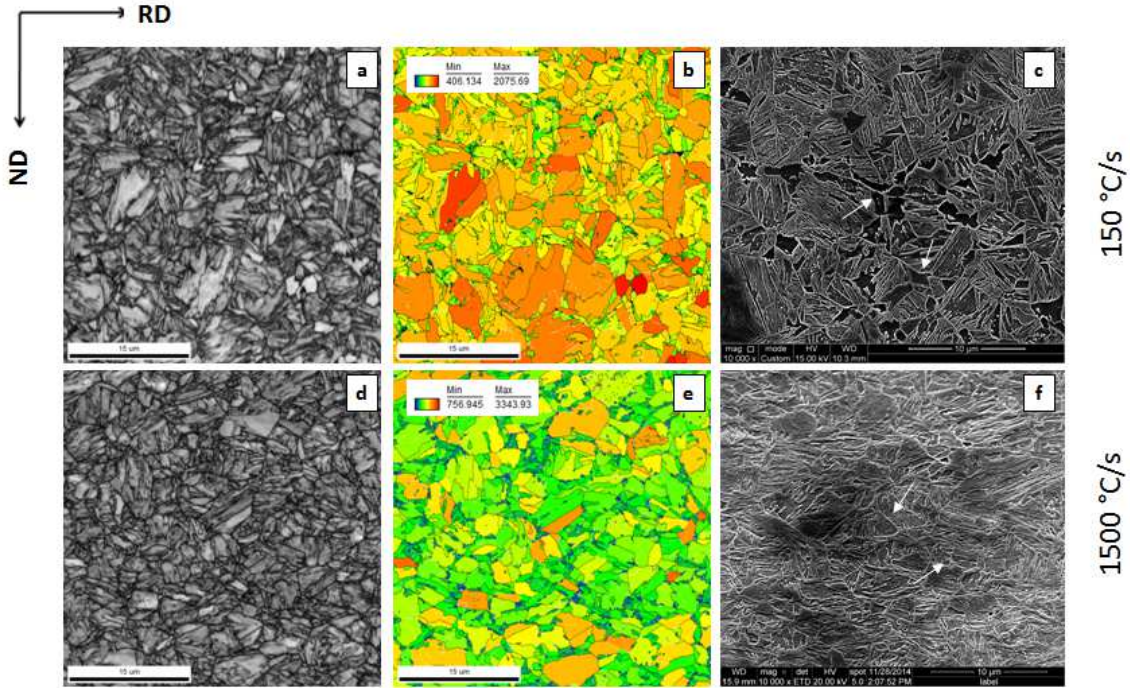

Fig. VI-14. (a, d) and (b, e) are respectively the IQ and GAIQ maps of a samples heated at 150 °C/s and 1500 °C/s to a peak temperature of 1000 °C and quenched. (c, f) are SEM images of a sample heated at 150 °C/s and at 1500 °C/s to a peak temperature of 1000 °C and quenched, showing a mixture of martensite and ferrite (white arrows) at parent austenitic grain boundaries. In (b, e), high carbon martensite is represented by the blue-green grains, whereas low carbon martensite is represented by light green-yellow grains. Ferrite grains are colored in orange-red. Scale bar in a,b, d, and e is 15 µm, c, f 10 µm.

VI-4.3.3 Growth into proeutectoid ferrite

The growth of the austenite into the pearlite and in the proeutectoid ferrite are simultaneous processes. However, there is a remarkable kinetic difference between one and the other [30]. The kinetics of the austenite growth into the proeutectoid ferrite is slower compared to the advance of austenite into pearlite, since the carbon must now diffuse longer distances than the interlamellar spacing of pearlite. The diffusion of carbon to the γ/α interface will control the reaction rate while $G^{\alpha} > G^{\gamma}$ for any composition. This statement can be shown schematically in Fig. VI-12a. When the temperature is increased from any point slightly above the eutectoid, the common tangent to the Gibbs free energy curves of ferrite and austenite, G^{α} and G^{γ}, will define the α/γ equilibrium. When the temperature is increased to T', a new α/γ equilibrium is defined by $G^{\gamma\prime}$ with the compositions

$X_C^{\alpha/\gamma}$ and $X_C^{\gamma/\alpha}$. As the temperature is further increased, the α/γ equilibrium will always be defined by the Gibbs free energy curves of ferrite and austenite until $G^{\alpha} = G^{\gamma}$. In the case of Fe-C system, this temperature corresponds to the allotropic change from ferrite to austenite in pure iron (~912 °C). In higher order systems, the upper temperature will be defined by the austenite solvus line at $X_C \rightarrow 0$. The upper temperature will be called A_S. Under local equilibrium conditions, the composition of the α/γ interface will always be defined between the eutectoid and the A_m temperature and thus the mechanism of transformation will be diffusion controlled.

The slope S_2 in Fig. VI-2a is mainly related to the advance of the γ/α interface into proeutectoid ferrite in samples heated at 150 °C. Fig. VI-1b, 1c, 1e, and 1f show that the γ/α interface is mainly planar in samples heated at 150 °C/s and 1500 °C/s. The growth of austenite does not occur preferentially either into recrystallized nor into deformed ferrite, because the diffusion of carbon in austenite is controlling the reaction.

VI-4.3.4 Massive transformation of austenite

Depending on the heating rate, the formation of austenite might not be fully accomplished by carbon diffusion controlled mechanism. If any untransformed ferrite remains above the A_m temperature, it will be transformed into austenite by a massive mechanism. When austenite is formed by a massive mechanism, it will inherit the chemical composition of the ferrite. Hence, there will be austenite formed at early stages of transformation with very high carbon content, and austenite formed massively at final stages with a very low carbon content. Since the experiments were performed under very small holding time (less than 0.5 s), it is likely that the carbon heterogeneities in austenite will remain. Thus martensite will inherit the carbon content of austenite after quenching. The heterogeneities in martensite are shown in Fig. VI-14a and 5d (IQ maps) for samples heated at 150 °C/s to 1000 °C, and 12b and 12e (GAIQ map) for samples heated at 1500 °C/s to 1050 °C. The different degree of gray in Fig. VI-14a is due to the contrast between low and high IQ values. The IQ values of the diffraction patterns are sensitive to the level of distortion in the lattice. Therefore, a highly distorted lattice (like in high carbon martensite) will give rise to a low image quality, and consequently less distorted lattice (as in very low carbon martensite) will produce electron diffraction patterns with high image quality. GAIQ maps in Fig. VI-14b and 5e colors the contrast between high carbon martensite (blue-green) and low carbon martensite (yellow).

The first nucleated austenite grains will have the most time for growth and therefore they are the largest in the microstructure. An estimation of the size of the prior austenite grains can be given by the maximum diameter of martensitic grains, measured by EBSD. Fig. VI-2b show a smooth increase in the maximum diameter of martensite in samples heated at 150 °C/s and 1500 °C/s, indirectly indicating that the transition from the carbon diffusion controlled mechanism to the interface controlled mechanism [22] (massive) is rather gradual. The growth of the austenite is a function of the γ/α interface velocity, which is described as

$$v = M \cdot \xi \qquad 2$$

where *v, M* and ξ are respectively the velocity of the γ/α interface, the mobility of the γ/α interface and the driving force for the massive formation of austenite. As the heating rate is increased, both the interface mobility and the diffusivity of carbon are increasing. The balance between the available pressure for the interface advancing and the carbon diffusion has been expressed elsewhere [55] as a multiplying factor in the driving force ξ term of Eq. VI-2. However, carbon diffusion speed grows faster, and it gradually overcomes the mobility of the γ/α interface (above A_S). Thus, one should expect a smooth growth in the austenitic grain size, as indirectly shown in Fig. VI-2b. Larger maximum diameters of martensite were measured in samples heated at 150 °C/s, compared to samples heated at 1500 °C/s. It is suggested that the difference in maximum martensitic grain diameter is a consequence of the lower heating rates of heated at 150 °C/s, enabling thus more time for carbon diffusion.

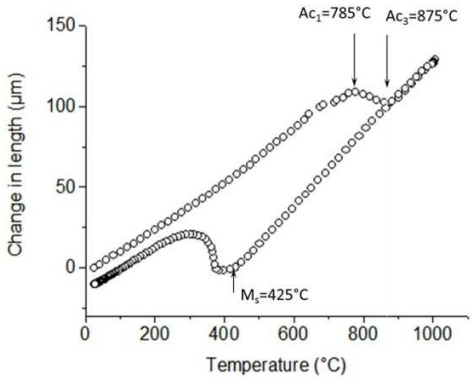

Fig. VI-15. Change in length versus temperature obtained by dilatometry for material heated at 150 °C/s to 1000 °C and quenched. The formation of austenite during heating was complete.

VI-4.3.5 Transformation of proeutectoid ferrite during cooling

Dilatometric data in Fig. VI-15 indicates that the formation of austenite during heating at 150 °C/s to 1000 °C was complete. However, the microstructure revealed the presence of ferrite (cf. arrows in Fig. VI-14c). Therefore, the ferrite was formed during cooling. In all cases, this ferrite was formed either at triple junctions or grain boundaries of parent austenitic grains. Ferrite was also observed in samples UFH at 1500 °C/s to 1050°C and quenched (cf. arrows in Fig. VI-14f). Similar morphology of ferrite after UFH have been recently reported in quenched and partitioned (Q&P) steel [3]. The explanation of this unexpected fraction of ferrite stems in the massive formation of austenite at later stages.

As described in the previous section, the massive austenite will inherit the carbon content of proeutectoid ferrite and the quick quenching will prevent further carbon homogenization in austenite. Therefore, the uneven carbon distribution in austenite will define different driving

forces for the transformation of austenite into ferrite. The available driving force for the transformation of austenite can be schematically illustrated with the aim of Fig. VI-12a. Let us consider the case of a fully austenitic structure with carbon content heterogeneously distributed between $X_C \approx 0$ and some X_C carbon content. During cooling to a temperature below A_S, for instance, T', there will be available driving force for the transformation of ferrite for all carbon contents until the composition X_0, where $G^{\alpha} = G^{\gamma}$. At very low carbon contents (i. e. $X_C \rightarrow 0$), as in the case of austenite formed massively during heating, the available driving force will be only dissipated in the moving of the α/γ interface. The transformation will not require long range carbon diffusion, only short-range iron diffusion. Thus, it can take place by a massive mechanism. There will be some point during the advancing of the α/γ interface where it will reach an area with higher carbon content and thus the movement of the flat interface will be hindered. A possible case can occur where a bump in the moving α/γ interface can nucleate and further grow into austenite as Widmanstätten ferrite. The velocity of growth of plate of Widmanstätten ferrite is inversely proportional to the tip radius [54]. Thus, a very thin plate can further advance into austenite even during quenching. Examples of Widmanstätten ferrite in samples heated at 150 °C/s and 1500 °C/s are illustrated in Fig. VI-1c and 1f. As the temperature is quickly decreasing, it is likely that the carbon rich areas in austenite will reach their respective M_S temperature and transform into martensite. The actual microstructure formed after UFH at 150 °C/s and 1500 °C/s and quenching is in fact a mixture of ferrite with different morphologies, partially spheroidized cementite and martensite of heterogeneous carbon content, as previously described. It should be noted that ferrite transformed at γ/γ boundaries (cf. circles in Fig. VI-1c and 1e) is also found in samples heated at 150 °C/s to 838 °C and in samples heated at 1500 °C/s to 842 °C. The carbon gradients in austenite and the high diffusivity of carbon can account for the formation of allotriomorphs of ferrite during cooling.

VI-4.3.6 Texture inheritance effect in martensite

Fig. VI-16 displays the ODF at $\varphi = 45°$ of samples heated at 150 °C/s and 1500 °C/s. The microstructure after quenching from 1000 °C is a mixture of ferrite and martensite for both heating rates. The orientations in martensite (cf. Fig. VI-16b, and 7d) for both heating rates are essentially the same as in cold-rolled microstructure (cf. Fig. VI-16b). The maximum intensities in martensite orientations are close to {111}⟨112⟩ and are ~50% the intensities in cold-rolled steel. The texture memory effect in steel was discussed by Hutchinson and Kestens [56]. It was pointed out that the variant selection during nucleation austenite at α/α interface, and the subsequent nucleation of ferrite (or martensite) at γ/γ grain boundaries can satisfactory explain the similar orientations between parent and product phases. In their experiments, however, the microstructure was fully recrystallized before the phase change took place. In the case of UFH experiments, the initial microstructure is more complex and mainly consist in a mixture of recrystallized and non-recrystallized ferrite. The nucleation of austenite is taking place mainly in the α/θ interface, but it was shown that nucleation at α/α interface was also occurring. One can thus suggest that in both cases the austenite nucleated with some specific orientation

relationships (OR) to ferrite, and although with less intensity the same OR were preferred during the transformation of martensite on cooling.

It should be noted that ODF´s of martensite heated at 150 °C/s and to 1500 °C/s are the same, within the intrinsic spread of the measurements. These results also suggest that the oriented nucleation of austenite might have occurred at low temperatures, where a considerable fraction of non-recrystallized ferrite was present in the microstructure of samples heated at 150 °C/s and 1500 °C/s (cf. Fig. VI-2a).

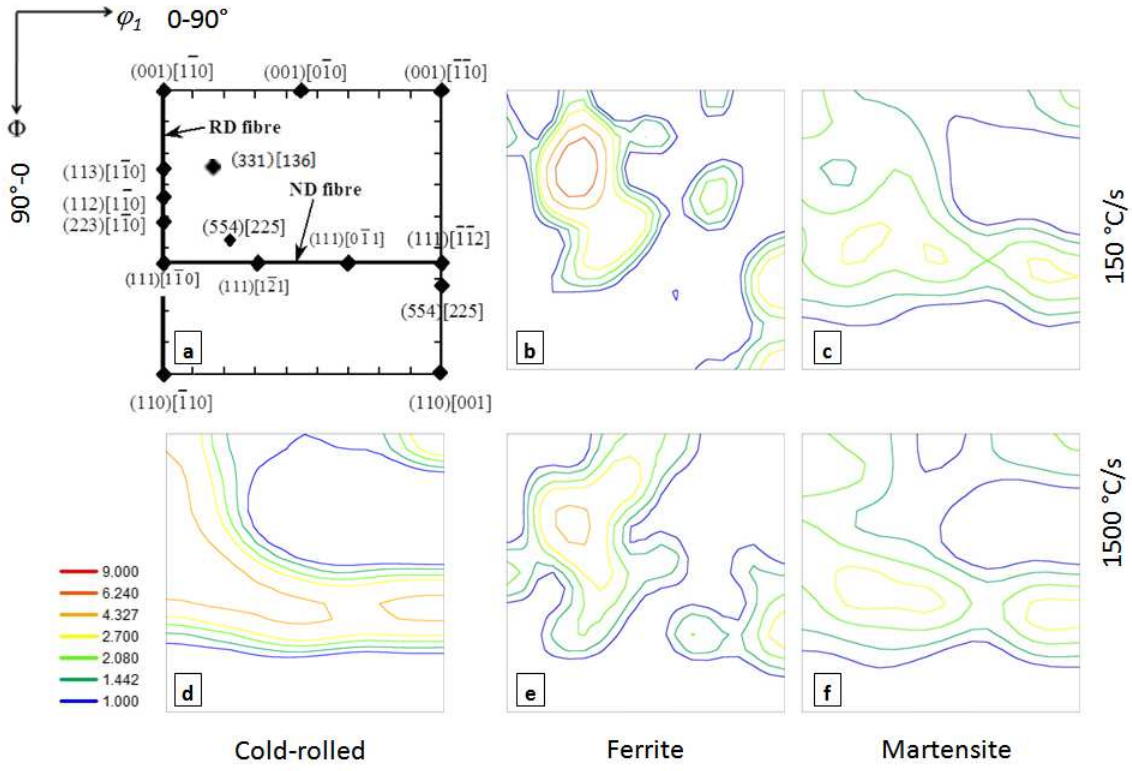

Fig. VI-16. (a) Ideal positions of the most important BCC texture components in the φ_2 = 45° section of Euler space. (b-f) are ODF at φ_2 = 45° from samples heated at 150 °C/s (b and c) to 1000 °C and water quenched, cold -rolled material (d), and heated at 1500 °C/s (e and f) to 1050 °C and water quenched. (b) and (e) correspond to ferrite, whereas (c) and (f) to martensite.

The orientations resulting from the transformation of ferrite during quenching from 1000 °C are shown in Fig. VI-16a and 16c respectively for samples heated at 150 °C/s and 1500 °C/s. The highest intensity is around the {331}⟨136⟩ component. It is claimed [43] that this orientation originates from specific deformation features, like intra-grain deformation bands in deformed ferrite of RD {hkl}⟨110⟩ fiber. However, our experiments suggest that it can be a product of the transformation of proeutectoid ferrite from austenite in low-carbon steel. Goss component (cf. Fig. VI-16a) is also present in sample heated at 150 °C/s to 1000 °C. Such component is claimed to form in shear bands during recrystallization, and also as an austenite transformation product [20].

VI-5 Conclusions

Ultrafast heating experiments at 150 °C/s and 1500 °C/s to different peak temperatures have been conducted on a cold-rolled low carbon steel. The ferrite recrystallization, the texture evolution, and the phase transformations were studied via detailed microstructural characterization. The results indicate that the recrystallization was not 100 % complete before the full formation of austenite. It is suggested that the ferritic grains between pearlitic colonies are accumulating larger amounts of strain, compared to pearlitic colonies. Thus, the driving force for recrystallization of ferrite is higher in these areas.

The nucleation of recrystallized ferrite took place at grain boundaries, as well as in shear bands. However, in samples heated at 1500 °C/s the shear band nucleation of ferrite took place at higher temperatures, compared to samples heated at 150 °C/s. The effect of heating rate in carbon diffusion can justify the observed nucleation of recrystallized ferritic grains in shear bands, and thus the appearance of recrystallized grains in the vicinity of the Goss {110}⟨110⟩ component.

Experimental measurements indicate that an important fraction of recrystallized ferritic grains of diameter less than 1 μm are formed in a rather continuous fashion during heating, and the fraction of such grains is increasing as the heating rate is increased. The measurements suggest that the continuous nucleation of recrystallized ferrite is enhanced by applying ultrafast heating rates.

The texture evolution of ferrite in early stages of recrystallization in samples heated at 1500 °C/s is taking place close to ND {111}⟨uvw⟩ fiber components as well as in the vicinity of {110}⟨110⟩ high stored energy components. When the time for the releasing of stored energy is comparatively longer (as in the case of samples heated at 150 °C/s) the orientations in recrystallized ferrite are mainly close to ND {111}⟨uvw⟩ and RD {hkl}⟨011⟩ fiber components. The increase in the intensity of RD {hkl}⟨011⟩ fiber components in recrystallized ferrite observed at both heating rates is possibly related to the continuos nucleation in low stored energy grains.

Cementite plates and spheres might act as a barrier for the advance of the α/α interface during recrystallization. The maximum ferritic recrystallized grain diameter evolves with the temperature, being defined by the interaction of the α/α interface with the cementite particles at early stages of recrystallization. At later stages (i. e., higher temperatures), the growth of austenite into ferrite will determine the size of the maximum ferritic grain diameter.

The nucleation and growth of austenite are primarily occurring at the α/θ interface. However, evidence of nucleation at the α/α interface is provided and rationalized from the thermodynamic point of view.

The degree of spheroidization of cementite in samples heated at 150 °C/s is larger, compared to samples heated at 1500 °C/s. This has a notorious impact in the morphology of austenite at early stages of growth, which is banded in samples heated at 1500 °C/s and more equiaxed in samples heated at 150 °C/s.

Ultrafast heating experiments enable the formation of massive austenite during heating, and the subsequent transformation of a mixture proeutectoid and Widmanstätten ferrite, and martensite of heterogeneous carbon content. Experimental evidence supporting the change from diffusional to massive transformation is discussed from the thermodynamic point of view.

A texture memory effect in martensite is was measured in samples heated at 150 °C/s and 1500 °C/s. It is suggested that the oriented nucleation of austenite is playing a major role in the crystallographic orientations of martensite.

VI-6 References

[1] T. Lolla, G. Cola, B. Narayanan, B. Alexandrov, S.S. Babu, Development of rapid heating and cooling (flash processing) process to produce advanced high strength steel microstructures, Mater. Sci. Technol. 27 (2011) 863–875. doi:10.1179/174328409x433813.

[2] Q. Meng, J. Li, H. Zheng, High-efficiency fast-heating annealing of a cold-rolled dual-phase steel, Mater. Des. 58 (2014) 194–197. doi:10.1016/j.matdes.2014.01.055.

[3] D. De Knijf, A. Puype, C. Föjer, R. Petrov, The influence of ultra-fast annealing prior to quenching and partitioning on the microstructure and mechanical properties, Mater. Sci. Eng. A. 627 (2015) 182–190. doi:10.1016/j.msea.2014.12.118.

[4] A. Puype, Developing of advanced high strength steel via ultrafast annealing, Master Thesis, Ghent University, 2013. doi:10.1017/CBO9781107415324.004.

[5] L. Kestens, A.C.C. Reis, W.J. Kaluba, Y. Houbaert, Grain Refinement and Texture Change in Interstitial Free Steels after Severe Rolling and Ultra-Short Annealing, Mater. Sci. Forum. 467–470 (2004) 287–292. doi:10.4028/www.scientific.net/MSF.467-470.287.

[6] R. Petrov, J. Sidor, W.J. Kaluba, L. Kestens, Grain Refinement of a Cold Rolled TRIP Assisted Steel after Ultra Short Annealing, Mater. Sci. Forum. 715–716 (2012) 661–666. doi:10.4028/www.scientific.net/MSF.715-716.661.

[7] R.H. Petrov, A. Puype, D. De Knijf, L. Kestens, Ultrafast heating of advanced high strength steels, in: M. Militzer, G. Botton, L.-Q. Chen, J. Howe, C. Sinclair, H. Zurob (Eds.), Proc. Int. Conf. Solid-Solid Phase Transform. Inorg. Mater. 2015, 2015: pp. 1157–1158.

[8] F.M. Castro Cerda, C. Goulas, I. Sabirov, S. Papaefthymiou, A. Monsalve, R.H. Petrov, Microstructure, texture and mechanical properties in a low carbon steel after ultrafast heating, Mater. Sci. Eng. A. (2016). doi:10.1016/j.msea.2016.06.056.

[9] V.T. G. Griffay, M. Anderhuber, P. Klinkenberg, New continuous annealing technology with high-speed induction heating followed by ultra-fast cooling, 2002.

[10] M. Atkinson, Bifurcation of thermal restoration processes in deformed iron and steel, Mater. Sci. Eng. A. 262 (1999) 33–38. doi:10.1016/S0921-5093(98)01031-4.

[11] M. Ferry, D. Muljono, D.P. Dunne, Recrystallization Kinetics of Low and Ultra Low Carbon Steels during High-rate Annealing, ISIJ Int. 41 (2001) 1053–1060.

doi:10.2355/isijinternational.41.1053.

[12] D. Muljono, M. Ferry, D.P. Dunne, Influence of heating rate on anisothermal recrystallization in low and ultra-low carbon steels, Mater. Sci. Eng. A. 303 (2001) 90–99. doi:10.1016/S0921-5093(00)01882-7.

[13] M. Atkinson, On the credibility of ultra rapid annealing, Mater. Sci. Eng. A. 354 (2003) 40–47. doi:10.1016/S0921-5093(02)00830-4.

[14] J. Stockemer, P. Vanden Brande, Recrystallization of a cold-rolled low-carbon steel by cold-plasma-discharge rapid annealing, Metall. Mater. Trans. A. 34 (2003) 1341–1348. doi:10.1007/s11661-003-0245-3.

[15] T. Senuma, K. Kawasaki, Y. Takemoto, Recrystallization Behavior and Texture Formation of Rapidly Annealed Cold-Rolled Extralow Carbon Steel Sheets, Mater. Trans. 47 (2006) 1769–1775. doi:10.2320/matertrans.47.1769.

[16] N. Yoshinaga, L. Kestens, B.C. De Cooman, α→γ→α Transformation Texture Formation at Cold-Rolled Ultra Low Carbon Steel Surfaces, Mater. Sci. Forum. 495–497 (2005) 1267–1272. doi:10.4028/www.scientific.net/MSF.495-497.1267.

[17] R. Petrov, L. Kestens, Y. Houbaert, Recrystallization of a Cold Rolled Trip-assisted Steel during Reheating for Intercritical Annealling., ISIJ Int. 41 (2001) 883–890. doi:10.2355/isijinternational.41.883.

[18] R. Petrov, L. Kestens, W.J. Kaluba, Y. Houbaert, Recrystallization and austenite formation in a cold rolled TRIP steel during ultra fast heating, Steel Grips. 1 (2003) 289–293.

[19] R.K. Ray, J.J. Jonas, R.E. Hook, Cold rolling and annealing textures in low carbon and extra low carbon steels, Int. Mater. Rev. 39 (1994) 129–172. doi:10.1179/095066094790326112.

[20] R.K. Ray, J.J. Jonas, Transformation Textures in Steels, Int. Mater. Rev. 35 (1990) 1–36. <Go to ISI>://WOS:A1990DE71200001.

[21] Y.Y. Meshkov, E.V. Pereloma, Phase Transformations in Steels, Elsevier, 2012. doi:10.1533/9780857096104.4.581.

[22] J.W. Christian, The Theory of Transformations in Metals and Alloys, 3rd ed., ELSEVIER SCIENCE Ltd, Oxford, UK, 2002. doi:10.1016/B978-0-08-044019-4.50036-2.

[23] W.J. Kaluba, R. Taillard, J. Foct, The Bainitic Mechanism of Austenite Formation During Rapid Heating, Acta Mater. 46 (1998) 5917–5927.

[24] H.I. Aaronson, J.F. Nie, DISCUSSION TO “THE BAINITIC MECHANISM OF AUSTENITE FORMATION DURING RAPID HEATING,” Scr. Mater. 42 (1998) 505–509.

[25] M. Hillert, COMMENTS ON “ THE BAINITE MECHANISM OF AUSTENITE FORMATION DURING RAPID HEATING ,” 43 (2000) 1045–1046.

[26] R.R. Judd, H.W. Paxton, Kinetics of austenite formation from a spheroidized ferrite-carbide aggregate, Trans. AIME. 242 (1968) 206–215.

[27] G.R. Speich, A. Szirmae, Formation of austenite from ferrite and ferrite-carbide aggregates, Trans. AIME. 245 (1969) 1063–1073.

[28] M. Hillert, K. Nilsson, L.-E.Torndahl, Effect of Alloying Elements on the Formation of Austenite and Dissolution of Cementite, J. Iron Steel Inst. (1971) 49–66.

[29] E. Schmidt, Y. Wang, S. Sridhar, A Study of Nonisothermal Austenite Formation and Decomposition in Fe-C-Mn Alloys, Metall. Mater. Trans. A. 37A (2006) 1799–1810. doi:10.1007/s11661-006-0122-y.

[30] E.D. Schmidt, E.B. Damm, S. Sridhar, A study of diffusion- and interface-controlled migration of the Austenite/Ferrite front during Austenitization of a case-hardenable alloy steel, Metall. Mater. Trans. A Phys. Metall. Mater. Sci. 38 (2007) 698–715. doi:10.1007/s11661-007-9208-4.

[31] R.C. Dykhuizen, C. V Robino, G.A. Knorovsky, A method for extracting phase change kinetics from dilatation for multistep transformations: Austenitization of a low carbon steel, Metall. Mater. Trans. B. 30 (1999) 107–117. doi:10.1007/s11663-999-0011-z.

[32] V.I. Savran, S.E. Offerman, J. Sietsma, Austenite Nucleation and Growth Observed on the Level of Individual Grains by Three-Dimensional X-Ray Diffraction Microscopy, Metall. Mater. Trans. A. 41 (2010) 583–591. doi:10.1007/s11661-009-0142-5.

[33] R.H. Petrov, L.A.I. Kestens, Advanced High-Strength Steels: Electron Backscatter Diffraction (EBSD), in: Encycl. Iron, Steel, Their Alloy., n.d.: pp. 46–69. doi:10.1081/E-EISA-120050786.

[34] P.T. Pinard, A. Schwedt, A. Ramazani, U. Prahl, S. Richter, Characterization of Dual-Phase Steel Microstructure by Combined Submicrometer EBSD and EPMA Carbon Measurements, Microsc. Microanal. 19 (2013) 996–1006. doi:10.1017/S1431927613001554.

[35] A. Oddy, J. Mcdill, L. Karlsson, Microstructural predictions including arbitrary thermal histories, reaustenization and carbon segregation effects, Can. Metall. Q. 35 (1996) 275–283. doi:10.1016/0008-4433(96)00001-8.

[36] M. Onink, F.D. Tichelaar, C.M. Brakman, E.J. Mittemeijer, S. van der Zwaag, An in situ hot stage transmission electron microscopy study of the decomposition of Fe-C austenites, J. Mater. Sci. 30 (1995) 6223–6234.

[37] S.L. Semiatin, I.M. Sukonnik, V. Seetharaman, An analysis of static recrystallization during continuous, rapid heat treatment, Metall. Mater. Trans. A. 27 (1996) 2051–2053. doi:10.1007/BF02651955.

[38] T.A. Kop, Dilatometric study of the austenite/ferrite interface mobility, Ph. D. Thesis, TU Delft, 2000.

[39] V.I. Savran, Austenite formation in C-Mn steel, Ph. D. Thesis, TU Delft, 2009.

[40] J.Y. Kang, B. Bacroix, H. Réglé, K.H. Oh, H.C. Lee, Effect of deformation mode and grain orientation on misorientation development in a body-centered cubic steel, Acta Mater. 55 (2007) 4935–4946. doi:10.1016/j.actamat.2007.05.014.

[41] W.B. Hutchinson, Development and control of annealing textures in low-carbon steels, Int.

Met. Rev. 29 (1984) 25–42. doi:10.1179/imtr.1984.29.1.25.

[42] T. Nguyen-Minh, J.J. Sidor, R.H. Petrov, L.A.I. Kestens, Occurrence of shear bands in rotated Goss ({110}〈110〉) orientations of metals with bcc crystal structure, Scr. Mater. 67 (2012) 935–938. doi:10.1016/j.scriptamat.2012.08.017.

[43] P. Gobernado, R.H. Petrov, L.A.I. Kestens, Recrystallized {3 1 1}〈1 3 6〉 orientation in ferrite steels, Scr. Mater. 66 (2012) 623–626. doi:10.1016/j.scriptamat.2012.01.056.

[44] X. Wang, H.S. Zurob, G. Xu, Q. Ye, O. Bouaziz, D. Embury, Influence of Microstructural Length Scale on the Strength and Annealing Behavior of Pearlite, Bainite, and Martensite, Metall. Mater. Trans. A. 44 (2013) 1454–1461. doi:10.1007/s11661-012-1501-1.

[45] K. Hono, M. Ohnuma, M. Murayama, S. Nishida, A. Yoshie, T. Takahashi, Cementite decomposition in heavily drawn pearlite steel wire, Scr. Mater. 44 (2001) 977–983. doi:10.1016/S1359-6462(00)00690-4.

[46] F.J. Humphreys, M. Hatherly, Recrystallization and Related Annealing Phenomena, Elsevier, 2004. doi:10.1016/B978-008044164-1/50015-3.

[47] G.S. Rohrer, ``Introduction to Grains, Phases, and Interfaces---an Interpretation of Microstructure,'' Trans. AIME, 1948, vol. 175, pp. 15--51, by C.S. Smith, Metall. Mater. Trans. A. 41 (2010) 1063–1100. doi:10.1007/s11661-010-0215-5.

[48] C.S. Smith, Grains, Phases, and Interfaces—an Interpretation of Microstructure, Trans. AIME. 175 (1948) 15–51.

[49] J.Y. Kang, D.I. Kim, H.C. Lee, Texture development in low carbon sheet steels for automotive application, in: A. Haldar, S. Suwas, D. Bhattacharjee (Eds.), Microstruct. Texture Steels Other Mater., Springer London, London, 2009: pp. 85–101. doi:10.1007/978-1-84882-454-6_5.

[50] I.L. Dillamore, P.L. Morris, C.J.E. Smith, W.B. Hutchinson, Transition Bands and Recrystallization in Metals, Proc. R. Soc. London. Ser. A, Math. Phys. Sci. 329 (1972) 405–420. doi:10.1098/rspa.1972.0120.

[51] K. Ushioda, W.B. Hutchinson, J. Ågren, U. von Schlippenbach, Investigation of structure and texture development during annealing of low-carbon steel, Mater. Sci. Technol. 2 (1986) 807–815. doi:10.1179/mst.1986.2.8.807.

[52] M. Hillert, The uses of free energy-composition diagrams, in: H.I. Aaronson (Ed.), Lect. Theory Phase Transform., Metallurgical Society of AIME, 1975: pp. 1–50.

[53] R.F. Mehl, The mechanism and rate formation of austenite from ferrite-cementite aggregates, Trans. ASM. 31 (1943) 613–650.

[54] C. Zener, Kinetics of Decomposition of Austenite, Trans. AIME. 167 (1946) 550–583.

[55] J. Sietsma, S. van der Zwaag, A concise model for mixed-mode phase transformations in the solid state, Acta Mater. 52 (2004) 4143–4152. doi:10.1016/j.actamat.2004.05.027.

[56] B. Hutchinson, L.A.I. Kestens, Origins of Texture Memory in Steels, in: Appl. Texture Anal.,

John Wiley & Sons, Inc., 2008: pp. 281--290. doi:10.1002/9780470444214.ch30.

Chapter VII

Microstructure, texture and mechanical properties in a low carbon steel after ultrafast heating[5]

Heating experiments in a wide range of heating rates from 10 to 1200 °C/s and subsequent quenching without isothermal soaking have been carried out on a low carbon steel. The thermal cycles were run on two different cold rolled microstructures, namely ferrite + pearlite and ferrite + martensite. It is shown that the average ferritic grain size, the ferrite grain size distribution, the phase fractions and the corresponding mechanical properties (ultimate tensile strength and ductility) after quenching are strongly influenced by the heating rates and the initial microstructure. The ferrite grain size distribution is significantly modified by the heating rate, showing a markedly bimodal distribution after fast annealing. The raise of the heating rate has produced a change in the relative intensities of texture components, favouring those of the cold deformed structure (RD fibre) over the recrystallization components (ND fibre).

VII-1 Introduction

Steel industry is nowadays facing the challenge of producing materials with enhanced properties to meet the safety and fuel efficiency standards of the strict environmental and legal authority regulations (EU and USA) [1]. The development of Advanced High Strength Steels (AHSS) was a reaction of the steel industry to these societal needs [2]. The beneficial combination of enhanced strength and toughness was reached due to unique microstructures generated in this steel family. Lately, new processing routes, such as the quenching and partitioning (Q&P) and the ultra-fast heating (UFH) path, attempt to further improve Interstitial Free (IF), Dual Phase (DP), Transformation-induced plasticity (TRIP) and Martensitic steel (MS) grades. Additionally, the design of steels via UFH can deliver very high strengths due to the initiation of a mixed and/or synergetic bainitic/martensitic transformation. The aforementioned new thermal routes carried out in laboratory [3–6] or in small scale industrial conditions [7] have produced steels with superb mechanical properties, which evince the large but not yet used potential of the UFH treatments in steel manufacturing. The heating with very high heating rates is not new practice in the heat treatment and it has found its place in the surface thermal treatment of the structural steels for general application i.e. steels with carbon content of 0.35 to 0.6%C (case hardening). However, its application to sheet materials and low carbon grades like AHSS is not yet studied in details. In

[5] This chapter has been partially published as F.M. Castro Cerda, C. Goulas, I. Sabirov, S. Papaefthymiou, A. Monsalve, R.H. Petrov, Microstructure, texture and mechanical properties in a low carbon steel after ultrafast heating, Mater. Sci. Eng. A. 672 (2016) 17–20. doi:10.1016/j.msea.2016.06.056

particular UFH stands out for its adaptability to the steel processing lines. Besides the improvement of the mechanical properties, UFH offers the opportunity of reducing the annealing steps for steel sheets and tube production. However, due to a number of technical difficulties of realization in large scale, UFH is not yet ready for industrial application in the existing continuous annealing lines.

The grain refinement effect of UFH in low carbon steel has been demonstrated [5,6,8–15]. Muljono et al. have reported a decrease in the recrystallized ferritic grain size after annealing cycles with heating rates up to 1000 °C/s [8]. The refining effect was also shown on IF steels [16], where the average ferritic grain (AFG) size was reduced to certain saturation point of 6 μm (at the heating rate of ~1000 °C/s), above which no further grain refining effect was observed. Such measurements were found to be consistent with later measurement of ferritic grain size versus heating rate in TRIP composition steels [6,9–12,14]. The much lower saturated AFG size measured (~1.5 μm) in the latter experiments in comparison to the one measured in IF steel suggests the interaction of the deformed ferrite with grains of second phase during recrystallization and phase transformation stages.

UFH influences not only the microstructure but the texture of the cold rolled steel [6,9–12,14,15,17]. In UFH treated cold rolled IF steel no general changes in the orientation components are observed when the recrystallization is finished before the onset of austenite formation [16]. The trends seem to be similar for low and very low carbon steel [17,18]. However, in cold rolled AHSS with initial microstructure of ferrite and pearlite after slow reheating (10 and 50°C/s) the cold rolling texture changes to are crystallization type texture, which is characterized by a strong {111}⟨uvw⟩ (ND fibre) with specific curvature, and in which the RD fibre component {hkl}⟨110⟩ is almost vanished or quite weak. Contrary, the texture of the cold rolled samples reheated at 1000°C/s and 3000°C/s remains almost unchanged even after reheating up to 880°C keeping the characteristic features of the BCC cold rolling texture [6,9–11,14]. Petrov et al. [6,9,14] have rationalized the influence of UFH on the texture as an effect of the stabilization in the recovered structure of deformed ferrite by carbide precipitates and its contribution to the overall texture. Insignificant changes in rolling texture were reported also after UFH and quenching of steels with initial microstructure of cold rolled ferrite and martensite [10,12].

Analysis of the existing literature shows that very fine grained microstructures and correspondingly high ultimate tensile strength and elongation can be obtained in AHSS after employing fast and ultra-fast heating rates without isothermal soaking. The heating rates above 1000°C/s allow recrystallization to be partially or completely suppressed and the crystallographic texture after UFH without isothermal soaking remains almost the same as the texture before the UFH treatment. On the other hand, the experiments in [6,9–11] clearly show that heating rates above 1500°C/s do not contribute to grain refinement. However, the thermal treatment cycles reported in the literature are very difficult for practical implementation and the re-scaling to industrial conditions still remains a challenge, although the work of Cola et al. [7] shows that it is possible.

The aim on this work is to obtain a better understanding of the effect of heating rates and initial microstructure on phase transformations, recrystallization, texture and mechanical properties of a low carbon steel. To study the possibilities for an industrial implementation, all processing parameters are varied in a range which is considered as realistic for industry [15]. For the present study, the heating rates have been classified in the following ranges: conventional, (maximum of 10 °C/s), fast (from 10 to 100 °C/s) and ultrafast (higher than 100 °C/s).

VII-2 Experimental

VII-2.1 Material and heat treatments

The chemical composition of the studied steel is shown in Table VII-1. Steels with this composition are used as transformation induced plasticity (TRIP) assisted steel for automotive applications.

Table VII-1. Chemical composition of the studied steel.

C	Mn	Al	Si	Fe
0.19	1.61	1.06	0.50	Rest

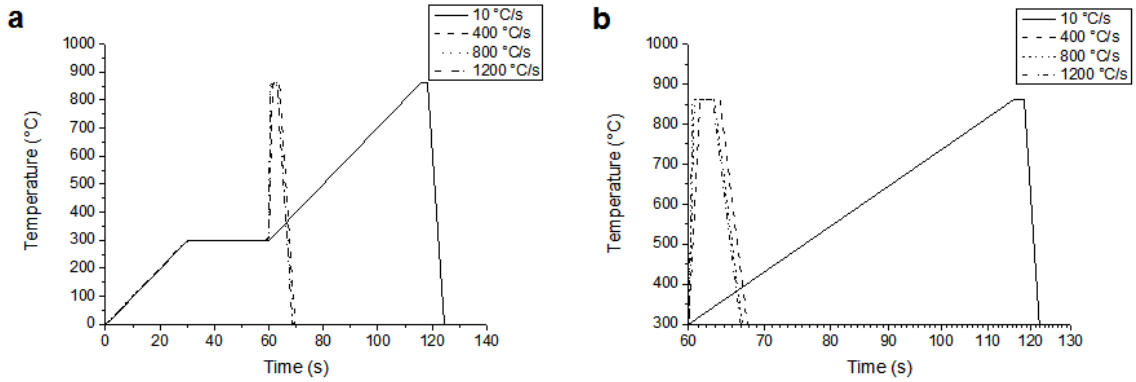

Fig. VII-1. Representation of the heat treatments. (a) shows the full thermal cycle and (b) shows the stages 3 and 4 for the different heating rates.

The steel sheet of 1 mm thickness and a microstructure of ferrite and pearlite was received in condition after 50% cold rolling. Two sets of specimens with different initial microstructures were prepared from the selected steel. The first set of specimens denominated further as (50% F+P) set was kept in the as-received state, i.e. with the 50% cold deformation. The second set of samples (denominated as 50% M) was produced by annealing the initial steel sheet in the intercritical temperature range, where the microstructure consists of 50% ferrite and 50% austenite, and subsequently water quenched to produce a mixture of approximately 50% ferrite and 50% martensite. Next, the heat treated sheet was 50% cold rolled. Specimens of 80x25x1 (50% F+P) and 80x20x0.5 (50% M) mm^3size were cut from each initial material and subject to different het treatments, microstructural analyses and mechanical tests. The phase transformation temperatures A_{C1} and A_{C3} of the steel were measured at a heating rate of 10°C/sin the DIL805AD

Bähr dilatometer. The measured critical temperatures were Ac_1^{10} = 728 °C and Ac_3^{10} = 923 °C. It was earlier reported that the transformation temperatures depend on the heating rate as well as on the initial microstructure [18]. Thus, the actual transformation temperatures for the heating rates above 10°C/s will be different. Critical temperatures at heating rates of 400°C/s and 1000°C/s could not be measured by dilatometry with acceptable accuracy due to the instability of the system.

The specimens were subjected to different rapid heating cycles followed by subsequent ~~water~~ quenching. Motivated by the capacity of current continuous annealing lines [15], it was decided to study continuous heating cycles with two heating rates as shown in Fig. VII-1. Each thermal cycle contains 4 stages. On the first and second stage, the specimens were heated at 10 °C/s to 300 °C and next isothermally held at 300 °C for 30 s. These stages simulate a preheating stage in some industrial continuous annealing lines. On the third stage, the specimens were heated from 300 °C to 860 °C at four different heating rates, 10, 400, 800 and 1200 °C/s, and held at 860 °C for 1.5 s. The heating temperature was selected to be in the intercritical temperature range, where different fractions of ferrite and austenite are in equilibrium. The isothermal holding time was strictly controlled and never exceeded 1.5 s. Lastly, the specimens were water quenched from 860 °C to room temperature. The cooling rate achieved was ~-130 °C/s. The heat treatments were carried out in a Gleeble 3800 thermo-mechanical simulator. The specimens are heated by the electrical current passing throughout the plate specimen and then quenched with a water spray. The temperature is controlled by means of a “type K” thermocouple, spot welded to the midsection of each specimen. A homogeneous heat treated zone with a minimum length of 10 mm was produced in this way. The homogeneity of the temperature was controlled by 3 thermocouples and after the heat treatment was proved by hardness measurements along the sample length.

VII-2.2 Microstructural characterization

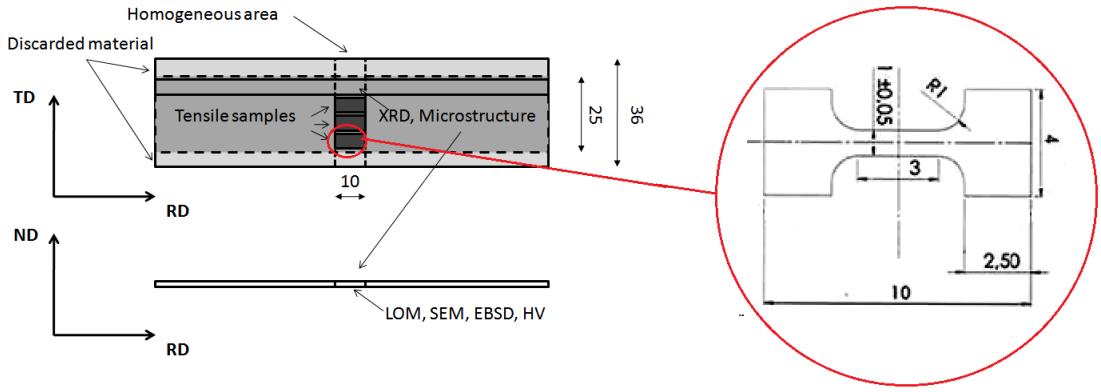

Fig. VII-2. Schematic representation of heat treated samples with the position and a drawing of the tensile sample.

Samples were cut from midsection of each heat treated specimen (as shown in Fig. VII-2) in order to characterize the microstructure and properties of the material in zone, which has undergone strictly controlled temperature-time cycle. For mechanical tests, 3 sub-size tensile samples were cut from each heat treated specimen parallel to the rolling direction (RD). The gage length and width of the tensile samples are 3x1 mm^2, respectively. The microstructure evolution was followed by Optical (OM) and Scanning Electron Microscopy (SEM). Samples were prepared according to the standard procedure, i.e., by grinding and polishing to 1 μm diamond paste, and the microstructure was revealed by etching with solution of 4%HNO_3 in ethanol (Nital4%) for ~10 s at room temperature. Electron backscatter diffraction (EBSD) analyses were performed on samples after grinding and polishing with final polishing step with 0.035μm colloidal silica for 40 min and polishing force of ~5N. The EBSD patterns were acquired on FEI Quanta™ 450-FEG-SEM (described in Chapter IV) with step size of 50nm.

The orientation data were analysed using the following grain definition: misorientation higher than 5°, minimum 4 points per grain and points with a confident index (CI) lower than 0.1 were not considered in data analysis as dubious.

X-ray diffraction analysis was carried out using a Siemens D5000diffractometer, equipped with Mo source(λ = 0.7107 Å).The angular range 2θ between26°and 40° was scanned with a step size 0.03°/step and time per step 20 s.

Vickers hardness (HV_3) was measured on each sample after thermal cycle and the hardness value was accepted as an average of minimum five measurements per sample.

VII-3 Results

VII-3.1 Microstructure

Fig. VII-3 displays SEM images of the two sets of specimens with different initial microstructures after cold rolling (Fig. VII-3a, d), cold rolling followed by heating at 400°C/s (Fig. VII-3b, e) and 1200°C/s (Fig. VII-3c, f) to 860°C and quenching. Typical cold rolled microstructures consisting of elongated grains of deformed ferrite and pearlite (Fig. VII-3a) or deformed ferrite and martensite (Fig. VII-3d) are observed. After the second stage of the annealing cycle (30 s isothermal holding at 300 °C), no significant changes in the morphology of the phases in F+P initial material were observed. However, in 50% cold rolled samples with mixed microstructure of ferrite and martensite the tempering of martensite takes place. This was noticed by the observation of the well-known structure of tempered martensite with cementite precipitates (Fig. VII-4a).

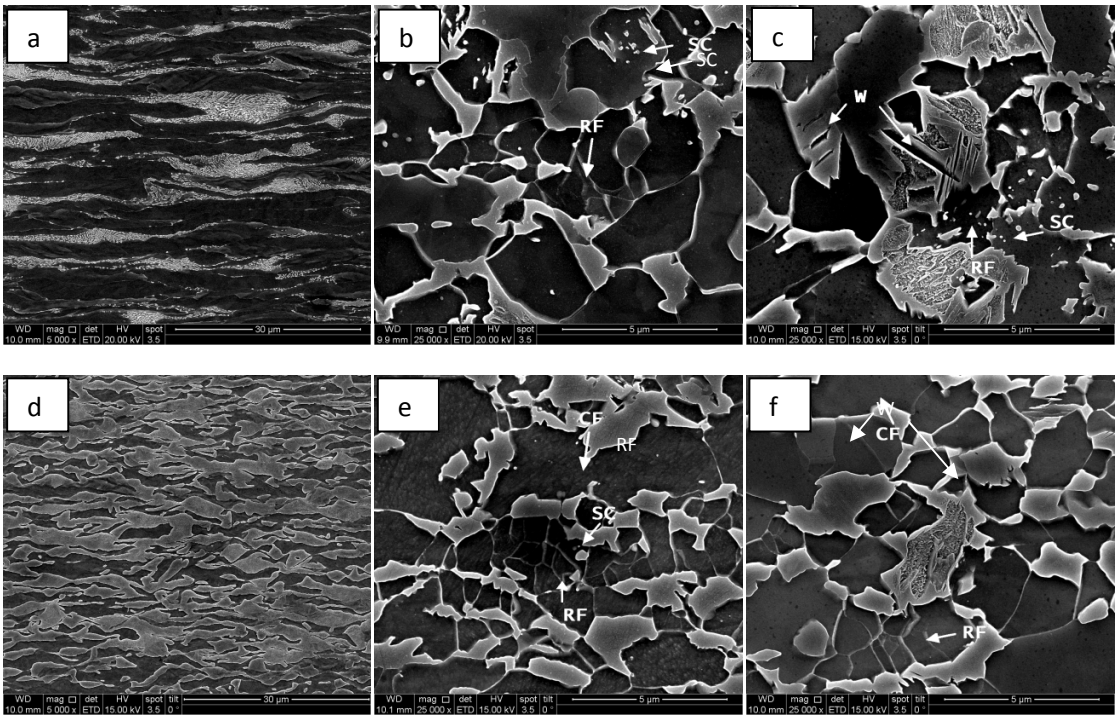

Fig. VII-3.SEM images of (a) 50% cold rolled F+P microstructure before heat treatment; (b), cold rolled F+P samples heated at 400 °C/s to 860°C and quenched; (c) cold rolled F+P sample heated at 1200 °C/s to 860°C and quenched; (d) samples 50% M microstructure after cold rolling, (e) after heating at 400 °C/s to 860°C and quenching and (f)after heating at1200 °C/s to 860°C and quenching. All samples are etched with 4% Nital. Scale bar in a, d is 10 µm, others 5 µm.

The microstructures after complete annealing treatments in all cases are mixtures of recovered ferrite (marked by arrows in Fig. VII-4) and/or recrystallized ferrite, newly formed martensite (light gray-white areas) and retained austenite. In all cases, different ferrite grain morphologies were observed. The ferrite phase in the microstructure is composed of large and small equiaxed ferrite grains. Different morphologies of Widmanstätten ferrite (W) were also observed, probably formed at the early stages of cooling. Fig. VII-4c - d shows ferrite plates of different types, according to Aaronson [19]. Notice that a mixture of upper and lower bainite (marked by arrows) is surrounding the ferrite plate in Fig. VII-4e.

As-quenched martensite is mainly distributed along bands in both F+P samples and at grain corners in 50% M samples. Large martensitic blocks normally lock inside one or several plates of Widmanstätten ferrite. Part of the retained austenite grains are located inside the martensite blocks, and the other part within large ferrite grains or in grain triple junctions as spherical particles. Spheroidized cementite (SC) was observed in areas of unrecrystallized ferrite and inside martensite blocks. In 50% cold rolled F+P material heated at 800 °C/s, partial decomposition of the pearlite structure into austenite (transformed into martensite on cooling) was observed (Fig. VII-4f).

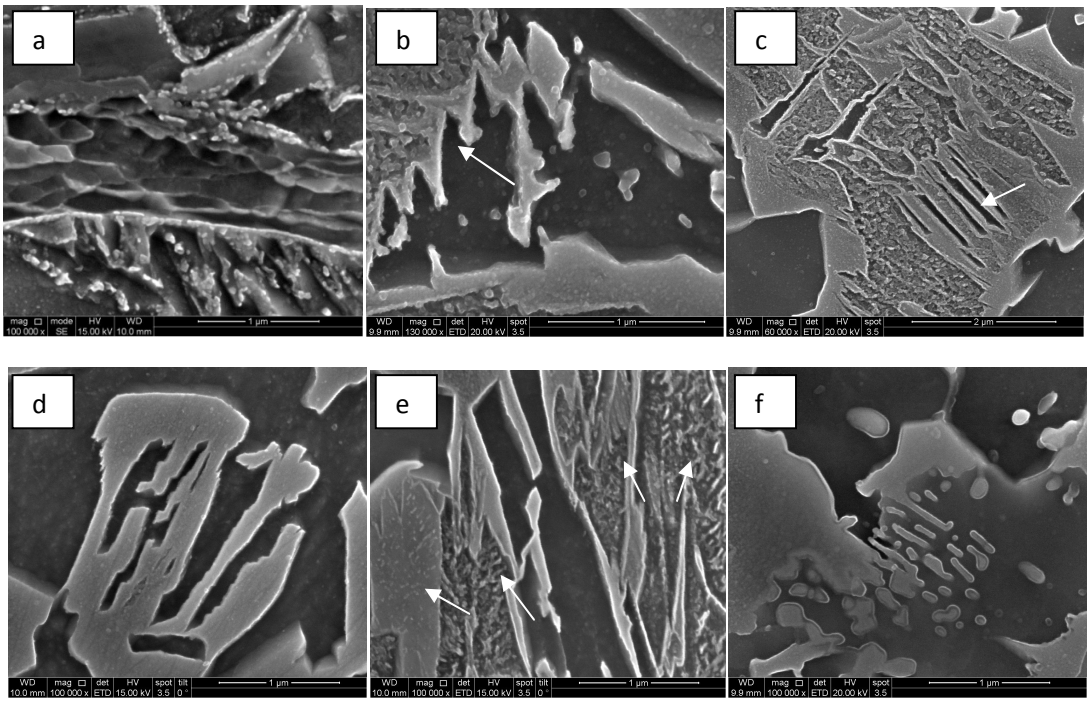

Fig. VII-4. (a) 50% cold rolled steel with ferrite-martensite microstructure, heated at 10 °C/s to 300 °C for 30s and quenched. Tempered martensite (upper and lower grains) and deformed ferrite (center);(b) and (c) are 50%cold rolled steel with F+P microstructure heated at 400 °C/s to 860°C and quenched. In (b), secondary 'sawteeth' and in (c) intragranular (lenticular) Widmanstätten ferrite plates are seen.(d) cold rolled 50% M microstructure, heated at 10°C/s to 860°C and quenched showing type B degenerated plates [19]. (e) 50% cold rolled steel with F+P microstructure heated at 1200 °C/s to 860 °C and quenched, degenerated Widmanstätten ferrite plate surrounded by upper and lower bainite (marked by arrows), (f) 50% cold rolled steel with F+P microstructure heated at 800 °C/s to 860 °C and quenched showing partially dissolved pearlite colony. Scale bar in c is 2 μm, others 1 μm.

For further analysis of the microstructure the transformation products of the austenite formed during heating will be referred to as “martensite”, even though it is very clear that their microstructure is much more complex, as it was shown above. The resulting average ferritic grain (AFG) size is shown in Fig. VII-5a (lower set of curves). There is a noticeable decrease of the AFG size as the heating rate is raised up to 400 °C/s. The decrease of the AFG size with increasing heating rate is better pronounced in the steel with initial F+P microstructure. At heating rates of 400 °C/s and higher, the AFG size tends to reach a plateau, and the grain refining effect is negligible. The grain refining effect in the samples with 50% M is weaker than in the F+P samples in the same range of heating rates. The martensite grain size was also influenced by the heating rate.

The fractions of martensite at different heating rates are shown in Fig. VII-5b. The phase fractions are influenced by the heating rate in all cases, and the samples with 50% M initial microstructure

display lower sensitivity of the martensite fraction to the heating rate in comparison to the F+P samples. Nonetheless, the shape of the two curves is similar, and they both show a risen the formed martensite fraction as the heating rate is increased up to 800 ^{o}C/s. At the heating rate of 1200°C/s martensite fractions drop down, because the fraction of the transformed austenite during heating decreases due to the shift of the Ac_3temperature towards higher values. A somewhat similar variation of the retained austenite (RA) fraction was measured. Cold rolled F+P initial microstructure displays similar dependence of RA fraction on the heating rate, with an increasing tendency up to 800 °C/s and then an abrupt decrease (Fig. VII-5d). Similar tendency is observed in the samples with 50% M initial microstructure with the maximum RA fraction at 400 °C/s (Fig. VII-5d).

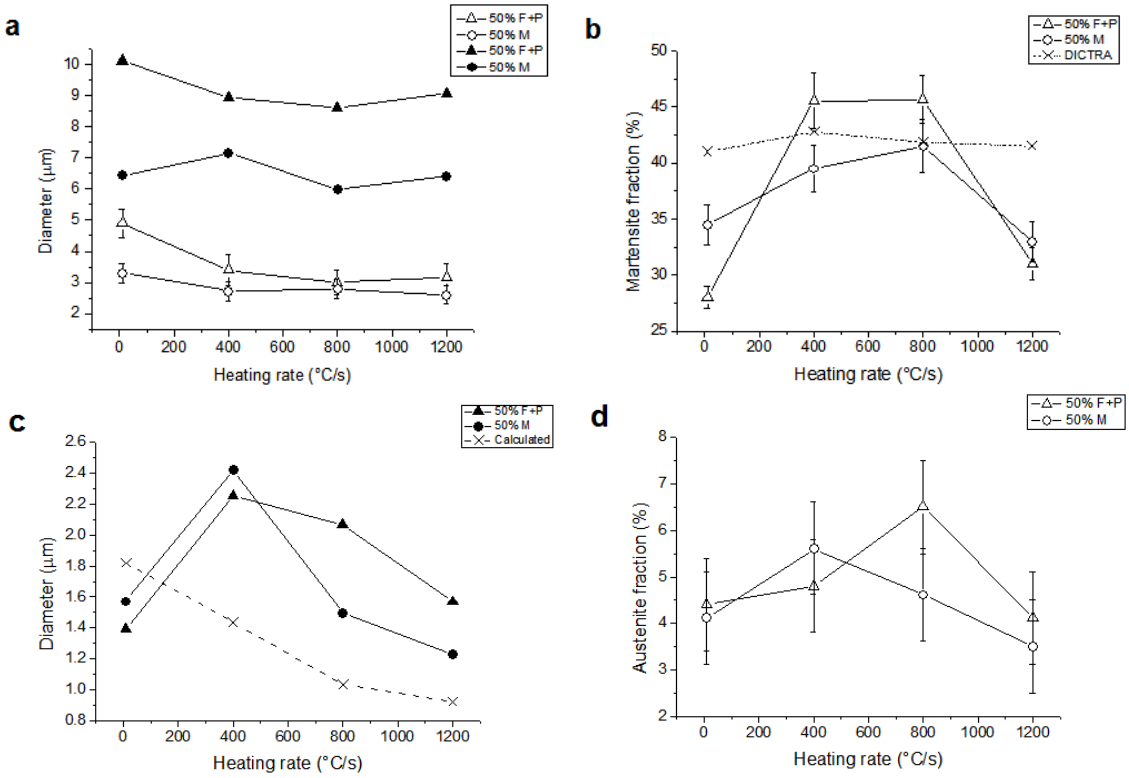

Fig. VII-5. (a) AFG size (lower set, outlined marks) and maximum ferritic grain size (upper set, filled marks), (b) Martensite phase fraction,(c) Maximum martensite grain size measured by EBSD and (d) retained austenite (RA) fraction versus heating rate. The annealing temperature and the holding time are 860 °C and 1.5 s, respectively.

VII-3.2 Texture

Fig. VII-6 shows the key for the main BCC texture components in φ_2 = 45° section of the Euler space. Fig.7 displays the calculated Orientation Distribution Functions (ODF) at ϕ_2 = 45° for ferrite in samples with both F+P and 50% M initial microstructures for heating rates of 10 °C/s and 1200 °C/s. The cold rolled samples with F+P initial microstructure (Fig. VII-7a,b,c) have noticeable

texture variations with increasing heating rate, whereas 50%M samples (Fig. VII-7d,e,f) show weak texture intensities after all thermal cycles. The initial textures after cold rolling (fig.7a, d) show alpha {uvw}⟨110⟩ and gamma {111}⟨uvw⟩ textures with pronounced maxima in the vicinity of the {111}⟨110⟩ components of ~6 mrd (multiples of random density). and weaker {112}⟨110⟩ with intensity of 2.7mrd for the F+P samples. The texture of 50%M samples is represented mainly by gamma {111}⟨uvw⟩ fibre with maximum of 2.7 mrd in the vicinity of the {111}⟨112⟩ texture component. Both textures are similar and typical for low carbon steels after cold rolling. After the first stage of annealing, (300°C for 30s) no significant variations in the texture morphology were observed, compared to the texture of the cold rolled steel. The minor variations in the texture intensities can be associated to the statistical variations of the data.

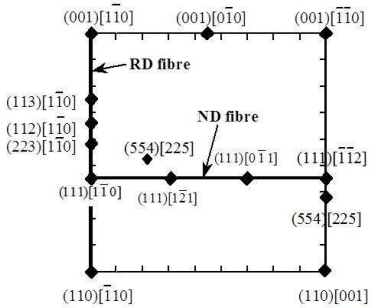

Fig. VII-6. Main BCC texture components shown in φ_2= 45°section of the Euler space.

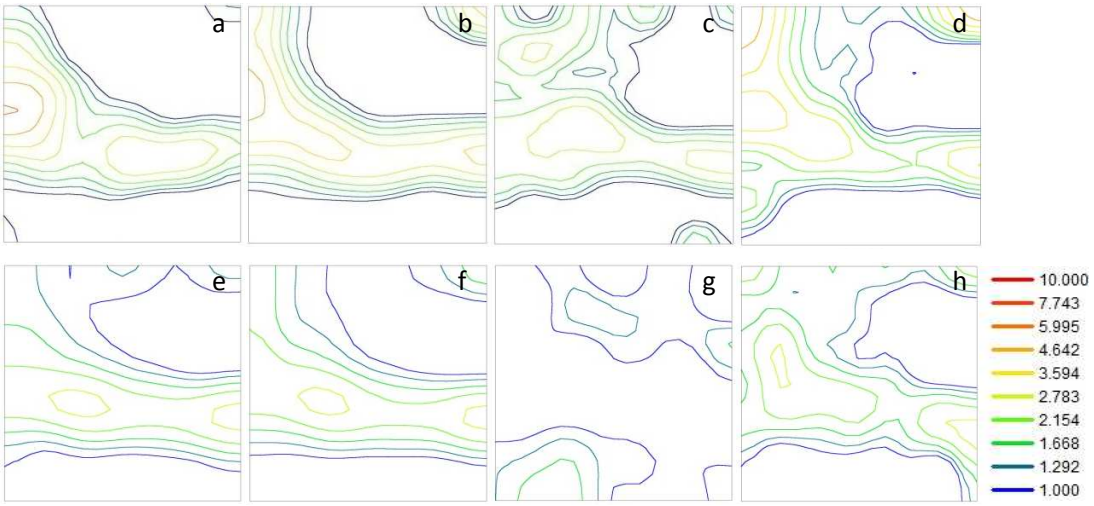

Fig. VII-7. ODFs at φ_2= 45° of ferrite in both samples after 50% cold rolling and heat treatment as follows: (a), (e)- initial texture after 50% cold rolling; (b) ,(f) -specimens held at 300 °C for 30 s then quenched, (c), (g)- heated at 10 °C/s to 300 °C and held for 30 s then heated at 10 °C/s to 860 °C held for 1.5 s and quenched and (d), (h)- specimens heated at 10 °C/s to 300 °C and held for 30 s then heated at 1200 °C/s to 860 °C for 1.5 s then quenched. (a), (b), (c) and (d) initial microstructure of ferrite and pearlite, (e), (f), (g) and (h) initial microstructure ferrite and 50% M.

The texture of the 50% F+P samples heated at 10°C/s shows components with maximum intensity on the gamma fibre {111}⟨uvw⟩ texture components of 2.7mrd. This specific curved shape of the gamma fibre texture is associated and used often as an indication for recrystallization texture in mild steels [20]. As the heating rate is increased to 1200°C/s, the texture is similar to the one after cold rolling with even similar intensities of the alpha{uvw}⟨110⟩ and gamma {111}⟨uvw⟩ fibres. Besides the change in the predominant components with the heating rate, the maximum intensity value also increases with increasing heating rate (Fig.7,d).

Very similar effect of the heating rate on texture is observed in the samples with 50% M initial microstructure. Besides that the alpha–gamma-alpha phase transformation took place after reheating at 1200°C/s to 860°C and quenching, the texture (Fig. VII-7, h) remains with similar morphology and intensity like after cold rolling or cold rolling and annealing at 300°C for 30s.

These observations are indication that after reheating with heating rates as high as 1200°C/s the recrystallization of the cold rolled structure is strongly suppressed.

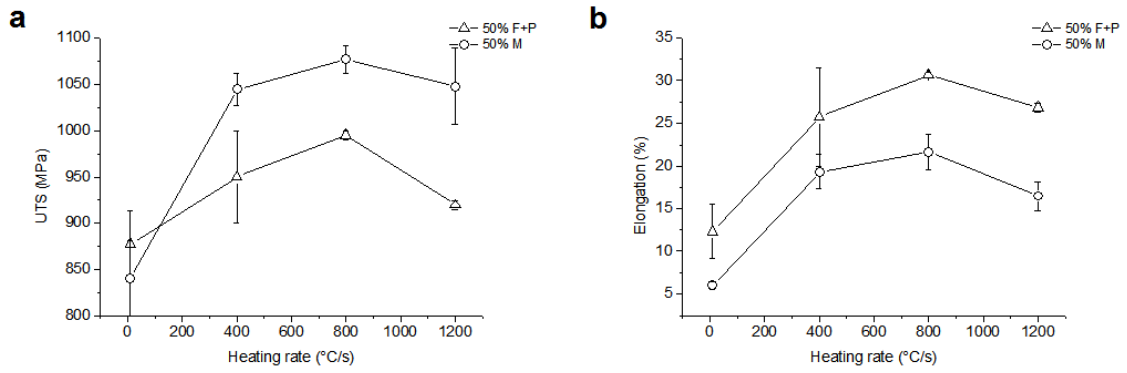

Fig. VII-8. (a) UTS values and (b) elongation to fracture versus heating rate. The annealing temperature and the holding time are 860 °C and 1.5 s, respectively.

VII-3.3 Tensile tests

The ultimate tensile strength (UTS) and elongation to fracture were determined in all heat treated specimens, and the data is shown in Fig. VII-8. In all materials, the UTS increases with increasing heating rate up to 800 °C/s, then it drops. As with the hardness measurements, the highest values of UTS were measured in 50% M samples. In this case, the sensitivity of the UTS to the heating rate is higher for the range between 10°C/s and 400 °C/s for 50% M samples, in comparison to the F+P samples. The 50% M samples show an increment of ~200 MPa from 10 to 800°C/s heating rate. The final elongation also shows a marked increment between 10 °C/s and 400 °C/s, similar to the UTS values. Above 400 °C/s, the elongation to fracture is in the range between ~25% and ~30% for 50% F+P, and between ~16% and ~22% for 50% M material. VII-50% F + P material shows higher ductility than 50% M for all heating rates.

VII-4 Discussion

VII-4.1 Ferrite recrystallization and growth

In order to distinguish ferrite from martensite, average EBSD image quality (IQ) maps were used to assess both phases. Recrystallized ferrite normally produces high IQ patterns, whereas martensite produces lower quality patterns. Fig. VII-9c shows the histogram obtained from the plot of average IQ versus the area fraction of the grains. The phase identification was thus straightforward, since the microstructure after has a bimodal distribution. The data was subsequently divided in high average IQ data (red bars), which corresponds to ferrite, and low average IQ data (green bars) corresponding to martensite. Calculations of the average grain size and texture were, therefore, carried out in each phase separately.

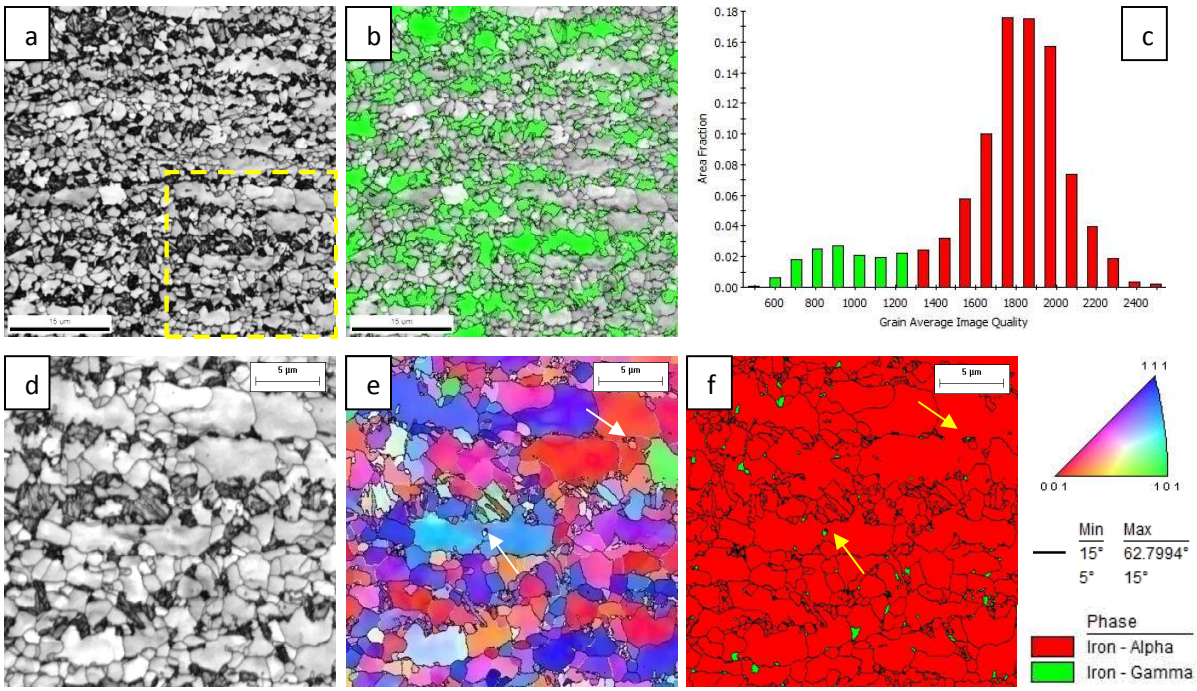

Fig. VII-9. EBSD scan of 50% F+P material heated at 400 °C/s. (a) IQ map, (b) IQ map with low average IQ grains (martensite) highlighted, (c) plot of the average IQ versus area fraction of grains, (d) selected area of the IQ map in (a), (e) inverse pole figure (IPF) and (f) phase map of the selected area. Step size 50 nm. Scale bar in a, b is 15 µm, others 5 µm.

A relatively uniform distribution of equiaxed grains of ferrite was observed in material heated at 10 °C/s. However, as the heating rate is increased, large isolated elongated grains seem to stand out from the matrix. The formation of such large grains influences the histograms of grain size distribution shown in Fig. VII-10. Blue curves represent material heated at 10 °C/s, whilst red curves represent material heated at 1200 °C/s. It can be readily noticed that the increase in the heating rate shifts average grain size towards lower values. Nevertheless, the most remarkable

feature in red curves is the change in the shape of the histogram. At first glance, blue curves have 2 peaks, one small at around 2,5 µm and another at higher grain size. Red curves show that, after UFH at 1200 °C/s, the first peak grows in intensity with respect to the second peak. This means that the fraction of finer grains has increased, whereas the second peak is still noticeable in all red curves. The grains that recrystallized first during heating and had more time to grow are larger and represented by part of the curve that contains the second peak. EBSD data clearly shows that these first recrystallized grains have grown by the mechanism of coalescence [20,21].

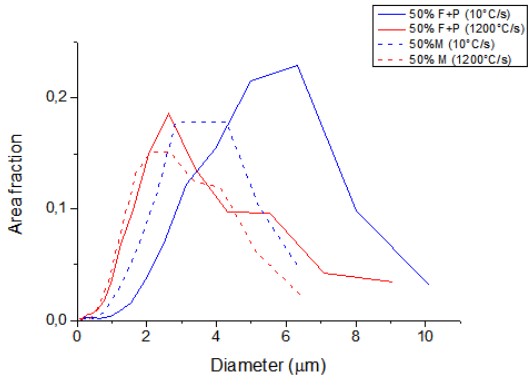

Fig. VII-10. Plot of grain diameter versus area fraction of grains. Data obtained from EBSD measurements. Solid and dashed lines represent 50% F+P and 50% M, respectively.

Evidence of the coalescence of ferrite grains is shown in Fig. VII-9e. The misorientation angles (MA) between 15 and 63° are marked by black lines, whereas the MA between 5 and 15° are outlined in white. Arrows in the Inverse Pole Figure (IPF) map show grains with similar orientation, although some small variations within the grains are noticeable. Such variations are in all cases lower than 5°. The large elongated grains have grown by the coalescence of smaller grains. The grains that seem to fast coalesce into large aggregates have, in most cases, MA below 15°. Grain boundaries with MA greater than 15° (HAGBs) seems not to be preferred to coalesce into large ones. Thus, the growth of fast coalesced grains will produce grain morphologies of irregular shape which, in most cases, is different from morphology of the equiaxed ferritic grain. Nonetheless, such morphologies can be easily rationalized assuming the coalescence mechanism. Similar, coalesced grain structure can be observed in all micrographs of fast annealed experiments in Fig. VII-3 (CF), although not as evident as in EBSD maps. In some cases, large single coalesced ferrite grains contain RA or martensite grains inside, as marked by yellow arrows in Fig. VII-9f. It is believed that, during heating, small pearlite colonies are trapped as result of the coalescence of ferrite grains. After the temperature of transformation is reached, austenite is formed and it is retained or transformed to martensite during further quenching.

Although the amount of cold deformation apparently influences the maximum size of recrystallized ferrite grains (Fig. VII-5a), once it reaches a saturation heating rate (around 400 °C/s), it does not seem to be strongly affected by the heating rate. Considering that the largest grains are probably the first ones to recrystallize, it is possible to state that heating rate has either a narrow effect on the kinetics of recrystallization or that larger grains grow noticeably fast

(irrespective of heating rate) until they impinge some sort of barrier that hinders further advance of the interface. It is well known that heating rate has actually an influence on the recrystallization starting temperature (T_R) [8,16,22,23] and on the recrystallization kinetics [8,23,24]. In spite of that, the current experiments are not conclusive regarding such parameters of ferrite recrystallization. It is believed that the size of the largest recrystallized grains is influenced primarily by the phase distribution in the initial microstructure. Moreover, it has been acknowledged that fine particles can act as barriers for the migration of grain boundaries [20,25]. Such interaction can take place during the tempering of martensite, and might as well explain the flat size profile measured in 50% M initial microstructure samples (Fig. VII-5a).

A modification of the recrystallization response of the material is certainly triggered by UFH. This statement becomes even more evident after establishing that the size of larger ferritic grains are slightly affected by the heating rate, particularly in 50% M initial microstructure. Previous experiments on the same steel with 50% F+P microstructure have revealed a decrease in the recrystallized fraction with increasing heating rate [11]. The most significant contribution to the grain refinement, therefore, lies in the grains that have 'recovered' structure and the grains that have recrystallized later, at higher temperatures. Areas of recovered structure were observed in all samples treated above 10°C/s. These areas are characterized by groups of small grains (having size less than 1 µm), as indicated by white arrows in Fig. VII-4. It is believed that such areas correspond to recovered ferrite for two reasons that stem on EBSD data. Firstly, because of the presence of low angle grain boundaries; and secondly, EBSD data of these zones have revealed IQ values comparable with those of recrystallized grains. Recovered grains should not be misled with large coalesced grains, (marked by arrows in Fig. VII-9e).

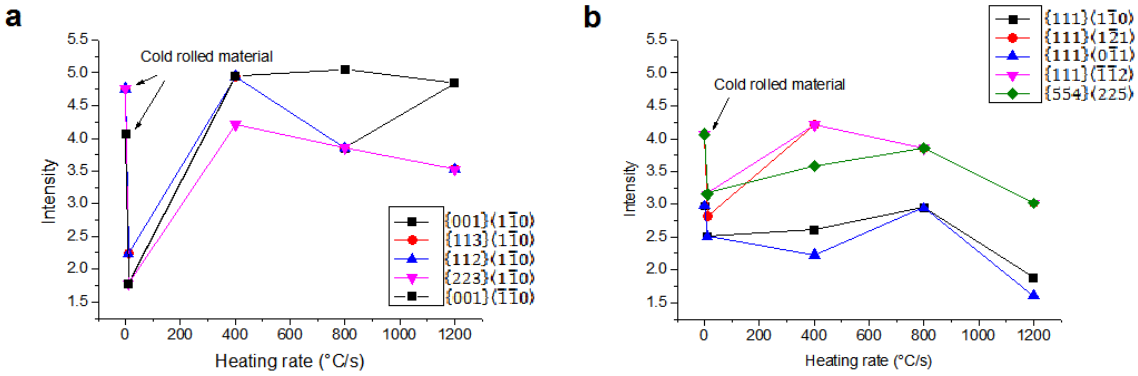

Fig. VII-11. Intensities of selected orientation components of 50% F+P initial microstructure in RD fibre (a) and ND fibre (b) versus heating rate.

VII-4.2 Texture after UFH

The texture intensity in 50% M samples is very weak, as it was also reported in early works [6,10–12]. However, a slight increase in the maximum intensity of components of ND-fibre was measured as the heating rate is raised. The most noticeable features were, however, measured in

samples with 50% F+P initial microstructure. Texture components are in fair agreement with previous results on TRIP composition steels [6,9–11]. The orientations observed after the second stage of the annealing cycle (30 s at 300 °C, Fig. VII-5b and f) suggest that recrystallization have not been activated yet. Only recovery has taken place at that stage. Although it has been established that the heating rate does not affect significantly the recrystallization textures in low carbon and IF steel below A_3 [16,17,26], it seems that this might not be true for TRIP composition steel. Fig. VII-11a shows the evolution of some components of alpha and gamma fibre in 50% F+P initial material. At lower heating rates, ND fibre components have slightly higher intensities than the components of alpha fibre. As the heating rate is increased, alpha fibre components are growing in intensity whilst ND fibre grains display a relatively constant intensity. At 1200 °C/s, ND fibre components have decreased intensities. It is well accepted that alpha fibre store less deformation energy than gamma fibre components [27–29], thus having less driving force for recrystallization. At lower heating rates, such low stored energy grains are consumed by recrystallized ND fibre grains which may have growth advantage (first nucleate –first grow). However, high heating rates could trigger the conditions for these RD fibre grains to reach the onset or recrystallization [22,23]. It is also reasonable to expect that a fraction of low stored energy grains will only activate the recovery, which contributes to the raise in the intensity of RD fibre components. Examples of recrystallized and recovered RD fibre grains can be observed in Fig. VII-9e (red grains). In consequence, recrystallization and growth of RD fibre grains might occur at higher temperatures, compared with most favourable ND fibre grains, and hence increasing the intensity of RD fibre components.

Notice that the change in the ferrite grain size distribution (Fig. VII-10) can serve as an indirect evidence of the change in the recrystallization behaviour described in the former section. At lower heating rates, the early recrystallized ND fibre grains (second peak from left to right) will grow at the expense of RD grains and therefore produce larger AFG. As the heating rate increases, the fraction of smaller grains (first peak) becomes much more significant, since the RD fibre grains with low stored energy are either able to reach the onset or recrystallization and thus nucleate new ferrite grains or rearranged into recovered low misorientation angle sub grain structure.

Widmanstätten ferrite grains also contribute to the overall ferrite texture. Nevertheless, the fraction is too small to have a significant contribution to the texture. The predominant orientation component in RA in all cases was the brass component $(110)[1\bar{1}2]$. A faint copper component $(112)[11\bar{1}]$ was measured with a maximum of around 1/6 of the intensity of the brass component. Both match the typical orientations of deformed austenite [30]. At the intercritical region, the transformation of austenite can only take place at the ferrite/cementite interface. Therefore, the orientation of ferrite-cementite aggregates that are retained to intercritical temperatures will determine the orientation of RA.

VII-4.3 Austenite transformation

According to equilibrium calculations, the relative volume fraction of austenite at 860 °C is 60%. The measured phase fractions are thus close to the equilibrium value, in spite of the short annealing time. UFH experiments have produced curves of austenite formation with a maximum of austenite fraction at intermediate heating rates, as shown in Fig. VII-5b. Similar shape in martensite fraction versus heating rate has been measured at 825 °C [11].

In order to evaluate the contribution of the heating rate to the kinetics of austenite formation, calculations with the Dictra software were performed. The software solves the one-dimensional moving boundary problem by calculation of local equilibrium conditions in each time step. It was assumed an initial volume of radius equal to 2.5 μm (in accordance with the maximum martensite grain size measured by EBSD, Fig.5c). Only the heating and the holding stages at the intercritical range (stages 2 and 3, respectively) were simulated. The dissolution of cementite was assumed to be complete at 724 °C. The initial fraction of austenite was calculated with ThermoCalc (database TCFE6). The value was then corrected assuming that carbon does not contribute to the volume change in the system. Corrected volume fractions correspond to a value close to the initial pearlite fraction in 50% F+P microstructure. The quenching stage was not considered in the calculations. The results are shown in Fig. VII-5b (semi dotted-dashed line).

The calculated variation of the austenite fraction was virtually unaffected by the heating rate. The simulated curve seems to fit slightly better the 50% M initial microstructure, probably because the assumption of fully dissolved cementite is more appropriately approached by a finer cementite distribution product of the tempering of martensite. The deviations observed at low and high heating rates are therefore likely to be related with the variables that were not taken into account in the simulations, such as nucleation rate, cementite coarsening and transformation of ferrite during cooling, as demonstrated in Fig. VII-3 and Fig. VII-4. The largest austenite grains are probably the ones that nucleated first, and thus had the longest time for growth. Consequently, if the kinetics of transformation is calculated after the overall reaction time, the results should fit better the maximum grain size, instead the average value, for instance. Such approach has been previously applied to the calculation of the plate growth kinetics of Widmanstätten ferrite and bainite in carbon steel [31]. The maximum martensite packet size is normally of a length comparable to the diameter of the parent austenite grain. It seems, thus, reasonable to relate the intercritical austenite growth kinetics to the largest martensitic grain, as shown in Fig. VII-5c. In the range from 400 to 1200 °C/s, a decreasing tendency is observed. This might be caused mainly by the delayed austenite nucleation, or the so-called 'shifting' of the intercritical curves triggered by the heating rates. Previous experiments [32] have shown that, when the transformation starts from initial martensitic structure, the effect is less pronounced. One could estimate the effect of the heating rate in the carbon gradient in austenite for anisothermal (peak annealing) experiments in the intercritical ($\alpha+\gamma$) region with known parameters. The following analysis is only valid for austenite on heating. For simplicity, the sharp interface model is accepted and capillarity effects and volume changes associated to transformation shall be excluded. Let us define the final carbon gradient in austenite as

$$\frac{\Delta X}{\Delta y} = \frac{X_C^{\theta/\gamma} - X_C^{\gamma/\alpha}}{\Delta L} \quad (1)$$

where $\Delta X/\Delta y$ is the carbon gradient for the isothermal formation of austenite at some temperature within the intercritical (α+γ) region, $X_C^{\theta/\gamma}$ is the carbon content (mole fraction) of austenite in equilibrium with cementite, $X_C^{\gamma/\alpha}$ is the carbon content (mole fraction) of austenite in equilibrium with ferrite and ΔL is the width of the austenite grain. The radius of the austenite grain will be defined by some average velocity $\bar{v}$ of the interface during the time interval Δt

$$\bar{v} = \frac{\Delta L}{\Delta t} \quad (2)$$

The velocity of the austenite-ferrite interface shall be determined by the mobility of the austenite-ferrite interface and the chemical driving force for the growth stage, as defined elsewhere [33]. Solving for ΔL

$$\Delta L = \Delta t \cdot \bar{v} \quad (3)$$

and replacing in (1)

$$\frac{\Delta X}{\Delta y} = \frac{X_C^{\theta/\gamma} - X_C^{\gamma/\alpha}}{\Delta t \cdot \bar{v}} \quad (4)$$

in the case of anisothermal transformation under constant heating rate, the following definition can be made

$$\beta = \frac{\Delta T}{\Delta t} \quad (5)$$

where β is the constant heating rate and ΔT is the temperature range of the onset to the stop austenite formation. For the case of the present experiments,

$$\Delta T = T_P - A_{C1} \quad (6)$$

being T_P the peak temperature (860 °C) and A_{C1} the onset of austenite formation. Eq. (4) can thus be expressed as

$$\frac{\Delta X}{\Delta y} = \frac{\beta\left(X_C^{\theta/\gamma} - X_C^{\gamma/\alpha}\right)}{(T_P - A_{C1}) \cdot \bar{v}} \quad (7)$$

It´s interesting to note that, assuming $\bar{v}$ as constant in the entire temperature range defined in Eq. (6), Eq. (7) predicts a value of ΔL depending on the factor $(T_P - A_{C1})/\beta$. A_{C1} is known to increase with β [18,32], thus, a steeper effect can be predicted. A simple linear relation between the equilibrium temperature A_1 and A_{C1} could predict the variation shown by the dashed line in Fig 5c, which is decreasing over the UFH region, in agreement with the measured variation of maximum

martensitic grain size with heating rate for both initial microstructures. The calculated diameters in Fig 5c (dashed line) were computed with the maximum interface velocity obtained with DICTRA (Fig. VII-12a). The value of $\bar{v}$ might as well be estimated numerically from Fig. VII-12a, assuming that

$$\bar{v} = \frac{1}{(t_f - t_i)} \int_{t_i}^{t_f} v \cdot dt \qquad 8$$

where t_i and t_f represent the onset and the finishing of the austenite formation and v is the instantaneous velocity of the γ–α interface. The calculated carbon gradient is shown in Fig 12b.

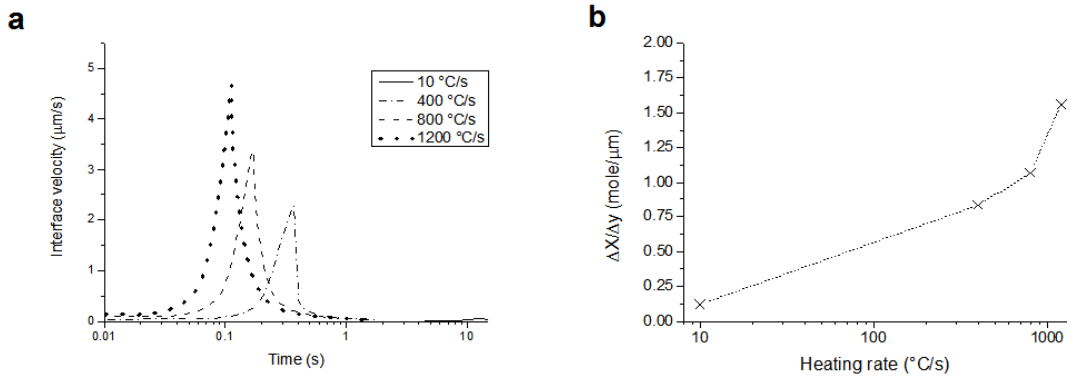

Fig. VII-12. (a) DICTRA simulations if the velocities of the γ–α interface versus temperature at different heating rates and (b) carbon gradient versus heating rate, as calculated from Eq. (7) and Eq. (8) assuming $A_{C1} = A_1 + p\beta$, with $p = 0.01s$. The other parameters used where $X_C^{\theta/\gamma} - X_C^{\gamma/\alpha} = 0.038$, $T_P = 860\,°C$ and $A_1 = 730\,°C$. All thermodynamic parameters where calculated using ThermoCalc software, database TCFE6.

The modification in the cementite structure is also playing a role in the lower maximum diameter values and phase fractions of martensite at 10 °C/s. In F+P initial material, it was found that the cementite lamellas were almost fully spheroidized after 10 °C/s. It has been stated [34,35] that the nucleation of austenite in spheroidized microstructures takes place at the sites where the cementite is in contact with grain boundaries between two adjacent ferrite grains. Thus, not all the cementite/ferrite boundaries will serve as an active nucleation site for austenite. It is reasonable to expect that recrystallized and spheroidized structure, as in samples of both initial materials heated at 10 °C/s to 860 °C, will have less potential nucleation sites for austenite than partially deformed F+P microstructure in specimens treated at higher heating rates. The reduced number of active nucleation sites will substantially reduce the diameter and fraction of transformed austenite. For this reason, is Eq. VII-7 is unable to predict the actual variation of austenite diameter in the range of conventional heating rates (below 10 °C/s). At higher heating rates (above 400 °C/s, Fig. VII-4f), the pearlitic structure was virtually not modified before reaching the intercritical range, hence the available pearlite/pearlite and pearlite/ferrite boundaries for austenite nucleation was kept constant and, thus, the main factor affecting the diameter and austenite phase fraction is the heating rate, as previously described. In 50% M initial

microstructure samples, the Ostwald ripening of tempered carbides at lower heating rates may be producing an effect similar to spheroidized cementite in 50% F+P initial microstructure. At heating rates above 400 °C/s, the heating rate plays the most important role.

Eq. (7) describes the influence of heating rate on the gradient of carbon produced in austenite after peak annealing. It is clear that for heating rates infinitely low, carbon gradients should be inexistent due to the factor β. The carbon gradient is expected to grow for high heating rates until, $(T_P - A_{C1}) = 0$, which determines the maximum carbon gradient. Above this limit, the transformation has not taken place. Hence, carbon gradient can be reasonably expected in peak annealing experiments after certain intermediate heating rate, as shown by Fig. VII-12b, and it should become steeper as the heating rate is increased.

Cementite dissolution was incomplete after all thermal cycles. This is also indirectly confirmed by the calculated carbon content in austenite by XRD. In all cases, a consistent value of ~1.1 %C was estimated [36]. According to calculations with Thermo-Calc, the carbon content of austenite in equilibrium with cementite at 860 °C is 1.19 %C.

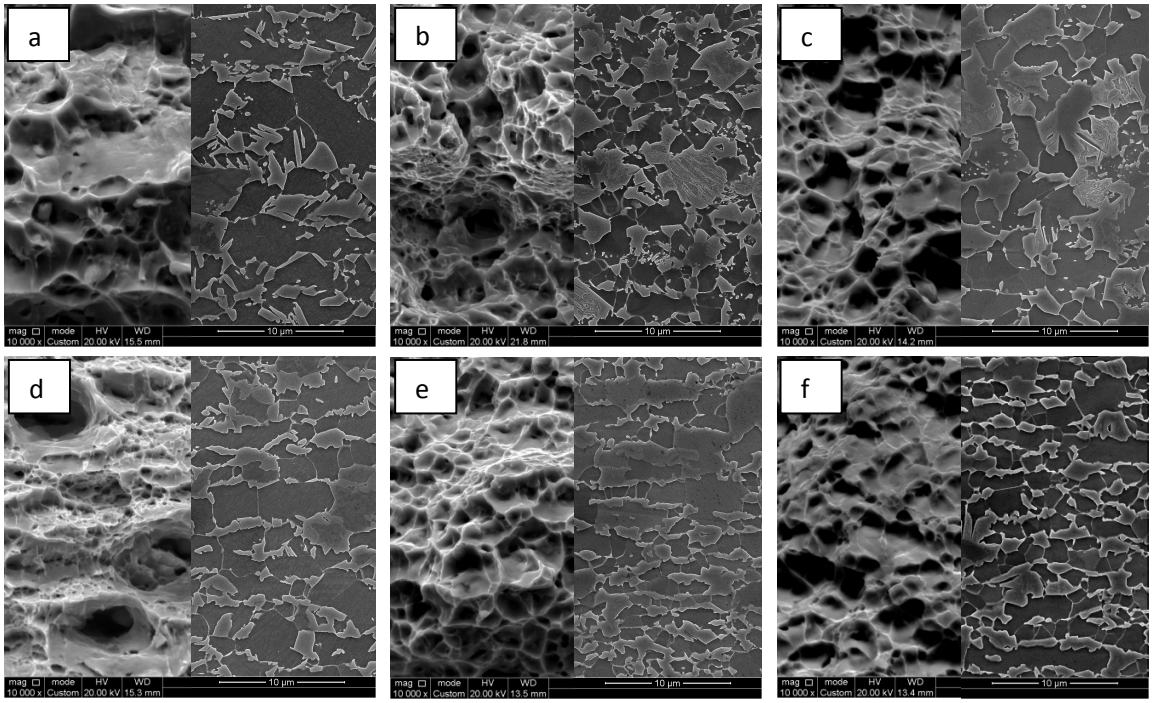

Fig. VII-13. Fracture surface of the material after tensile test. (a), (b), (c) correspond to 50% F+P and (d), (e), (f) correspond to 50% M initial microstructure, respectively. (a) and (d), (b) and (e), and (c) and (f) correspond to samples heated at 10 °C/s, 800 °C/s and 1200 °C/s, respectively. In each image, the right hand side half corresponds to the microstructure before tensile test. Scale bar is 10 μm.

VII-4.4 Mechanical properties

Results of tensile test show that the UTS of the material after UFH cycles is primarily influenced by the phase fraction of ferrite and then by the ferritic grain size. The general shape of the variation of the UTS with the heating rate (Fig. VII-8a) is largely similar to the martensite fraction (Fig. VII-5b). The highest UTS values were recorded for 50% M initial microstructure, which shows the finest average ferritic grain size. VII-50% F+P microstructure has in most of the points approximately 50 MPa lower strength than 50% M microstructure. Such values are also consistent with the hardness measurements. In 50% M samples, a relatively flat AFG and martensite fraction variation with the heating rate may satisfactorily explain the variations in UTS. VII-50% F+P samples have more significant variations in AFG size and the martensite fraction, and the strength is lower at most of the heating rates.

The variations of the elongation at fracture with the heating rate display a tendency similar to the variations in UTS values. However, 50% F+P material shows higher ductility than 50% M, consistent with the higher UTS values of 50% M samples shown in Fig. VII-8a. Analysis of fracture surfaces has shown that the ductility of martensite is playing an important role in the overall deformation behaviour of the tensile specimens. Each picture in Fig. VII-13 illustrates, on the left hand side, the fracture surface of tensile specimens and, on the right hand side, the microstructure corresponding to 50% F+P (13a, 13b and 13c) and 50% M (13d, 13e and 13f) after different thermal cycles. Figs 13a and 13d, which correspond respectively to 50% F+P and 50% M treated at 10 °C/s, clearly show areas that accumulates large and small amount of plastic deformation during the fracture process. By comparison between left and right hand sides on the aforementioned images, one can conclude that the areas that are heavily deformed correspond to ferrite and the rest are martensite. Figs. VII-13b, 13c, 13e and 13f, which correspond to heating rates of 800 °C/s (Figs. VII-13b and 13e) and 1200 °C/s (13c and 13f), are showing a more homogeneous distribution of strain in the microstructure. By analogy, this indicates that the martensite (or the martensite-bainite aggregates) are withstanding higher strain levels, compared to martensite aggregates in material of both initial conditions heated at 10 °C/s. In contrast, the fraction of ferrite is lower at heating rates above 10 °C/s, as indirectly displayed in Fig. VII-5c. Therefore, the amount of strain that the other constituents (martensite, bainite, retained austenite) undergo becomes more significant during necking and fracture.

It is reasonable to state that heterogeneous nature of the microstructure after UFH has a noticeable impact on the mechanical properties. This has been shown in other systems as well [37,38]. The specific deformation behaviour of the martensite-bainite aggregates is consequence of the composition and morphology of the austenite. As shown in Fig. VII-12b, carbon gradients can be reasonably expected in UFH experiments. It is, thus, also reasonable to conclude that the heating rate has a noticeable effect on the strength and ductility. Additional microstructural constituent like retained austenite (and a subsequent TRIP effect) could also play a role in the variation of the strength and ductility [39–41]. Furthermore, the unique microstructural features resulting from UFH, such as the described carbon gradients in austenite and partial restoration processes [3,28,29], significantly affect the mechanical properties of the material.

VII-5. Conclusions

Heating experiments in a wide temperature range (10 - 1200 ^{o}C/s) have been carried out on an Fe-0.2C-1.6Mn-1.06Al steel with two different initial microstructures and the results are summarised as follows:

The kinetics of ferrite to austenite transformation in the intercritical range is strongly influenced by the heating rate. It was shown that, in anisothermal (peak annealing) experiments, carbon gradients in austenite are to be expected above certain heating rate and will become steeper as the heating is increased up to a defined limit. Carbon gradients are playing a major role in the mechanical properties of the studied steels.

Thermal cycles under different heating rates produced a bimodal distribution of the ferritic grain size. The appearance of the bimodal grain size distribution depends on the initial microstructure and the recovery and recrystallization processes during ultra-fast heating.

It was confirmed that UFH significantly contributes to the grain refinement when heating rates above 10 °C/s are applied. The effect of UFH in the decrease of ferritic grain size is more pronounced in ferrite and pearlite initial microstructure.

Increasing heating rate strongly affects the relative intensities of texture components, favouring those of the cold deformed structure (RD fibre) over the recrystallization components (ND fibre). This is an indication that after reheating with heating rates as high as 1200°C/s the recrystallization of the cold rolled structure is suppressed.

The subsequent increase in the heating rate has produced an improvement in both strength and ductility at heating rates up to 800 °C/s ; when heating rates are 1200 ^{o}C/s, the UTS and elongation at fracture decrease. Such behaviour is primarily associated with the carbon gradients in austenite formed during UFH experiments, which defines the features of martensite-bainite aggregates and its fraction in the microstructure.

The initial microstructure strongly influences the properties after UFH. After all thermal cycles, the steels with microstructure ferrite and pearlite displayed higher ductility and lower strength than steels with 50% ferrite - 50% martensite initial microstructure.

It was found that, besides the tempering of martensite in the 50% M samples, the slow heating at 10 ^{o}C/s and holding at 300 °C for 30 s does not modify the overall texture nor the cementite morphology in F+P initial microstructure. This finding is important from a view point of potential industrial application of the UFH because it gives more degree of freedom in the design of the heating devices.

VII-6. References

[1] R. Kuziak, R. Kawalla, S. Waengler, Advanced high strength steels for automotive industry, Arch. Civ. Mech. Eng. VII-8 (2014) 511. doi:10.1016/S1644-9665(12)60197-6.

[2] E. De Moor, P.J. Gibbs, J.G. Speer, D.K. Matlock, A.S. Processing, Strategies for Third-Generation Advanced High-Strength Steel Development, AIST Trans. VII-7 (2015) 2010.

[3] Q. Meng, J. Li, H. Zheng, High-efficiency fast-heating annealing of a cold-rolled dual-phase steel, Mater. Des. VII-58 (2014) 194–197. doi:10.1016/j.matdes.2014.01.055.

[4] D. De Knijf, A. Puype, C. Föjer, R. Petrov, The influence of ultra-fast annealing prior to quenching and partitioning on the microstructure and mechanical properties, Mater. Sci. Eng. A. VII-627 (2015) 182–190. doi:10.1016/j.msea.2014.12.118.

[5] V. Massardier, A. Ngansop, D. Fabregue, S. Cazottes, J. Merlin, Ultra-Rapid Intercritical Annealing to Improve Deep Drawability of Low-Carbon, Al-Killed Steels, Metall. Mater. Trans. A. VII-43 (2012) 2225–2236. doi:10.1007/s11661-012-1096-6.

[6] R.H. Petrov, A. Puype, D. De Knijf, L. Kestens, Ultrafast heating of advanced high strength steels, in: M. Militzer, G. Botton, L.-Q. Chen, J. Howe, C. Sinclair, H. Zurob (Eds.), Proc. Int. Conf. Solid-Solid Phase Transform. Inorg. Mater. VII-2015, 2015: pp. VII-1157–1158.

[7] T. Lolla, G. Cola, B. Narayanan, B. Alexandrov, S.S. Babu, Development of rapid heating and cooling (flash processing) process to produce advanced high strength steel microstructures, Mater. Sci. Technol. VII-27 (2011) 863–875. doi:10.1179/174328409x433813.

[8] D. Muljono, M. Ferry, D.P. Dunne, Influence of heating rate on anisothermal recrystallization in low and ultra-low carbon steels, Mater. Sci. Eng. A. VII-303 (2001) 90–99. doi:10.1016/S0921-5093(00)01882-7.

[9] R. Petrov, J. Sidor, W.J. Kaluba, L. Kestens, Grain Refinement of a Cold Rolled TRIP Assisted Steel after Ultra Short Annealing, Mater. Sci. Forum. VII-715-716 (2012) 661–666. doi:10.4028/www.scientific.net/MSF.715-716.661.

[10] F. Ramos, Ultra Fast Annealing of High-Strength Low-Alloy Steels (HSLAS), Ghent University, 2012.

[11] A. Puype, Developing of advanced high strength steel via ultrafast annealing, Ghent University, 2013. doi:10.1017/CBO9781107415324.004.

[12] R. Petrov, L. Kestens, W.J. Kaluba, Y. Houbaert, Recrystallization and austenite formation in a cold rolled TRIP steel during ultra fast heating, Steel Grips. VII-1 (2003) 289–293.

[13] P. Gobernado, R.H. Petrov, L.A.I. Kestens, Recrystallized {3 1 1}〈1 3 6〉 orientation in ferrite steels, Scr. Mater. VII-66 (2012) 623–626. doi:10.1016/j.scriptamat.2012.01.056.

[14] R.H. Petrov, J. Sidor, L.A.I. Kestens, Texture Formation in High Strength Low Alloy Steel Reheated with Ultrafast Heating Rates, Mater. Sci. Forum. VII-702-703 (2012) 798–801.

[15] V.T. G. Griffay, M. Anderhuber, P. Klinkenberg, New continuous annealing technology with high-speed induction heating followed by ultra-fast cooling, 2002.

[16] L. Kestens, A.C.C. Reis, W.J. Kaluba, Y. Houbaert, Grain Refinement and Texture Change in Interstitial Free Steels after Severe Rolling and Ultra-Short Annealing, Mater. Sci. Forum. VII-467-470 (2004) 287–292. doi:10.4028/www.scientific.net/MSF.467-470.287.

[17] T. Senuma, K. Kawasaki, Y. Takemoto, Recrystallization Behavior and Texture Formation of Rapidly Annealed Cold-Rolled Extralow Carbon Steel Sheets, Mater. Trans. VII-47 (2006) 1769–1775. doi:10.2320/matertrans.47.1769.

[18] Y.Y. Meshkov, E.V. Pereloma, Phase Transformations in Steels, Elsevier, 2012. doi:10.1533/9780857096104.4.581.

[19] H.I. Aaronson, The proeutectoid ferrite and the proeutectoid cementite reactions, in: V.F. Zackay, H.I. Aaronson (Eds.), Decompos. Austenite by Diffus. Process., Metallurgical society of AIME, 1962.

[20] M. Hillert, ON THE THEORY OF NORMAL AND ABNORMAL GRAIN GROWTH, Acta Metall. VII-13 (1965) 227–238. doi:10.1017/CBO9781107415324.004.

[21] F.J. Humphreys, M. Hatherly, Recrystallization and Related Annealing Phenomena, Elsevier, 2004. doi:10.1016/B978-008044164-1/50018-9.

[22] M. Atkinson, Bifurcation of thermal restoration processes in deformed iron and steel, Mater. Sci. Eng. A. VII-262 (1999) 33–38. doi:10.1016/S0921-5093(98)01031-4.

[23] M. Atkinson, On the credibility of ultra rapid annealing, Mater. Sci. Eng. A. VII-354 (2003) 40–47. doi:10.1016/S0921-5093(02)00830-4.

[24] R.H. Goodenow, Recrystallization and grain structure in rimmed and aluminum killed low carbon steel, Trans. ASM. VII-59 (1966) 804–823.

[25] C.S. Smith, Grains, Phases, and Interfaces—an Interpretation of Microstructure, Trans. AIME. VII-175 (1948) 15–51.

[26] S.G. Chowdhury, E. V. Pereloma, D.B. Santos, Evolution of texture at the initial stages of continuous annealing of cold rolled dual-phase steel: Effect of heating rate, Mater. Sci. Eng. A. VII-480 (2008) 540–548. doi:10.1016/j.msea.2007.07.060.

[27] I. Samajdar, B. Verlinden, P. Van Houtte, D. Vanderschueren, γ-Fibre recrystallization texture in IF-steel: an investigation on the recrystallization mechanisms, Mater. Sci. Eng. A. VII-238 (1997) 343–350. doi:10.1016/S0921-5093(97)00455-3.

[28] J.Y. Kang, B. Bacroix, H. Réglé, K.H. Oh, H.C. Lee, Effect of deformation mode and grain orientation on misorientation development in a body-centered cubic steel, Acta Mater. VII-55 (2007) 4935–4946. doi:10.1016/j.actamat.2007.05.014.

[29] J.Y. Kang, D.I. Kim, H.C. Lee, Texture development in low carbon sheet steels for automotive application, in: A. Haldar, S. Suwas, D. Bhattacharjee (Eds.), Microstruct. Texture Steels Other Mater., Springer London, London, 2009: pp. VII-85–101. doi:10.1007/978-1-84882-454-6_5.

[30] R.K. Ray, J.J. Jonas, Transformation Textures in Steels, Int. Mater. Rev. VII-35 (1990) 1–36. <Go to ISI>://WOS:A1990DE71200001.

[31] M. Hillert, The growth of ferrite, bainite and martensite, in: J. Agren, Y. Brechet, C. Hutchinson, J. Philibert, G. Purdy (Eds.), Thermodyn. Phase Transform. Sel. Work. Mats Hillert, EDP Sciences, 2006: pp. VII-111–158.

[32] N.C. Law, D. V Edmonds, The formation of austenite in a low-alloy steel, Metall. Mater. Trans. A. VII-11 (1980) 33–46. doi:10.1007/BF02700436.

[33] M. Hillert, Phase Equilibria, Phase Diagrams and Phase Transformations: Their Thermodynamic Basis, Second ed, Cambridge University Press, New York, 2007.

[34] G.R. Speich, A. Szirmae, Formation of austenite from ferrite and ferrite-carbide aggregates, Trans. AIME. VII-245 (1969) 1063–1073.

[35] R.R. Judd, H.W. Paxton, Kinetics of austenite formation from a spheroidized ferrite-carbide aggregate, Trans. AIME. VII-242 (1968) 206–215.

[36] C.S. Roberts, Effect of carbon on the volume fractions and lattice parameters of retained austenite and martensite, Trans. AIME. VII-197 (1953) 203–204.

[37] W. Chen, K.C. Chan, P. Yu, G. Wang, Encapsulated Zr-based bulk metallic glass with large plasticity, Mater. Sci. Eng. A. VII-528 (2011) 2988–2994. doi:10.1016/j.msea.2010.12.077.

[38] W. Chen, J. Ketkaew, Z. Liu, R.M.O. Mota, K. O'Brien, C.S. da Silva, J. Schroers, Does the fracture toughness of bulk metallic glasses scatter?, Scr. Mater. VII-107 (2015) 1–4. doi:10.1016/j.scriptamat.2015.05.003.

[39] D. Xu, J. Li, Q. Meng, Y. Liu, P. Li, Effect of heating rate on microstructure and mechanical properties of TRIP-aided multiphase steel, J. Alloys Compd. VII-614 (2014) 94–101. doi:10.1016/j.jallcom.2014.06.075.

[40] J. Chiang, J.D. Boyd, A.K. Pilkey, Effect of microstructure on retained austenite stability and tensile behaviour in an aluminum-alloyed TRIP steel, Mater. Sci. Eng. A. VII-638 (2015) 132–142. doi:10.1016/j.msea.2015.03.069.

[41] Y.F. Shen, L.N. Qiu, X. Sun, L. Zuo, P.K. Liaw, D. Raabe, Effects of retained austenite volume fraction, morphology, and carbon content on strength and ductility of nanostructured TRIP-assisted steels, Mater. Sci. Eng. A. VII-636 (2015) 551–564. doi:10.1016/j.msea.2015.04.030.

Chapter VIII

The effect of the heating rate on the mechanical properties of cold-rolled DP-780 steel

Heating rates of 10 °C/s–1000 °C/s were applied to cold-rolled low carbon steels during peak annealing experiments in the partial and fully austenitic range. The resulting microstructure was characterized via Optical Microscopy (OM), Scanning Electron Microscopy (SEM), and Electron Backscatter Diffraction (EBSD) techniques. Tensile tests were performed on sub-size samples. The displacement during testing was measured and analyzed using a camera recording set-up and a Digital Image Correlation (DIC) method, respectively. The results indicated that ultrafast heating produces a rather complex microstructure where carbon gradients can be readily identified. The mechanical properties, particularly the elongation to fracture, were enhanced by the ultrafast heating rates. Moreover, strength and ductility values comparable to those of third generation advanced high strength steels were realized.

VIII-1 Materials and methods

The chemical composition of the initial material is shown in Table 1. The 1.5-mm-thick steel sheets were received in the 50% cold-rolled condition and specimens for heat treatment were cut from this material. Controlled-heating experiments were performed on 120×10×1.5 mm^3 specimens in a Gleeble 3800 thermomechanical simulator; the longest axis of each sample was kept parallel to the rolling direction (RD) of the cold-rolled sheet. The temperature was controlled by an S-type thermocouple spot welded to the midsection of each test sample. Specimens subjected to peak-annealing experiments were heated at various rates (10 °C/s, 400 °C/s, and 1000 °C/s) to a given temperature, held at temperature for <0.3 s, and subsequently quenched (quenching rate: ~-50 °C/s). This sequence was repeated for several temperatures. Table 2 shows the average heating rates and peak temperatures employed in these experiments.

Table 1. Chemical composition (in wt.%).

Material	C	Mn	Si	Cr	Mo	Nb	Fe
DP-780	0.11	1.87	0.03	0.45	0.18	0.03	Rest

VIII-2 Characterization

The microstructural evolution of the samples was evaluated via Optical (OM) and Scanning Electron Microscopy (SEM). Samples were cut from each heat-treated specimen. The zone of homogeneous microstructure in each specimen was determined by plotting the Vickers hardness (HV3) as a function of distance along the TD plane (i.e., the plane perpendicular to TD, see Fig. VIII-1). Subsequent characterization and data collection was performed within the limits of the

homogeneous zone. Samples taken from each tested specimen were prepared, in accordance with standard procedure, by grinding and polishing to a mirror-like finish using a 1-µm diamond paste, and etching to reveal the microstructure. The polished surface was swabbed in a solution of 4% v/v HNO_3 in ethanol (nital 4%) for ~4 s. Electron backscatter diffraction (EBSD) measurements were performed on a FEI Quanta™ 450-FEG-SEM (described in Chapter IV). Scans were performed at a step size of 0.3 µm. The corresponding orientation data were post-processed using the following grain definition: misorientation with neighboring grains: >5°, minimum number of points per grain: four, and confident index (CI): >0.1.

Table 2. Average heating rates and peak temperatures employed during peak-annealing of the DP-780 steel samples.

Heating rate, °C/s	**Peak Temperature, °C**		
10	771	791	826
400	781	803	841
1000	764	783	824

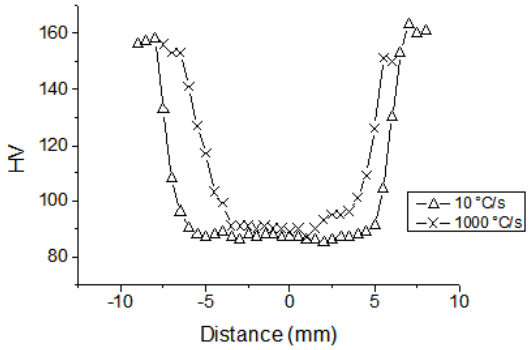

Fig. VIII-1. Hardness (HV3) profile of samples treated at 10 °C/s and 1000 °C/s, showing a zone of homogeneous hardness.

Three rolling direction (RD)-parallel tensile samples were cut from the homogeneous zone (Fig. VIII-1) of each heat-treated specimen. The geometry of the mechanical test samples is shown in Fig. VIII-2.

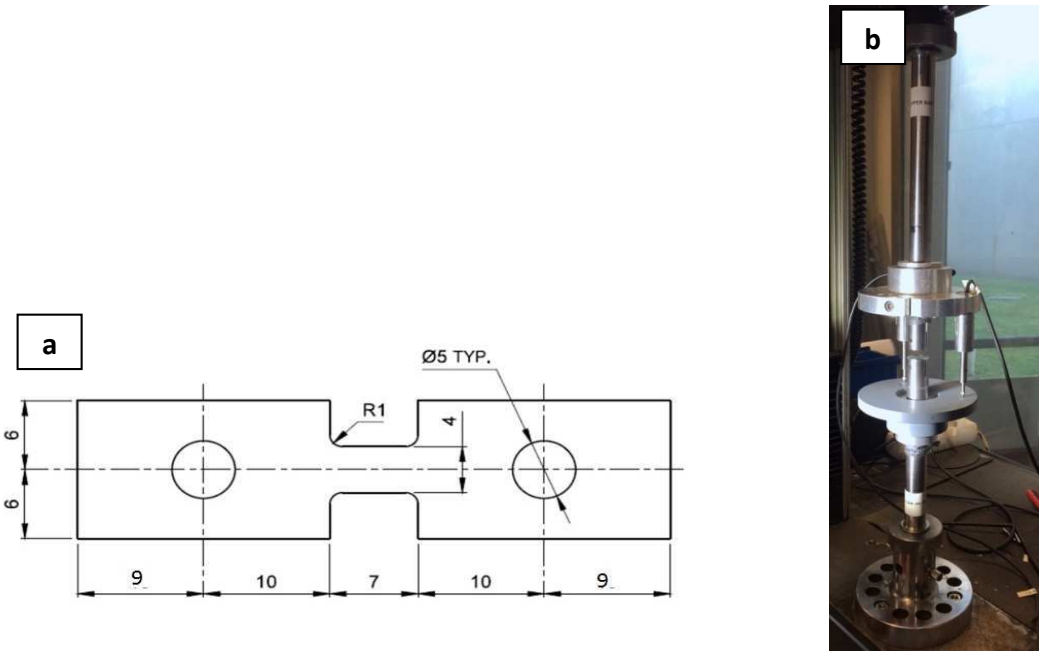

Fig. VIII-2. (a) Dimensions of the mechanical test samples and (b) quasi-static tensile setup.

Specimens were placed between two steel slitted bars and fixed with the same 5-mm-diameter pin. One bar was attached to a load cell, which has a maximum load capacity of 50 kN, and the other bar was fixed. The complete setup was then placed in an Instron 5569 tensile testing machine, as shown in Fig. VIII-2b. Displacements were measured using two linear variable displacement transducers, which were attached to disks placed on the bars. Samples were tested at a displacement rate of 1 mm/min, corresponding to a strain rate of 0.003 s^{-1}.

VIII-3 Analysis

The fraction of recrystallized ferrite was determined from the EBSD data using the TSL-OIM Analysis V6.3 software. Using this software, the raw EBSD data were post-processed (cleaned) and incorrectly indexed points were re-assigned via the grain CI standardization procedure. Grains were defined as the arrangement of at least four points with a misorientation angle of >5° and a confidence index of >0.1. The ferrite fraction accounts for both recrystallized and unrecrystallized grains. Several methodologies have been proposed [1–3] for separating the recrystallized microstructure from the matrix. In the present study, a plot of the Grain Average Misorientation (GAM) versus the area fraction was employed. This approach has been applied elsewhere [4] for identifying recrystallized grains. In this work, grains with GAM of <0.6° and those with a GAM of >0.6° were considered recrystallized and non-recrystallized, respectively. The strain values were determined via Digital Image Correlation (DIC). Images were captured using a 3D Limess DIC set operating at a frame capture rate of 2 Hz. Black speckles (average diameter: ~135 µm) were applied to a sample painted white. This corresponded to 5 pixels of the captured image, consistent with the proposed 3–5 pixel size [5,6]. The DIC analysis was performed via the Match3D software

operating with a zero-mean normalized cross correlation (ZNCC), and subset size, step size, and strain window of 41, 14, and 15, respectively.

VIII-4 Results

VIII-4.1 Initial microstructure

The initial microstructure (see Fig. VIII-4) consists of a homogeneous mixture of deformed ferritic grains (light gray zones in Fig. VIII-4a) and fine pearlite (dark gray zones in Fig. VIII-4a). Bainite and martensite are also present in the microstructure, as revealed via SEM analysis (Fig. VIII-4b).

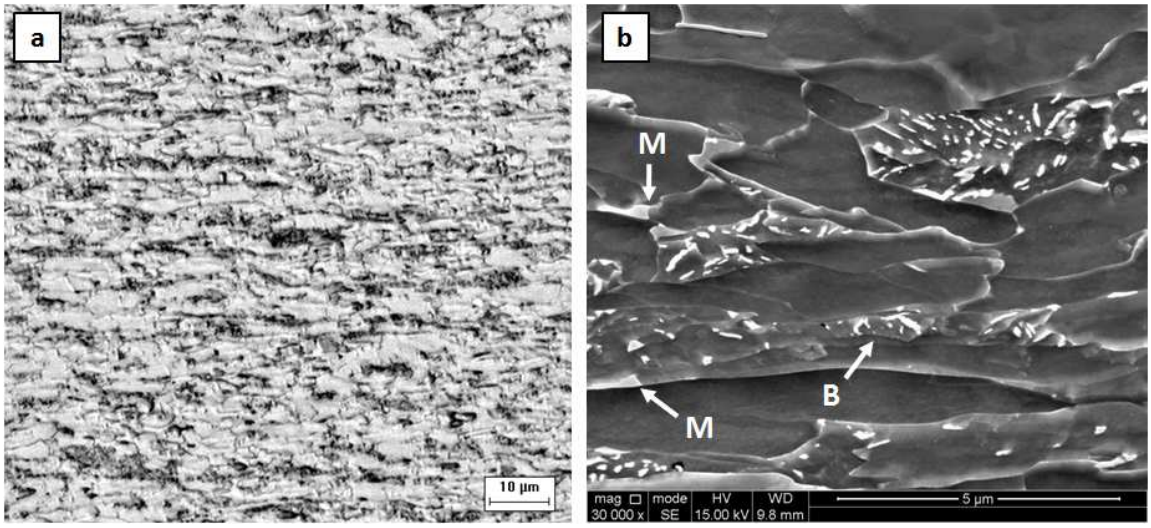

Fig. VIII-4. (a) Optical and (b) scanning electron micrographs of a cold-rolled DP-780 steel sample. M and B denote martensite and bainite, respectively. Scale bar in a and b are 10 and 5 µm, respectively.

VIII-4.2 Microstructure after heat treatments

The optical micrographs of the heat-treated microstructure are shown in Fig. VIII-5. The microstructure consists of a mixture of ferrite and martensite. Most of the ferrite is non-recrystallized at temperatures of ~770 °C (cf. Fig. VIII-5a, 5d, and 5g). However, samples heated at 10 °C/s to temperatures above 791 °C (cf. Fig. VIII-5b and 5c) are almost fully recrystallized. In addition, at all three heating rates, martensite forms along bands in samples heated to ~770 °C (cf. Fig. VIII-5a, 5d, 5e, and 5h). Significant structure refinement occurred in samples heated at 400 °C/s and 1000 °C/s to temperatures above 803 °C (cf. Fig. VIII-5e, 5f, and 5i).

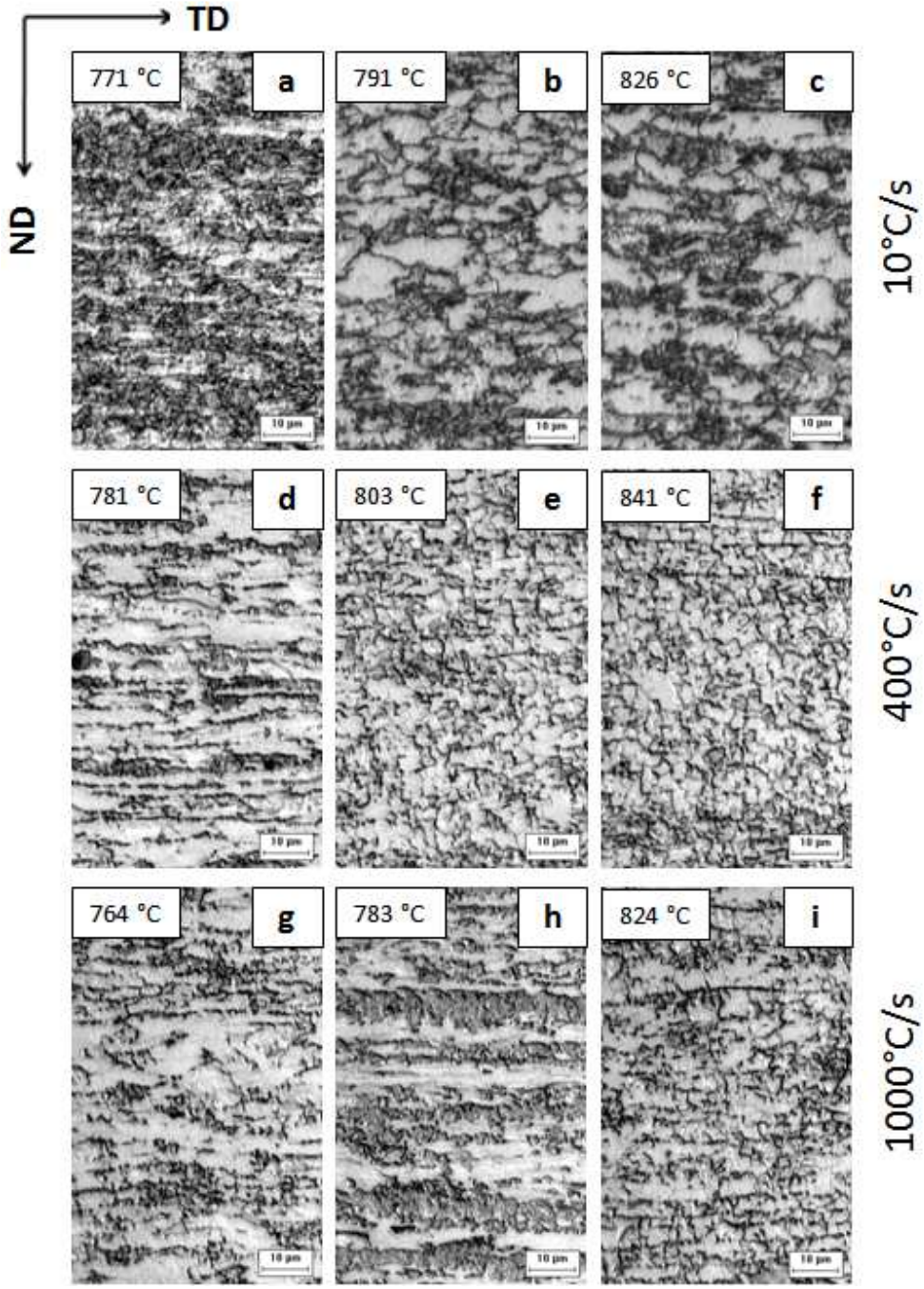

Fig. VIII-5. Optical micrographs of samples heated at 10 °C/s (a–c), 400 °C/s (d–f), and 1000 °C/s (g–i) to different peak temperatures, as indicated in each micrograph. Etched with nital 4%. Scale bar is 10 μm.

SEM images of the microstructure (see Fig. VIII-6) revealed that fully recrystallized ferrite occurs in only some of the samples. The dark-gray regions, initially associated with martensite (see Fig. VIII-5), consist of a mixture of martensite, bainite, retained austenite, and cementite.

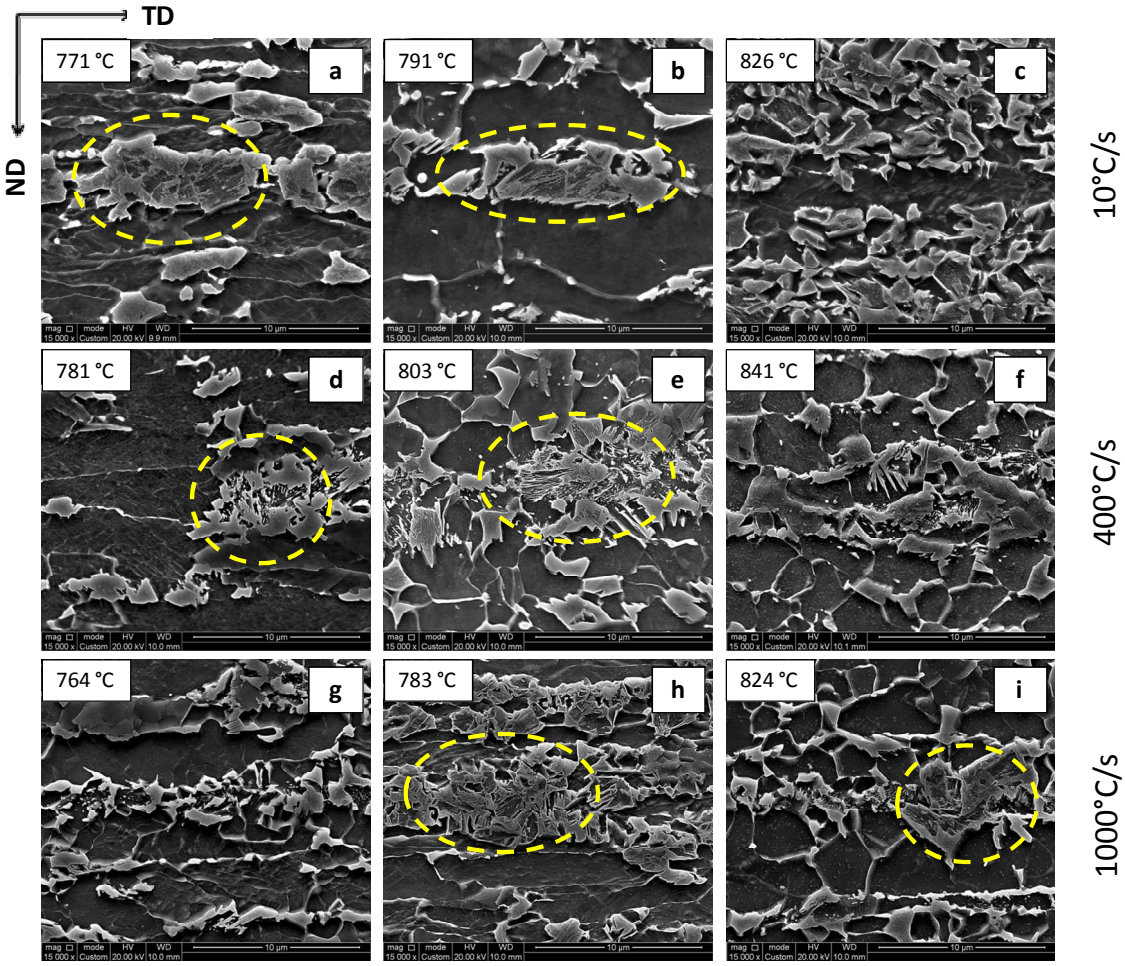

Fig. VIII-6. Scanning electron micrographs of samples heated at 10 °C/s (a–c), 400 °C/s (d–f), and 1000 °C/s (g–i) to different peak temperatures, as indicated in each micrograph. Etched with nital 4%. Scale bar is 10 µm.

The phase fraction of martensite and the corresponding average grain diameter are shown in Fig. VIII-7. In samples heated at 400 °C/s and 1000 °C/s, the fraction increases with increasing temperature, reaching a maximum of ~45% at ~803 °C and 770 °C, respectively, and decreases slightly thereafter. The martensite fraction of samples heated at 10 °C/s exhibits the opposite tendency, i.e., this fraction decreases to a minimum of ~42% at 791 °C and increases with increasing temperature thereafter. For all temperatures and heating rates, the measured fractions are higher than the initial fraction of the mixture constituents (dashed line in Fig. VIII-7).

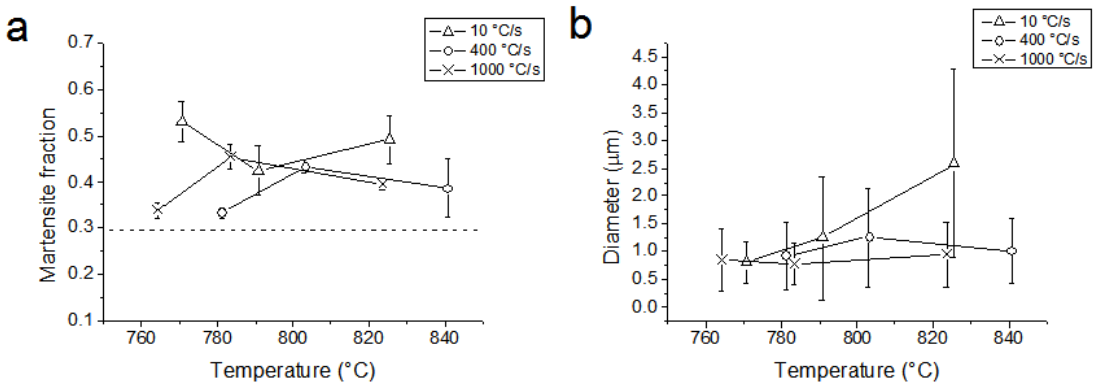

Fig. VIII-7. Temperature dependence of the martensite (a) fraction and (b) average diameter associated with different heating rates. Dashed line shows the initial fraction of the other microstructural constituents.

VIII-4.3 Mechanical properties

The mechanical properties are shown in Fig. VIII-8. As the figure shows, the samples have YS and UTS values of 250–600 MPa and 750–1150 MPa, respectively, and exhibit elongations of 15–38%. The samples heated at 10 °C/s and 1000 °C/s exhibit the largest temperature-induced variation in strength. In addition, the YS of samples heated at 400 °C/s decreases with increasing temperature, whereas the UTS is almost constant and the elongation to fracture increases. The elongation to fracture of samples heated at 1000 °C/s also increases with increasing temperature. In samples heated at 10 °C/s, the elongation increases to ~30% at 791 °C and decreases thereafter.

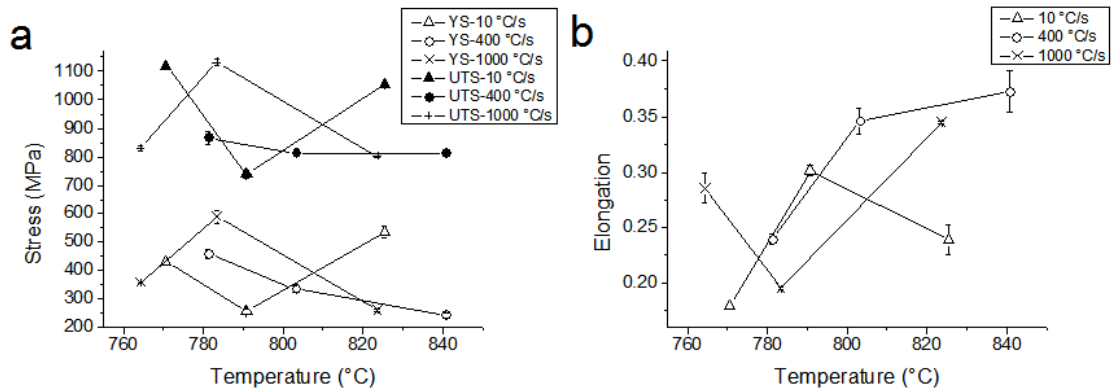

Fig. VIII-8. Temperature dependence of the (a) yield (outlined) and ultimate tensile stress (filled) and (b) elongation to fracture of samples treated at different heating rates.

VIII-5 Discussion

The heat-treated microstructure is composed of a complex blend of ferrite, martensite, bainite, and undissolved cementite, as indicated in Fig. VIII-6 (dashed circles) and Fig. VIII-9. The prior austenite grains are transformed into a mixture of ferrite, bainite, and martensite during cooling,

and the distribution of phases and constituents indicates that carbon gradients occur in these grains. The lowest-carbon phase (ferrite) is surrounded by bainite and, in some cases, by an outer layer of martensite (cf. Fig. VIII-9b and 9c). This indicates that UFH will produce a microstructure that differs from the classical ferrite plus martensite dual-phase steel microstructure. Therefore, UFH will have an impact on the mechanical properties.

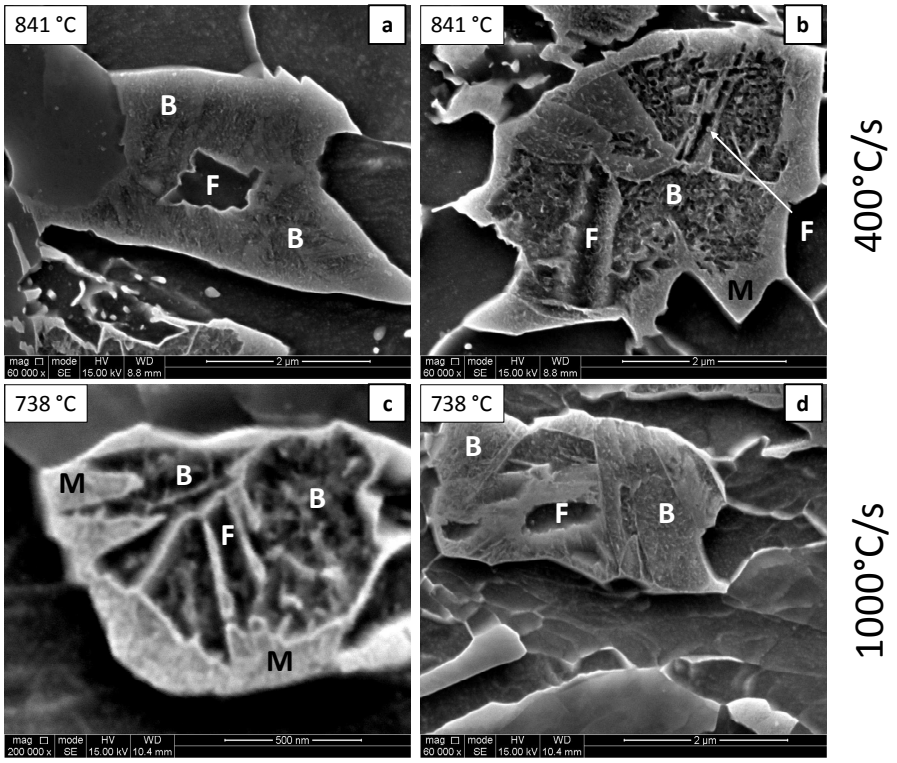

Fig. VIII-9. Microstructure of samples heated at 400 °C/s to 841 °C (a and b) and 1000 °C/s to 738 °C (c and d). Ferrite (F) formation at the center of each zone of mixed martensite (M) and bainite (B) suggests that carbon gradients occur in the austenite. Etched with nital 4%. Scale bar in c is 500 nm, others 3 μm.

Variations in the mechanical properties are attributed to microstructural changes. In subsequent paragraphs, the hard second constituent will be referred to as martensite, although this constituent may also contain bainite. Fig. VIII-8 shows that the YS of samples heated at 10 °C/s decreases with increasing temperature of up to 791 °C and increases thereafter, reaching a maximum of ~530 MPa. In addition, the fraction of non-recrystallized ferrite is expected to have an impact on the YS. Fig. VIII-6a shows that ferrite is only slightly recrystallized at 770 °C, but the microstructure is almost completely recrystallized at 791 °C (cf. Fig. VIII-5b and 6b). This increase in the fraction of recrystallized ferrite leads to a decrease in the YS at 791 °C. The increase in the fraction of ferrite also results in a temperature-dependent decrease in the YS of samples heated at 400 °C/s. At temperatures higher than 791 °C, the large fraction of martensite also affects the YS, leading to the increase shown in Fig. VIII-8a. In the case of samples heated at 1000 °C/s, the YS increases from ~350 MPa to ~590 MPa at temperatures ranging from 764 to 783 °C. Previous

studies [7,8] have shown that the onset temperature of ferrite recrystallization increases with increasing heating rate. A comparison of Fig. VIII-6g and 6h reveals a modest change in the fraction of recrystallized ferrite. However, the fraction of martensite has increased significantly (i.e., from ~34% to ~45%) leading to an increase in the YS. When the temperature is increased to 824 °C, the YS decreases to a value of ~260 MPa, which is similar to the YS of annealed ferrite.

The UTS values (denoted by filled symbols in Fig. VIII-8a) exhibit similar tendencies to the YS values. For example, the UTS of samples heated at 10 °C/s decreases from ~1120 MPa at 771 °C to ~740 MPa at 791 °C, and then increases to ~1050 MPa at 826 °C. The variation in the martensite fraction of samples heated at 10 °C/s and 1000 °C/s (Fig. VIII-7a) is closely correlated with the variation in the corresponding UTS values. The average martensite fraction of samples heated at 1000 °C/s to 783 °C is 8% lower than that of the sample heated at 10 °C/s to 771 °C. However, these samples have comparable UTS values (~1130 MPa vs. ~1120 MPa). Fig. VIII-7b shows that the samples heated at 10 °C/s and 1000 °C/s have average martensite diameters of ~1.2 μm and ~0.8 μm, respectively; the finer martensite grain diameter of the samples heated at 1000 °C/s might account for the higher UTS values revealed when the effect of martensite on the strength is considered. Similarly, the UTS (~740 MPa) of samples heated at 10 °C/s to 791 °C is slightly lower than the UTS (~800 MPa) of samples heated at 1000 °C/s to 824 °C. This lower value is obtained despite the fact that the martensite fraction of the former is 2% higher than that of the latter. Therefore, the higher UTS value of samples heated at 1000 °C/s is attributed to its finer martensite grain diameter, compared with that of samples heated at 10 °C/s. The values of strength measured in samples heated at 400 °C/s exhibit a relatively strong correlation to the martensite fractions shown in Fig. VIII-7a. A UTS value of ~870 MPa and martensite fraction of ~33% are obtained for samples heated to 781 °C. Similarly, a UTS and martensite fraction of ~830 MPa and ~34%, respectively, are obtained for samples heated at 1000 °C/s to 764 °C. Consistent with the martensite fractions and average diameters, the UTS values of samples heated at 400 °C/s varied only slightly at temperatures above 781 °C.

The fraction of recrystallized ferrite influences the ductility of the material. This fraction and, hence, the ductility are expected to increase with increasing temperature . Fig. VIII-8b shows that the final elongation increases with increasing temperature, except for the sample heated at 1000 °C/s, where the ductility decreases by ~10% at temperatures ranging from 764 °C to 783 °C. The fraction of martensite plays a significant role in the final elongation. For example, samples heated at 400 °C/s to 781 °C and at 1000 °C/s to 764 °C exhibit final elongations of ~24% and ~29%, for martensite fractions of 33% and 34%, respectively. The 9%-drop in ductility of samples heated at 1000 °C/s to temperatures of 764 °C–783 °C results from an increase (from 34% to 45%) in the martensite fraction. At temperatures ranging from 783 °C to 824 °C, the sharp increase in ductility results primarily from the recrystallization of ferrite (cf. Fig. VIII-6i) and secondarily from the ~5% decrease in martensite fraction (cf. Fig. VIII-7a). The martensite fraction of samples heated at 10 °C/s to temperatures ranging from 791 °C to 826 °C has also increased by ~5%. However, the ~6% variation in elongation may be attributed to intrinsic variations in the tensile tests. The ductility of samples heated at 400 °C/s increase, in general, with increasing heating rate. Nevertheless,

recrystallized ferrite grains contribute to the ductility and, hence, the increase in the final elongation is steeper than that expected from the martensite fraction (cf. circles in Fig. VIII-7a).

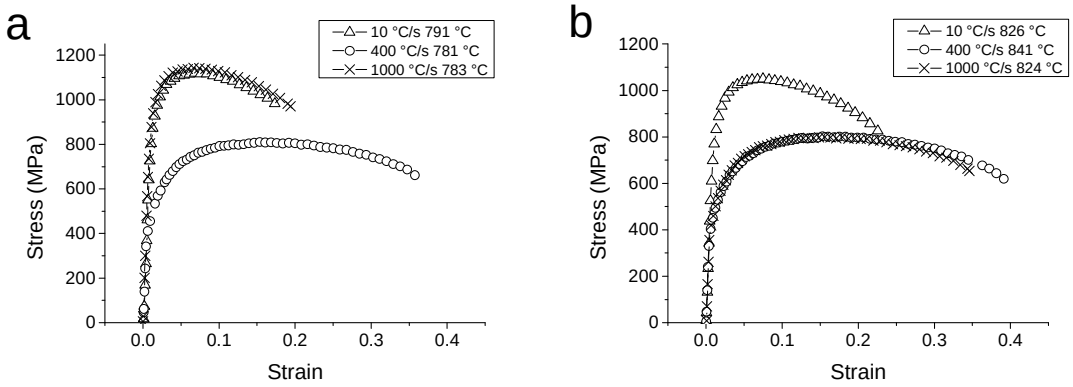

Fig. VIII-10. Engineering stress-strain curves obtained from tensile testing of samples heated at 10 °C/s (triangles), 400 °C/s (circles), and 1000 °C/s (crosses). Curves obtained at the (a) lower and (b) upper peak-annealing temperatures employed in the heating experiments.

Fig. VIII-10 shows the stress-strain curves obtained from tensile testing of material subjected to different heating rates. The curves corresponding to samples heated to the lower temperature range (783 °C–~791 °C) and the upper temperature range (824 °C–~841 °C) are shown in Fig. VIII-10a and Fig. VIII-10b, respectively. The UTS and the ductility vary from ~800 MPa to ~1100 MPa, and ~20% to ~35%, respectively. These values can be used define the range of mechanical properties that can be realized if heating rates of up to 1000 °C/s are applied. A comparison of the results obtained in this study with data from current steel grades used in the automotive industry [9] is shown in Fig. VIII-11. After UFH, mechanical properties comparable to those of third generation advanced high strength steels are realized for the cold-rolled DP-780 steel.

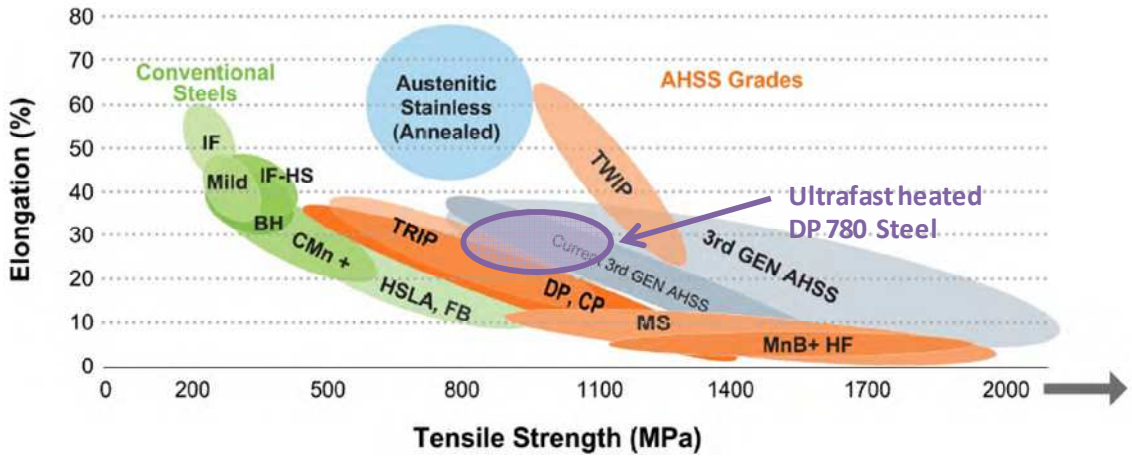

Fig. VIII-11. Tensile strength (MPa) versus elongation (%) of current steel grades [9], including the mechanical results of ultrafast heating experiments on cold-rolled DP-780 steel.

VIII-6 Summary

The effect of the heating rate on the mechanical properties was determined for a DP-780 steel. Prior to this determination, the cold-rolled microstructure was heated at rates of 10 °C/s, 400 °C/s, and 1000 °C/s to different peak temperatures, and then quenched. These heating rates generated microstructures characterized by a mixture of ferrite (recrystallized and non-recrystallized), martensite, bainite, and cementite. The mechanical properties, measured via tensile tests, vary with the relative fractions of these phases. Analysis of the test results revealed that the yield stress and elongation to fracture are mainly controlled by the fraction of recrystallized ferrite and to a lesser extent by the fraction of martensite. The ultimate tensile stress is mainly influenced by the fraction and average grain diameter of martensite. In addition, samples heated at 400 °C/s and 1000 °C/s exhibited significantly higher ductility and moderately higher strength, respectively, than those heated at 10 °C/s. A comparison with data from steels for automotive applications reveals that the properties achieved after UFH are comparable to those of third generation advanced high strength steels.

VIII-7 References

[1] D.P. Field, Quantification of partially recrystallized polycrystals using electron backscatter diffraction, Mater. Sci. Eng. A. 190 (1995) 241–246. doi:10.1016/0921-5093(94)09601-R.

[2] S.I. Wright, M.M. Nowell, D.P. Field, A review of strain analysis using electron backscatter diffraction., Microsc. Microanal. 17 (2011) 316–329. doi:10.1017/S1431927611000055.

[3] H. Jazaeri, F.J. Humphreys, Quantifying recrystallization by electron backscatter diffraction, J. Microsc. 213 (2004) 241–246. doi:10.1111/j.0022-2720.2004.01296.x.

[4] R. Petrov, L. Kestens, Y. Houbaert, Recrystallization of a cold rolled trip-assisted steel during reheating for intercritical annealling., ISIJ Int. 41 (2001) 883–890. doi:10.2355/isijinternational.41.883.

[5] P. Reu, All about speckles: Speckle size measurement, Exp. Tech. 38 (2014) 1–2. doi:10.1111/ext.12110.

[6] G. Lionello, L. Cristofolini, A practical approach to optimizing the preparation of speckle patterns for digital-image correlation, Meas. Sci. Technol. 25 (2014). doi:10.1088/0957-0233/25/10/107001.

[7] D. Muljono, M. Ferry, D.P. Dunne, Influence of heating rate on anisothermal recrystallization in low and ultra-low carbon steels, Mater. Sci. Eng. A. 303 (2001) 90–99. doi:10.1016/S0921-5093(00)01882-7.

[8] T. Senuma, K. Kawasaki, Y. Takemoto, Recrystallization behavior and texture formation of rapidly annealed cold-rolled extra low carbon steel sheets, Mater. Trans. 47 (2006) 1769–1775. doi:10.2320/matertrans.47.1769.

[9] S. Keeler, M. Kimchi, R. Kuziak, R. Kawalla, S. Waengler, Y. Weng, H. Dong, Y. Gan, Advanced high strength steels for automotive industry, Arch. Civ. Mech. Eng. 8 (2014) 511.

doi:10.1016/S1644-9665(12)60197-6.

Chapter IX

Conclusions and future work

IX-1 General conclusions

The approach to third generation high strength steels via ultrafast heating (UFH) was investigated in several alloy systems. Heating rates ranging from 1 °C/s to ~10^3 °C/s were applied either by Joule effect (Gleeble) or magnetic induction (Dilatometer), and the samples were then quenched. Given the nature of the tests, the thermal cycles were classified as 'anisothermal peak-annealing' experiments, where extremely short holding times were employed prior to cooling. Emphasis was placed on the microstructural evolution, as well as changes in the texture and mechanical properties of the alloys. The results were discussed in previous chapters, and the main findings are summarized in the following paragraphs.

Chapter IV describes the effect of heating rate on the microstructure and textures of ultra low carbon (ULC) steel. The initial microstructure of this material is 50% cold-rolled ferrite, which is an ideal system for studying the effect of heating velocity on the recrystallization of a single-phase material. The results revealed that the fraction of recrystallized ferrite changes slightly when the heating rate is increased. This results in displacement of the recrystallized fraction versus temperature curve to higher temperatures, as reported in several studies on ULC and low carbon (LC) steel. The heating rate had negligible effect on the average grain diameter of recrystallized ferrite. Texture evolution during recrystallization was evaluated via electron backscatter diffraction (EBSD). This evaluation revealed that sharp {111}⟨uvw⟩ ND-fiber components formed in the recrystallized ferrite, irrespective of the heating rate. However, some of the {hkl}⟨110⟩ components occurred in the calculated ODFs of the UFH-recrystallized ferrite grains. The presence of these components was attributed to the effect of UFH on the stored energy; this effect enables the recrystallization of grains that would have been overlapped by the growth of {111}⟨uvw⟩-oriented grains during conventional heating.

The thermodynamics and kinetics of austenite formation under conventional and UFH rates are discussed in Chapter V. The initial microstructure, i.e., ferrite plus pearlite, was selected because this is the most produced as-rolled microstructure in low and medium carbon steel. Therefore, this microstructure is the natural starting point in the production of cold-rolled and annealed third generation AHSS. Microstructural characterization of this material provided unique evidence of austenite nucleation and formation, by means of a massive transformation in the subsequent stages. The observations were discussed from a thermodynamic point of view and the driving forces were determined for each process associated with austenite formation during heating. The driving forces in UFH experiments are larger than those in CH experiments. Taking this into account, the results suggested that austenite nucleation at α/θ interfaces (which are less favorable

than α/α interfaces) is just as likely as austenite nucleation in bulk pearlite. The thermodynamics of the process indicated that austenite formation, via a massive transformation, is possible. Moreover, the kinetics associated with austenite formation via diffusion-controlled movement of the α/γ interface was described using a simplified model and simulated with the Dictra software. The simulations successfully predicted the effect of increased heating rate on the austenite fraction curves, thereby validating the simplified model and concurring with experimental results. The high temperature-dependent interface velocities predicted for UFH experiments, which (correspondingly) yield low temperature-dependent transformed-austenite fractions, were also explained by the simplified model. A_m (the temperature where austenite will be more stable than ferrite in equilibrium with austenite) was proposed as the temperature where the thermodynamic mechanism transitions from diffusion controlled to interface controlled. Continuous transformation diagrams for austenite formation during heating at different rates were constructed from the experimental data of both steels.

Chapter VI details the microstructural evolution and texture changes occurring in an alloy with a chemical composition typical of TRIP-assisted steel grades. The initial microstructure was composed of 70% cold-rolled ferrite plus pearlite. Therefore, the effect of elevated heating velocities on a mixture of constituents, rather than on individual components only (as in the case of previous studies), could be investigated. As in the case of experiments on ULC steel, UFH leads to the formation of high-stored-energy components in the initial stages of recrystallization. The occurrence of the rotated Goss component, not observed in ULC steel, is consistent with the higher carbon content of the studied steel. The formation of austenite is also consistent with the theory developed in Chapter V. In fact, the nucleation of austenite at the α/α interface is favored from a thermodynamic point of view. The formation of proeutectoid ferrite in samples heated above 1000 °C is attributed to the carbon gradients in austenite, rather than the incomplete formation of austenite during heating. Texture inheritance is also discussed. The results revealed that the texture components in martensite after quenching from initial stages of austenite formation are virtually the same as those measured during the final stages. In addition, the results suggest that an interaction occurs between austenite nucleation and the cold-rolled ferrite.

The microstructure and texture characterization, as well as the tensile properties of a 50% cold-rolled low carbon steel subjected to conventional heating (CH) and UFH conditions are discussed in Chapter VII. The effect of the initial microstructure on microstructural and texture evolution was determined for both ferrite plus pearlite and ferrite plus martensite aggregates. In this work, the approach to obtaining third generation AHSS considered two factors, namely: (1) the selected steel has the chemical composition of a standard grade of TRIP-assisted steel, and (2) the processing parameters are all suitable for industrial application. Specifically, a preheating step was added to the thermal cycle, along with heating rates achievable on the industrial scale. A slightly longer holding time, compared with that employed for experiments described in previous chapters, was also applied during peak annealing. The results revealed that grain refinement occurs when the heating rate is increased. The ferrite plus martensite initial microstructure undergoes slightly more refinement than other microstructures. The textures of the ferrite plus

martensite microstructure changed only slightly after the different thermal cycles. However, the heating rate resulted in significant changes in the texture components of the ferrite plus pearlite microstructure. The texture changes occurring in the initial microstructures are consistent with those described in previous studies. In addition, UFH resulted in considerable and simultaneous improvement in the strength and ductility. Fractography in the necked region of tensile samples revealed that the strain was microstructurally localized in samples subjected to CH, but more homogeneously distributed in samples treated at heating rates above 400 °C/s. Furthermore, a complex microstructure is formed owing to the occurrence of carbon gradients during UFH and the subsequent transformation of several austenite transformation products during cooling. The ferrite plus martensite initial microstructure has the best combination of strength and ductility, owing possibly to its finer grain size, compared with that of other initial microstructures. Nevertheless, both initial microstructures have mechanical properties that are comparable to those of third generation AHSS.

Finally, the effect of the heating rate on the microstructure and mechanical properties of a cold-rolled DP-780 steel is described in Chapter VIII. The microstructural evolution is consistent with that presented in previous Chapters. Furthermore, the distribution of phases and microconstituents after quenching is taken as indirect evidence of carbon gradients in austenite. The mechanical properties are attributed to the rather complex microstructure resulting from ultrafast heating. Yield stresses, ultimate tensile stresses, and elongations to fracture ranging from ~250 to ~600 MPa, ~800 MPa to ~1100 MPa, and ~20% to ~35%, respectively, are measured. A comparison with data from steels for automotive applications reveals that the properties realized after ultrafast heating are comparable to those of third generation advanced high strength steels.

IX-2 Challenges upon the application of ultrafast heating

The application of ultrafast heating rates plus relatively short holding times to cold-rolled steel plate is still a relatively new research field. However, the promising mechanical properties that have been obtained are a strong motivation to expand the current understanding of the influence of processing parameters. A list of key points regarding the application of UFH process to industrial lines has been given in Chapter I-2. In the present study, the point (iv) "Effect of UFH on the microstructure" has been investigated and the conclusions obtained thereof might serve as complementary information to develop the following points:

i. Other potential applications of UFH processes in flat products: Besides the production of third generation advanced high strength steels, the results suggest that UFH can have other specific applications. Three important findings were reported in Chapters IV and VI. (1) the recrystallization kinetics increase with the heating rate, (2) grain refinement effect increases as the heating rate increases and (3) negligible texture changes. It can be, then, predicted that UFH might be suitable for processes such as recrystallization annealing and tempering, with the corresponding advantages of very short thermal cycles.
   Microstructural observation revealed that, in the pearlitic structure which is partially transformed into austenite during UFH (Chapters V, VI, VII), the cementite also undergoes

spheroidization before full dissolution. The possibility of applying UFH to obtain steel in the soft-annealed (spheroidized) condition should be further evaluated.

ii. Large-scale mechanical characterization: Although anisotropy measurements were not carried out, texture analysis (Chapters IV) showed that recrystallized ferrite under UFH and CH rates are virtually the same. The measured orientations are close to <111>//RD, which predicts high *r* values and, consequently, good deep-drawability performance. This complements the proposed application of UFH to recrystallization annealling mentioned in (i), yet mechanical tests are still necessary.

iii. Transferability of laboratory-scale treatments into industrial standards: Chapter VII revealed that the optimum combination of strength and ductility occurs in the range of 800 °C/s. This sole result provides a suitable starting point of the design of future production lines. The evaluation of the microstructural changes introduced in the microstructure after a pre-heating stage (Chapter VII) indicates that no significant changes are introduced in the microstructure. Therefore, another degree of freedom for cold-rolled steel plate processing is enabled.

The inhomogeneous heat distribution in the heat-treatment specimens was tackled by cutting-off the material which was microstructurally heterogeneous. However, this cannot be done in an industrial process. In the experimental set-up, the heat was introduced either by magnetic induction (Dilatometry) or Joule effect (Gleeble). Between these two heat input principles, magnetic induction is the one which has better chances to be applied in industrial conditions. Therefore, further experiments on the application of UFH should focus on the understanding of the effect of induction heating (and magnetic fields) on the microstructure of plate steel.

As discussed in Chapter I, the industrial production of ultrafast heated material is so far restricted to the 'flash bainite' process by G. Cola Jr. This approach includes water quenching after the heating stage (cf. Fig I-2). The results found in Chapters V and VI revealed the formation of massive ferrite in specimens heated at 150 °C/s, 450 °C/s and 1500 °C/s after quenching the samples at ~-160 °C/s and ~-3.000 °C/s. In conclusion, extreme fast cooling rates (~-3.000 °C/s) do not produce significant differences when compared to moderated rates (~-160 °C/s), which are easier to achieve in industrial conditions. Going one step further, cooling rates of ~-60 °C/s were applied to ULC steel (Chapter IV), so the possible application of UFH to recrystallization annealing might also consider moderate cooling rates.

IX-3 Future research

The present study summarizes the contribution of several researchers at Ghent University, leaded by Prof R. Petrov and Prof L. Kestens, on the effect of heating rate in the microstructure, textures and mechanical properties of steel. The experiments developed hereby provide, among other results, fundamental understanding on the texture formation at early stages of ferrite recrystallization and the thermodynamics of austenite formation. These findings complement and

validate the previous observations. Nonetheless, there are still many fundamental questions to be answered. Among these I would like to mention three topics that can be further researched.

IX-3 .1 Recrystallization

As discussed in Chapter II, there is no consensus on the observed recrystallization behavior of cold worked metals. An interesting approach to this fundamental problem can be the study of the effect of heating rate and stacking fault energy (SFE) on the recrystallization. A suitable starting point could be a comparative study on the recrystallization of pure copper (high SFE) and brass (low SFE). The reason stems in that the metals with low and high SFE will behave differently on recovery, and thus on recrystallization.

IX-3 .2 Austenite formation

It was shown that the transition from diffusion controlled to massive formation of austenite is given by a thermodynamic threshold, which was termed A_m. However, the effect of segregation of alloying elements was not taken into account. It is suggested that the mapping of chemical composition, combined with thermodynamic calculation of 'local' A_m values, can provide a more realistic estimation of the transition from mechanism, hence a more accurate prediction of the microstructure.

The transition from one mechanism to another is claimed to occur under UFH rates. Nonetheless, the *critical heating rate* at which one can expect the massive formation of austenite on heating is not known. This fundamental question can be tackled from the experimental as well as theoretical point of view. The correct assessment of the effect of microstructural parameters on the critical heating rate which triggers the massive formation of austenite is a challenge for future alloy design.

The study of crystallographic aspects of austenite nucleation can be approached by the systematic measurement of the textures in martensite after quenching. The wealth of EBSD data which is now available can be rationalized, for instance, from the perspective of the origin of texture memory effect in steel. UFH applied to interrupted-quenching experiments provide unique conditions to apply parent microstructure reconstruction algorithms, thereby enhancing the understanding of the role of crystallography in early events of austenite formation.

IX-3 .3 Austenite decomposition

The complex mixture of phases and microconstituents after of UFH and quenching is explicitly shown in Chapters V, VI, VII, and VIII. However, the fractions of such constituents were not determined, simply because the characterization techniques either do not have enough resolution or are not statistically representative. The products of austenite decomposition are strongly influenced by chemical inhomogeneities in austenite, particularly carbon gradients. Such carbon

gradients can be readily estimated (up to certain extent) by the application of simple tools as DICTRA. One way of estimating the transformation products could be the application of different modeling approaches (Phase Field, Cellular Automata, etc) to calculate the fraction of phases and constituents after the different thermal cycles. Those models are to be complemented with experimental phase quantification.